

STUDY OF THE ASTROPHYSICALLY IMPORTANT STATES IN  
 $^{26}\text{Si}$

STUDY OF THE ASTROPHYSICALLY IMPORTANT STATES IN  
 $^{26}\text{Si}$  VIA THE  $p(^{27}\text{Si},d)^{26}\text{Si}^*$  REACTION AND THE  $p(^{25}\text{Al},p)^{25}\text{Al}$   
ELASTIC SCATTERING

By

JUN CHEN, B. Sc., M. Sc.

A Thesis

Submitted to the School of Graduate Studies  
in Partial Fulfilment of the Requirements  
for the Degree  
Doctor of Philosophy

McMaster University

© Copyright by Jun Chen, June 2009

The thesis of Jun Chen was reviewed and approved\* by the following:

Dr. Alan Chen  
Associate Professor, McMaster University  
Thesis Advisor, Chair of Committee

Dr. James Waddington  
Professor, McMaster University  
Committee member

Dr. Rajat Bhaduri  
Professor, McMaster University  
Committee member

Dr. Chang-Qing Xu  
Professor, McMaster University  
Committee member

\*Signatures are on file in the Graduate School.

**DOCTOR OF PHILOSOPHY (2009)**  
**(Physics and Astronomy)**

**McMaster University**  
**Hamilton, Ontario**

**TITLE:** Study of the Astrophysically Important  
States in  $^{26}\text{Si}$  via the  $p(^{27}\text{Si},d)^{26}\text{Si}^*$  Reaction  
and the  $p(^{25}\text{Al},p)^{25}\text{Al}$  Elastic Scattering

**AUTHOR:** Jun Chen  
B. Sc., Peking University  
Beijing, P. R. China, 2002  
M.Sc., McMaster University  
Hamilton, Canada, 2006

**SUPERVISOR:** Dr. Alan Chen

**NUMBER OF PAGES:** XVIII, 200

# Abstract

The radioactive  $^{26}\text{Al}$  is an important probe for the interstellar medium of our galaxy since it is observed through the emission of 1.8 MeV gamma rays from the decay of  $^{26g}\text{Al}$  produced by the proton capture on  $^{25}\text{Mg}$ . But the production of the galactic  $^{26}\text{Al}$  is now still not well determined partially due to the lack of knowledge of the important states in  $^{26}\text{Si}$  which dominate the large uncertainty in the  $^{25}\text{Al}(p,\gamma)^{26}\text{Si}$  reaction rate at nova temperatures.

In nova explosions, the proton capture of  $^{25}\text{Al}$  competes with its  $\beta$  decay and bypasses the production of  $^{26g}\text{Al}$ , since the capture product  $^{26}\text{Si}$  decays quickly to  $^{26m}\text{Al}$  instead of its ground state, without the emission of the 1.8 MeV gamma ray. But at even higher temperatures, such as in supernova explosions,  $^{26m}\text{Al}$  can be excited to the higher excited states by thermal excitation and then quickly de-excite to the ground state, thereby enhancing the production of  $^{26g}\text{Al}$ . The energy levels in  $^{26}\text{Si}$  in the Gamow window corresponding to these temperatures therefore need to be well understood in order to determine the  $^{25}\text{Al}(p,\gamma)^{26}\text{Si}$  reaction rate, and thus the production rate of  $^{26}\text{Al}$  in these explosive environments.

Two experiments were performed to study the important states in  $^{26}\text{Si}$  : one is the  $p(^{27}\text{Si},d)^{26}\text{Si}^*$  reaction at the NSCL, aiming to construct the level scheme of low lying states around the proton threshold; the other experiment is a measurement of the elastic scattering of  $^{25}\text{Al}+p$  with CRIB at RIKEN in order to obtain information on states in a broad range above the proton threshold. Details of these two experiments and their data analyses will be presented in this thesis.

*To my family.*

# Acknowledgments

First, I would like to thank my supervisor Dr. Alan Chen. He is not only a good supervisor but also a good friend. He is always able to give you kind suggestions and talk with you like a friend. As a supervisor, he always very nicely gives me clear and patient guidance that helps me conduct my research and directs me to fulfill this thesis. Thanks to his kind support to us, we have attended many wonderful conferences and summer schools, and participated in lots of experiments at different laboratories, which have greatly widened my horizon on physics research and enriched my knowledge base and experience for my future career.

I would also like to thank all of our collaborators at the NSCL laboratory and the CNS laboratory for their help in making our experiments successful. I especially thank Dani and Matt at NSCL and Yamaguchi-san at CNS.

I also owe my thanks to all the members in our group, Chris, Kiana and Daid, with whom I share the nice office and our happy graduate lifetimes, as well as many unforgettable experiment shifts at RIKEN, MSU and TRIUMF.

I would like to thank all other members on my supervisory committee.

Last but not least, I thank my parents and my brother for supporting me all the time and thank my beloved wife who always gives me the greatest support in my life. I thank all the people who have given me help and support during my studies.

# Table of Contents

Descriptive Note	ii
Acknowledgments	v
List of Figures	x
List of Tables	xvii
<b>Chapter 1</b>	
<b>Introduction and Motivation</b>	<b>1</b>
1.1 Stellar evolution, nucleosynthesis and abundance . . . . .	1
1.1.1 Quiescent burning processes . . . . .	2
1.1.2 Explosive burning processes . . . . .	3
1.1.3 Thermonuclear reactions . . . . .	6
1.2 Scientific motivation for the study of $^{26}\text{Si}$ . . . . .	7
1.2.1 $^{26}\text{Al}$ in the galaxy . . . . .	7
1.2.2 The importance of the $^{25}\text{Al}(p, \gamma)^{26}\text{Si}$ reaction . . . . .	9
1.2.3 Nuclear structure of $^{26}\text{Si}$ . . . . .	11
<b>Chapter 2</b>	
<b>Two experiments for the study of <math>^{26}\text{Si}</math></b>	<b>14</b>
2.1 The $p(^{27}\text{Si}, d)^{26}\text{Si}^*$ experiment at the NSCL facility . . . . .	14
2.1.1 Kinematics . . . . .	15
2.1.2 The NSCL facility . . . . .	17
2.1.2.1 S800 spectrograph . . . . .	18
2.1.2.2 SeGA detector array . . . . .	20
2.1.3 Experiment details . . . . .	20
2.2 The $p(^{25}\text{Al}, p)^{25}\text{Al}$ experiment at the CRIB facility . . . . .	21

2.2.1	Kinematics and the thick target method . . . . .	22
2.2.2	The CRIB facility . . . . .	25
2.2.2.1	Beam selector — the Wien Filter . . . . .	27
2.2.2.2	Experimental chamber (F3) . . . . .	28
2.2.3	Experiment details . . . . .	30
2.2.4	Electronics and Data Acquisition System (DAQ) . . . . .	31
<b>Chapter 3</b>		
<b>Some Basic Techniques in the Data Analysis</b>		<b>35</b>
3.1	Particle identification (PID) techniques . . . . .	35
3.1.1	PID using energy loss information in detectors — the $\Delta E$ -E method . . . . .	36
3.1.2	PID using time of flight between detectors — the TOF- $\Delta E$ method . . . . .	38
3.2	Data analysis procedure for nuclear experiments . . . . .	41
<b>Chapter 4</b>		
<b>Data Analysis for the <math>p(^{27}\text{Si},d)^{26}\text{Si}^*</math></b>		<b>45</b>
4.1	Particle identification of beam recoils at the S800 focal plane . . . .	45
4.2	Doppler broadening corrections for $\gamma$ -ray energies . . . . .	46
4.3	Attempts to make the Doppler correction more accurate . . . . .	50
4.3.1	Target position determination for more accurate Doppler correction . . . . .	50
4.3.2	Offset correction to the calibrated $\gamma$ energy for more accurate Doppler correction . . . . .	56
4.4	Peak information from the corrected $\gamma$ spectrum . . . . .	60
4.5	Coincidence analysis of $\gamma$ -rays . . . . .	72
4.5.1	The $\gamma$ - $\gamma$ matrix technique . . . . .	72
4.5.1.1	Constructing the $\gamma$ - $\gamma$ matrix . . . . .	72
4.5.1.2	Finding the coincidence spectra from the $\gamma$ - $\gamma$ matrix	73
4.5.1.3	Subtracting background coincidence events from the coincidence $\gamma$ spectrum . . . . .	78
4.5.2	The event-by-event technique . . . . .	89
4.5.3	The $\gamma$ - $\gamma$ - $\gamma$ cube technique . . . . .	90
4.6	Results and discussions . . . . .	92
<b>Chapter 5</b>		
<b>Data Analysis for the <math>p(^{25}\text{Al},p)^{25}\text{Al}</math></b>		<b>95</b>
5.1	Particle identification (PID) . . . . .	95
5.1.1	PID for the $^{25}\text{Al}$ beam . . . . .	95

5.1.2	PID for the proton recoils . . . . .	96
5.2	Energy calibration of the silicon detectors . . . . .	98
5.2.1	Primary calibration using $3\text{-}\alpha$ source . . . . .	98
5.2.2	Pulse height defect effect . . . . .	100
5.2.3	Secondary calibration using proton beams . . . . .	102
5.3	Energy loss correction for scattered protons . . . . .	107
5.3.1	The stopping power of charged particles in target materials .	107
5.3.2	Simple energy correction using the SRIM calculation . . . .	111
5.3.3	Event-by-event correction . . . . .	113
5.4	Deadlayer effect . . . . .	119
5.5	Background subtraction . . . . .	122
5.5.1	Normalization of yields from $CH_2$ and $C$ targets . . . . .	123
5.6	Cross section from the yield spectrum of protons . . . . .	126
5.7	Breit-Wigner analysis . . . . .	130
5.7.1	Breit-Wigner formula for resonant elastic scattering . . . . .	131
5.7.2	Breit-Wigner fit for the experimental cross section . . . . .	132
5.8	R-Matrix analysis . . . . .	137
5.8.1	R-matrix formula for the cross section of compound nuclear scatterings and reactions . . . . .	137
5.8.2	Boundary transformation from R-matrix parameters to phys- ical parameters . . . . .	140
5.8.3	R-matrix fit for the experimental cross section . . . . .	143
 <b>Chapter 6</b>		
	<b>Reaction Rate of <math>^{25}\text{Al}(p,\gamma)^{26}\text{Si}</math></b>	<b>149</b>
6.1	General derivation of the thermonuclear reaction rate . . . . .	149
6.1.1	Non-resonant reaction rate formalism . . . . .	155
6.1.2	Resonant reaction rate formalism . . . . .	157
6.2	Stellar reaction rate of the $^{25}\text{Al}(p,\gamma)^{26}\text{Si}$ reaction . . . . .	162
 <b>Chapter 7</b>		
	<b>Summary and Outlook</b>	<b>171</b>
 <b>Appendix A</b>		
	<b>Production of RIBs in laboratory</b>	<b>175</b>
A.1	ISOL – Isotope Separator On-Line . . . . .	175
A.2	In-flight method . . . . .	177
 <b>Appendix B</b>		
	<b>R-Matrix theory</b>	<b>178</b>

<b>Appendix C</b>	
<b>More analysis details</b>	<b>188</b>
C.1 File formats of the experimental data at CRIB and NSCL . . . . .	188
C.2 Input file for the R-Matrix fitting program . . . . .	191
C.3 Creating .spe file used in gf3 program . . . . .	192
C.4 Geometry of the detector system in the F3 chamber at CRIB . . . .	193
<b>Bibliography</b>	<b>195</b>

# List of Figures

1.1	Map of the $^{26}\text{Al}$ in the galaxy measured by the INTEGRAL telescope. The background image of the milky way is overlaid with the COMPTEL map of $^{26}\text{Al}$ emission. (Adapted from reference: MPE, 2005) . . . . .	8
1.2	1.8 MeV $\gamma$ transition from the decay of the ground state of $^{26}\text{Al}$ . . .	9
1.3	reaction paths toward the production of the $^{26}\text{Al}$ . . . . .	10
1.4	Communication between the $^{26g}\text{Al}$ and the $^{26m}\text{Al}$ via the intermediate excited states by thermal excitation at supernova temperatures. . . . .	11
1.5	In the $^{25}\text{Al}(p,\gamma)^{26}\text{Si}$ reaction, only states above proton threshold ( $S_p=5.518$ MeV) in $^{26}\text{Si}$ can be populated. The Gamow windows at the typical nova and supernova temperatures are indicated by arrows. . . . .	12
1.6	Level schemes of $^{26}\text{Al}$ and its mirror nucleus $^{26}\text{Mg}$ . The color bands indicate the Gamow windows at different stellar temperatures; for example, the red band is for the nova temperature range and the blue one is for supernova temperatures. . . . .	13
2.1	schematic diagram of a beam target in collision with a target particle. . . . .	16
2.2	Correlations between the excitation energy of $^{26}\text{Si}^*$ and the energy of the scattered deuteron at various scattering angles with the beam energy $E_b=89$ MeV/A. . . . .	17
2.3	schematic diagram of the NSCL facility with the two cyclotrons K500 and K1200, the A1900 fragment separator and the S800 spectrograph indicated. . . . .	18
2.4	schematic diagram of the S800 spectrograph and additional components of the upstream beamline. . . . .	19
2.5	schematic diagram of the focal plane detector system at the end of the S800 spectrograph. . . . .	21

2.6	Photograph of the SeGA array from the front view. . . . .	22
2.7	schematic diagram of the elastic scattering in inverse kinematics. . .	23
2.8	schematic diagram of the CRIB facility. . . . .	27
2.9	schematic diagram of the side view of the Wien Filter. . . . .	28
2.10	Set-up of the detectors in the experimental chamber. . . . .	29
2.11	A photograph of the experimental chamber (F3). . . . .	30
2.12	schematic diagram of the beam transport line along the CRIB, and the beam tracking and proton detection systems in the F3 chamber.	31
2.13	Diagram of the electronics for the detectors, adapted from [24]. . . .	32
2.14	Electronic diagram of the DAQ trigger, adapted from [24]. . . . .	34
3.1	Simulation of particle identification using the $\Delta E$ vs $E$ histogram. .	37
3.2	schematic diagram of the $\Delta E$ - $E$ PID method. . . . .	38
3.3	An example of PID for beam particles using the $\Delta E$ vs TOF his- togram, adapted from [27]. . . . .	40
3.4	Another example of PID for beam particles using the $\Delta E$ vs TOF histogram, adapted from [27]. . . . .	41
3.5	A simulation of PID using the $\Delta E$ -TOF histogram for continuous $\Delta E$ . . . . .	42
4.1	A 2-dimensional histogram of $\Delta E$ vs $TOF$ for the PID of $^{26}\text{Si}$ . The area within the red gate corresponds to the $^{26}\text{Si}$ ions. . . . .	46
4.2	Coordinate system for segments of the SeGA array.. . . .	48
4.3	Gamma-ray spectrum before Doppler correction in coincidence with the $^{26}\text{Si}$ recoils for the whole runs. . . . .	48
4.4	Doppler corrected gamma-ray spectrum in coincidence with the $^{26}\text{Si}$ recoils for the whole runs, including gamma-rays measured in all SeGA detectors. The energies indicated are from skewed Gaussian fits for the peaks. . . . .	49
4.5	Deviations relative to 1796 keV of the 1796 keV peak centroids mea- sured by different SeGA detectors with the target at (0, 0, 0). Blue and red stars represent the SeGA detectors at the $37^\circ$ and the $90^\circ$ , respectively. . . . .	52
4.6	Projections of SeGA detectors on the target plane with the target at (0, 0, 0). The projections in the inner and outer ring represent the SeGA detectors in the $37^\circ$ ring and the $90^\circ$ ring, respectively. .	53
4.7	Deviations from the 1796 keV of the 1796 keV peak centroids mea- sured by different SeGA detectors with the target at the optimized position (0, -0.25, 0.25). Blue and red stars represent the SeGA detectors at the $37^\circ$ and the $90^\circ$ , respectively. . . . .	57

4.8	An example of a 2-dimensional histogram of $\cos\theta$ vs $E_{measured}$ for calculating the average of $\cos\theta$ of a detector over the detected $\gamma$ emissions of the 1796 keV peak. This is for detector No.10 in the $37^\circ$ ring with the Doppler-corrected peak of 1796 keV at 1802 keV.	60
4.9	The final corrected $\gamma$ spectrum for the whole energy range of the detected $\gamma$ -rays.	61
4.10	The final corrected $\gamma$ spectrum — an enlargement from 3700 keV to 4600 keV where a new peak around 4100 keV is found.	62
4.11	The skewed Gaussian fit example for the 1796 keV peak with the fit curve in black solid line, the Gaussian component in red dotted line, the skewed Gaussian component in blue dashed line, and the quadratic background in green dotted-dashed line.	64
4.12	The fits for the peaks at 843 keV, 989 keV and 1326 keV in the gamma spectrum.	65
4.13	The fits for the peaks at 1404 keV, 1533 keV and 1954 keV in the gamma spectrum.	66
4.14	The fits for the peaks at 2024 keV, 2360 keV and 2648 keV in the gamma spectrum.	67
4.15	The fits for the peaks at 2785 keV and 3000 keV in the gamma spectrum.	68
4.16	The skewed Gaussian fits for the newly found peaks at around 2260 keV and 4100 keV.	69
4.17	An example of filling the $\gamma$ - $\gamma$ matrix—the 2-dimensional coincidence histogram. The demonstration is for a single beam event only and each point represents a coincidence.	74
4.18	A 2D histogram of the $\gamma$ - $\gamma$ matrix constructed from the experimental data using the technique described in the previous subsection.	75
4.19	Top: gating on the $X$ axis for 1796 keV and projecting the gated region onto the $Y$ axis to find all the coincidence events with the 1796 keV $\gamma$ -ray as the larger of the two energies in coincidence. Bottom: the coincidence spectrum obtained from the projection.	76
4.20	Top: gating on the $Y$ axis for 1796 keV and projecting the gated region onto $X$ axis to find all the coincidence events with the 1796 keV $\gamma$ -ray as the smaller of the two energies in coincidence. Bottom: the coincidence spectrum obtained from the projection.	77
4.21	The coincidence spectrum obtained by combining the projections on the $X$ axis and the $Y$ axis shown in figure 4.19 and 4.20.	78

4.22	Top: choosing the background gates on the tails of the gated peak if they are flat enough, gates for 1796 keV peak with the red one indicating the peak gate and blue ones the background gates. Bottom: choosing the background gates on the smooth regions close to the gated peak if other peaks sit on its tails, with the main gate on the 2647 keV peak. . . . .	80
4.23	An example of a coincidence $\gamma$ -ray spectrum for the 1404 keV $\gamma$ -ray in black with its background shown in red. . . . .	81
4.24	Coincidence $\gamma$ -ray spectra for 843 keV and 989 keV $\gamma$ -rays in black with the background shown in red. . . . .	82
4.25	Coincidence $\gamma$ -ray spectra for 1326 keV and 1533 keV $\gamma$ -rays in black with the background shown in red. . . . .	83
4.26	Coincidence $\gamma$ -ray spectra for 1796 keV and 1954 keV $\gamma$ -rays in black with the background shown in red. . . . .	84
4.27	Coincidence $\gamma$ -ray spectra for 2024 keV and 2260 keV $\gamma$ -rays in black with the background shown in red. . . . .	85
4.28	Coincidence $\gamma$ -ray spectra for 2360 keV and 2648 keV $\gamma$ -rays in black with the background shown in red. . . . .	86
4.29	Coincidence $\gamma$ -ray spectra for 2785 keV and 3000 keV $\gamma$ -rays in black with the background shown in red. . . . .	87
4.30	Level scheme of $^{26}\text{Si}$ based on the results from this analysis. . . . .	89
4.31	Distribution of multiplicities of all the data showing that most of the events have only one or two $\gamma$ -rays in coincidence. This indicates that the $\gamma$ - $\gamma$ matrix technique is adequate enough for the data analysis. . . . .	91
5.1	Particle identification of $^{25}\text{Al}$ and $^{24}\text{Mg}$ using RF time. Left columns correspond to the $^{24}\text{Mg}$ while right columns correspond to the $^{25}\text{Al}$ . The Y axis label represents the number of the RF resonators. . . . .	96
5.2	Particle identification of $^{25}\text{Al}$ and $^{24}\text{Mg}$ using X&Y positions of beam particles on PPACs. $^{25}\text{Al}$ particles accumulate at the center of the PPAC and the $^{24}\text{Mg}$ accumulate to the right of the center. . . . .	97
5.3	$^{25}\text{Al}$ beam particles on PPACs after applying the RF cuts for $^{25}\text{Al}$ on the histogram of RF time. . . . .	98
5.4	Particle identification of protons using a 2-D histogram of E versus $\Delta E$ for the silicon telescope at zero degrees only for identifying scattered protons punching through the PSD. . . . .	99
5.5	Particle identification of protons using a 2-D histogram of $\Delta E$ versus time-of-flight (TOF) for identifying scattered protons both punching through the PSD and stopping in the PSD. . . . .	100

5.6	Histogram of all PSD channels before calibration for the data runs using a 3- $\alpha$ source. . . . .	101
5.7	An example of $\alpha$ calibration for a PSD channel. Shown in green is the linear fit of channel vs energy. . . . .	102
5.8	Histogram of $\alpha$ energies for all PSD channels after applying the calibration parameters for each detector channel. . . . .	103
5.9	An example of the proton calibration for a PSD-SSD telescope. . .	104
5.10	Top: the energy spectrum of protons measured by the telescope at 0°. Bottom: the energy spectrum of protons measured by the telescope at 17° . . . . .	105
5.11	The energy spectrum of protons measured by the telescope at 27°. .	106
5.12	Stopping power vs beam energy in $CH_2$ (red) and pure carbon target (black), calculated with SRIM. . . . .	109
5.13	Fits to the stopping power data calculated by SRIM. Two simple functions are used for fitting the lower and higher energy parts separately. . . . .	110
5.14	Energy loss correction from the SRIM calculation for the $CH_2$ (top) and the C target (bottom). The fits to the plots are also shown, as well as the plots for the ideal situations with no energy loss. . . . .	112
5.15	Layout of the beam tracking in the detector system obtained using the two PPACs before the target and the PSD after the target. . . .	114
5.16	Coordinate system for particle tracking in the detector chamber. . .	115
5.17	Illustration of the paths of a scattering in the target (not to scale). .	117
5.18	An example of the proton spectrum with the energy loss correction, with the $X$ axis representing the center-of-mass energy ( $E_{cm}$ ) transformed from the proton energy. . . . .	118
5.19	The layout of the Silicon detector telescope (PSD-SSDs) with the deadlayers sketched in. . . . .	119
5.20	Energy loss in the PSD active layer only and energy loss in the PSD and Al deadlayer together as functions of the proton energy when leaving the target (from SRIM simulation). The energies for just punching through the active layer, and through the whole PSD, are indicated. . . . .	120
5.21	Energy loss in just the Al deadlayer only vs the proton energy after leaving the target (from SRIM simulation). . . . .	121
5.22	Background proton spectrum from runs with the pure carbon target. .	123
5.23	Proton spectrum from runs with the $CH_2$ target and the background from figure 5.22 (without normalization) is also shown in red. . . .	124
5.24	Proton spectrum after background subtraction. . . . .	125

5.25	Excitation function at $0^\circ$ in the center of mass frame after energy loss correction and background subtraction. The bottom one is the enlargement of this spectrum in the range of 1200 keV to 3400 keV.	128
5.26	Excitation function at $17^\circ$ in the center of mass frame after energy loss correction and background subtraction. . . . .	129
5.27	Excitation function at $27^\circ$ in the center of mass frame after energy loss correction and background subtraction. . . . .	130
5.28	Calculated proton spectrum using the Breit-Wigner formula with realistic values of the parameters in the formula. . . . .	133
5.29	Breit-Wigner fits for the resonances at $E_R=1.634$ MeV (top) and at $E_R=2.170$ MeV (bottom). . . . .	135
5.30	A Breit-Wigner fit for the resonance at $E_R=3.100$ MeV. . . . .	136
5.31	An R-Matrix fit for the three resonances at $E_R \sim 1.62$ MeV, 1.97 MeV and 2.13 MeV, with s-wave ( $l=0$ ) scattering for all and $J^\pi=2^+$ , $2^+$ and $3^+$ , respectively. . . . .	146
5.32	A R-Matrix fit for the three resonances at $E_R \sim 1.62$ MeV, 1.97 MeV and 2.13 MeV, with s-wave ( $l=0$ ) scattering for the first two and p-wave scattering ( $l=1$ ) for the third resonance ( $J^\pi=2^+$ , $2^+$ and $3^-$ , respectively). . . . .	148
6.1	The probability distribution of a thermonuclear reaction with respect to the stellar energy $E$ in the stellar environment at a given temperature $T$ . It results from the combined effect of the Maxwell-Boltzmann distribution for the stellar gas and the energy dependent penetrability function arising from the Coulomb barrier in the cross section of the thermonuclear reaction. Instead of peaking at the maximum of the MB distribution, the combined distribution has its so-called Gamow peak at an energy $E_0$ , representing the most probable energy for which the thermonuclear reaction will happen.	153
6.2	The Maxwell-Boltzmann distribution and a narrow resonance. . . . .	160
6.3	The $^{25}\text{Al}(p,\gamma)^{26}\text{Si}$ reaction rates from direct capture reaction and individual resonances from our study. . . . .	166
6.4	The $^{25}\text{Al}(p,\gamma)^{26}\text{Si}$ reaction rates from direct capture reaction and from the major contributing resonances. The sum of all contributions is also shown as the solid line. . . . .	167
6.5	The ratios of the total reaction rates from our calculations to the rates from Bardayan <i>et al.</i> [12] and Parpottas <i>et al.</i> [11] . . . . .	170
A.1	The schematic diagram of the RIB productions by the ISOL method and the in-flight method. . . . .	176

C.1	Event format of data file at NSCL. . . . .	189
C.2	Data format of the .rdf file at CRIB. . . . .	190
C.3	Geometry of detectors in the F3 chamber at CRIB, from top view. .	193

# List of Tables

2.1	Characteristic parameters of the S800 spectrograph, adapted from [16].	20
4.1	List of peak centroids measured by different SeGA detectors for the 1796 keV peak. . . . .	51
4.2	List of the smallest RMS obtained under different conditions. . . . .	56
4.3	List of the peak parameters of all the peaks extracted from the best fits and the calculated peak areas, along with the uncertainties. The uncertainties in the parentheses for the energies is just the statistical uncertainty taken directly from the fit results for the peak energies.	70
4.4	The final results for all $\gamma$ peaks: their energies, relative intensities with respect to that of the strongest $\gamma$ ray, and the corresponding uncertainties in intensity. The results from the present work are compared with previous results [13]. . . . .	71
4.5	The energy levels and associated $\gamma$ transitions extracted from the analysis. . . . .	88
5.1	List of energies of the 3- $\alpha$ source for the energy calibration of the silicon detectors. . . . .	100
5.2	List of Breit-Wigner parameters of three resonances for the Breit-Wigner fits of the experimental differential cross sections. $E_R$ and $\Gamma_R$ are in units of keV. The $\chi^2/d.o.f$ represents the chi-square per degree of freedom ( $d.o.f$ ) for each fit. The quoted uncertainties are directly from the fits. . . . .	136
5.3	List of all possible combinations of channel spin $S$ , relative orbital angular momentum $l$ , and spin-parity $J^\pi$ of the compound nucleus.	144

5.4	List of parameters of resonances from a R-Matrix fit to the three resonances in the experimental differential cross section in the energy range 1424 keV — 2484 keV. The pole energy $E_\lambda$ , the resonance energy $E_R$ and the level energy $E_x$ are in units of MeV and the resonance width $\Gamma_R$ is in units of keV. The proton separation energy (or proton threshold energy) is $S_p=5.518$ MeV. The uncertainties quoted are directly from the fits. . . . .	147
6.1	List of parameters to be used in the calculations of the $^{25}\text{Al}(p, \gamma)^{26}\text{Si}$ stellar reaction rate. The parameters of the last two resonances are adopted from Ref [12]. . . . .	165
6.2	List of calculated rates $N_A\langle\sigma v\rangle$ of the $^{25}\text{Al}(p, \gamma)^{26}\text{Si}$ stellar reaction from individual resonances at different stellar temperatures, in units of $\text{cm}^3\text{s}^{-1}\text{mol}^{-1}$ . . . . .	168
6.3	Cont'd: List of calculated rates $N_A\langle\sigma v\rangle$ of the $^{25}\text{Al}(p, \gamma)^{26}\text{Si}$ stellar reaction from individual resonances at different stellar temperatures, in units of $\text{cm}^3\text{s}^{-1}\text{mol}^{-1}$ . . . . .	169
C.1	List of measured distances (mm) in the detector system in F3 chamber at CRIB for our experimental set-up (refer to figure C.3). . . . .	194

# Introduction and Motivation

In this chapter, an introduction to some relevant background knowledge on nuclear astrophysics which is the research field of this thesis will be given briefly. Following this is the explanation of the scientific motivation for the study of  $^{26}\text{Si}$ .

## 1.1 Stellar evolution, nucleosynthesis and abundance

We know today that our universe started from the Big-Bang (BB) which makes the first-ever nuclei to fill up the universe from hydrogen up to beryllium, with most of them hydrogen and helium. As the universe cooled down after the BB explosion, the hydrogen and helium gas contracted due to gravity to form the molecular clouds from which the first stars were born due to the further contraction until the final gravitational collapse. Upon its formation, the star steps into its long journey of stellar evolution starting as a main sequence star<sup>1</sup> for 90% of its lifetime. Here we will only give a simple introduction to the stellar evolution associated with the

---

<sup>1</sup>Most of the stars spend most of their lifetimes in burning hydrogen and are thus categorized as a group of stars named the main sequence stars when they are in the hydrogen burning stage.

nucleosynthesis of elements in the nuclear burning processes during the various stages of the stellar evolution. More general knowledge of nuclear astrophysics and more profound details about the following content can be found in many references, such as [1] and [2].

### 1.1.1 Quiescent burning processes

When a star forms as a main sequence star out of the contracting molecular cloud in the interstellar medium (ISM), it will still undergo further contraction because the inward gravitational force still overcomes the outward internal pressure in the star. Therefore the core of the star gets heated by the thermal energy continuously generated from the conversion of gravitational energy. The core temperature and the matter density keep increasing until a critical condition ( $T \sim 0.01$  GK;  $\rho \sim 10^2$  g/cm<sup>3</sup>) when hydrogen ions (protons) gain enough kinetic energy from the heating to tunnel through the Coulomb barrier between two protons which makes it possible for protons to fuse together and release tremendous nuclear energy. This process of burning hydrogen goes smoothly and the continuously generated outward nuclear radiation impedes further gravitational contraction. Finally, the two competing forces come to an equilibrium, where the core stops contracting. This hydrogen burning process will last for a very long time since at this temperature the protons have energies far below the Coulomb barrier making the fusion of protons very slow. This is why most of stars remain in main sequence burning hydrogen for most of their lives. During this process another abundant element, Helium, is produced via the pp-chain reaction at low temperatures and CNO cycle reactions at higher temperatures [1].

When all the hydrogen in the core has been burned up with only Helium remaining (but still with hydrogen outside the core), the main sequence of stars ends and no nuclear energy will be generated to prevent the core from contracting because at this time the core temperature has not become high enough for the Helium ions to fuse together. The core eventually gets heated up again by the

thermal energy from the gravitational contraction, and the core temperature and density keep increasing until the critical conditions for Helium burning are reached ( $T \sim 0.1\text{--}0.4$  GK;  $\rho \sim 10^2\text{--}10^5$  g/cm<sup>3</sup>, [2]). The core comes to an equilibrium again with Helium burning inside the core and Hydrogen burning still in the hydrogen shell around the Helium core.

Such burning process will repeat in the subsequent Carbon burning, Neon burning, Oxygen burning and the final quiescent burning — Silicon burning, which will result in, for a massive star, a very hot silicon burning core surrounded by layers of burning shells of lighter elements from the Oxygen burning shell to the outer hydrogen burning shell. Since the nuclear burning is ignited by the thermal energy converted from the gravitational contraction of a star, how far a star can go in the burning stages is then essentially determined by its mass. For low mass stars, they spend their whole lives burning hydrogen, at most up to helium burning and then die as white dwarfs since their thermal energy is too small to ignite further nuclear burning, while for massive stars, the gravitational contraction can provide enough energy for them to go all the way to the last quiescent burning stage.

These quiescent burning processes can make contributions to the nucleosynthesis and abundances of the elements up to iron since iron is the most stable element and it is impossible for the any nucleus to overcome the large Coulomb barrier to fuse with a iron nucleus under the quiescent stellar burning conditions. Other mechanisms are therefore required to explain the nucleosynthesis of the elements beyond iron — the explosive burning processes, to be described in the following section.

### 1.1.2 Explosive burning processes

The explosive burning occurs in conditions of extremely high temperature and density, which can never be achieved during the quiescent burning processes, and is characterized by an abrupt increase in temperature and huge amount of nuclear energy release in a extremely short time period (usually in about one second),

compared with the relatively mild character and millions of years long journey of the quiescent stellar burning. It happens when a massive star or a close binary system comes to the end of its life. Recall that a massive star can keep burning nuclei in its core until nothing can be burned leaving iron in the core. The star then starts contracting again. The iron nuclei cannot be burned to counter the further contraction. However the contraction confines the free electrons in the core to become a degenerate electron gas, the internal pressure of which then stops the contraction of the core. But as more and more mass in the shells around the core becomes degenerate and is deposited to the core to make it reach a critical mass, even the degenerate gas pressure can no longer support the core and the star then ends its life by a core collapse and a subsequent explosion, ejecting their envelopes rich in various materials into the interstellar medium where new stars will be born.

This scenario discussed above is just one of various explosive events in the universe and is called Type II supernova explosion. Similar events to Type II supernovae are the Type Ib and Ic supernovae with differences in that the massive progenitor star of the Type Ib has its outer hydrogen layer blown off by stellar winds or a companion star, and the progenitor star of the Type Ic has both the hydrogen and helium layer stripped off. The progenitor stars of the Type Ib/Ic are usually called the Wolf-Rayet stars.

Other explosive scenarios are the nova explosion and Type Ia supernova explosion in a binary system including a carbon-rich (CO) white dwarf and a companion star — usually a main-sequence star or a red giant star. Due to the strong gravity of the electron-degenerate matter in the white dwarf, the hydrogen-rich material keeps being transferred from the companion star via the equipotential surface (Roche lobes) of the two objects to the white dwarf, forming an accretion disk around the white dwarf. When the material reaches the surface of the white dwarf, it will quickly become degenerate due to the strong gravity of the white dwarf, resulting in the increase of temperature. Depending on the accretion rate and the mass of the white dwarf, the white dwarf can end up with a nova explosion

or a more explosive Type Ia supernova explosion. If the companion star is a low mass star, the accretion rate will be low which allows thermonuclear runaway to take place due to the high temperature near the bottom of accreted layers around the surface of the white dwarf, associated with large amount of energy release. This is the scenario of the nova explosion. If the companion star is a massive star, the material will be quickly accreted from the star to the white dwarf and accumulated in the degenerate form on its surface. As a consequence, the mass of the white dwarf will soon exceed the Chandrasekhar limit and an explosion occurs disrupting the whole white dwarf. This is the scenario of Type Ia supernova explosion.

During the explosion, the light elements, hydrogen and helium, in the outer shells are burned in a completely different manner from that in the quiescent burning processes due to the extreme explosive conditions. Light elements can be also synthesized in the explosive hydrogen and helium burning, i.e., via hot CNO cycles or breakout sequences from the hot CNO cycles. The heavier elements will only be synthesized via the neutron capture processes (s-process and r-process) and proton capture processes (p-process)<sup>2</sup> which can only occur under the extreme conditions of explosive events. The neutrons in the s- process are produced in the star before explosion, i.e., in carbon burning and oxygen burning stage, while the neutrons in the r- process are due to the neutronization by the weak interaction at the time of hydrodynamic contraction of later stage stars, i.e., presupernovae. Nucleosynthesis in the s-process goes along a path close to the group of stable nuclei and nucleosynthesis in the r-process goes along a path close to the neutron drip-line. The p-process path in turn runs close to the group of stable neutron-deficient nuclei. The s-process is responsible for nucleosynthesis of half of the elements beyond iron while r-process makes the other half. It should be pointed out that nova explosions and supernova Type Ia explosions contribute mainly to the nucleosynthesis of light elements up to iron and have no important contributions to nucleosynthesis of elements beyond iron.

---

<sup>2</sup>s- and r- represent slow neutron capture and rapid neutron capture, respectively and p-represents proton capture.

### 1.1.3 Thermonuclear reactions

Thermonuclear reactions occur throughout the whole course of stellar evolution, from initial quiescent hydrogen burning to the explosive burning stages. It is the dominant source of the energy generation in our universe and is the way by which all elements including those in human beings are produced. At different stages of the stellar evolution, different thermonuclear reactions take place due to the different conditions characterized by the temperature, responsible for the production of specific groups of elements determined and limited by those conditions. The abundances of different isotopes in the universe are calculated from the network calculations using the thermonuclear reaction rates of various reactions occurring in different stellar scenarios at different temperatures and matter densities.

Since in the stellar matter all elements exist in the form of a gas, the particles should be treated collectively and their collective motions are therefore constrained by the gas model, normally the Boltzmann-Maxwell (BM) velocity distribution. So the calculation of the reaction rate will be weighted by the BM distribution of the velocity. Besides, from the nuclear reaction point of view, the occurrence of reactions between individual charged particles are prevented by the resistance due to the repulsive Coulomb force between them, that is, the Coulomb barrier. To represent the possibility that a charged particle overcomes the barrier to react with another charged particle, a penetrability factor is introduced into the cross section for the nuclear reaction according to quantum mechanics. The higher the energy of the reacting particles, the higher the penetrability and thus the easier a reaction takes place. Combining these two effects together, the thermonuclear reaction rate for a specific nuclear reaction will peak with the total energy (total kinetic energy in the center-of-mass frame) at an energy only determined by the stellar temperature (besides the masses and charges of the reacting particles). Therefore, a thermonuclear reaction can take place with highest probability within a window around the peak energy, called the Gamow window. Since the energy levels populated in the compound nucleus in a stellar capture reaction is directly

related to the total energy, the most populated energy levels will be those corresponding to the total reaction energies right within the Gamow window. In the calculation of the reaction rate, those levels in the compound nucleus have the dominant contributions while contributions from levels out of the Gamow window can be negligible. So it is crucial for the network calculations of element abundances to locate accurately the positions of energy levels of astrophysical interest in compound nuclei in the important stellar thermonuclear reactions. More details and the derivations of the thermonuclear reaction rates are given in Chapter 6.

## 1.2 Scientific motivation for the study of $^{26}\text{Si}$

### 1.2.1 $^{26}\text{Al}$ in the galaxy

The radioisotope  $^{26}\text{Al}$  (half-life  $t_{1/2} = 0.72 \times 10^6$  years) is an important probe for Inter-Stellar Medium (ISM) of a galaxy, which is the birthplace of newly formed stars. The presence of  $^{26}\text{Al}$  in the ISM has been confirmed by searching for the characteristic 1.809 MeV  $\gamma$ -rays from  $^{26}\text{Al}$  decay. It was discovered first by the HEAO3 satellite through the detection of the 1.809 MeV  $\gamma$ -rays and was later mapped out in an all-sky distribution over the Galaxy by the COMPTEL telescope installed on the CGRO satellite. It is through the Doppler-shift measurements of this 1.809 MeV line by the next-generation telescope INTEGRAL that the galactic  $^{26}\text{Al}$  is confirmed to co-rotate with the Galaxy and therefore be distributed throughout the whole Galaxy [3]. Figure 1.1 shows the all-sky maps of  $^{26}\text{Al}$  from the COMPTEL results and the INTEGRAL as well.

Regarding the stellar sources of the the galactic  $^{26}\text{Al}$ , there is always a discrepancy between the observed data from the satellites and the stellar models. The all-sky map clearly shows that the  $^{26}\text{Al}$  is more densely distributed in the spiral arm of the Galaxy, which consists of mainly massive stars and indicates that novae and low-mass star cannot be the major sources. One thing we are sure about is that in the Galaxy there is about 1-3 solar mass of  $^{26}\text{Al}$ . However, according to

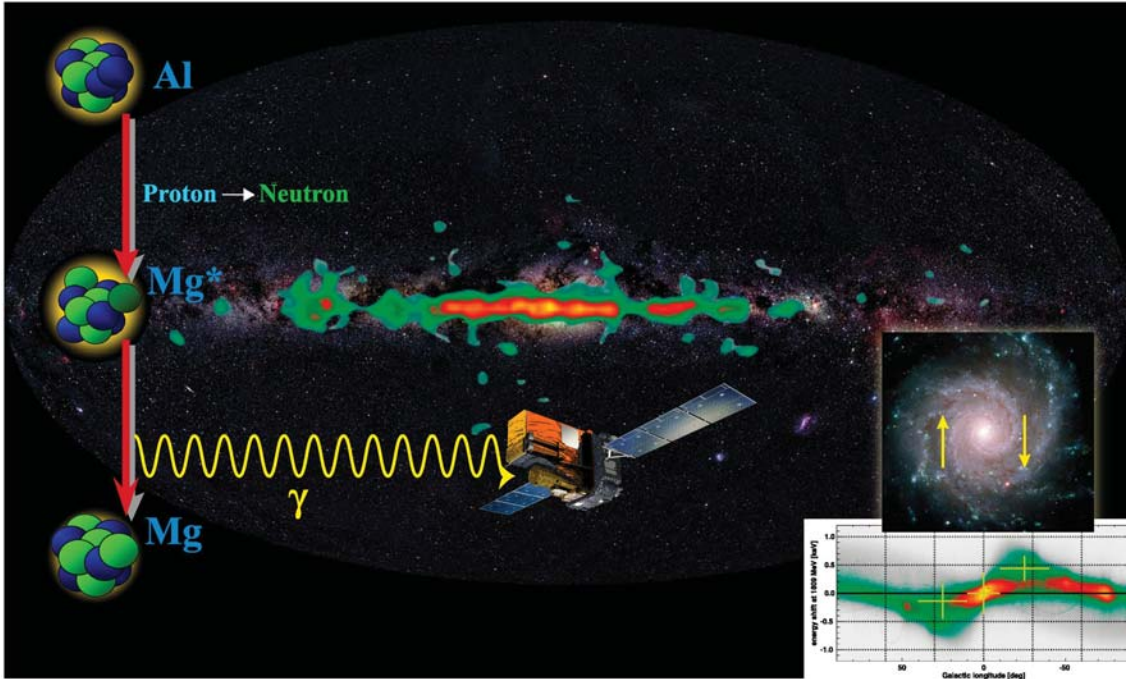


Figure 1.1: Map of the  $^{26}\text{Al}$  in the galaxy measured by the INTEGRAL telescope. The background image of the Milky Way is overlaid with the COMPTEL map of  $^{26}\text{Al}$  emission. (Adapted from reference: MPE, 2005)

the classical nova models, classical novae should be among the major contributors to the production of  $^{26}\text{Al}$  [4, 6, 7]. A recent study on the nucleosynthesis of massive stars suggests that the  $^{26}\text{Al}$  is mainly from the Type II supernova explosions and the Wolf-Rayet stars [8] which fits very well to the observed data. In spite of this, the current situation is still unclear and we still do not have a full understanding about the sources of the  $^{26}\text{Al}$ . Nevertheless, now we know that apart from the major contributors, AGB stars can also be a site for  $^{26}\text{Al}$  production and nova explosions are still significant contributors. Since there are large uncertainties in the important reaction rates for the production of  $^{26}\text{Al}$  in explosive hydrogen burning due to lack of the knowledge about the details of the explosive events [5] and since they significantly affect the production of  $^{26}\text{Al}$ , it is necessary for us to perform more accurate measurements to reduce these uncertainties so that we can put firmer constraints on the stellar model calculations and therefore gain more

knowledge about the Galaxy as well as the ISM.

### 1.2.2 The importance of the $^{25}\text{Al}(p, \gamma)^{26}\text{Si}$ reaction

The characteristic decay  $\gamma$ -rays from  $^{26}\text{Al}$  are produced in the following way: the proton capture of  $^{25}\text{Mg}$  leads to  $^{26}\text{Al}$  in its ground state, then the ground state  $^{26}\text{Al}$  mostly decays to the first excited state of  $^{26}\text{Mg}$  by  $\beta^+$  and electron capture, followed by the  $\gamma$  decay of  $^{26}\text{Mg}$  to its ground state with an emission of the 1.809 MeV  $\gamma$ -ray. This 1.809 MeV  $\gamma$  can be only produced from the the decay of the ground state of  $^{26}\text{Al}$  ( $T_{1/2} = 7.17 \times 10^5$  years) and the  $^{26}\text{Al}$  in its isomeric state ( $T_{1/2} = 6.36$  s) will directly decay to the ground state of  $^{26}\text{Mg}$  without any  $\gamma$  emission. Figure 1.2 shows how this characteristic 1.809 MeV  $\gamma$  transition occurs.

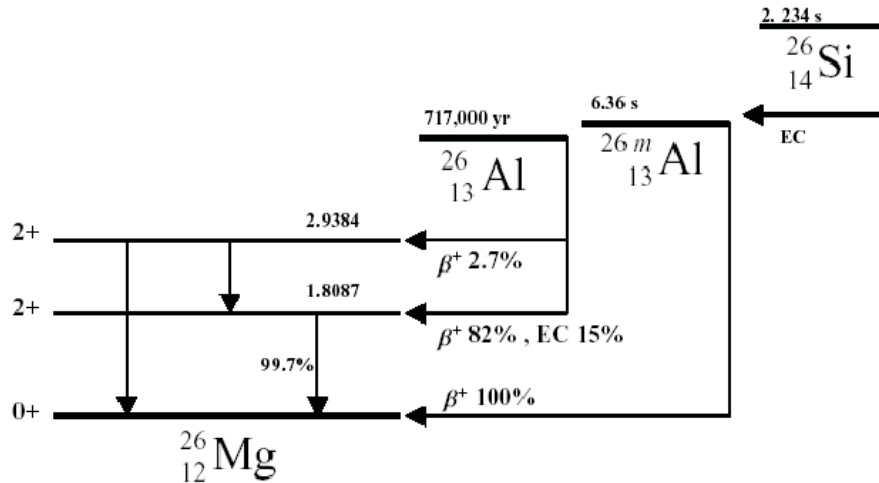
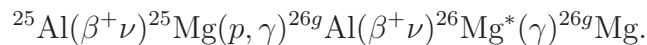


Figure 1.2: 1.8 MeV  $\gamma$  transition from the decay of the ground state of  $^{26}\text{Al}$ .

The reaction path toward the production of the ground state of  $^{26}\text{Al}$ , denoted by  $^{26g}\text{Al}$ , is



In nova explosions (typical temperature  $T_9 = 0.1 - 0.4$ ), the proton capture

of  $^{25}\text{Al}$  competes with its  $\beta^+$  decay and bypasses the production of  $^{26g}\text{Al}$  since the capture product  $^{26}\text{Si}$  decays quickly to the 0.228 MeV isomeric state in  $^{26}\text{Al}$  (denoted by  $^{26m}\text{Al}$ ) instead of its ground state, resulting in no emission of 1.809 MeV gamma rays. Since the transition between the ground state and the isomeric state is almost impossible due to their large spin difference ( $\Delta J = 5$ ), a thermal equilibrium cannot be established between the two states and therefore the  $^{26}\text{Al}$  nuclei in the two states should be considered as two different nuclei instead of the same one, which therefore complicates the  $^{26}\text{Al}$  production and makes the  $^{25}\text{Al}(p, \gamma)^{26}\text{Si}$  reaction very important. The reaction path toward the production of the isomeric state of  $^{26}\text{Al}$  follows

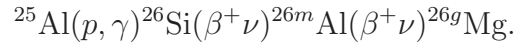


Figure 1.3 shows in the chart of nuclei the different reaction paths toward the production of the  $^{26}\text{Al}$  for different conditions.

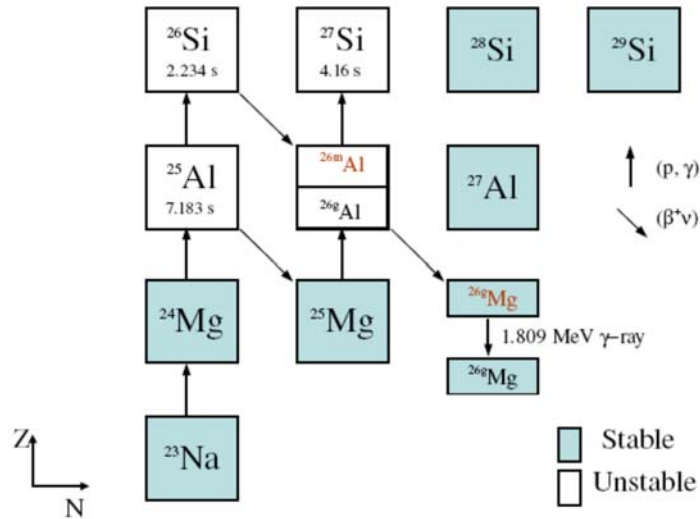


Figure 1.3: reaction paths toward the production of the  $^{26}\text{Al}$ .

At even higher temperatures in supernova explosions (typical temperature  $T_9 > 1$ ),  $^{26m}\text{Al}$  can be excited to the higher excited states, such as the 0.417

MeV state ( $J^\pi = 3^+$ ) and the 1.058 MeV state ( $J^\pi = 1^+$ ), by thermal excitation, and then quickly decay and produce  $^{26g}\text{Al}$  again [14]. It is in this way that the ground state of  $^{26}\text{Al}$  communicates with its isomeric state and achieves an indirect thermal equilibrium between them via the intermediate higher excited states. Figure 1.4 demonstrates such communication. A study in Ref. [14] has shown that at such high temperatures the  $^{25}\text{Al}(p, \gamma)^{26}\text{Si}$  reaction dominates over that of the  $^{25}\text{Mg}(p, \gamma)^{26}\text{Al}$  reaction and as a result, instead of producing the  $^{26m}\text{Al}$ , the  $^{25}\text{Al}(p, \gamma)^{26}\text{Si}$  reaction will produce most of the  $^{26}\text{Al}$  in its ground state.

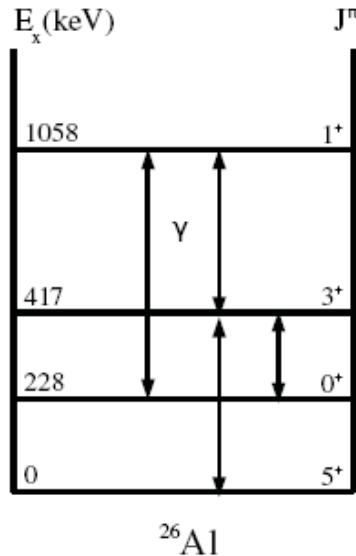


Figure 1.4: Communication between the  $^{26g}\text{Al}$  and the  $^{26m}\text{Al}$  via the intermediate excited states by thermal excitation at supernova temperatures.

### 1.2.3 Nuclear structure of $^{26}\text{Si}$

We have already mentioned that the thermonuclear reaction rates of stellar capture reactions are determined by the energy levels of the compound nuclei within the Gamow windows corresponding to the stellar temperatures at which these reactions occur. Therefore states in  $^{26}\text{Si}$  within the corresponding windows at nova temperatures and supernova temperatures need to be well understood in order

to determine the  $^{25}\text{Al}(p,\gamma)^{26}\text{Si}$  reaction rate and thus the production rate of  $^{26}\text{Al}$  in these explosive environments. In the  $^{25}\text{Al}(p,\gamma)^{26}\text{Si}$  reaction, only states above proton threshold ( $S_p=5.518$  MeV) in  $^{26}\text{Si}$  can be populated, as shown in figure 1.5.

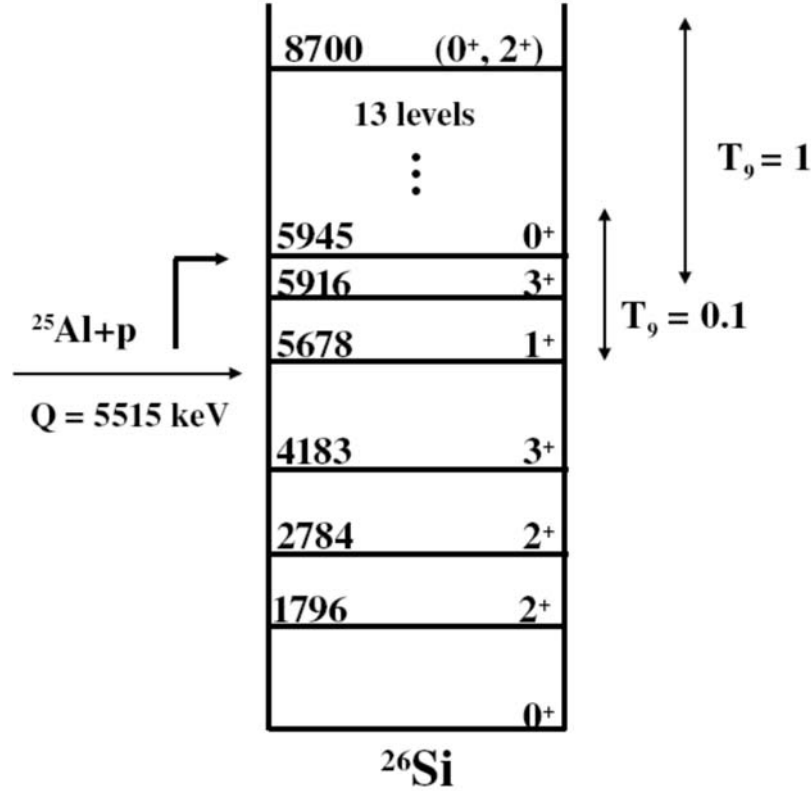


Figure 1.5: In the  $^{25}\text{Al}(p,\gamma)^{26}\text{Si}$  reaction, only states above proton threshold ( $S_p=5.518$  MeV) in  $^{26}\text{Si}$  can be populated. The Gamow windows at the typical nova and supernova temperatures are indicated by arrows.

Figure 1.6 shows the level scheme of  $^{26}\text{Si}$  compared with that of its mirror nucleus  $^{26}\text{Mg}$ .

The astrophysically important states in  $^{26}\text{Si}$  have been studied with different reactions [9, 10, 11, 12, 13] due to their dominant contributions to the large uncertainty in the  $^{25}\text{Al}(p,\gamma)^{26}\text{Si}$  reaction rate at nova temperatures (red band region in figure 1.6). But controversies exist on the spin-parity assignments for some dominant states, such as the 5.912 MeV and 5.946 MeV states, and the level en-

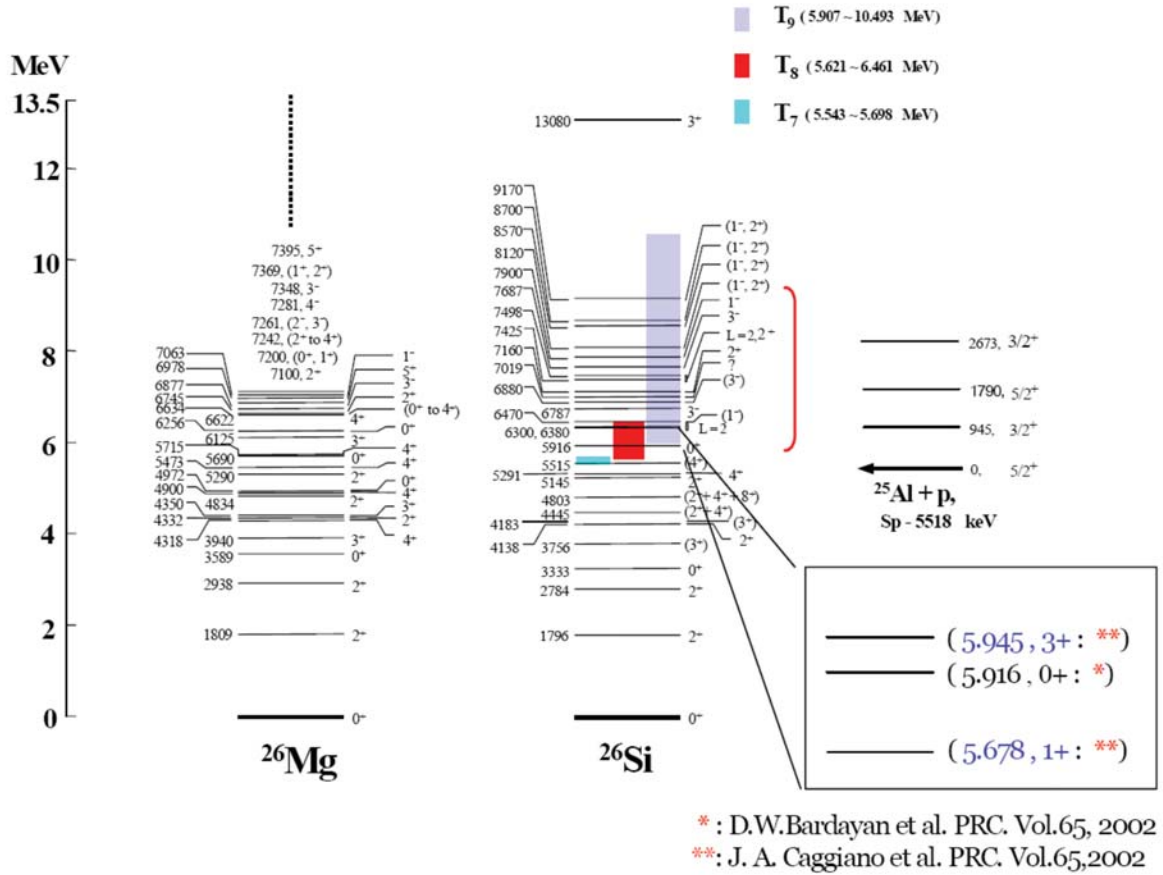


Figure 1.6: Level schemes of  $^{26}\text{Al}$  and its mirror nucleus  $^{26}\text{Mg}$ . The color bands indicate the Gamow windows at different stellar temperatures; for example, the red band is for the nova temperature range and the blue one is for supernova temperatures.

energies and spin-parities of the newly found states from those measurements also need to be confirmed. Furthermore, comparison with the mirror nucleus points to the possible existence of new states in  $^{26}\text{Si}$ , which may contribute strongly to the  $^{25}\text{Al}(p,\gamma)^{26}\text{Si}$  rate at supernova temperatures. To address these issues, we performed two experiments: one is the  $p(^{27}\text{Si},d)^{26}\text{Si}^*$  reaction at the NSCL aiming to construct the level scheme of low lying states around the proton threshold; the other one is the elastic scattering of  $^{25}\text{Al}+p$  with CRIB [21] at RIKEN in order to obtain information on states in a broad range ( $E_x=5.6$  MeV - 8.6 MeV) above the proton threshold [23].

# Two experiments for the study of $^{26}\text{Si}$

This chapter covers all the descriptions of the two experiments performed at two different laboratories — NSCL and CRIB — including facility introduction, experimental techniques and set-up, radioactive beams in use, detector configurations for each experiment, and so on. For the production of the radioactive beams, more details can be found in Appendix A.

## 2.1 The $p(^{27}\text{Si},d)^{26}\text{Si}^*$ experiment at the NSCL facility

This experiment aimed to measure the  $\gamma$ -decays from the low-lying proton-unbound excited states of the product nuclei  $^{26}\text{Si}$ . At higher excited states, the  $^{26}\text{Si}$  becomes unstable and is destroyed by the more preferred particle decays. For this reason, this  $\gamma$  spectroscopy measurement was only used to study levels of  $^{26}\text{Si}$  in the low energy range for which the beam energy was chosen according to the kinematics. In the following, I will begin with the kinematics of this reaction.

### 2.1.1 Kinematics

Let us consider the general case of a incoming beam particle in collision with a target particle (two-body kinematics, non-relativistic). Figure 2.1 shows the schematic diagram of the collision. Let us make the following notation:

$m_b$	mass of the beam particle
$m_t$	mass of the target particle
$m_r$	mass of the recoiling heavy particle
$m_o$	mass of the detected light particle
$T_b$	kinetic energy of the beam particle before collision
$Q_{gs}$	Q-value of the reaction with the residue in the ground state
$T_r$	kinetic energy of the recoiling heavy particle after collision
$T_o$	kinetic energy of the detected light particle after collision
$E_x$	excitation energy of the recoiling heavy particle after collision
$\theta$	scattering angle of the light particle relative to the beamline direction
$\theta_r$	scattering angle of the heavy particle relative to the beamline direction

Using the conservation of the total energy and momentum before and after the collision, we have the following equations

$$\begin{aligned}
 T_b + Q &= T_o + T_r + E_x \\
 \sqrt{2m_b T_b} &= \sqrt{2m_o T_o} \cos \theta + \sqrt{2m_r T_r} \cos \theta_r \\
 \sqrt{2m_o T_o} \sin \theta &= \sqrt{2m_r T_r} \sin \theta_r
 \end{aligned}$$

where  $\sqrt{2mT}$  is the momentum of a particle of mass  $m$  with kinetic energy of  $T$ . We know  $T_b$ ;  $T_o$  is measured by detectors and  $\theta$  is calculated from the geometry of the target and detector as well as the hit position on the positive sensitive detector. The remaining quantities are unknown:  $T_r$ ,  $\theta_r$  and  $E_x$ , among which the  $E_x$  is of

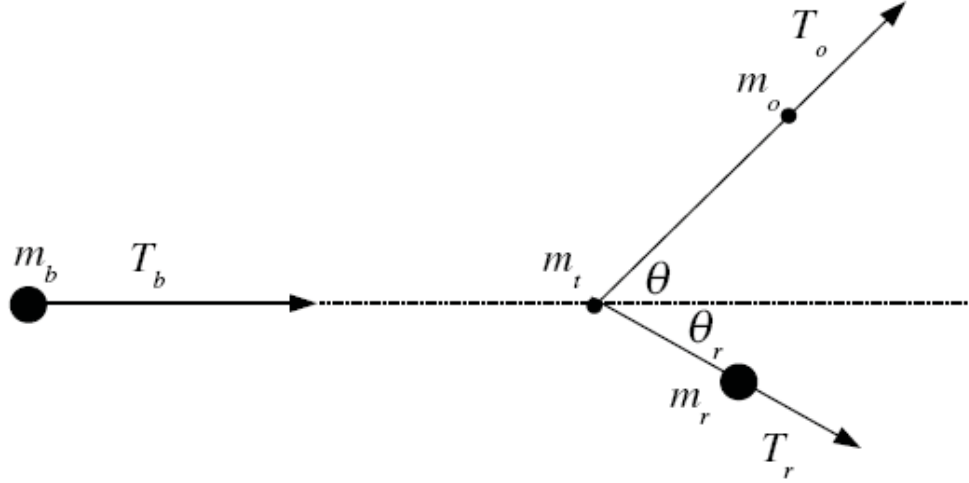


Figure 2.1: schematic diagram of a beam target in collision with a target particle.

interest. It is given by solving the above equations as a function of  $T_b$ ,  $T_o$  and  $\theta$

$$E_x = Q + \left(1 - \frac{m_b}{m_r}\right) T_b - \left(1 + \frac{m_o}{m_r}\right) T_o + \frac{2\sqrt{m_b m_o T_b T_o}}{m_r} \cos \theta$$

For our case, we have  $m_b = m(^{27}\text{Si}) \approx 27$  amu (atomic mass unit),  $m_t = m(^1\text{H}) \approx 1$  amu,  $m_o = m(^2\text{H}) \approx 2$  amu and  $m_r = m(^{26}\text{Si}) \approx 26$  amu.<sup>1</sup> Then the expression of  $E_x$  can be rewritten as

$$\begin{aligned} E_x &= \left(1 - \frac{m(^{27}\text{Si})}{m(^{26}\text{Si})}\right) T_b - \left(1 + \frac{m(^2\text{H})}{m(^{26}\text{Si})}\right) T_o + \frac{2\sqrt{m(^{27}\text{Si})m(^2\text{H})T_b T_o}}{m(^{26}\text{Si})} \cos \theta \\ &= -\frac{1}{26} T_b - \frac{14}{13} T_o + \frac{\sqrt{54}}{13} \sqrt{T_b T_o} \cos \theta + Q \end{aligned}$$

Figure 2.2 shows plots of the correlations between  $E_x$  and the deuteron energy  $T_o$  at various scattering angles that the scattered deuteron makes with the beam-line, with the beam energy  $E_b = 89$  MeV/A. These plots can be used to determine the scan range of excitation energies we can obtain for a given beam energy. As

<sup>1</sup>All the masses in this thesis are adopted from the Atomic Mass Evaluation.

we can see from the plots, the range of our interest ( $E_x = 5 - 8 \text{ MeV}$ ) can be achieved by using the  $89 \text{ MeV}/A$  beam energy .

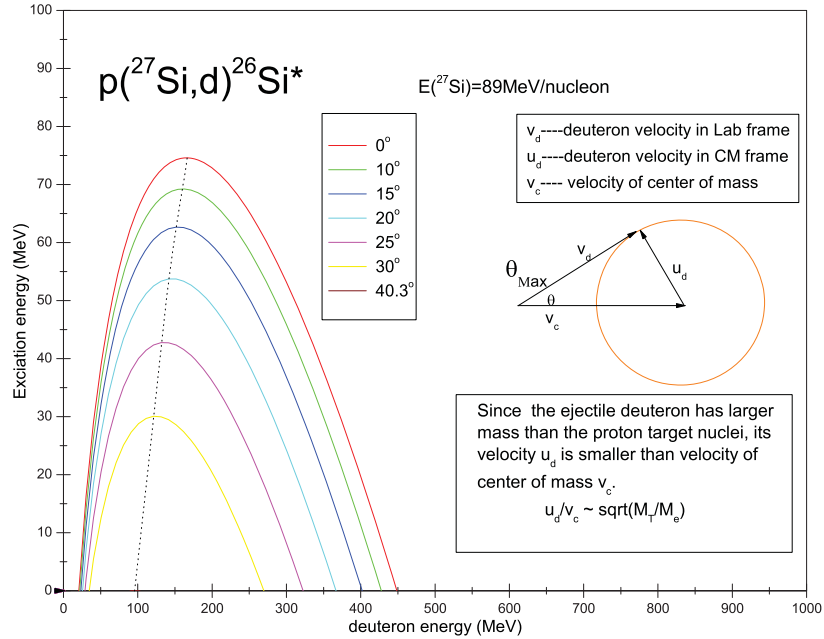


Figure 2.2: Correlations between the excitation energy of  $^{26}\text{Si}^*$  and the energy of the scattered deuteron at various scattering angles with the beam energy  $E_b=89 \text{ MeV}/A$ .

### 2.1.2 The NSCL facility

The NSCL (National Superconducting Cyclotron Laboratory) is located on the campus of Michigan State University and is a world leader in rare isotope research and nuclear science education. It primarily consists of two superconducting cyclotrons — K500 and K1200, which are coupled together to make it possible to produce many rare isotopes with the in-flight (fragmentation) method<sup>2</sup>.

Figure 2.3 shows the schematic diagram of the NSCL facility.

<sup>2</sup>See Appendix A for the methods of beam production

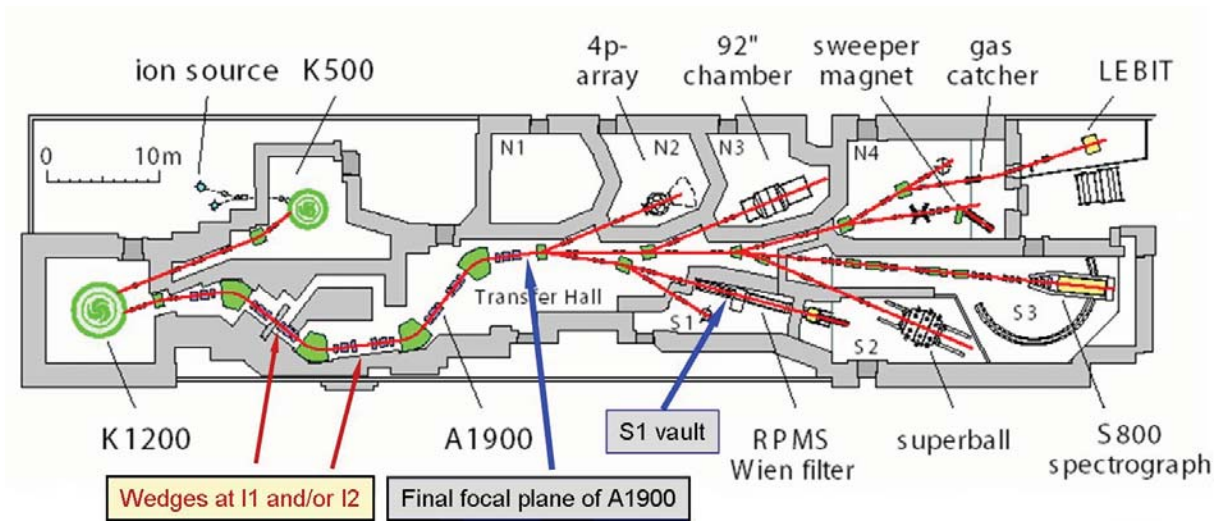


Figure 2.3: schematic diagram of the NSCL facility with the two cyclotrons K500 and K1200, the A1900 fragment separator and the S800 spectrograph indicated.

The charged particles of the primary beam are produced from an electron cyclotron resonance ion source (ECR) and then injected into the first K500 cyclotron to gain the first acceleration. Following that is the further acceleration of the charged particles in the K1200 cyclotron where the beam particles get fully stripped from the electrons and sent to the production target of the A1900 separator to produce the secondary (reaction) beam by fragmentation. Besides the beam particle of interest, many other contaminant particles can be produced at the same time as well. So right after the secondary beam production, the beam separation is performed to separate out only the beam particles of interest which then can be transmitted through the remaining part of the A1900 separator and delivered to the different experimental lines, i.e. the S800 spectrograph.

### 2.1.2.1 S800 spectrograph

The S800 spectrograph is a magnetic device with large acceptance and high resolution for charged particle spectroscopy and is specially designed for nuclear reaction experiments with radioactive beams [15]. The design is unique in that the spectrograph is installed vertically on a carriage instead of the traditional horizontal

installation. This not only saves space but also makes it possible to rotate the spectrograph from  $0^\circ$  to  $60^\circ$  for different experiment purposes. The S800 can be operated in two different modes: a focus mode with the best momentum acceptance ( $\pm 2\%$ ) but limited resolution (1 in 1000 in energy), and a dispersion matching mode with the best resolution (1 in 5000 in energy for a 1 mm beam spot) but limited momentum acceptance ( $\pm 0.5\%$ ). More detailed descriptions of the two modes can be found in Ref. [15]. Figure 2.4 shows the schematic diagram of the S800 spectrograph. Table 2.1 lists some characteristic specifications of the S800.

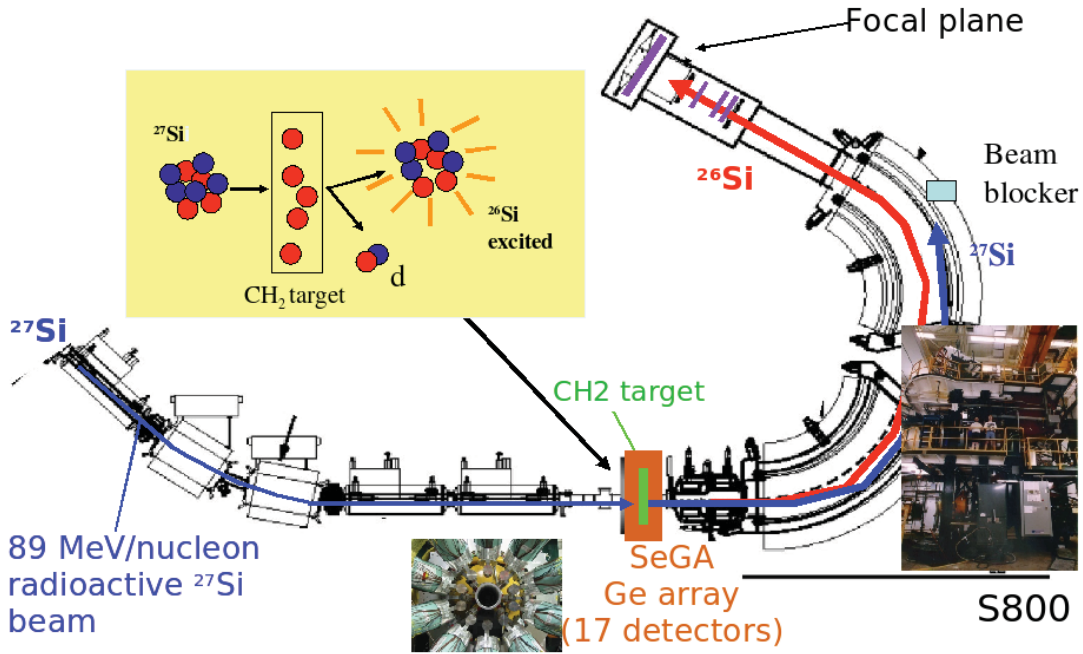


Figure 2.4: schematic diagram of the S800 spectrograph and additional components of the upstream beamline.

In figure 2.4 the target position in the S800 analysis line is also indicated. Surrounding the target, a  $\gamma$ -ray detector array SeGA is installed, which will be described in the following section. The SeGA array detects the  $\gamma$ -rays from the decay of the heavy reaction recoils, in coincidence with the detection of these recoils at the S800 focal plane. An ultra-fast and radiation-hard detectors made from a single-crystal diamond is installed in the S800 before the target for timing.

Table 2.1: Characteristic parameters of the S800 spectrograph, adapted from [16].

Energy resolution	1 in 10000 FWHM
Dispersion	9.6 cm/% ( $\Delta P/P$ )
Momentum Acceptance	5% ( $P$ )
Angular acceptance in dispersive	7°
Angular acceptance in no-dispersive	10°
Angular resolution	2 mrad
Position resolution	0.4

At the end of the S800 is the focal plane [15, 16]. The detector system at the focal plane consists of a pair of cathode readout drift chambers (CRDC) for beam tracking information, followed by a multi-segmented ion chamber for energy loss measurement, and three large plastic scintillators for timing and total energy measurements. Figure 2.5 shows the schematic diagram of the focal plane at the end of the S800 spectrograph.

### 2.1.2.2 SeGA detector array

SeGA is a highly segmented germanium detector array. It consists of 24 separate germanium detectors arranged in two rings at 37° and 90° with 12 detectors for each ring. Each individual detector is divided into 32 segments providing accurate 3-dimensional position for Doppler broadening correction of the measured  $\gamma$ -ray energies. Further details on the SeGA array can be found in reference [17]. Figure 2.6 shows a photo of the SeGA detector array from the front view.

### 2.1.3 Experiment details

The radioactive  $^{27}\text{Si}$  ( $T_{1/2}=4.16\text{s}$ ) beam in the experiment at NSCL was produced by fragmenting 150 MeV/nucleon  $^{36}\text{Ar}$  primary beam ions on a 940 mg/cm<sup>2</sup>  $^9\text{Be}$  target, resulting in a beam energy of 89 MeV/nucleon, an intensity of about  $1 \times 10^7$

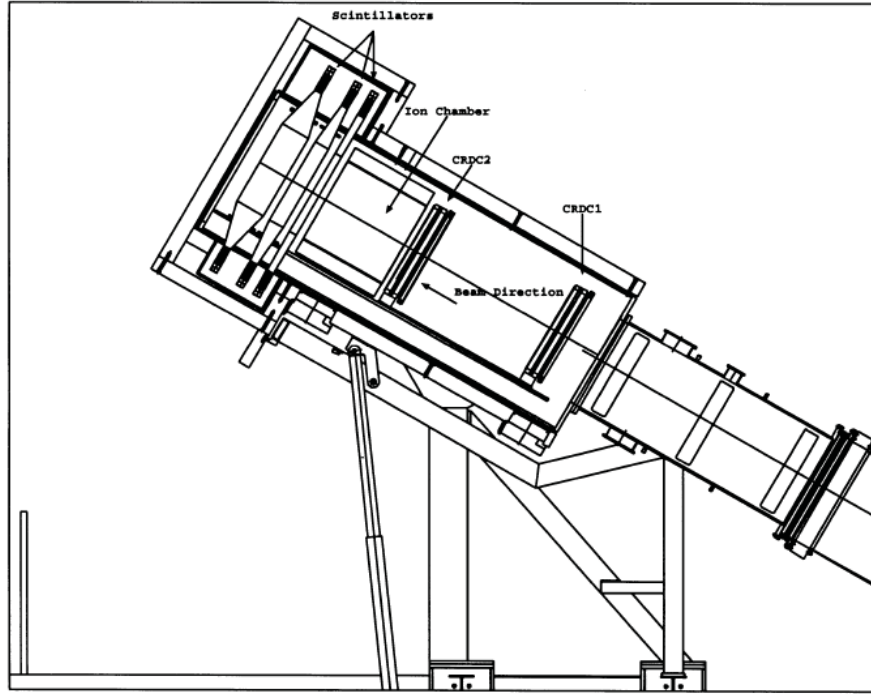


Figure 2.5: schematic diagram of the focal plane detector system at the end of the S800 spectrograph.

pps and purity of about 36%. A  $250 \text{ mg/cm}^2$  polypropylene foil ( $\text{CH}_2$ ) was used as the secondary target which is surrounded by the highly segmented germanium detector array (SeGA) detecting the gamma rays from the decay of  $^{26}\text{Si}^*$  recoils. These gamma rays were detected in coincidence with the detection of the  $^{26}\text{Si}$  recoils at the S800 focal plane. The  $^{26}\text{Si}$  recoils were identified by the time of flight (TOF) between the diamond detector and the scintillator together with the energy loss in the ion chamber.

## 2.2 The $p(^{25}\text{Al},p)^{25}\text{Al}$ experiment at the CRIB facility

We performed an elastic scattering experiment by bombarding a thick proton target (polyethylene,  $\text{CH}_2$ ) with a radioactive heavy-ion beam of  $^{25}\text{Al}$ . With the beam

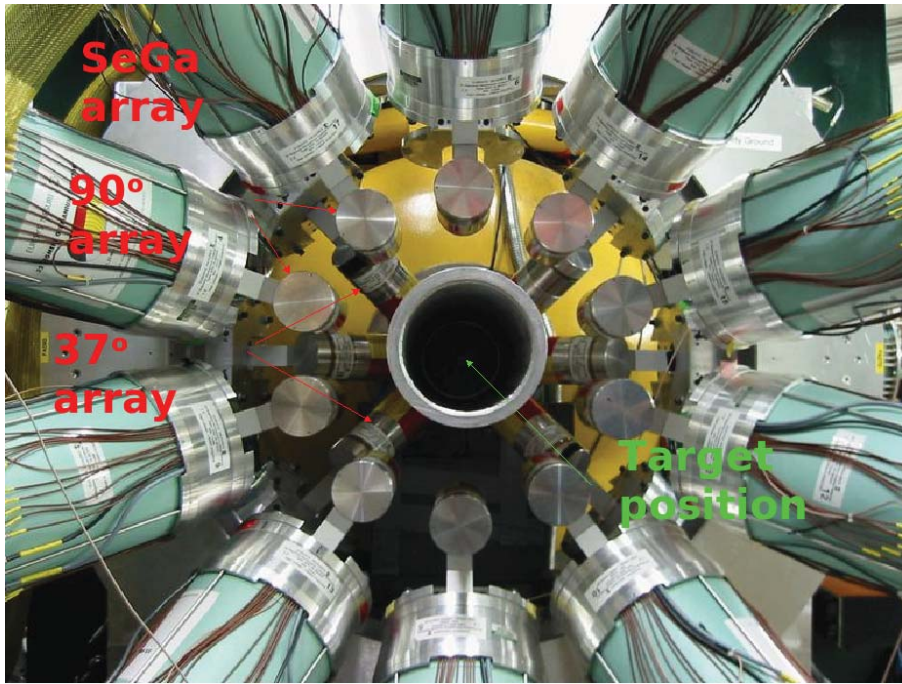


Figure 2.6: Photograph of the SeGA array from the front view.

losing energy and finally stopping in the thick target, a wide range of resonance energies can be scanned in the inverse kinematics. Because only states above the proton threshold ( $S_p=5.518$  MeV)<sup>3</sup> in the intermediate compound nucleus of  $^{26}\text{Si}$  can be populated in the scattering, this experiment aims to study only the resonances above that, as complementary to the aforementioned NSCL experiment.

### 2.2.1 Kinematics and the thick target method

Usually in a nuclear experiment, a light stable beam is used to bombard a target made of a relatively heavier long-lived particle and thus the normal kinematics applies. But in experiments involving radioactive beams, especially those for nuclear astrophysics study, one uses heavy radioactive beam particles to bombard light target nuclei and therefore the kinematics is reversed. To obtain the proper reac-

<sup>3</sup>the Q-value of the nuclear reaction in which a proton and a heavy nucleus form a compound nucleus; only energy levels above this Q-value in the compound nucleus can be populated by the mechanism of compound nuclear scatterings and reactions.

tion information for compound nuclear reactions or scatterings, such as resonant energies and the excitation function, the motion of the interacting particles should be calculated in inverse kinematics, in which all quantities should be converted from the laboratory frame to the center-of-mass (CM) frame.

Although we can deduce all the energies in the CM frame by the same normal kinematics as used for deducing the excitation energy in the  $p(^{27}\text{Si},d)^{26}\text{Si}^*$  experiment, there is simpler way to do that due to the symmetry and simplicity of the elastic scattering in inverse kinematics. Figure 2.7 shows the schematic diagram of the elastic scattering with both the quantities in the laboratory frame and their corresponding quantities in the CM frame indicated explicitly.

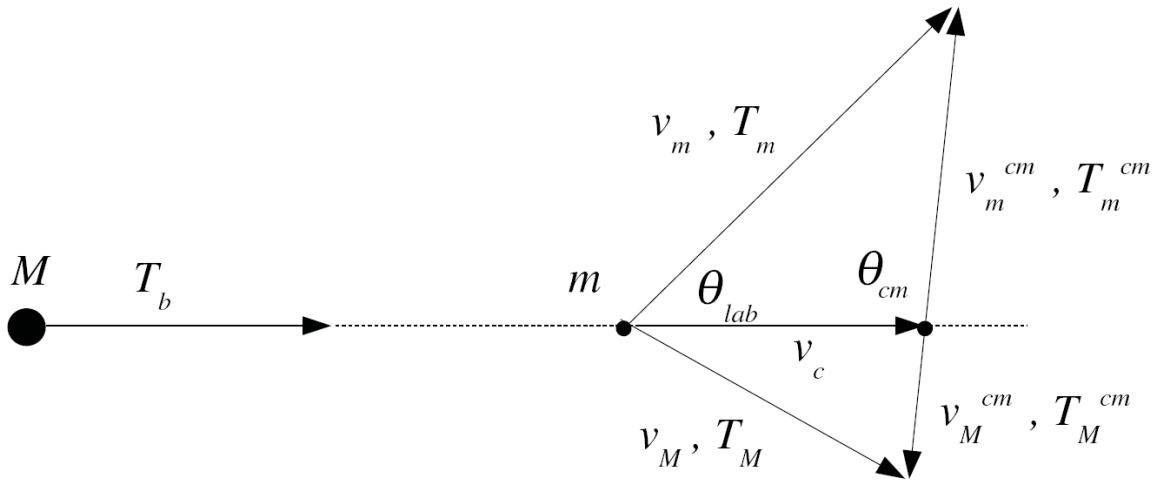


Figure 2.7: schematic diagram of the elastic scattering in inverse kinematics.

The notation in the figure is explained as follows:

$m$	mass of the light target particle, i.e. proton
$M$	mass of the heavy beam particle
$v_c$	velocity of the center of mass
$v_m$	lab velocity of $m$ after collision
$v_m^{cm}$	CM velocity of $m$ after collision
$v_M$	lab velocity of $M$ after collision
$v_M^{cm}$	CM velocity of $M$ after collision
$T_b$	lab kinetic energy of $M$ before collision
$T_m$	lab kinetic energy of $m$ after collision
$T_m^{cm}$	CM kinetic energy of $m$ after collision
$T_M$	kinetic energy of $M$ after collision
$T_M^{cm}$	CM kinetic energy of $M$ after collision
$\theta_{lab}$	lab scattering angle of $m$ relative to the beamline direction
$\theta_{cm}$	CM scattering angle of $m$ relative the beamline direction

According to the simple trigonometry, we can easily find the following relations, setting  $v_m^{cm} = v_c$  for elastic scatterings:

$$v_m = 2v_m^{cm} \cos \theta_{lab}$$

$$2\theta_{lab} + \theta_{cm} = 180^\circ$$

And then from conservation of momentum and kinetic energy, we finally obtain the relation between the total kinetic energy in the CM frame  $E_{cm}$  and the detected proton energy  $T_m$ , as well as the relation between  $E_{cm}$  and the beam energy  $T_b$ ,

$$E_{cm} = \frac{M + m}{4M \cos^2 \theta_{lab}} T_m$$

$$E_{cm} = \frac{m}{M + m} T_b$$

In order to scan a wide range of resonance energies, the thick target method [18, 19] was used. In this method, the target, usually a polypropylene target ( $\text{CH}_2$ ), is chosen to be thick enough to fully stop the radioactive beam but thin enough for the recoiling light particles, usually protons, to exit the target. In the travel path of the beam particle from its beginning in the target to its final stop, the beam particle continuously loses energy mainly due to the collisions with the electrons in the target [20], and collides with the light target particles to scatter them mostly into the forward solid angles in the laboratory system. Therefore, a wide range of energy levels can be scanned simultaneously with only one beam energy, with the maximum of the range corresponding to the beam energy; and the scattered light particles can be detected at forward angles in the laboratory system. According to the above derivations, we can express  $E_{cm}$  in terms of the initial beam energy  $T_o$  before entering the target, the stopping power [20] of the beam particles in the target  $dE/dx$  and the differential target thickness the beam ion has traveled, as follows,

$$E_{cm} = \frac{m}{M+m} T_b = \frac{m}{M+m} \left( T_o - \int_0^x \frac{dE}{dx} dx \right)$$

where  $x$  is the length that the beam has traveled in the target when a scattering occurs.

For our case of the  $^{25}\text{Al}+p$  elastic scattering,  $m \approx 1$  amu and  $M \approx 25$  amu. Then we can rewrite all the relations as

$$E_{cm} = \frac{26}{100} \frac{1}{\cos^2 \theta_{lab}} T_m$$

$$E_{cm} = \frac{1}{26} T_b = \frac{1}{26} \left( T_o - \int_0^x \frac{dE}{dx} dx \right)$$

## 2.2.2 The CRIB facility

CRIB is the CNS (Center for Nuclear Study) Radioactive Ion Beam separator located at the RIKEN campus at Wako in Japan. Figure 2.8 shows the schematic

diagram of the CRIB facility. The primary stable beam, typically a few 100 pA (particles per nano ampere<sup>4</sup>), is produced and accelerated at an AVF cyclotron, and then can be delivered into different experimental halls including CRIB for different purposes. CRIB then uses the primary beam to bombard a primary gas target at the F0 chamber to produce different low energy (<10 MeV/u) radio-isotope (RI) beams by the in-flight (fragmentation) method. The produced various RI beams are then passed through two dipole magnets to separate them according to the characteristic mass-to-charge ratios ( $A/q$ ) of different nuclei or different charge states ( $q$ ) of the same nucleus. The rigidities<sup>5</sup> ( $B\rho$ ) of the magnets are set to select the desired beam particles with proper  $A/q$  based on the following relation,

$$B\rho = \frac{A}{q}v \quad (2.1)$$

where  $B$  is the magnetic field;  $\rho$  is bending radius of the dipole magnet; and  $A$ ,  $q$ ,  $v$  are the particle's atomic mass number, charge state and velocity, respectively.

After the first selection through the bending dipole magnets according to the magnetic rigidity, a Wien filter, installed downstream of the two dipole magnets as shown in the schematic diagram, provides further separation for beam particles of the same magnetic rigidity but different masses ( $A$ ) according to the velocity of the beam particle. The Wien filter will be described in detail in the following section.

With these techniques, the CRIB facility can produce intense and good-quality RI beams with a typical intensity of  $10^4$  to  $10^6$  pps (particles per second<sup>6</sup>), which are applicable for various studies of nuclear physics, especially for those related to the nuclear astrophysics that needs high intensity and high purity RI beam [21].

---

<sup>4</sup>1 pA = 1 nano ampere/1 charge unit (e)  $\simeq 6.3 \times 10^9$  particle per second

<sup>5</sup>This also refers to a particle's momentum per unit charge in a magnetic field.

<sup>6</sup>For stable beams, we use the high intensity unit of pA; for radioactive beams, we use the unit of pps due to their low intensities relative to the stable beams.

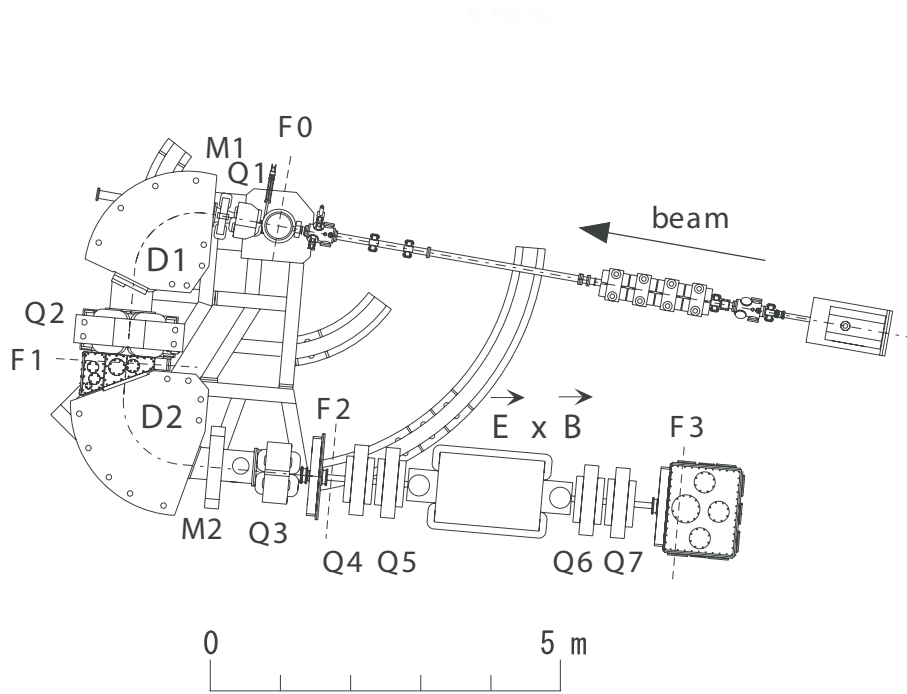


Figure 2.8: schematic diagram of the CRIB facility.

### 2.2.2.1 Beam selector — the Wien Filter

After the beam separation using magnetic dipole according to the different magnetic rigidities of different nuclei, the radioactive beam is still greatly contaminated by radioisotopes with the same mass-to-charge ratios ( $A/q$ ) but different masses. Therefore, a secondary beam selector called a Wien Filter is used and it performs the separation based on the different momenta. In this sense, the Wien Filter is also called momentum separator. Figure 2.9 shows the schematic diagram of the Wien Filter.

When it is working, there are two fields applied inside: a vertical electric field and a horizontal magnetic field perpendicular to the beam line. The directions are set in such that when a charge particle passes through, it will experience the downward or upward electric force and the opposite magnetic force. Only when the two forces balance each other can the charged particle go straight along the beam line through the filter. Otherwise, the particles will deviate from the beam

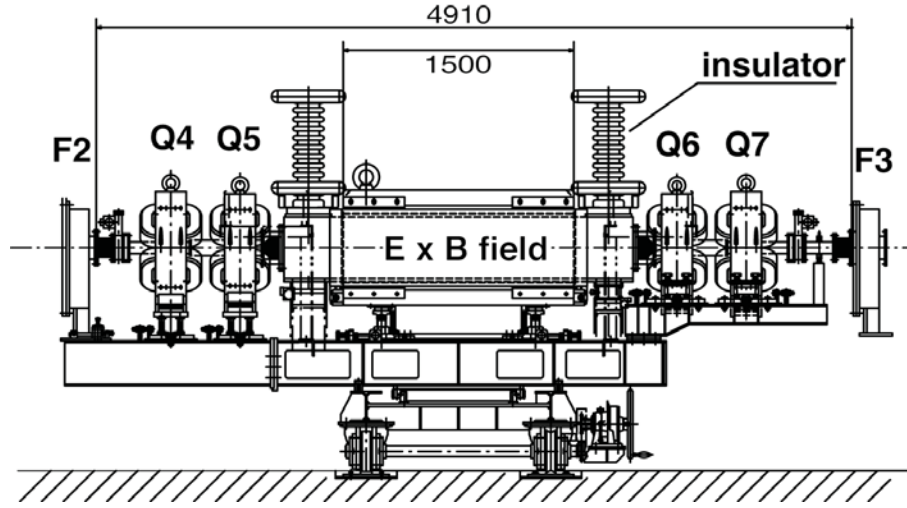


Figure 2.9: schematic diagram of the side view of the Wien Filter.

line and stop within the filter. When the two forces are equal, we can determine the “passing-through” velocity in terms of the magnetic field  $B$  and the electric field  $E$  as

$$v = \frac{E}{B} \quad (2.2)$$

Since we can find the beam velocity from the energy and mass of the beam particle, by applying the proper electric field and magnetic field, we can select only particles with the right velocity and therefore prevent the contaminants with different velocities from passing through the filter and proceeding to the target.

### 2.2.2.2 Experimental chamber (F3)

After the beam particles pass through the Wien Filter, they enter the experimental chamber in which they will be identified and tracked using two PPAC ( Parallel Plate Avalanche Counter) [?] detectors before they bombard the target. It is because even the Wien Filter can not filter out the unwanted particles with the same mass and the same charge as the desired beam particles and they will co-exist with the beam particles and also react with the target. For example, for

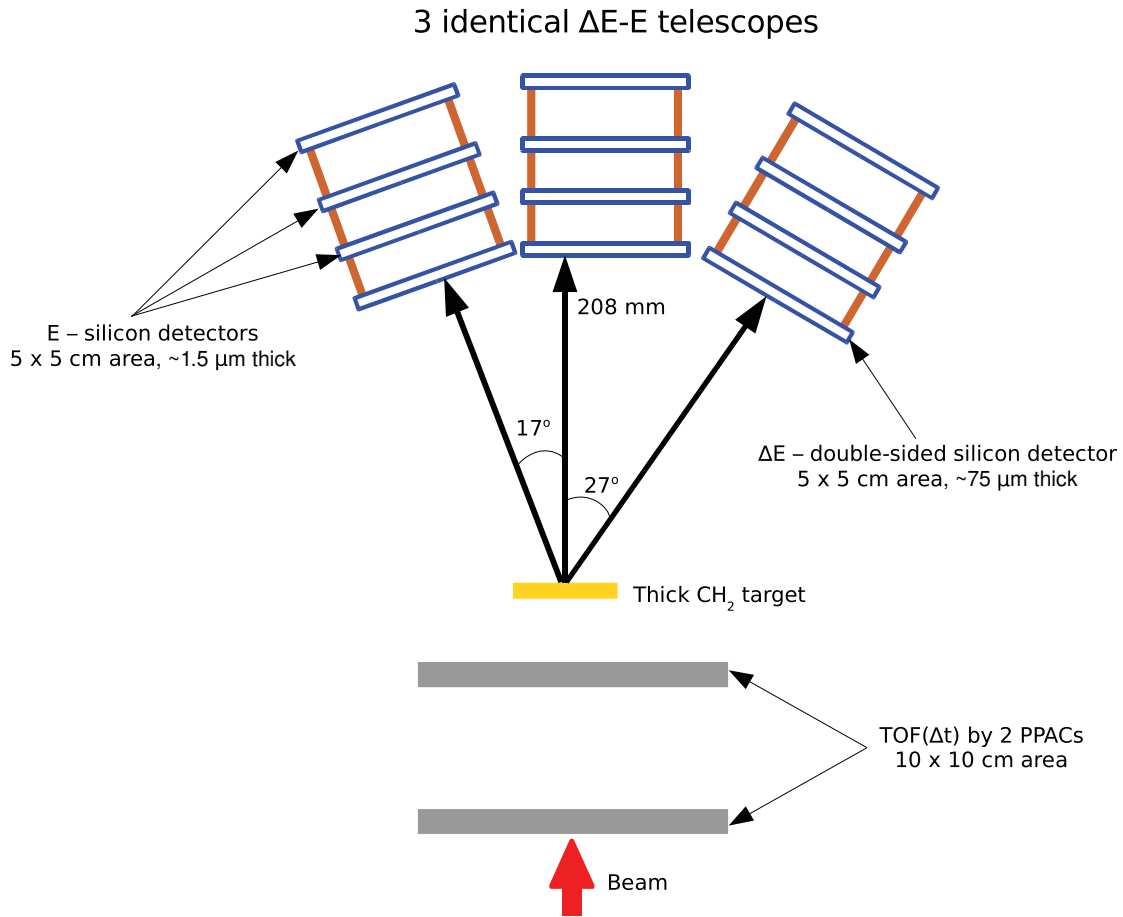


Figure 2.10: Set-up of the detectors in the experimental chamber.

our experiment, the final radioactive  $^{25}\text{Al}$  beam on target is still contaminated greatly by its mirror nucleus  $^{25}\text{Mg}$  in the same charge state. Since in the inverse kinematics the light target particles will be scattered primarily into the forward scattering angles, the silicon detectors for detection of the scattered particles are placed at such angles. Figure 2.10 shows the set-up of the detectors in the detector chamber and figure 2.11 shows a photograph of the experimental chamber.

In case of inelastic scattering in which the heavy particle is scattered out in its first excited state and immediately decays to its ground state with a  $\gamma$ -emission, a NaI  $\gamma$ -ray detector array is installed right above the target for detection of the  $\gamma$ -rays in coincidence of the detection of the light recoils (protons) in the silicon detectors. By this coincidence measurement, we can not only identify the

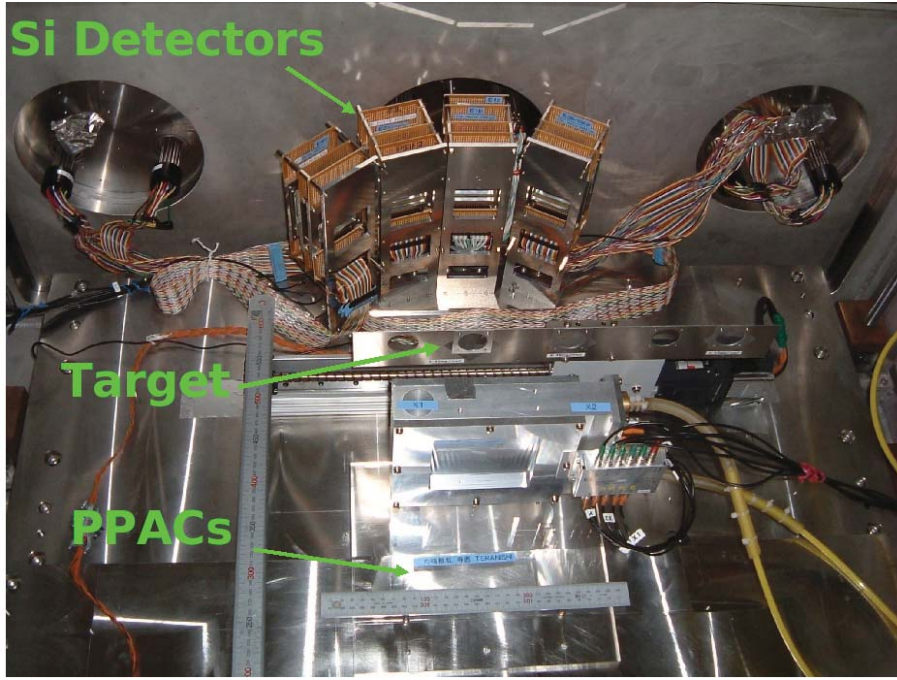


Figure 2.11: A photograph of the experimental chamber (F3).

resonances in the inelastic scattering events, but also remove protons from these events due to the measured proton spectrum of the elastic scattering events.

### 2.2.3 Experiment details

The elastic scattering experiment was performed using a 7.5 MeV/A  $^{24}\text{Mg}^{8+}$  primary beam. The reaction  $^2\text{H}(^{24}\text{Mg},n)^{25}\text{Al}$  was used to produce the secondary  $^{25}\text{Al}$  beam with energy of about 3.4 MeV/A, purity of about 50% and intensity of up to  $1.2 \times 10^6$  pps. The secondary beam was identified by two PPACs (Parallel Plate Avalanche Counters) which were also used for beam tracking to determine the beam position on target and the scattering angle when combined with the proton position measured on a PSD (Position-sensitive Silicon Detector). The secondary target was a  $6.58 \text{ mg/cm}^2$   $\text{CH}_2$  target, which was thick enough to stop the  $^{25}\text{Al}$  beam ions. The elastically scattered protons after the target were measured downstream by 3 sets of  $\Delta E$ -E telescopes at  $0^\circ$ ,  $17^\circ$  and  $27^\circ$ , respectively. Each telescope

consists of one  $75\mu\text{m}$  double-sided  $16\text{ch}\times 16\text{ch}$  PSD and two  $1500\mu\text{m}$  single channel SSDs (Silicon Strip Detectors). Right above the target, 10 NaI detectors were used to detect  $\gamma$ -rays from the decay of the first excited state of the  $^{25}\text{Al}$  produced in the inelastic scattering.

Figure 2.12 shows a schematic diagram of the beam transport line along the CRIB, and the beam tracking and proton detection systems in the F3 chamber.

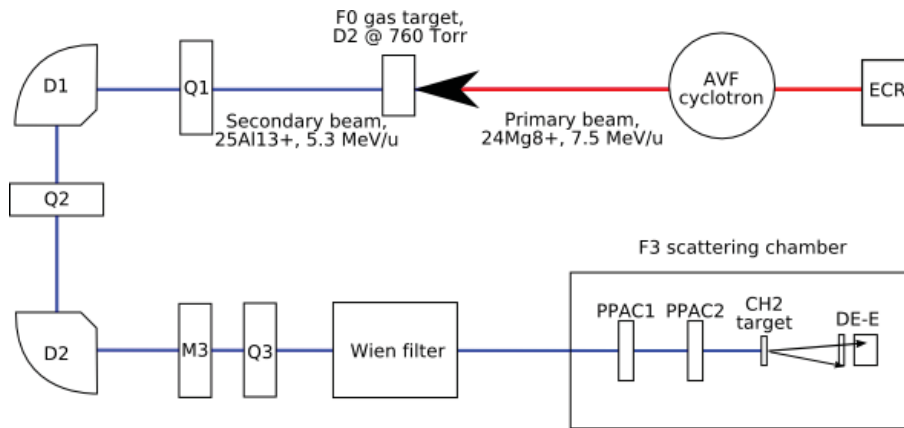


Figure 2.12: schematic diagram of the beam transport line along the CRIB, and the beam tracking and proton detection systems in the F3 chamber.

The Si detectors — PSDs and SSDs — were calibrated separately with three alpha sources ( $^{237}\text{Np}$ ,  $E_\alpha=4.788$  MeV;  $^{241}\text{Np}$ ,  $E_\alpha=5.486$  MeV;  $^{244}\text{Np}$ ,  $E_\alpha=5.805$  MeV). A further calibration with proton beams of 5 MeV, 9MeV and 14 MeV was used to correct for the pulse height defect of alphas in the Si detector. Since the energy range of protons in the PSD used in this experiment is about 2 MeV, the proton beams will punch through the PSDs, enabling the  $\Delta E$ -E telescope to be calibrated as a whole.

#### 2.2.4 Electronics and Data Acquisition System (DAQ)

Each SSD has one channel and is only used for an energy measurement. Each PSD has  $16\times 16$  channels and it also provides the energy measurement for reconstructing the total proton energy and for  $\Delta E$ -E particle identification. Besides, it can also

provide 2-dimensional position information for calculating the scattering angles and the timing information for particle identification using the TOF (Time Of Flight) method only by which the low-energy scattered proton stopping in the PSDs can be identified. The 2-dimensional position information in each PPAC, which is used for beam identification and beam tracking (constructing the scattering angle together with the positions from PSDs), is calculated from the four timing signals it provides with two signals determining one dimension.

Figure 2.13 shows the diagram of the electronics for the detectors.

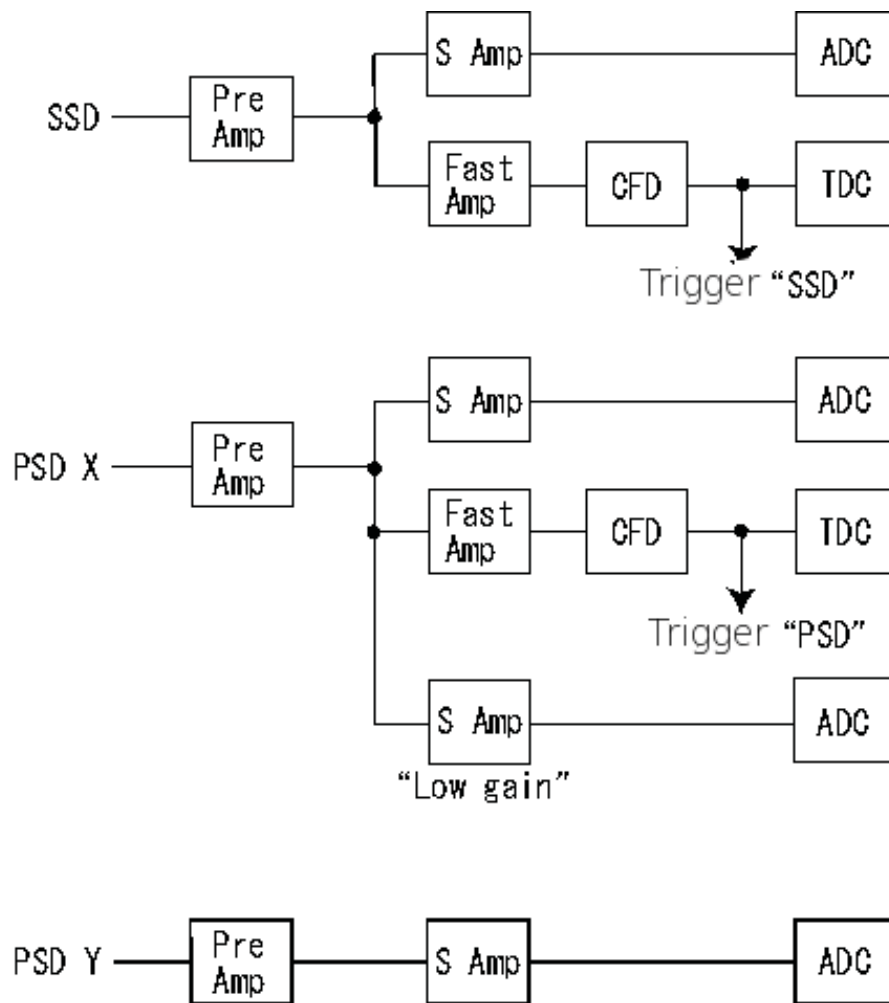


Figure 2.13: Diagram of the electronics for the detectors, adapted from [24].

There are three trigger modes: beam singles trigger (PPAC signals), beam

coincidence trigger (beam and PSD signals) and pile-up trigger. The beam singles mode is used when fine tuning the beam before directing the beam to the target and it triggers events with no PSD signals. The pile-up trigger is used for flagging the pile-up events which will be removed from the total events. The working trigger is the coincidence trigger provided by the beam signals (PPAC signals) combined with the PSD signal, and let through only events which have the beam particles with the right energies and the protons with energies deposited in the PSD. Figure 2.14 shows the electronic diagram of DAQ triggers.

The DAQ used at CRIB is the Barbel system and the online data analysis is performed using the ANAPAW analysis package, both of which can be discussed in more detail on the RIKEN DAQ website [25].

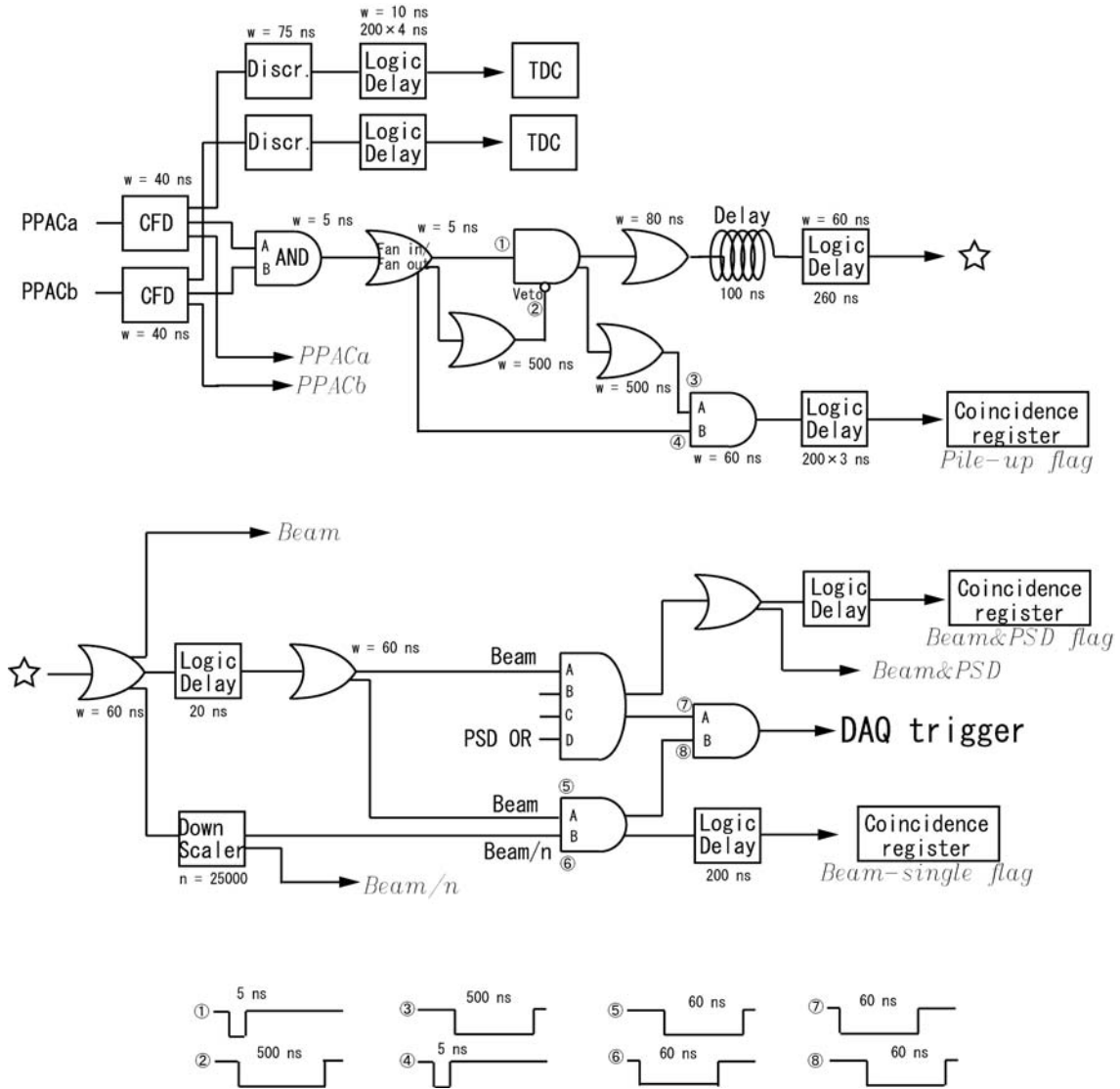


Figure 2.14: Electronic diagram of the DAQ trigger, adapted from [24].

# Some Basic Techniques in the Data Analysis for Nuclear Experiments

In this chapter, before describing the detailed data analysis for our two experiments, some basic analysis techniques and procedures used in our experiments and also common in nuclear physics experiments will be introduced, such as the particle identification techniques.

## 3.1 Particle identification (PID) techniques

Normally in nuclear beam experiments, especially for radioactive beam experiments, the resulting beam can not be 100% pure and is inevitably contaminated during the beam production. Also the reaction recoils are contaminated either by the unreacted beam particles and the contaminants from the beam or by the other reaction products. So we have to filter out the contaminants in order to get the desired beam for the expected nuclear reactions. There is currently no electronics or detectors which can recognize nuclear isotopes and automatically filter out unwanted information in nuclear experiments. The techniques normally used now are the energy loss and the time-of-flight method which use combinations of detectors to identify the measured particles based on their properties.

### 3.1.1 PID using energy loss information in detectors — the $\Delta E$ -E method

When a charged particle passes through the matter in a detector, it will interact mainly with the electrons in the matter via the Coulomb interaction. The particle will therefore lose its energy toward creating electron-ion pairs, which can then be collected as an electric signal whose size is a measurement of the energy deposited in the detector. Its energy loss per unit length in the matter is then related to its charge (proton number  $Z$ ) as well as its mass  $M$ <sup>1</sup>, and is given by the Bethe-Bloch formula (see Eq.5.3 in Chapter 5) from which we find that

$$\frac{E}{\Delta x} \propto \frac{Z^2}{v^2} \quad (3.1)$$

where  $v$  is the velocity of the particle. If a detector is thin enough to let the particle pass through, the total energy deposited in the detector can be approximated as the  $\Delta E$  in the above relationship with  $\Delta x$  as the thickness of the thin target. So for different charged particles passing through the target,  $\Delta x$  is the same and we can rewrite the proportionality as

$$\Delta E \propto \frac{Z^2}{v^2}. \quad (3.2)$$

Since we have the total energy of the particle  $E = \frac{1}{2}Mv^2$ , we can find based on the proportionality above that

$$\Delta E \times E \propto M \times Z^2. \quad (3.3)$$

In the plot of  $\Delta E$  vs  $E$ , this corresponds to a hyperbolic curve for continuously varying  $E$  or a point on such a curve for a single  $E$ <sup>2</sup>, with the curvature uniquely

---

<sup>1</sup>Of course, the energy loss is also related to proton number and mass density of the matter of the detector and since we always use the same detectors in an experiment can treat them as constants.

<sup>2</sup>The light reaction products usually have continuously varying energies according to the reaction kinematics and the beam particles or the heavy reaction products in inverse kinematics

determined by the mass  $M$  and proton number  $Z$  of the detected particle. By measuring the energy loss  $\Delta E$  in a thin detector and total energy in a following thick detector (thick enough to stop the particle) and plotting them in the  $\Delta E$  vs  $E$  histogram, different particles can be clearly identified. Figure 3.1 shows the simulation of the  $\Delta E$ - $E$  curves of different nuclei.

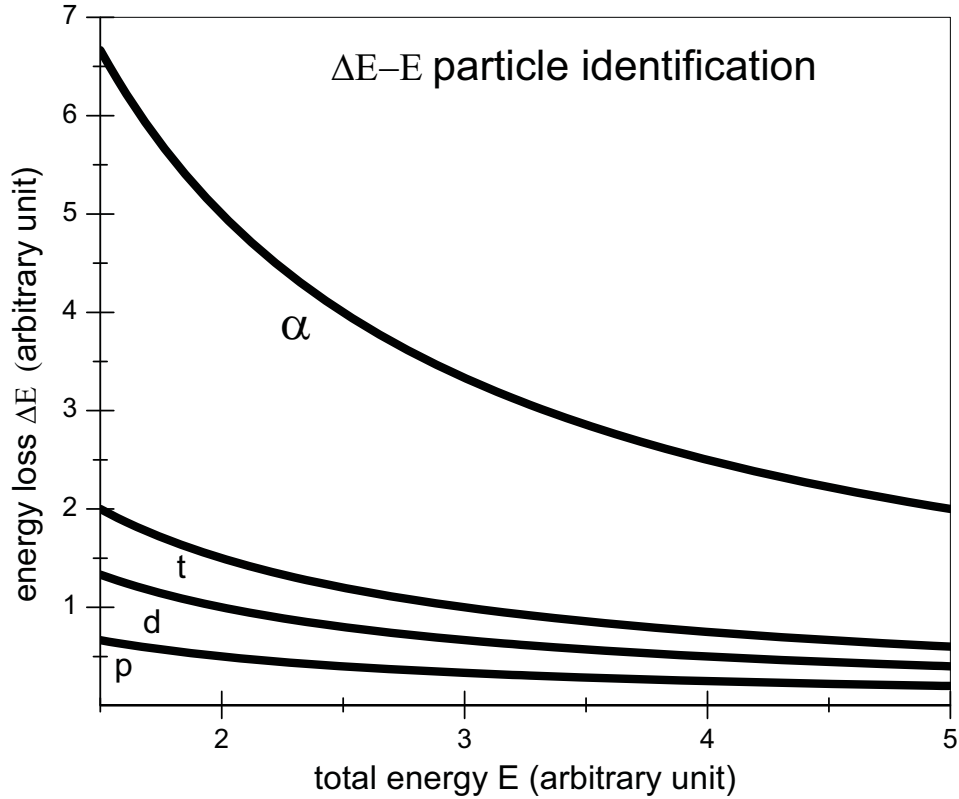


Figure 3.1: Simulation of particle identification using the  $\Delta E$  vs  $E$  histogram.

Since in real experiments the particles (beam particles or scattered products) do not necessarily go perpendicularly into the  $\Delta E$ - $E$  array instead at an angle  $\theta$  with the perpendicular direction, the proportionality for  $\Delta E$  should be corrected by a factor of  $1/\cos\theta$ , as shown in figure 3.2. But the histogram in figure 3.1 still applies except for that there is a minor extension of width for each curve upward to account for particles scattered into the rest angles. Examples from our experiments can be seen in the PID section in Chapter 5.

usually have fixed energies or energies varying in a very small range.

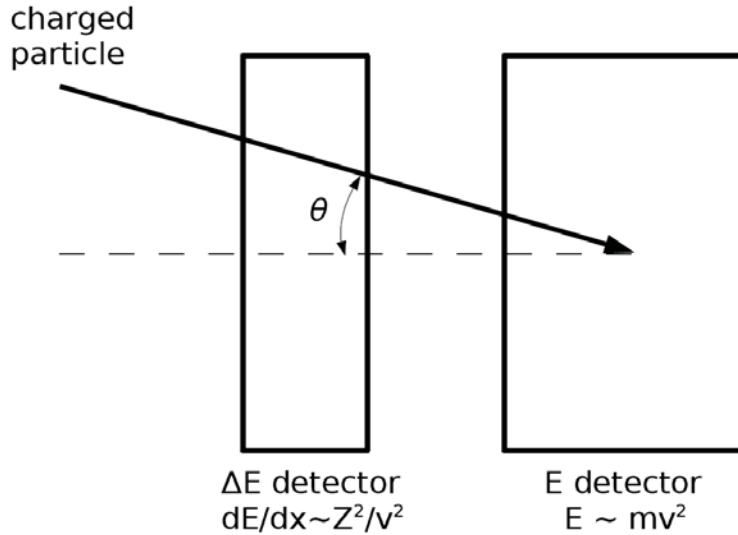


Figure 3.2: schematic diagram of the  $\Delta E$ - $E$  PID method.

### 3.1.2 PID using time of flight between detectors — the TOF- $\Delta E$ method

The effectiveness of the  $\Delta E$ - $E$  method is limited by the particle energy and its intensity on the detectors, since particles of high energy and high intensity will damage the expensive detectors, for example in our experiments, the silicon PSD (Position Sensitive Detector) detectors. So it is usually used for the identification of low-energy, low-intensity light charged particles, such as protons and alpha particles, but it is not useful for particles with energies too low to pass through the thin  $\Delta E$  detector, e.g., the PSDs in our CRIB experiment. For example, to straightly penetrate through a  $75\mu m$  PSD, a proton needs a kinetic energy of at least about 2 MeV and protons with energies under this 2 MeV threshold energy will stop in the PSD and therefore will not be identified uniquely using the  $\Delta E$  vs  $E$  histogram. For these situations, another widely used PID method using the time of flight (TOF) of the ions between detectors comes to play a role, since it is just a time measurement between a “start” signal and a “stop” signal and thus not limited by particle energies. Actually the TOF method is the most used method for

neutron energy measurements. In the following section, we will discuss separately the PID techniques using the TOF method for beam particles and scattered light particles.

Let  $L$  be the distance between the two detectors providing the start and stop signals and  $t$  the time difference between the two timing signals. Then the velocity of the particle can be calculated as  $v = L/t$  and the kinetic energy  $E$  of the particle can be written as

$$E = \frac{1}{2}Mv^2 = \frac{1}{2}M \left( \frac{L}{t} \right)^2 \quad (3.4)$$

First let us discuss the PID using the  $\Delta E$ -TOF method for beam particles or heavy reaction products which have many contaminants with energies that are either fixed or varying in a small range. Usually their energies are high enough for them to pass through the thin detectors for the energy loss measurement and thus Eq. 3.2 can be used for  $\Delta E$ . Then we find that

$$\frac{\Delta E}{t^2} \propto Z^2. \quad (3.5)$$

In the  $\Delta E$  vs time (of TOF) histogram, this corresponds to locus in parabolic bands representing different isotopes with the same  $Z$  but different masses with the masses increasing from left to right as the TOF increases. This is due to the fact that usually these particles have similar energies, i.e., their  $E$  is almost the same. Thus according to Eq.3.4, the smaller the mass  $M$ , the shorter the TOF should be. Or according to the correlation between the magnetic rigidity,  $B\rho$ , and the mass-to-charge ratio of the particle,  $A/q$ , that is  $B\rho = (A/q)v$ , we can find the time-of-flight  $t = L/v = (A/q)L/B\rho$ . Since the  $B\rho$  value is the same for all particles, for isotopes with the same  $Z$  (or  $q$ ), the bigger the mass ( $A$ ), the longer the time-of-flight. Similarly according to  $\Delta E \propto Z^2/v^2 = 2MZ^2/E$ , for the same  $Z$ , the smaller the mass  $M$ , the smaller the  $\Delta E$ . For the same  $M$ , the bigger the  $Z$ , the bigger the  $\Delta E$ . Figure 3.3 and figure 3.4 show an example of PID for beam

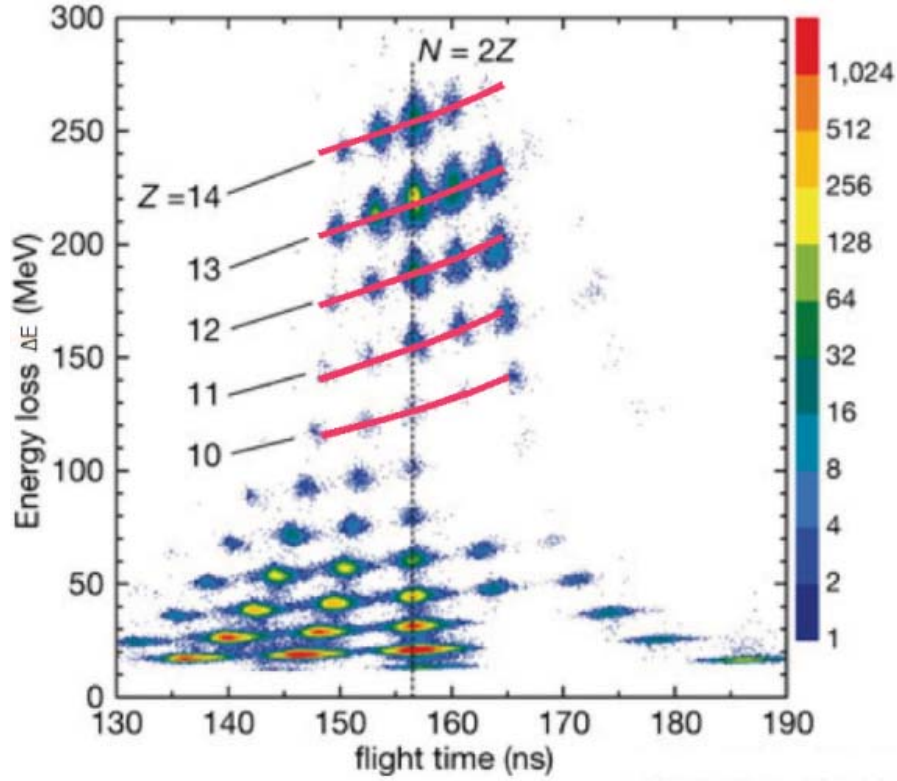


Figure 3.3: An example of PID for beam particles using the  $\Delta E$  vs TOF histogram, adapted from [27].

particles using the  $\Delta E$  vs TOF histogram.

The PID for light reaction products is slightly different since the energies vary continuously according to the kinematics as discussed above. For particles passing through the  $\Delta E$  detectors, the PID is the same as that described above and each particle species is represented by a parabolic band. But for particles stopping in the thin detector, their energy losses cannot be approximated using Eq. 3.2 since the energy deposited is just the total energy  $E = \frac{1}{2}Mv^2$ . Using  $t = L/v$ , we find that

$$\Delta E \times t^2 \propto M^2. \quad (3.6)$$

According to this, these light particles can be identified in the  $\Delta E$ -TOF histogram

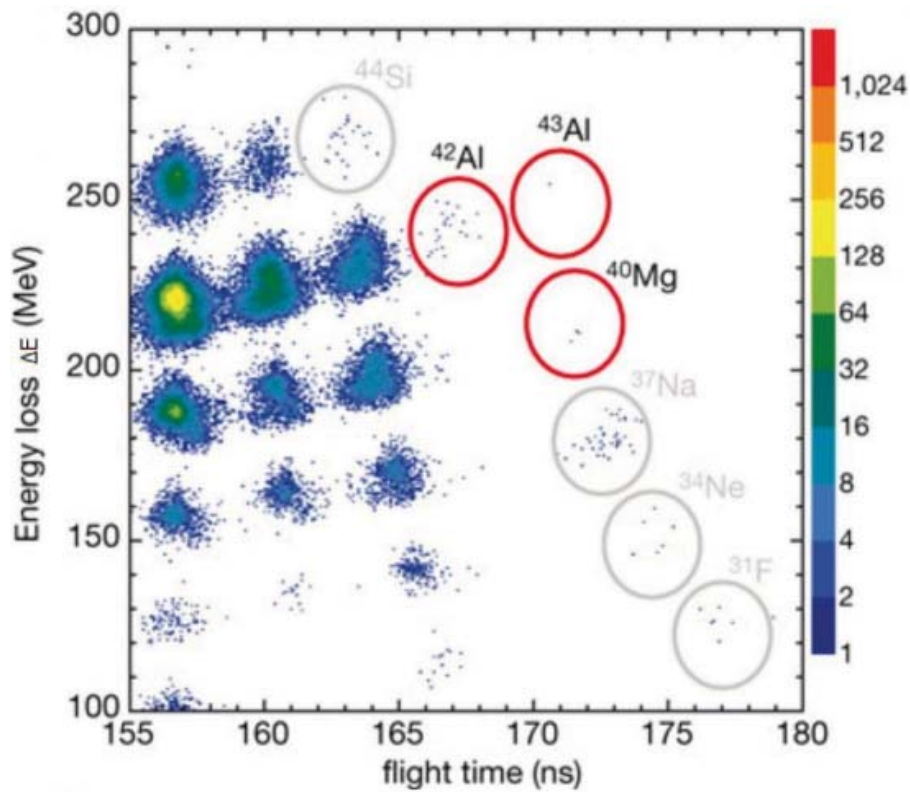


Figure 3.4: Another example of PID for beam particles using the  $\Delta E$  vs TOF histogram, adapted from [27].

by their masses. Figure 3.5 shows a simulation of PID using this method for particles whose energies span a wide range.

## 3.2 Data analysis procedure for nuclear experiments

When we have an idea for an experiment on our research subject, we write a proposal and apply for beamtime. After the proposal is approved, we begin to think about the detailed run plan and prepare for the experiment set-up. We then work on the beam development, detector set-up, target preparation, electronics, and finally the data collection. At this stage, it may seem that the experiment has

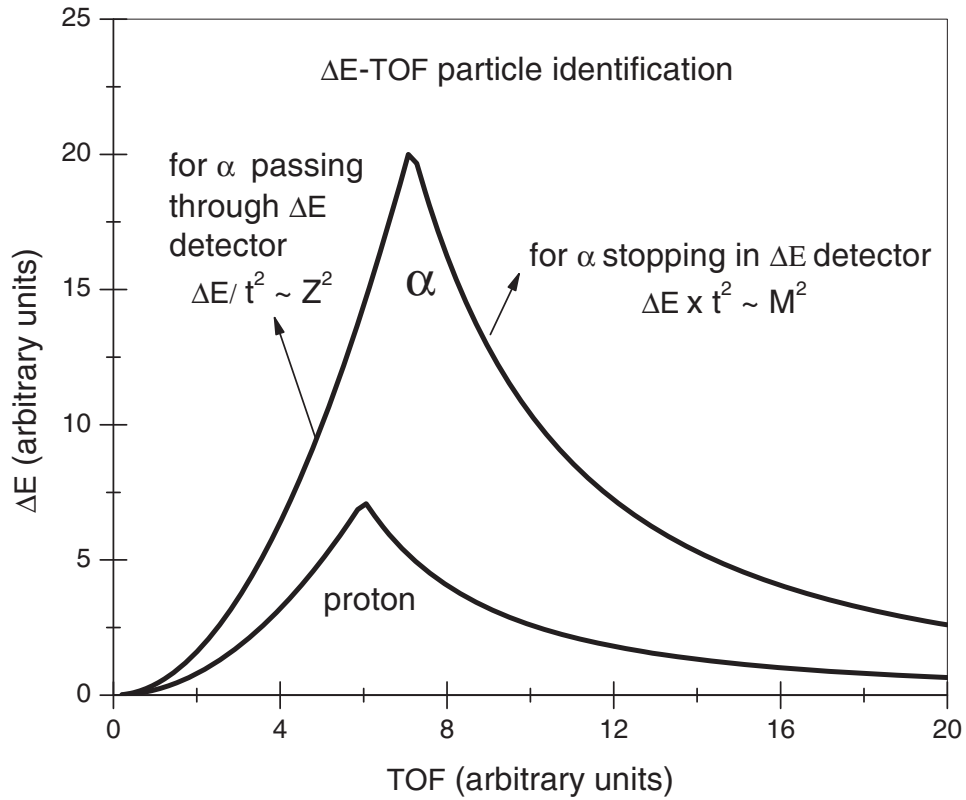


Figure 3.5: A simulation of PID using the  $\Delta E$ -TOF histogram for continuous  $\Delta E$ .

been successfully done. However, this is not completely true. The experiment is just halfway being done since what we got during the experiment time is simply the recording of the experiment — that is, the raw information about the experimental runs — and we are still on the way to finding the results from the experiment. This remaining job is the *data analysis*: it is part of the experiment and is as important as the experimental runs themselves.

The raw data are obtained and converted from the electronic signals by the data acquisition (DAQ) electronics, and then encoded into binary data for easy storage and access. The raw data for our two experiments performed at two different laboratories were encoded in different ways and their formats are given in the Appendix C. The first step of the data analysis is then the decoding and sorting of the raw binary data to the normal accessible data formats that depend on the analysis program that will be used. Of course, we can directly analyze the raw

binary file with the decoding and sorting included in the analysis program, but it is always good and convenient for future further analysis to decode and sort all raw data into new easily accessible data formats. And it is also good for the standardization of the analysis programs since almost all the different laboratories have different raw data formats and their own analysis programs and it is very inconvenient and difficult for researchers at different laboratories to communicate with each other, especially for researchers who are not based in a laboratory. For example, the CRIB data is encoded into `.rdf` format and the NSCL data is encoded into `.evt` format. To analyze these data directly, one needs to use their own analysis program packages, which are the ANAPAW analysis tool [28] for CRIB data and the SpecTcl analysis tool [29] for NSCL data. To reduce the complexity of learning and using multiple programs for our data analysis, we can use just their own decoding programs to sort our data (`.rdf` and `.evt`) into the same data format (`.root`), respectively, so that we can use the same analysis tool for both datasets. The most used general analysis tool is the C++ based ROOT data analysis tool package [30]. In ROOT, we can decode the raw data of different formats separately using the corresponding decoding method and sort them into the same format — the `.root` format, which can be easily accessed and analyzed by any user-customized ROOT program.

After the raw data is converted to `.root` format files, we can re-sort them by placing constraints on the data and plot any data in the files for preliminary analysis. At this stage, we can perform PID analysis by making the histograms as discussed in the previous section. we can then write codes to make any necessary corrections, i.e. for our experiments, energy loss correction for proton energies and Doppler shift correction for  $\gamma$ -emissions, as well as the background subtraction if there is any. After all of those analyses, we are finished with the raw data and we can then proceed to the next advanced stage of data analysis. The fits using theoretical functions can be made to the analyzed data from which the final physical parameters will be extracted. These extracted results are then compared

with the existing results from other experiments if these exist, or with theoretical calculations. Only then can we really say that the whole experiment has been completed.

# Data Analysis for the $p(^{27}\text{Si},d)^{26}\text{Si}^*$ Experiment at the NSCL Facility

## 4.1 Particle identification of beam recoils at the S800 focal plane

Since the secondary beam on the  $\text{CH}_2$  target is contaminated by lots of unwanted particles, there are also  $\gamma$ -ray emission from the reactions of the contaminants with the target, which therefore contaminate the expected spectra from the decay of the excited states of  $^{26}\text{Si}$  recoils. To eliminate the contaminant  $\gamma$ -ray, we select the  $\gamma$ -ray emission events coincident with the  $^{26}\text{Si}$  recoils by gating on the  $^{26}\text{Si}$  recoils at the S800 focal plane. The particle identification (PID) of  $^{26}\text{Si}$  was made using the  $\Delta E$  vs  $TOF$  technique. The information of time of flight (TOF) is from the diamond detectors and the scintillators while the  $\Delta E$  is the energy loss in the ion chamber at the S800 focal plane. Figure 4.1 shows the 2-dimensional histogram of  $\Delta E$  vs  $TOF$  used for the PID. The area inside the red cut corresponds to the  $^{26}\text{Si}$  recoils. It is clearly seen that the  $^{26}\text{Si}$  recoils can be easily separated from the other contaminants in this spectrum. To implement this PID in the code using ROOT, we can use the `TCutG` class to define a cut around the  $^{26}\text{Si}$  region in this PID histogram and then apply the cut during the scanning through the raw data

to obtain the spectrum of only the  $\gamma$ -rays coincident with the  $^{26}\text{Si}$  recoils.

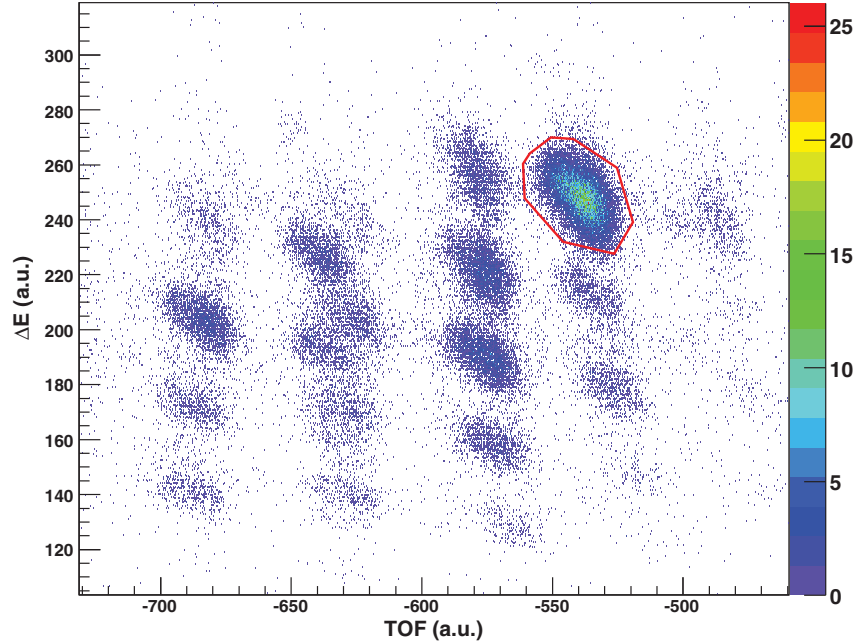


Figure 4.1: A 2-dimensional histogram of  $\Delta E$  vs  $TOF$  for the PID of  $^{26}\text{Si}$ . The area within the red gate corresponds to the  $^{26}\text{Si}$  ions.

## 4.2 Doppler broadening corrections for $\gamma$ -ray energies

Due to the high velocity of the beam particles, the Doppler broadening is prominent for the gamma ray energy measurement. It is corrected for as follows:

$$E_{\gamma,dop} = \frac{1 - \beta \cos \theta}{\sqrt{1 - \beta^2}} E_{\gamma,measured}$$

where  $E_{\gamma,dop}$ ,  $E_{\gamma,measured}$ ,  $\beta$ , and  $\theta$  represent the corrected gamma ray energy, the measured gamma ray energy, the ratio of the  $^{27}\text{Si}$  beam velocity to the speed of

light ( $\beta = v/c$ ) and the  $\gamma$ -ray emission angle, respectively.

Here we use the  $^{27}\text{Si}$  beam velocity for the recoil velocity, which is  $v=0.386c$  for all  $\gamma$  emissions in this experiment. The reason is that the energy loss due to the reaction with the target and the  $\gamma$  emission is negligible compared to the high beam energy, also the recoil has a mass comparable with that of the beam particle and thus the velocity of the recoils can be simply regarded the same as the beam velocity. And it is also because that the recoil energies can not be easily and accurately measured. Actually such measurements are unnecessary since the above estimate is accurate enough when the beam energy is high and the energy loss is low. When end detectors with high energy resolution are used to measure the recoil energy, it is better we use the recoil velocity instead of the beam velocity for this correction.

The  $\gamma$ -ray emission angle  $\theta$  is calculated according to the geometry of the SeGA detectors and target. The SeGA array has 22 individual detectors and each detector has 32 segments. The detectors are arranged at fixed locations and each segment is assigned a coordinate in 3 dimensions. Figure 4.2 shows the coordinate system for our experiment, with the direction of  $z$ -axis points to the downstream along the horizontal beamline. The target is assumed to be at the origin and center on the beam axis..

In the  $\gamma$ -ray measurement, the  $\gamma$ -ray detected by the germanium detector (SeGA) can be scattered within the crystal and deposit its energy in different segments of the detector. The hit position of a  $\gamma$ -ray in a detector during each single event is chosen to be the position of the segment which has the highest deposited energy. Let  $(x, y, z)$  be the coordinates of a SeGA segment and  $(x_t, y_t, z_t)$  the coordinate of the target, which ideally should be at  $(x_t, y_t, z_t)=(0, 0, 0)$ . Then the emission angle can be calculated via,

$$\cos \theta = \frac{z - z_t}{\sqrt{(x - x_t)^2 + (y - y_t)^2 + (z - z_t)^2}}$$

Figure 4.3 and 4.4 show the uncorrected and corrected gamma ray spectra in

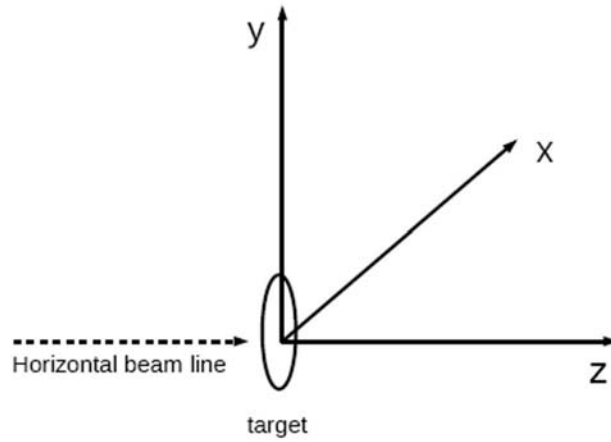


Figure 4.2: Coordinate system for segments of the SeGA array..

coincidence with the  $^{26}\text{Si}$  recoils for the whole runs.

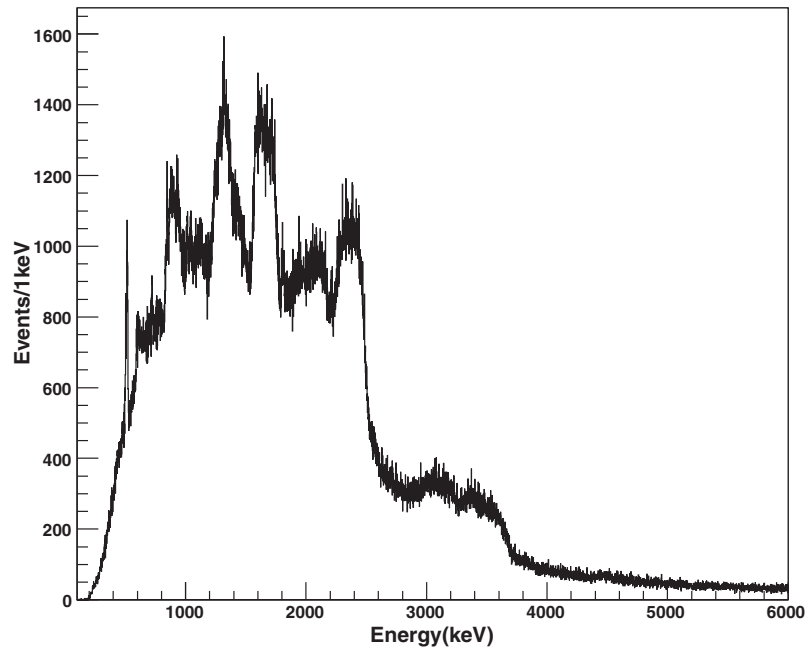


Figure 4.3: Gamma-ray spectrum before Doppler correction in coincidence with the  $^{26}\text{Si}$  recoils for the whole runs.

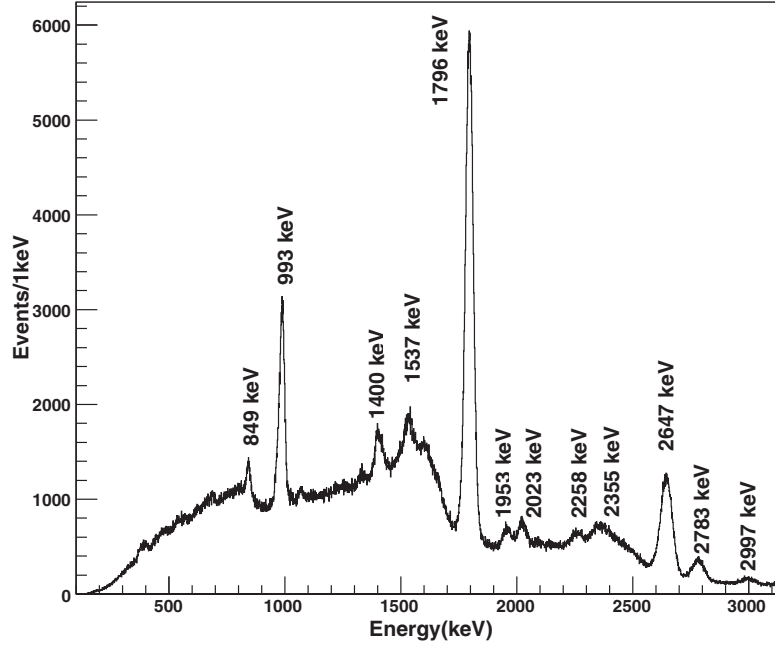


Figure 4.4: Doppler corrected gamma-ray spectrum in coincidence with the  $^{26}\text{Si}$  recoils for the whole runs, including gamma-rays measured in all SeGA detectors. The energies indicated are from skewed Gaussian fits for the peaks.

But in reality the target center does not sit exactly on the beam axis and it can be shifted slightly from the origin up and down, or upstream and downstream. If zero positions are still assumed in the calculation, this will result in, for a same transition or  $E_{\gamma,measured}$ , different corrected energies in different detectors, which will consequently broaden the  $\gamma$  energy peak, worsen the energy resolution, and increase the uncertainty in the determination of the peak centroid. Therefore, it is necessary first to determine the target position more accurately before proceeding to the next step of the data analysis. The procedure for improving the determination of the target position for better Doppler correction will be discussed in the following section.

## 4.3 Attempts to make the Doppler correction more accurate

Here I describe two attempts to make the Doppler correction more accurate: one is the target position determination mentioned above, and the other is an offset correction for the calibrated  $\gamma$  energy before the Doppler correction.

### 4.3.1 Target position determination for more accurate Doppler correction

Ideally, a given  $\gamma$  peak should always have the same peak centroid in the different spectra from different SeGA detectors, ignoring the statistics uncertainties in determining the centroids. But we found that peak centroids measured by different SeGA detectors for a same  $\gamma$  peak differ greatly. For example, table 4.1 lists the peak centroids for the 1796 keV peak corresponding to the strongest  $E2 \rightarrow 0$  transition, extracted from spectra of different SeGA detectors with the target position of  $(0, 0, 0)$  and Figure 4.5 shows how every peak centroid shifts relative to 1796 keV. Figure 4.6 shows the projections of all SeGA detectors on the target plane. In this experiment, SeGA detector3, 7, 8, 11, 15, 16, 23, 24 were not used.

By changing the target position used in the Doppler correction, we can slightly change the peak centroids in the corrected  $\gamma$ -ray spectra and thus minimize the root-mean-square (RMS) deviations from the expected value. By trying different target positions within a small and reasonable range around  $(0, 0, 0)$  and comparing the RMS deviation, we can find the optimal target position which has the smallest RMS.

To find the optimized target position, firstly we fixed the  $z_t$  coordinate of the target position to be zero and scanned the  $(x_t, y_t)$  space to find the  $(x_t, y_t)$  with the smallest RMS deviation for the SeGA detectors in the  $37^\circ$  ring. The reason why we fixed the  $z_t$  is that, the change in  $z_t$  has negligible effect on the final correction for the detectors in the  $37^\circ$  ring considering their long distance to the target in

Table 4.1: List of peak centroids measured by different SeGA detectors for the 1796 keV peak.

detector No.	peak centroid (keV)
1	1805
2	1827
4	1801
5	1800
6	1806
9	1796
10	1802
12	1787
13	1798
14	1769
17	1788
18	1789
19	1773
20	1780
21	1771
22	1781

the  $z$ -axis. Secondly we fixed the  $(x_t, y_t)$  to be the value found from the first step, and iterated over  $z_t$  to find the  $z_t$  with the smallest RMS for the  $90^\circ$  ring. The effect on the final correction for the detectors in the  $90^\circ$  ring due to the change in  $(x_t, y_t)$  is minor compared to that due to the change in  $z_t$ . This is why we fixed  $(x_t, y_t)$  in the second step. Ideally, we should scan the whole  $(x_t, y_t), z_t$  space in one step, but it is heavily limited by the computer power due to the requirements of large storage and computing speed. The  $(x_t, y_t)$  from the first step and the  $z_t$  from the second step together give the optimized the target position  $(x_t, y_t, z_t)$ . The reason we iterated  $(x_t, y_t, z_t)$  in two steps instead of just iterating it in one step for detectors both in the  $37^\circ$  ring and the  $90^\circ$  ring, is that the latter would occupy much more computer memory, making the procedure very slow due to the large file size, sometimes becoming impossible. Also, the effect on the detectors in the  $90^\circ$  ring due to the change of  $(x_t, y_t)$  of the target position is minor compared

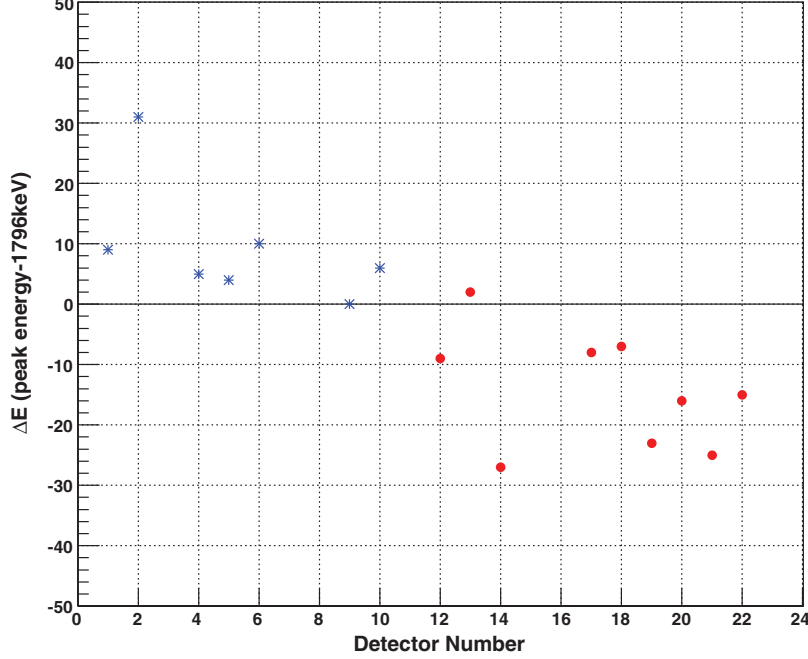


Figure 4.5: Deviations relative to 1796 keV of the 1796 keV peak centroids measured by different SeGA detectors with the target at (0, 0, 0). Blue and red stars represent the SeGA detectors at the 37° and the 90°, respectively.

with the effect on those in the 37° ring. The opposite is true when iterating the  $z_t$  of the target position in the second step.

Before the iteration, it is necessary to determine the step size and the range of the iterations for  $(x_t, y_t, z_t)$ . To this end, I performed an analysis of the effect of the step size on the RMS. Initially a step size of 0.05cm was used to iterate  $x_t$  and  $y_t$  within the range of (-1cm, 1cm). (In the following content, if not specified, the unit of the position is in cm.) We choose a segment at  $(x, y, z)=(10, 10, 20)$  in a detector of the 37° ring, with  $z_t=0$  unchanged and  $\theta$  as the angle the segment makes with the down-stream direction of the beam axis (direction of  $z$  axis). By applying a change  $\Delta x_t$  on  $x$ , we get the following change in  $\cos \theta$ ,

$$\Delta(\cos \theta) = \cos(\theta - \Delta\theta) - \cos \theta \quad (4.1)$$

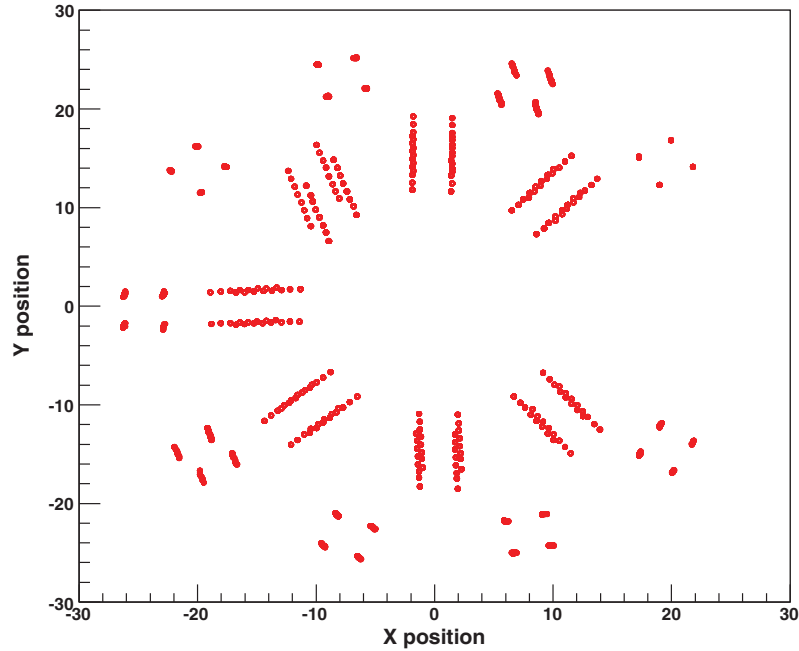


Figure 4.6: Projections of SeGA detectors on the target plane with the target at  $(0, 0, 0)$ . The projections in the inner and outer ring represent the SeGA detectors in the  $37^\circ$  ring and the  $90^\circ$  ring, respectively.

where  $\Delta\theta$  is the change of  $\theta$  due to  $\Delta x$ , and  $\cos\theta$  and  $\cos(\theta - \Delta\theta)$  are calculated by

$$\cos\theta = \frac{Z}{\sqrt{X^2 + Y^2 + Z^2}} \quad (4.2)$$

with

$$X = x - x_t \approx 10, Y = y - y_t \approx 10, Z = z - z_t = z = 20; \quad (4.3)$$

and

$$\begin{aligned}
\cos(\theta - \Delta\theta) &= \frac{z}{\sqrt{(X - \Delta x_t)^2 + Y^2 + Z^2}} \\
&= \frac{Z}{\sqrt{X^2 + Y^2 + Z^2}} \frac{1}{\sqrt{1 - 2\frac{\Delta x_t \cdot X}{X^2 + Y^2 + Z^2} + \frac{(\Delta x_t)^2}{X^2 + Y^2 + Z^2}}} \\
&\approx \cos \theta \frac{1}{\sqrt{1 - 2\frac{\Delta x_t \cdot X}{X^2 + Y^2 + Z^2}}} \\
&\approx \cos \theta \left(1 + \frac{\Delta x_t \cdot X}{X^2 + Y^2 + Z^2}\right)
\end{aligned} \tag{4.4}$$

where we use the first order Taylor expansion to arrive at the last step.

Combining Eq. 4.2 and Eq. 4.4, we find

$$\begin{aligned}
\Delta(\cos \theta) &\approx \cos \theta \cdot \frac{\Delta x_t \cdot X}{X^2 + Y^2 + Z^2} \\
\frac{\Delta(\cos \theta)}{\cos \theta} &\approx \frac{\Delta x_t \cdot X}{X^2 + Y^2 + Z^2} \\
&\approx 0.08\%
\end{aligned} \tag{4.5}$$

The change in Doppler corrected  $\gamma$  energy due to the change in the target position is then,

$$\begin{aligned}
\Delta E_{dop} &= E_{measured} \frac{1 - \beta \cos \theta}{\sqrt{1 - \beta^2}} - E_{measured} \frac{1 - \beta \cos(\theta - \Delta\theta)}{\sqrt{1 - \beta^2}} \\
&= E_{measured} \frac{\beta \Delta \cos \theta}{\sqrt{1 - \beta^2}}
\end{aligned} \tag{4.6}$$

Then, we find,

$$\begin{aligned}
\frac{\Delta E_{dop}}{E_{dop}} &= \frac{\beta \Delta \cos \theta}{1 - \beta \cos \theta} \\
&\approx \frac{\beta \cos \theta \times 0.08\%}{1 - \beta \cos \theta} \\
&\approx \frac{0.386 \times 0.8 \times 0.08\%}{1 - 0.386 \times 0.8} \\
&\approx 0.04\%
\end{aligned}$$

where  $\beta=0.386$  and  $\cos\theta=0.8$  for detectors in the  $37^\circ$  ring.

Based on the above calculation, for the 1796 keV  $\gamma$  energy, for example, the change resulting from the change in the target position ( $\Delta x_t = 0.5\text{mm}$ ) is,

$$1796 \times 0.04\% \approx 0.7 \text{ keV} \quad (4.7)$$

To find out the effect of  $\Delta E_{dop}=0.7$  keV on the RMS deviation, we assume that RMS=10 keV for the 16 detectors measuring the 1796 keV  $\gamma$  energy; that is,

$$RMS = \sqrt{\frac{\sum_{i=1}^{16} (E_{dop}^i - E_{mean})^2}{16}} = 10 \text{ keV} \quad (4.8)$$

Then,

$$\begin{aligned} RMS + \Delta(RMS) &= \sqrt{\frac{\sum_{i=1}^{16} (E_{dop}^i - E_{mean} + \Delta E_{dop})^2}{16}} \\ &\approx \sqrt{10^2 + 0.7^2} \\ &\approx 10 + 0.03 \text{ keV} \end{aligned} \quad (4.9)$$

So each step of iteration of the target position will result in a change in RMS,

$$\Delta(RMS) = 0.03 \text{ keV} \quad (4.10)$$

This assures us that the iteration step length  $\Delta x = 0.05$  cm is small enough to find the best range of target positions.

Using the step length  $\Delta x = 0.05$  cm, the best target position with the least RMS was found to be (0, -0.25, 0).

In order to further verify this result, we iterated the target position for  $(x_t, y_t)$  around the one above using a shorter step length of  $\Delta x = \Delta y = 0.01$  cm. The best result stays the same.

With the best  $(x_t, y_t)$  found, we then iterated  $z_t$  in the range of (-1,1) for the

Table 4.2: List of the smallest RMS obtained under different conditions.

$(x, y, z)$	Smallest RMS		
	37 degree array	90 degree array	total
$(x, y)$ vary $z=0, \text{fixed}$	least RMS=2.1189 at $(x, y)=(0, -0.25)$	10.379	10.694
$(x, y)=(0, -0.25)$ fixed, $z$ vary	4.431	smallest RMS=2.0 at $z=0.25$	8.724

$\gamma$  energies measured by the detectors in the  $90^\circ$  array and the best result is at  $z_t=0.25$ . Table 4.2 shows the list of the smallest RMS deviations obtained in each iteration, as well as the smallest RMS calculated for all SeGA detectors combined.

The optimized target position we found is  $(x_t, y_t, z_t)=(0, -0.25, 0.25)$ . All  $\gamma$ -ray energies were subsequently corrected using this position. Figure 4.7 shows how every peak centroid shifts relative to the 1796 keV using the optimized target position.

### 4.3.2 Offset correction to the calibrated $\gamma$ energy for more accurate Doppler correction

From figure 4.7 even with the optimized target position, we can see that the peak centroids measured by different detectors for the 1796 keV  $\gamma$ -ray still have considerable deviations from the expected value, with a mean deviation of the detectors in the  $37^\circ$  ring of 9.286 keV and 7 keV for those in the  $90^\circ$  ring. What causes this deviation even after we have done an accurate energy calibration for the detectors and corrected the target position? The intrinsic energy resolution of the SeGA detectors may contribute partially but is not be the major source, since the SeGA detectors have high energy resolution of about 1-2 keV. The 1796 keV  $\gamma$  peak is the strongest transition among all transitions and is now well determined with an uncertainty of about 0.2-0.5 keV. All these considerations cannot explain the considerable deviations. But we can think about that they might come from

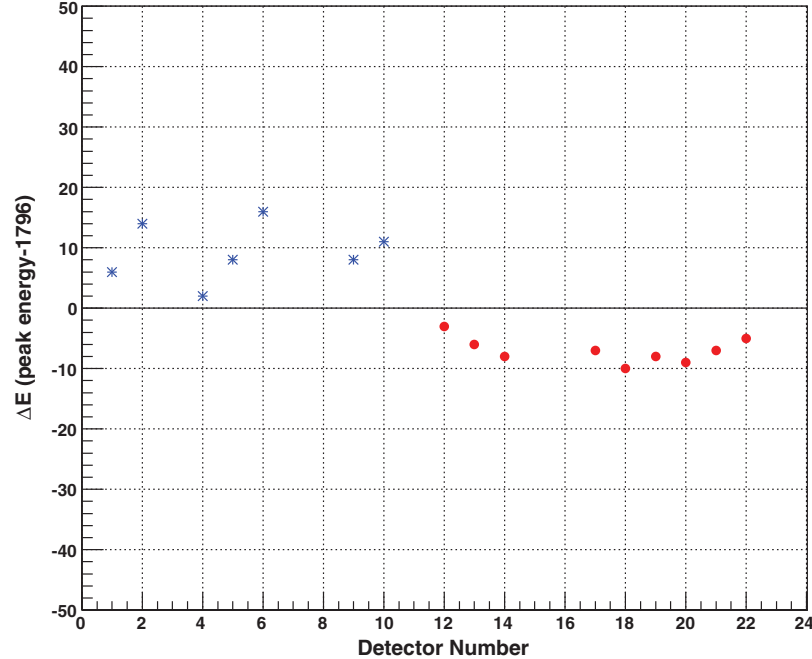


Figure 4.7: Deviations from the 1796 keV of the 1796 keV peak centroids measured by different SeGA detectors with the target at the optimized position (0, -0.25, 0.25). Blue and red stars represent the SeGA detectors at the 37° and the 90°, respectively.

some factors we do not know, which altogether result in an offset to the energy measurement for each single detector. Actually this is just like a second calibration using a well-determined peak from the measured spectrum. Here we use the 1796 keV peak as a calibration source to find the offset for each detector, since, as mentioned, its energy is very well known.

Due to the motion of emission source, the measured  $\gamma$ -energies should be corrected for Doppler Broadening in order to obtain the real transition energies of the  $\gamma$  rays. But, because the measurements by the detectors are made for the  $\gamma$  energies deposited in the detectors, the offsets we want to find should be applied to these energies rather than the  $\gamma$  energies after the Doppler correction. Then, how can we find these offsets from the  $\gamma$  energy spectra? Let us start with the

formula of Doppler correction but now with the offset added, that is,

$$E_{dop}^{final} = (E_{measured} + offset) \frac{1 - \beta \cos \theta}{\sqrt{1 - \beta^2}} \quad (4.11)$$

where  $E_{dop}^{final}$  now is the final  $\gamma$  energy after Doppler correction and offset correction,  $E_{measured}$  is still the energy deposited in the detector and  $offset$  is the energy offset due to the possible causes we already mentioned above. Since the energy in the present Doppler-corrected  $\gamma$  spectrum was obtained by

$$E_{dop} = E_{measured} \frac{1 - \beta \cos \theta}{\sqrt{1 - \beta^2}} \quad (4.12)$$

then we can find that,

$$E_{dop}^{final} = E_{dop} + offset \frac{1 - \beta \cos \theta}{\sqrt{1 - \beta^2}} \quad (4.13)$$

It follows that

$$offset = (E_{dop}^{final} - E_{dop}) / \left( \frac{1 - \beta \cos \theta}{\sqrt{1 - \beta^2}} \right) \quad (4.14)$$

Apparently we cannot use this equation to find the offset because we don't know what  $E_{dop}^{final}$  corresponds to a given combination of  $E_{dop}$  and  $\theta$ , which is exactly what we want to find after finding the offset first. But we can assume that a same group of events making a peak in a particular range of energies in the spectrum of  $E_{dop}$  should also make a peak in the spectrum of  $E_{dop}^{final}$  at the expected energy that the peak should have after we make the offset correction. For example, for the 1796 keV peak, we may find a peak at 1800 keV in a  $\gamma$  spectrum measured by one of the detectors and we expect that, after adding the offset, all energies in the previous 1800 keV peak region will now peak at 1796 keV. With this assumption, and with the fact that all energies measured by the same detector have the same offset and the average of all the involved energies corresponds to the peak energy, we should be able to calculate the offset by taking the average of the angles  $\theta$  of

all the  $\gamma$  events that make up a peak and using the peak centroids; that is

$$offset = \frac{E_{peak}^{final} - E_{peak}}{\frac{1 - \beta \cdot \overline{\cos \theta}}{\sqrt{1 - \beta^2}}} \quad (4.15)$$

where  $E_{peak}^{final}$  and  $E_{peak}$  represent the expected peak energy and the measured peak energy in the Doppler corrected spectrum, respectively;  $\overline{\cos \theta}$  is the average of  $\cos \theta$  over all the involved  $\gamma$ -emissions making the peak.

Here are the details for finding the offsets. By using the 1796 keV peak as a calibration peak,  $E_{peak}^{final} = 1796$  keV for all detectors.  $E_{peak}$  is the peak value corresponding to the 1796 keV peak in the  $\gamma$  spectrum measured by each detector. we still need to know the  $\cos \theta$ , which will be calculated for each detector using a 2-dimensional histogram of  $\cos \theta$  vs  $E_{measured}$  for the  $\gamma$  events making up the peak corresponding to the 1796 keV peak. Figure 4.8 shows an example of this histogram.

Of course, the offset correction is just an approximation and not a perfect approach, since only one known peak is used to calibrate and calculate the offsets which are then applied to all the other peaks. Different offsets might be obtained if we use different peak or multiple peaks for calibration. Strictly speaking, it cannot be simply assumed that the same offset calculated using one peak is valid for other peaks to correct their peak centroids. However, since the 1796 keV peak we used for calibration is the dominant peak and is much stronger than the other peaks, it alone will give the best correction results compared with those obtained using other peaks with low statistics, or using the combination of the 1796 keV and other peaks, both of which result in more uncertainty than the approach involving only the strongest peak. We did find finally that with the offset correction, the quality of the spectrum was improved. Further improvement might be achieved by introducing a gain to each detector which can be calculated to compensate for the offsets. It will then be similar to the linear calibration.

After all offsets for the 16 SeGA detectors in both  $37^\circ$  and  $90^\circ$  were obtained,

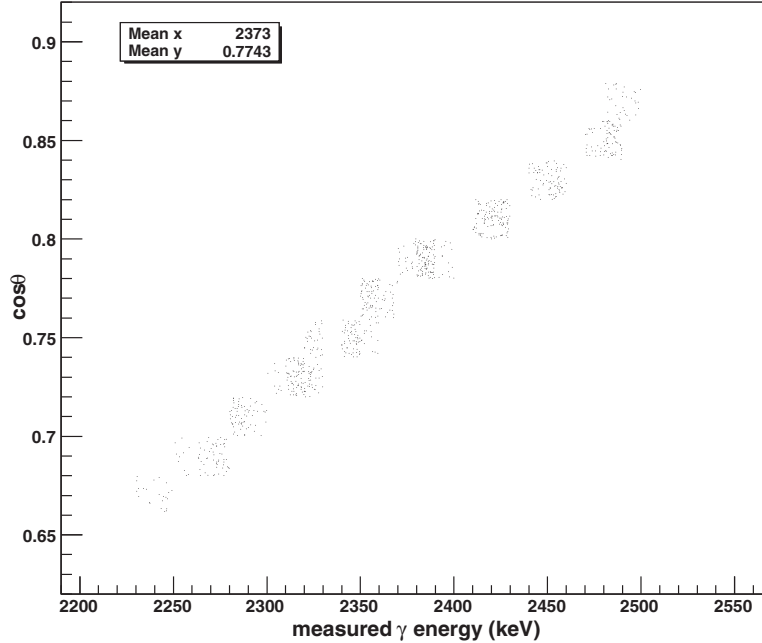


Figure 4.8: An example of a 2-dimensional histogram of  $\cos\theta$  vs  $E_{measured}$  for calculating the average of  $\cos\theta$  of a detector over the detected  $\gamma$  emissions of the 1796 keV peak. This is for detector No.10 in the  $37^\circ$  ring with the Doppler-corrected peak of 1796 keV at 1802 keV.

they were be applied to these detectors in the sorting program to resort the raw experimental data.

#### 4.4 Peak information from the corrected $\gamma$ spectrum

Figure 4.9 is the final fully corrected  $\gamma$  spectrum, in which a new  $\gamma$  ray is found at 2260 keV; and figure 4.10 shows the same spectrum from 3700 keV to 4600 keV, where another new peak around 4100 keV is found. In gamma spectroscopy, a Gaussian shape function is used for fitting the  $\gamma$  peak to extract the peak information, such as peak centroid energy, peak intensity and corresponding uncertain-

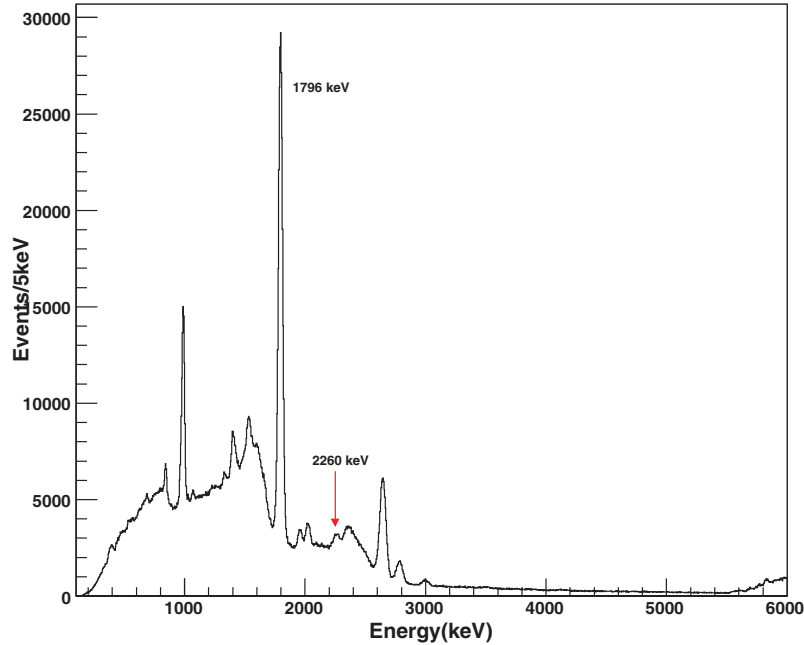


Figure 4.9: The final corrected  $\gamma$  spectrum for the whole energy range of the detected  $\gamma$ -rays.

ties [58, 59]. For the formula used for the fitting, there are various forms which are slightly different from one another in format, but essentially the same [58, 60] in that they generally consist of three components: a main pure Gaussian shape of the peak, a skewed Gaussian shape on the low energy side of the peak caused by the pile-up effect and incomplete charge collection of the detector; and a quadratic background at the bottom of the Gaussian shape. Here we use the following formula which is adapted from the formula in the gamma analysis package GF3 [60], and has the pure Gaussian, skewed Gaussian and quadratic background terms listed below in order.

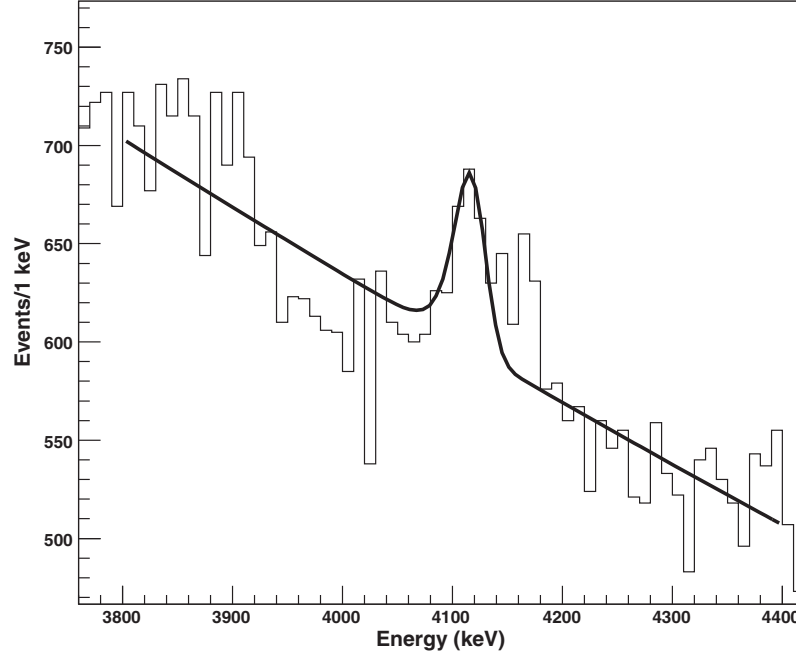


Figure 4.10: The final corrected  $\gamma$  spectrum — an enlargement from 3700 keV to 4600 keV where a new peak around 4100 keV is found.

$$\begin{aligned}
 Y &= A \cdot \left(1 - \frac{R}{100}\right) \cdot \exp\left[-\frac{(X - X_0)^2}{2 \cdot \sigma^2}\right] \\
 &+ A \cdot \frac{R}{100} \cdot \exp\left[\frac{(X - X_0)}{\sigma}\right] \cdot \operatorname{erfc}\left[\frac{(\sigma + X - X_0)}{(\sqrt{2} \cdot \sigma)}\right] \\
 &+ a \cdot X^2 + b \cdot X + c
 \end{aligned} \tag{4.16}$$

where

- Y — yield of  $\gamma$  rays;
- A — a normalization factor;
- R — contribution of the skewed Gaussian, out of 100;
- $X_0$  — peak centroid (keV);
- $\sigma$  — standard deviation of the peak centroid (keV);

From the fitting the peak shape, the peak centroid and peak resolution can

be obtained directly. The peak intensity is represented by the total counts within the peak range. In gamma spectroscopy, a relative intensity is usually used with the strongest transition having an intensity of 100, and the rest having intensities relative to 100, given by the ratio between their yield and that of the strongest peak. The total yield in a peak in the spectrum is equal to the area under that peak and is calculated using the area of the fit function excluding the background term for that peak<sup>1</sup>. The area of the fit function is calculated as below:

Peak Area

$$\begin{aligned}
&= \int_{-\infty}^{+\infty} (\text{Gaussian term} + \text{skewed Gaussian term})dX \\
&= \int_{-\infty}^{+\infty} \left( A \cdot \left(1 - \frac{R}{100}\right) \cdot \exp\left[-(X - X_0)^2 / (2 \cdot \sigma^2)\right] \right) dX \\
&+ \int_{-\infty}^{+\infty} \left( A \cdot \frac{R}{100} \cdot \exp\left[(X - X_0) / \sigma\right] \cdot \text{erfc}\left[(\sigma + X - X_0) / (\sqrt{2} \cdot \sigma)\right] \right) dX \quad (4.17) \\
&= A \cdot \left(1 - \frac{R}{100}\right) \cdot \sqrt{2\pi}\sigma + \frac{A \cdot R}{100} \cdot \frac{2\sigma}{\sqrt{e}} \\
&= A\sigma\left(\sqrt{2\pi} + \frac{2 - \sqrt{2e\pi}}{100\sqrt{e}}R\right)
\end{aligned}$$

and the uncertainty of the area is given by

$$\frac{\delta Area}{Area} = \sqrt{\left(\frac{\delta A}{A}\right)^2 + \left(\frac{\delta \sigma}{\sigma}\right)^2 + \left(\frac{\delta R}{R}\right)^2} \quad (4.18)$$

When making the fitting, we can fit each peak individually or fit all peaks together simultaneously. Here we choose to use the former option. The fitting procedure is as follows: firstly, we roughly decide the peak energy range of the peak to be fitted and make a fit; secondly, we fine tune both sides of the peak range and repeat the fitting; finally, we compare all fitting results and choose the fit with the smallest  $\chi^2$  to extract the peak parameters and their uncertainties, and to calculate the peak area and its uncertainty by error propagation using the

<sup>1</sup>only when the histogram has a binning of 1keV/bin; otherwise, the bin size has to be taken into account when calculating the yield using the area.

extracted peak information. Figure 4.11 shows an example of the skewed Gaussian fit for the 1796 keV peak with each component in the fit function plotted in the figure also. Figures 4.12 to 4.15 show the final fits for the other potential peaks in the final  $\gamma$  spectrum and the fits for the newly found peaks around 4110 keV and 2260 keV are shown in figure 4.16. All these fits are obtained by varying the fit range, and making the parameter  $R$  fixed or free to vary to find the smallest  $\chi^2$ . Table 4.3 lists the extracted peak parameters and peak areas, and table 4.4 lists the final energies for all  $\gamma$  peaks, their relative intensities with respect to that of the strongest  $\gamma$  ray, and the uncertainties in the intensities and energies.

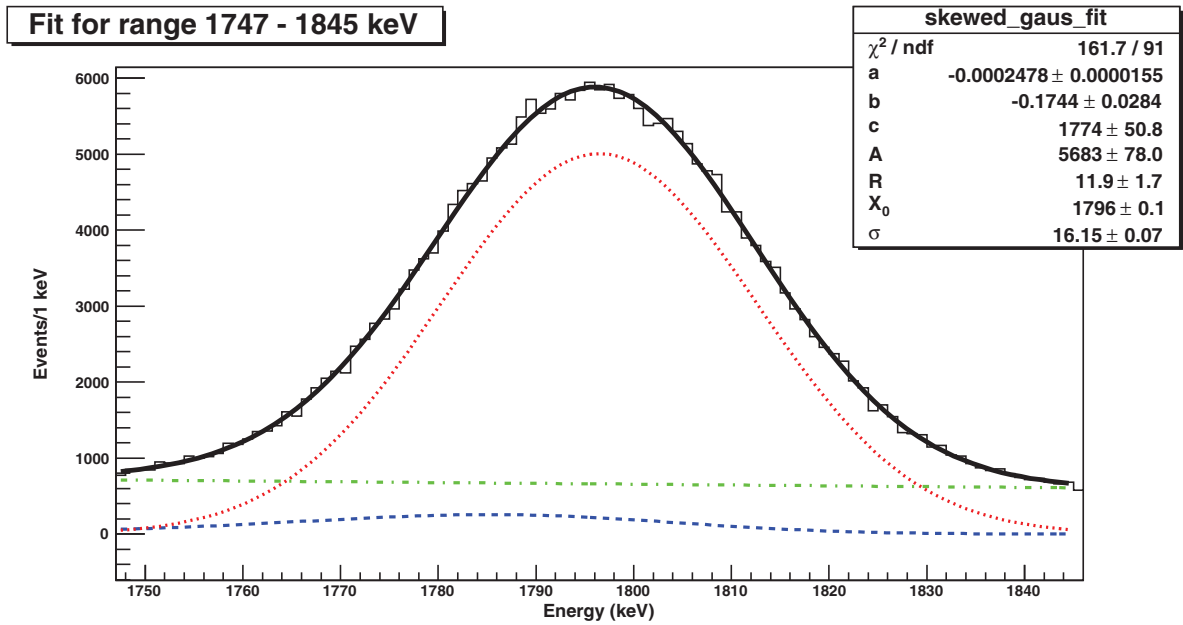


Figure 4.11: The skewed Gaussian fit example for the 1796 keV peak with the fit curve in black solid line, the Gaussian component in red dotted line, the skewed Gaussian component in blue dashed line, and the quadratic background in green dotted-dashed line.

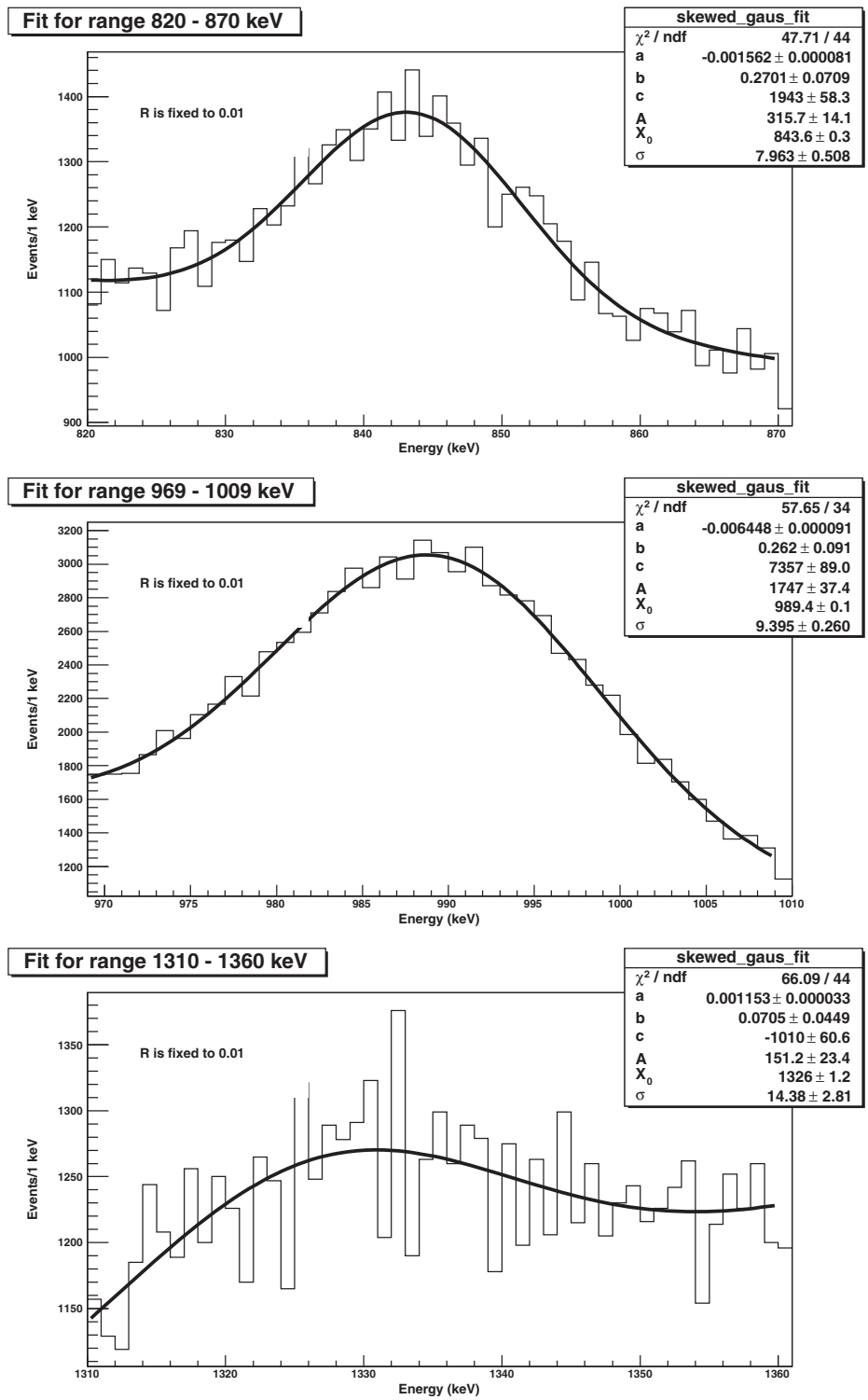


Figure 4.12: The fits for the peaks at 843 keV, 989 keV and 1326 keV in the gamma spectrum.

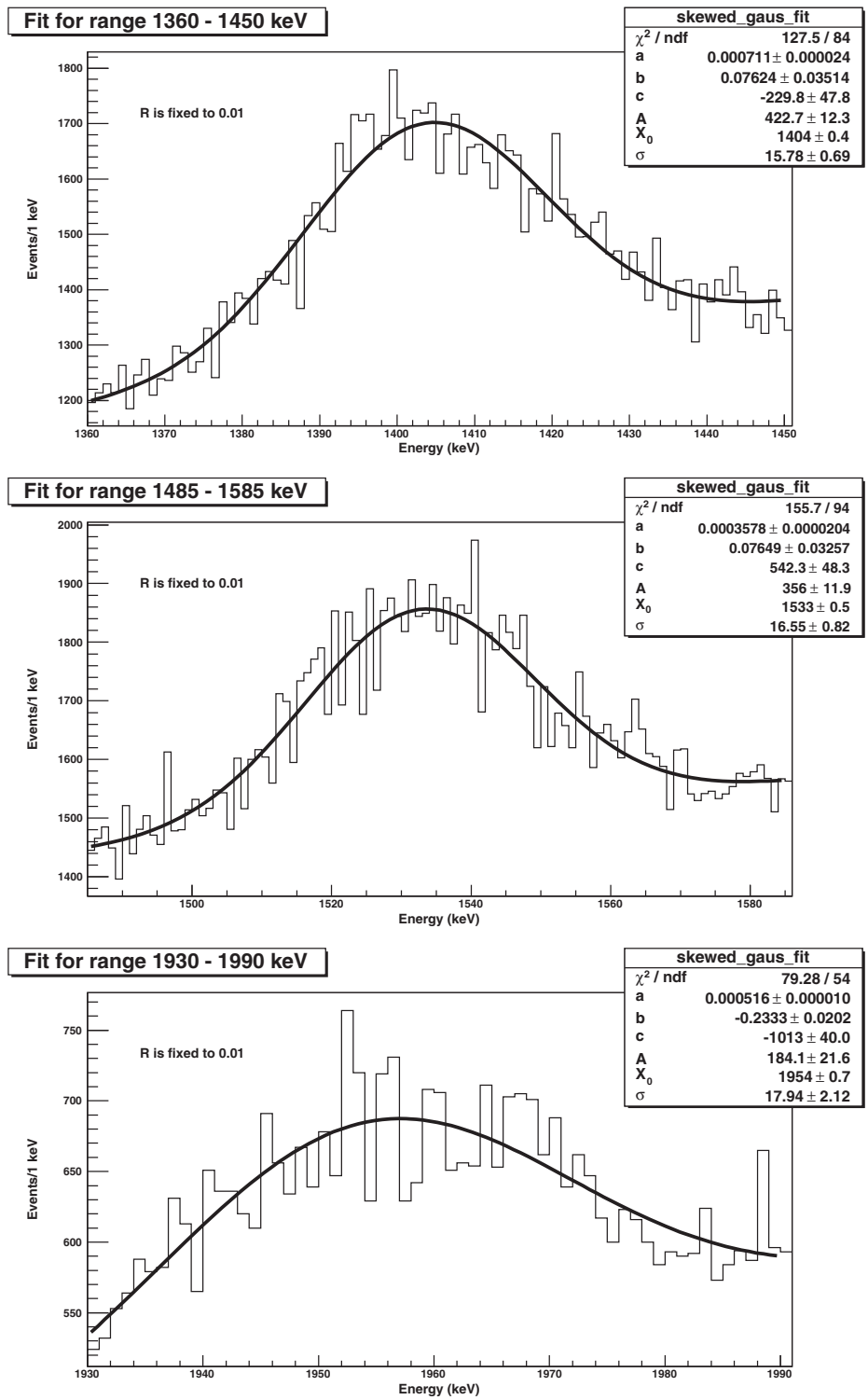


Figure 4.13: The fits for the peaks at 1404 keV, 1533 keV and 1954 keV in the gamma spectrum..

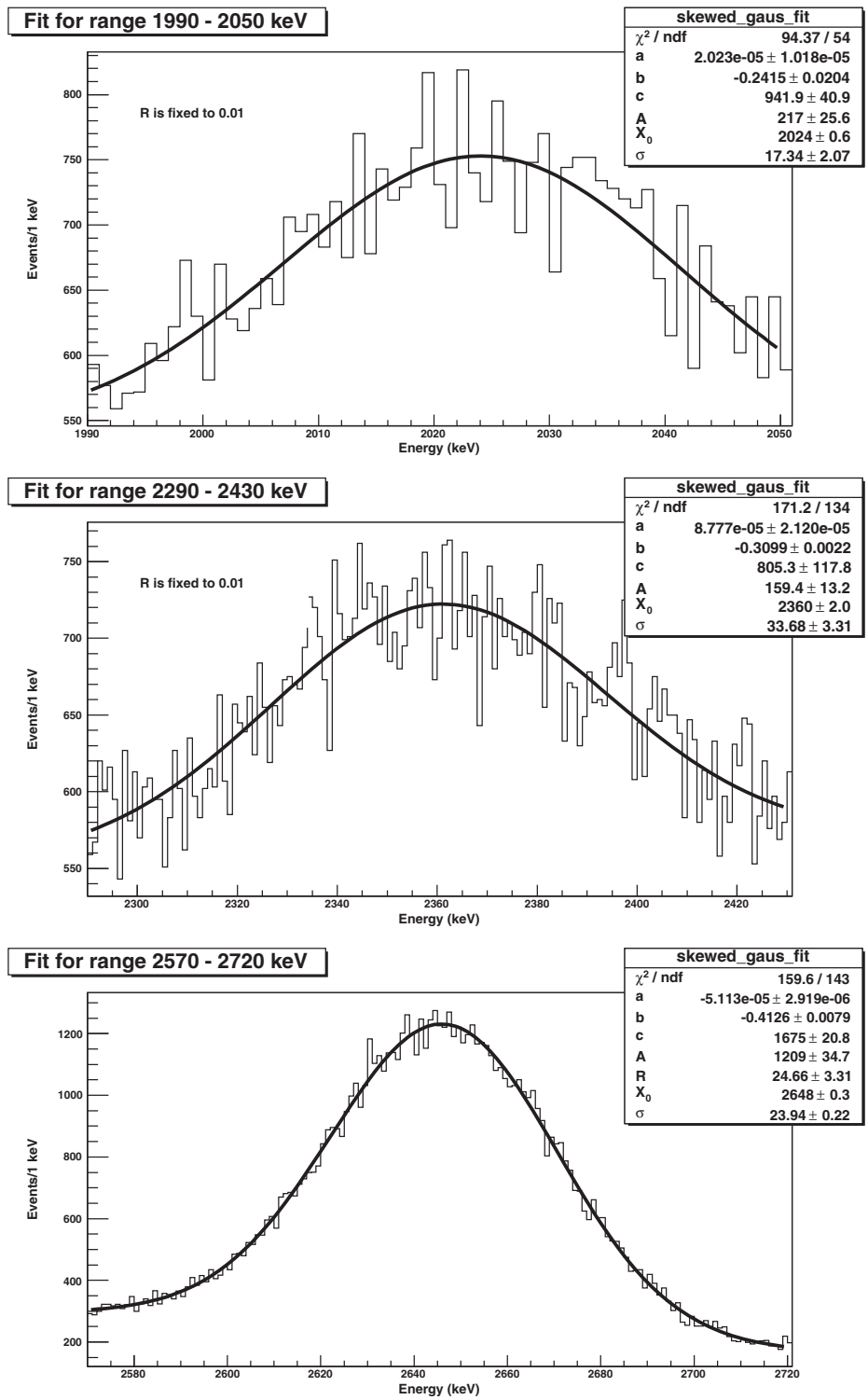


Figure 4.14: The fits for the peaks at 2024 keV, 2360 keV and 2648 keV in the gamma spectrum.

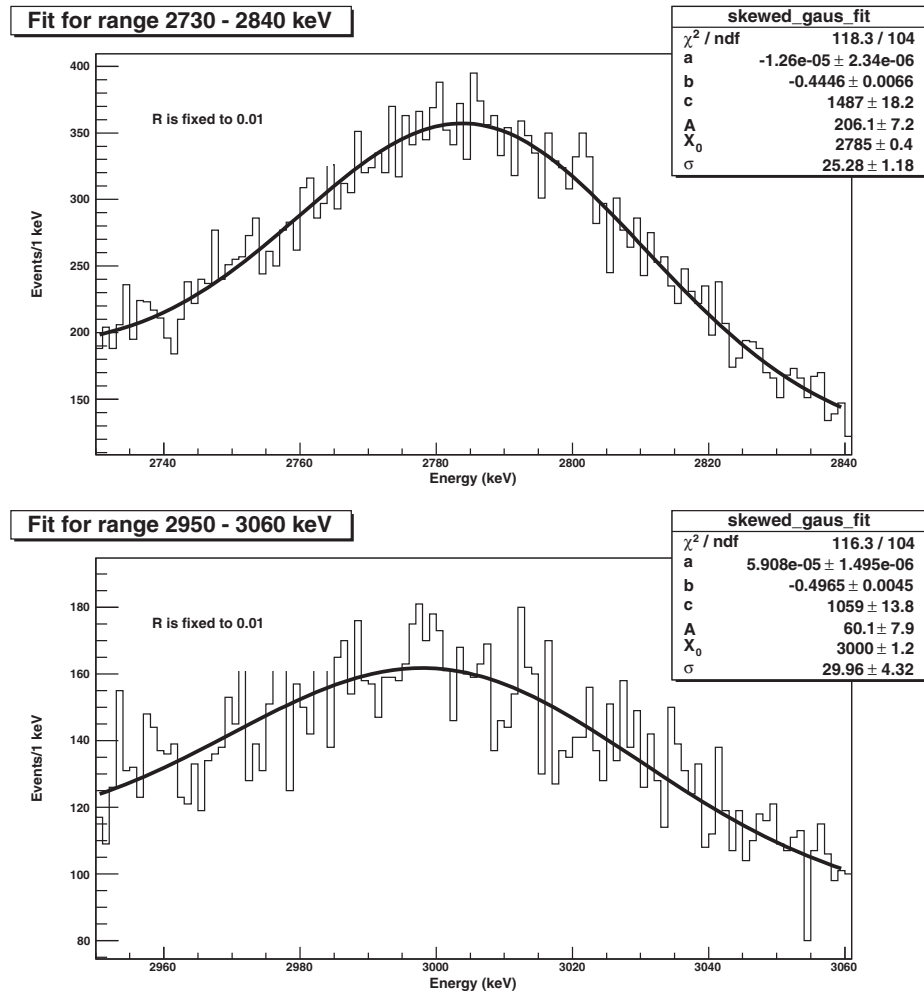


Figure 4.15: The fits for the peaks at 2785 keV and 3000 keV in the gamma spectrum.

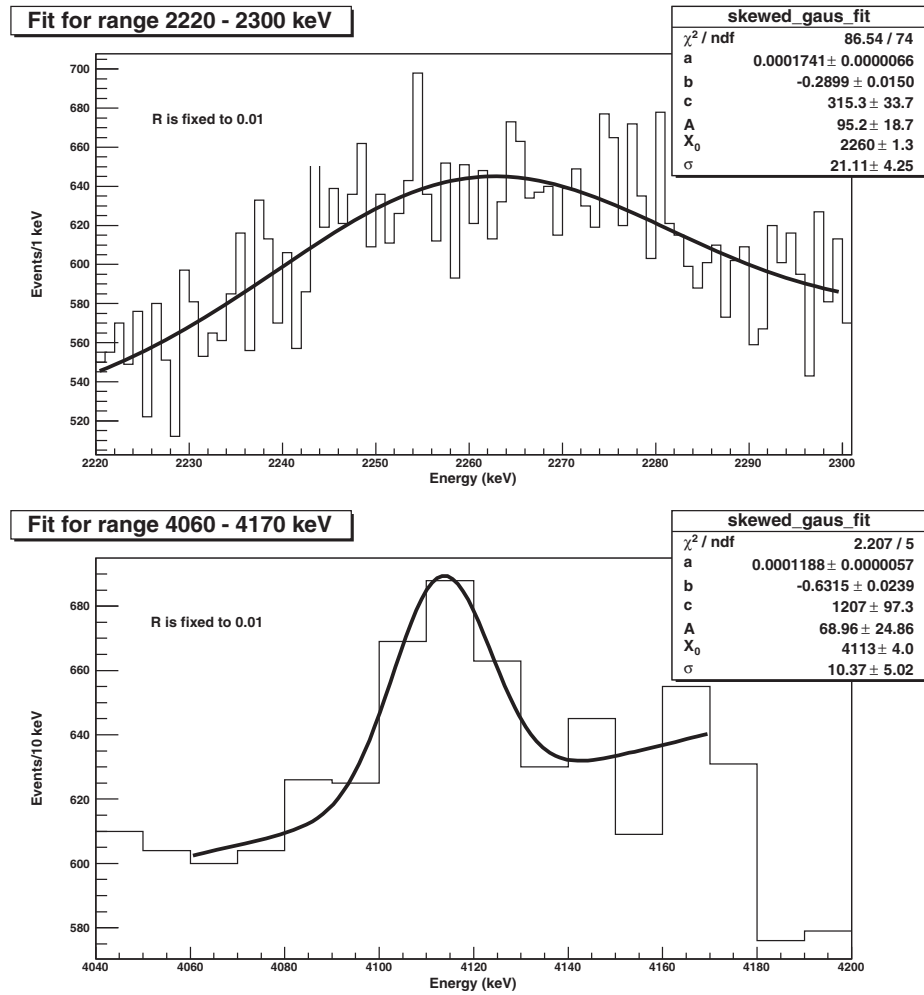


Figure 4.16: The skewed Gaussian fits for the newly found peaks at around 2260 keV and 4100 keV.

Table 4.3: List of the peak parameters of all the peaks extracted from the best fits and the calculated peak areas, along with the uncertainties. The uncertainties in the parentheses for the energies is just the statistical uncertainty taken directly from the fit results for the peak energies.

peak centroid (keV)	$\sigma$ (keV)	peak area (counts)	$\chi^2$
843.6(3)	8.0(5)	6300(682, 7.8%)	1.08
989.4(1)	9.4(3)	41134(1439, 3.5%)	1.70
1326.0(12)	14.4(28)	5448(1357, 25%)	1.50
1404.0(4)	15.8(7)	16725(876, 5.2%)	1.52
1533.0(5)	16.6(8)	14768(881, 6.0%)	1.66
1796.0(1)	16.3(1)	211961(31214, 14.5%)	1.79
1954.0(7)	17.9(22)	8976(1375, 16.6%)	1.47
2024.0(6)	17.3(21)	9435(1583, 16.8%)	1.75
2260.0(13)	21.1(43)	5038(1416, 28%)	1.17
2360.0(20)	33.7(33)	13456(1726, 12.8%)	1.28
2648.0(3)	23.9(3)	63296(8717, 13.8%)	1.12
2785.0(4)	25.3(12)	13061(760, 5.8%)	1.14
3000.0(12)	30.0(43)	4513(882, 19.6%)	1.12
4113(4)	10(5)	<200	0.44

Table 4.4: The final results for all  $\gamma$  peaks: their energies, relative intensities with respect to that of the strongest  $\gamma$  ray, and the corresponding uncertainties in intensity. The results from the present work are compared with previous results [13].

present work		other work	
$E_\gamma$ (keV)	$I_\gamma$	$E_\gamma$ (keV)	$I_\gamma$
843.6(3)	3.0(3)	842.1(3)	3.6(4)
989.4(1)	19.4(7)	988.8(1)	26.4(7)
1326.0(12)	2.6(7)	1329.4(3)	3.9(4)
1404.0(4)	7.9(4)	1400.7(2)	10.1(6)
1533.0(5)	7.0(4)	1531.1(5)	4.8(5)
1796.0(1)	100(15)	1797.2(1)	100.0(5)
1954.0(7)	4.3(7)	1960.4(2)	10.6(6)
2024.0(6)	4.5(8)	2024.2(5)	4.3(5)
2260.0(13)	2.4(7)	—	—
2360.0(20)	6.4(8)	2360.2(8)	3.6(5)
2648.0(3)	30(4)	2648.8(3)	17.3(8)
2785.0(4)	6.2(4)	2785.5(3)	12.9(7)
3000.0(12)	2.2(4)	3001.0(4)	12.4(8)
4113(4)	<0.1	—	—

## 4.5 Coincidence analysis of $\gamma$ -rays

Since a cascade of gamma rays can be emitted simultaneously from an excited state in a single reaction, the  $\gamma$ -ray coincidence analysis technique is usually used to construct the level scheme. This analysis is made by gating on any gamma peak energy of interest to get all gamma rays coincident with the gated one. Various methods have been developed for pre-sorting of the data for this purpose [43, 42]. In this section, three methods for  $\gamma$ - $\gamma$  coincidence analysis which differ according to how the coincidence spectrum is obtained are described here : by  $\gamma$ - $\gamma$  matrix, event-by-event and by  $\gamma$ - $\gamma$ - $\gamma$  cube. The one generally used is the  $\gamma$ - $\gamma$  matrix technique which was also used for this project. More details will be given in this section.

### 4.5.1 The $\gamma$ - $\gamma$ matrix technique

The procedure of this method follows three steps: (1) making a  $\gamma$ - $\gamma$  matrix from the sorted data after decoding the raw experimental data; (2) finding the expected coincidence spectra from the matrix by applying corresponding gates on it; (3) finding the coincidence spectra of the corresponding background and subtracting it from the spectra obtained in step (2). The background subtraction is also a big concern for this analysis and it will be explained in more detail in the following text.

#### 4.5.1.1 Constructing the $\gamma$ - $\gamma$ matrix

We can start with a simple example assuming that during a single reaction event, there are 4  $\gamma$  emissions with energies of 1, 2, 3, and 4 keV, after excluding all contaminant energies by applying proper conditions. Since they are emitted in the same event, they are in coincidence with one another and thus they are in a cascade of emissions from an excited state to lower states. Finding all combinations of  $\gamma$ -rays emitted in all events, we will be able to find out which  $\gamma$  peaks in the final  $\gamma$  spectrum in figure 4.9 are in coincidence, which then provides us with information

for constructing the level scheme. Among the four coincident energies we can immediately find that there are 6 different 2 dimensional combinations: (1, 2), (1, 3), (1, 4), (2, 3), (2, 4), (3, 4), each of which represents a detection coincidence of two  $\gamma$  rays with the indicated energies and a position in the 2 dimensional histogram with the  $X$  axis and  $Y$  axis in  $\gamma$  energy. We can fill the histogram with all the combinations. For simplicity and convenience, we use the bigger energy value as the  $X$  energy and the smaller one as  $Y$  energy for each combination when we fill the histogram, since the order of the two energies in the combination does not matter. Then we can see that we always fill one half of the matrix below the diagonal, as demonstrated in figure 4.17. By filling the matrix with coincidence combinations from all events, all  $\gamma$ - $\gamma$  coincidence information including that of background is then stored in the matrix. All of the following coincidence analysis will be made directly on the  $\gamma$ - $\gamma$  matrix.

#### 4.5.1.2 Finding the coincidence spectra from the $\gamma$ - $\gamma$ matrix

Figure 4.18 shows a 2D histogram of the  $\gamma$ - $\gamma$  matrix constructed from the experimental data. By placing a peak gate on the  $X$  axis and projecting the gated region onto the  $Y$  axis, we select all the coincidence events with the larger one of the two  $\gamma$  energies within the applied energy gate. Similarly, by placing the same gate on the  $Y$  axis and projecting the gated region onto  $X$  axis, we select all the coincidence events with the smaller one of the two  $\gamma$  energies within the applied energy gate. Adding the two projections together gives the spectrum of all  $\gamma$  rays in coincidence with the  $\gamma$  energies in the applied energy gate, i.e., the coincidence spectrum of the  $\gamma$  peak in the gate.

The bigger the size of the energy gate we choose, the more coincidence events we can select and also the more contaminant coincidence  $\gamma$  rays and background there will be. But if the gate size is too small, the statistics in the coincidence spectrum will be very low and give less coincidence information. Therefore, we have to compromise between the statistics and accuracy and try carefully to find

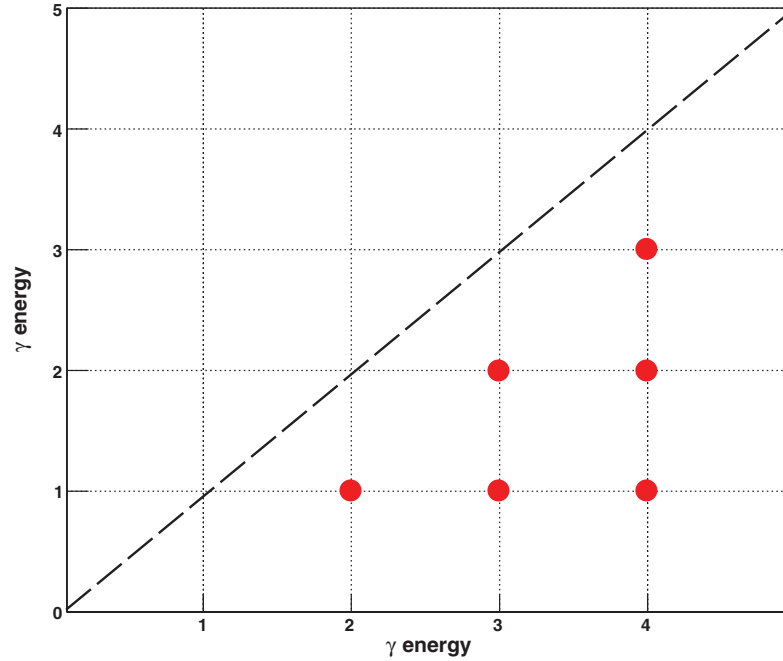


Figure 4.17: An example of filling the  $\gamma$ - $\gamma$  matrix—the 2-dimensional coincidence histogram. The demonstration is for a single beam event only and each point represents a coincidence.

the optimal coincidence gate. Figure 4.19 to figure 4.21 show the gating process and the resulting coincidence spectra for the peak at 1796 keV.

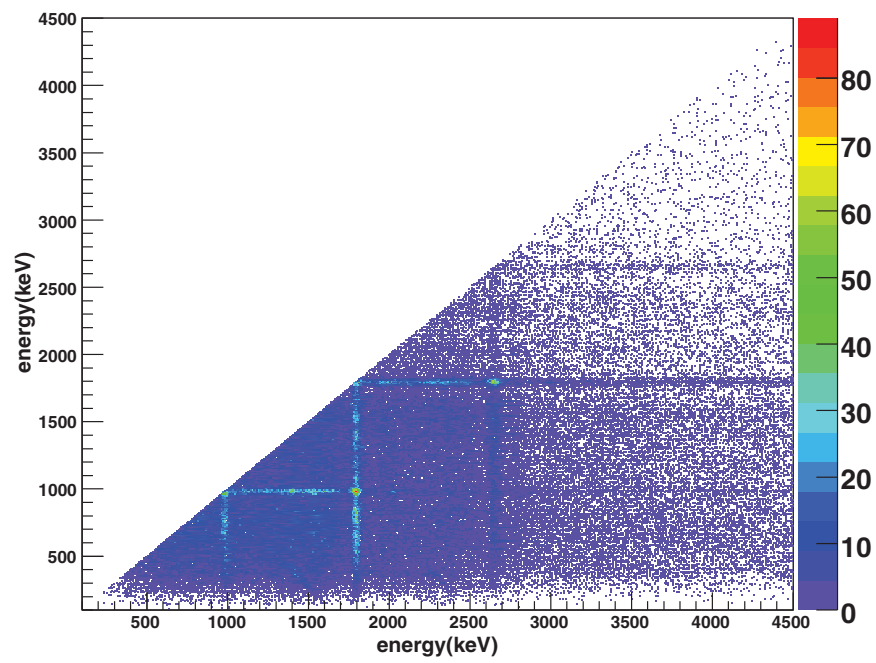


Figure 4.18: A 2D histogram of the  $\gamma$ - $\gamma$  matrix constructed from the experimental data using the technique described in the previous subsection.

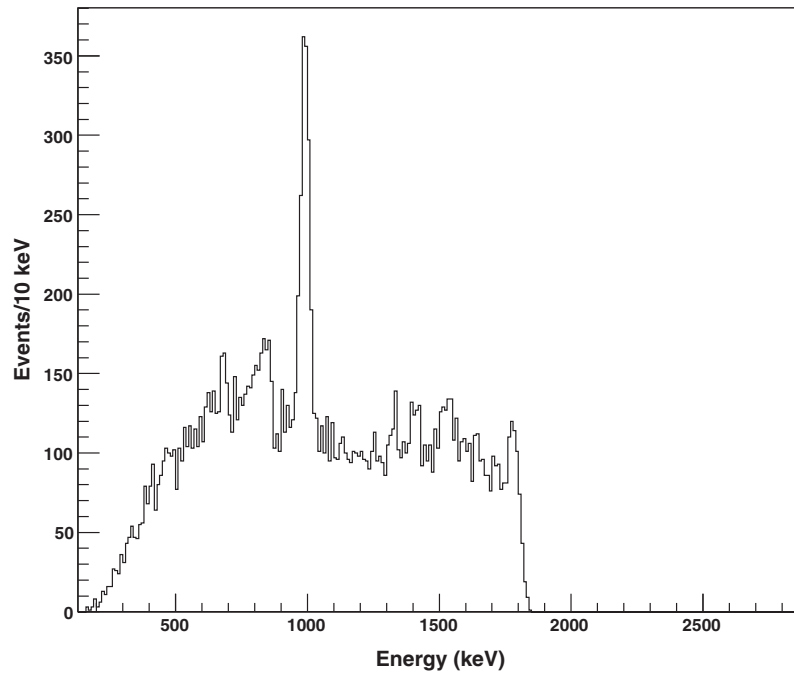
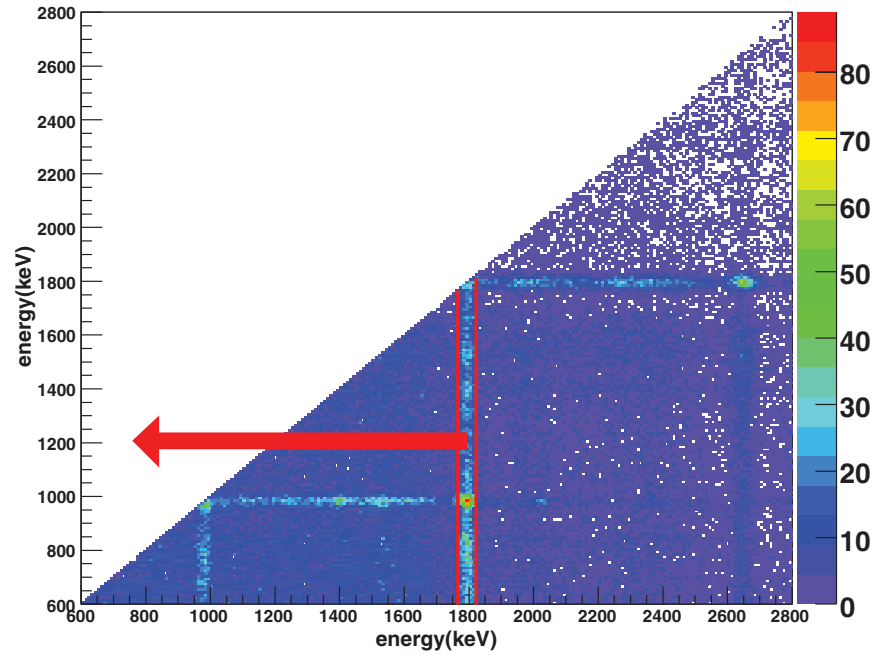


Figure 4.19: Top: gating on the  $X$  axis for 1796 keV and projecting the gated region onto the  $Y$  axis to find all the coincidence events with the 1796 keV  $\gamma$ -ray as the larger of the two energies in coincidence. Bottom: the coincidence spectrum obtained from the projection.

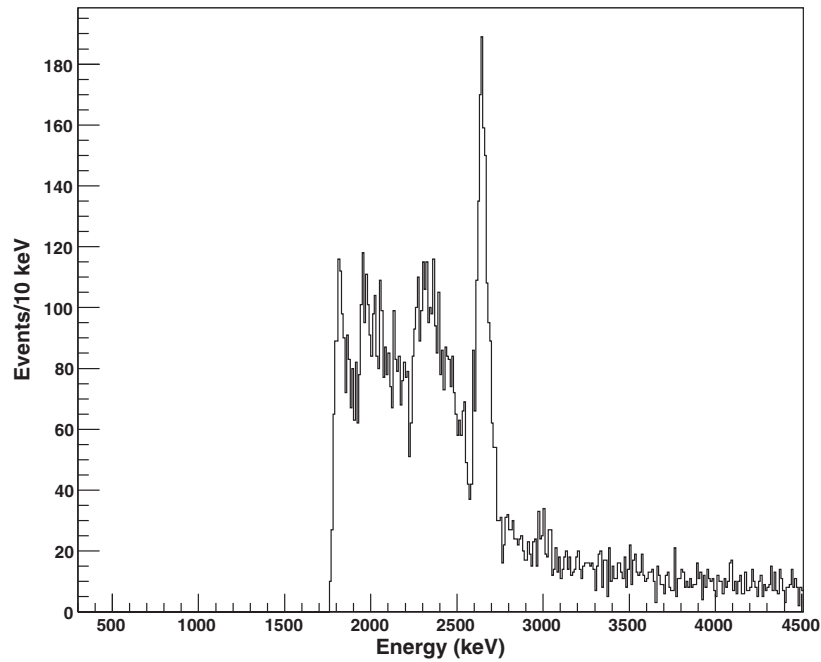
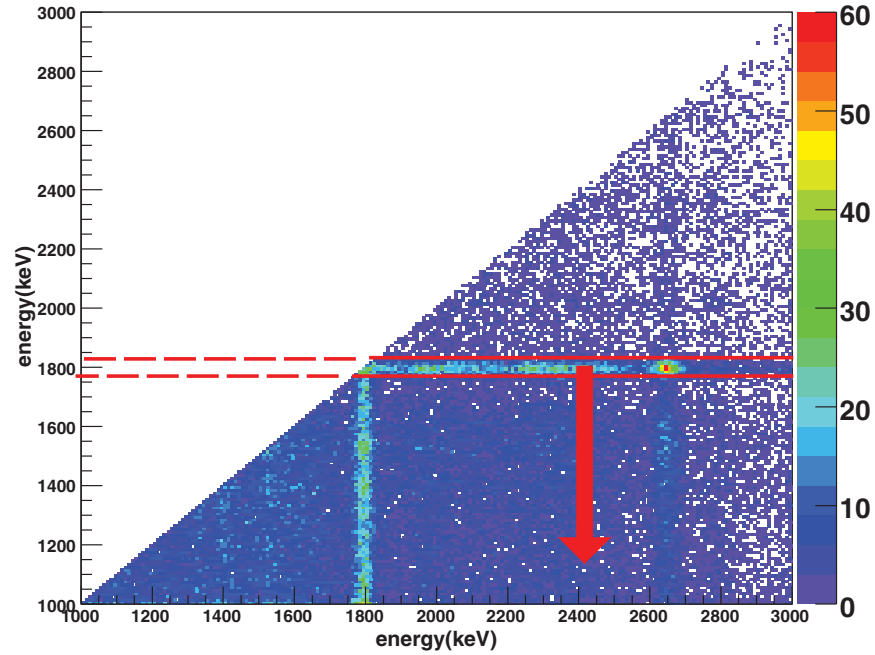


Figure 4.20: Top: gating on the  $Y$  axis for 1796 keV and projecting the gated region onto  $X$  axis to find all the coincidence events with the 1796 keV  $\gamma$ -ray as the smaller of the two energies in coincidence. Bottom: the coincidence spectrum obtained from the projection.

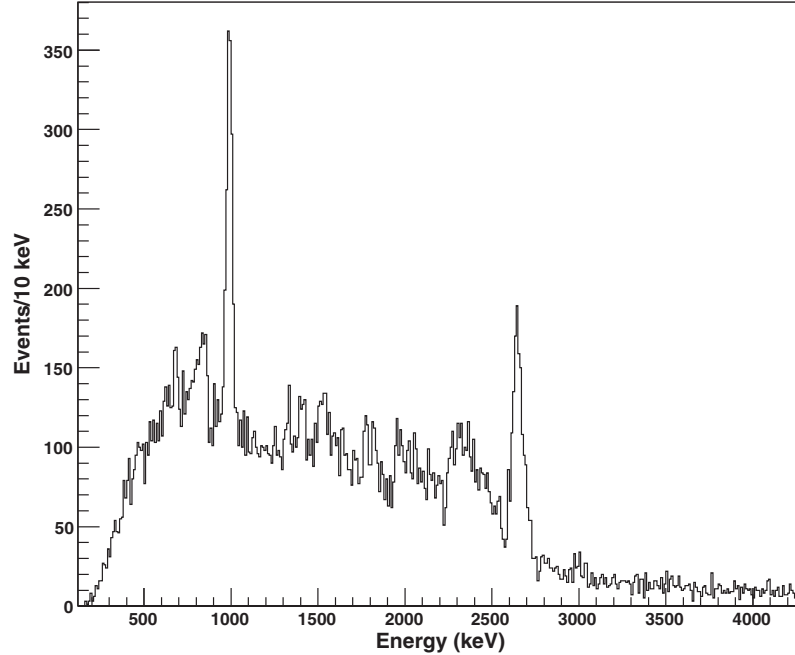


Figure 4.21: The coincidence spectrum obtained by combining the projections on the  $X$  axis and the  $Y$  axis shown in figure 4.19 and 4.20.

#### 4.5.1.3 Subtracting background coincidence events from the coincidence $\gamma$ spectrum

When we gate on an energy range to get the coincidence spectrum for a peak in this range, what we actually obtain is a mixture of the coincidence spectrum of the peak  $\gamma$  rays and that of the background  $\gamma$ -rays in the same peak range. This brings considerable contaminant  $\gamma$  rays disguised as real coincident  $\gamma$ -rays into the coincidence spectrum making it impossible to decide whether a peak in the coincidence spectrum is a real coincident peak or only a contaminant one from the background coincidence. Therefore it is necessary to find the background coincidence spectrum and subtract it from the peak coincidence spectrum.

There are different methods commonly used now for background subtraction

of the  $\gamma$  coincidence spectrum [44, 45, 46, 47, 48, 49], but the basic ideas are the same: to simulate or estimate the background in the coincidence spectrum and then subtract it from the spectrum. What I want to clarify here is that the background to be subtracted is from estimation or simulation rather than the real background, since it is impossible to separate the background  $\gamma$ -rays from the actual transition  $\gamma$ -rays in the energy range of the gated peak. Because of this, there is not a very precise way to do the background subtraction. The method used in this analysis, which is the usual way for background subtraction in  $\gamma$ - $\gamma$  analysis, is to place two energy gates on the tails on the both sides of the gated peak, with the sum of the two gate width equal to the gate width on the peak, to estimate the coincidence  $\gamma$ -ray background inside the gate on the peak. For peaks with other peaks sitting closely on their tails, gating on tails will bring plenty of contaminant coincident  $\gamma$ -rays of the neighbour peaks. For these cases, gates are be chosen on the nearby smooth regions as close to the gated peak region as possible, and the widths of the background gates are not necessarily made equal. Figure 4.22 demonstrates how the gates are chosen for the two situations.

Figure 4.23 (black histogram) shows an example of a coincidence spectrum of the  $\gamma$  peak at 1404 keV from the transition between the excited state of  $^{26}\text{Si}$  at 4184 keV to the excited state at 2783 keV [50]. The energy of the 4184 keV state can then be confirmed within the uncertainty range by the existence of a cascade of  $\gamma$ -rays of 1404 keV, 989 keV and 1796 keV. Also shown in red is its corresponding background spectrum, which is estimated by placing gates on the tails around the gated peak, since it is not practical to separate the background  $\gamma$  rays from the actual transition  $\gamma$  rays inside the gated peak energy range.

Figure 4.24 to figure 4.29 show the coincidence spectra for other peaks.

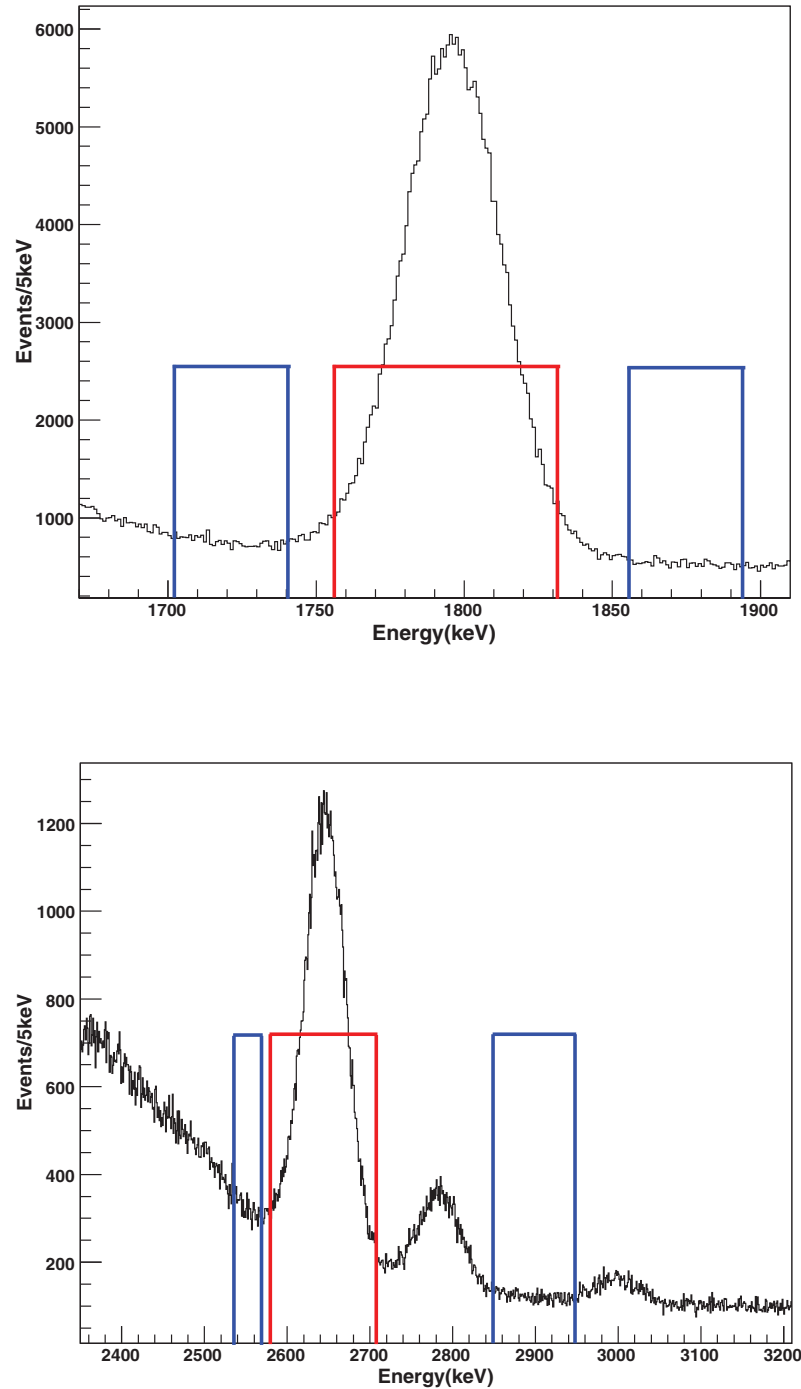


Figure 4.22: Top: choosing the background gates on the tails of the gated peak if they are flat enough, gates for 1796 keV peak with the red one indicating the peak gate and blue ones the background gates. Bottom: choosing the background gates on the smooth regions close to the gated peak if other peaks sit on its tails, with the main gate on the 2647 keV peak.

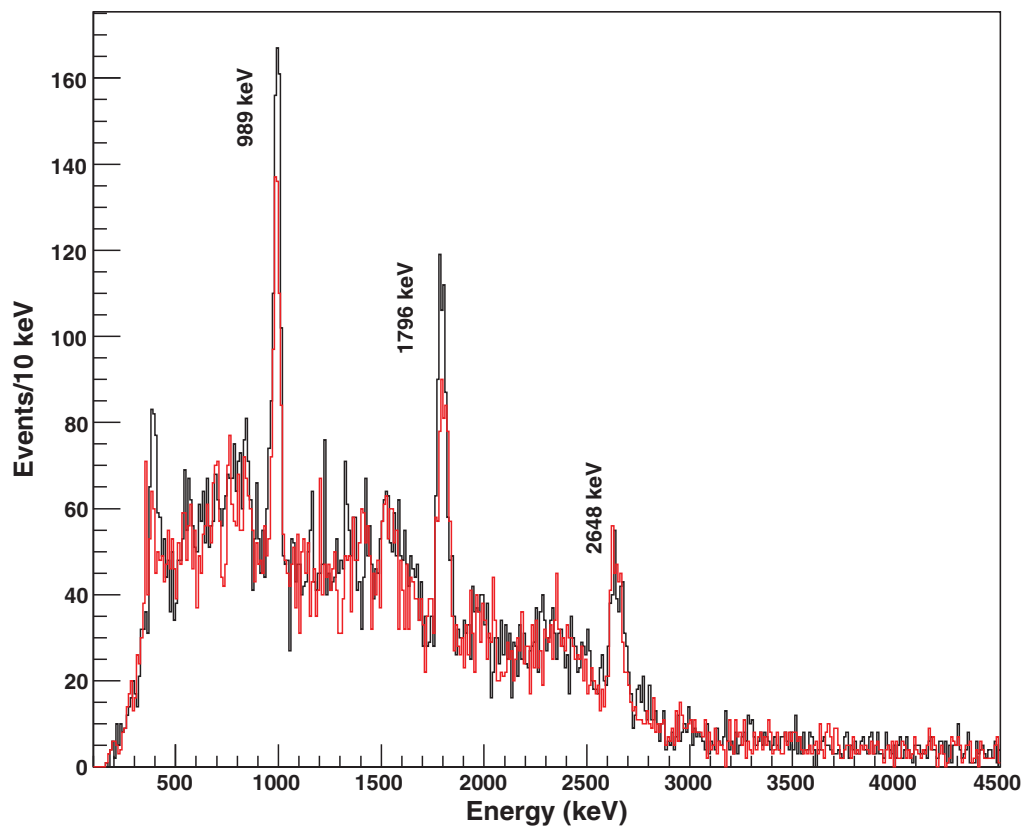


Figure 4.23: An example of a coincidence  $\gamma$ -ray spectrum for the 1404 keV  $\gamma$ -ray in black with its background shown in red.

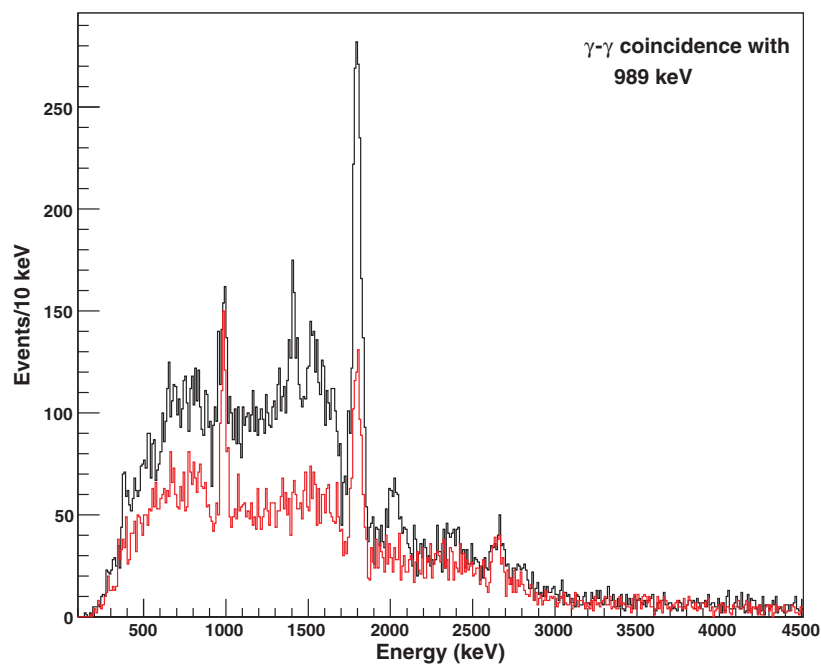
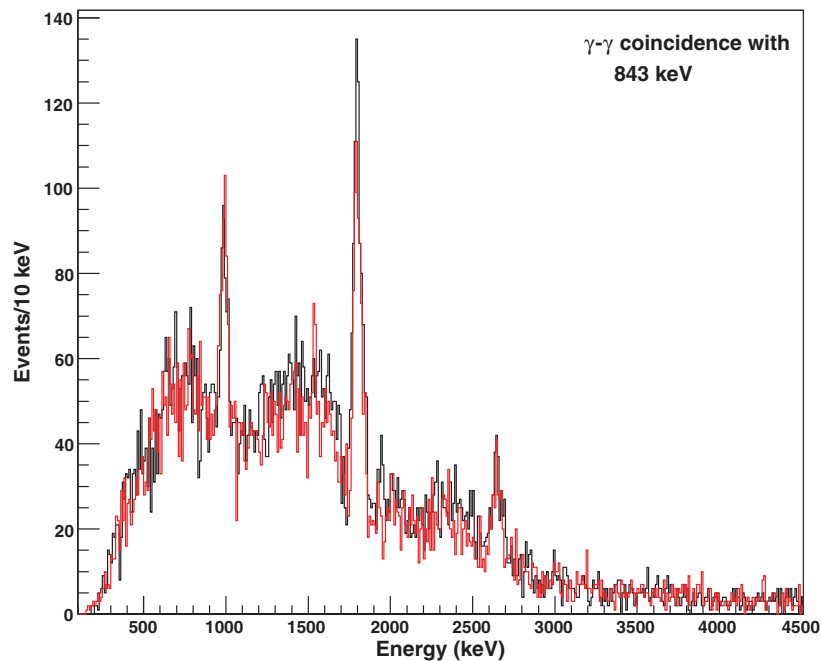


Figure 4.24: Coincidence  $\gamma$ -ray spectra for 843 keV and 989 keV  $\gamma$ -rays in black with the background shown in red.

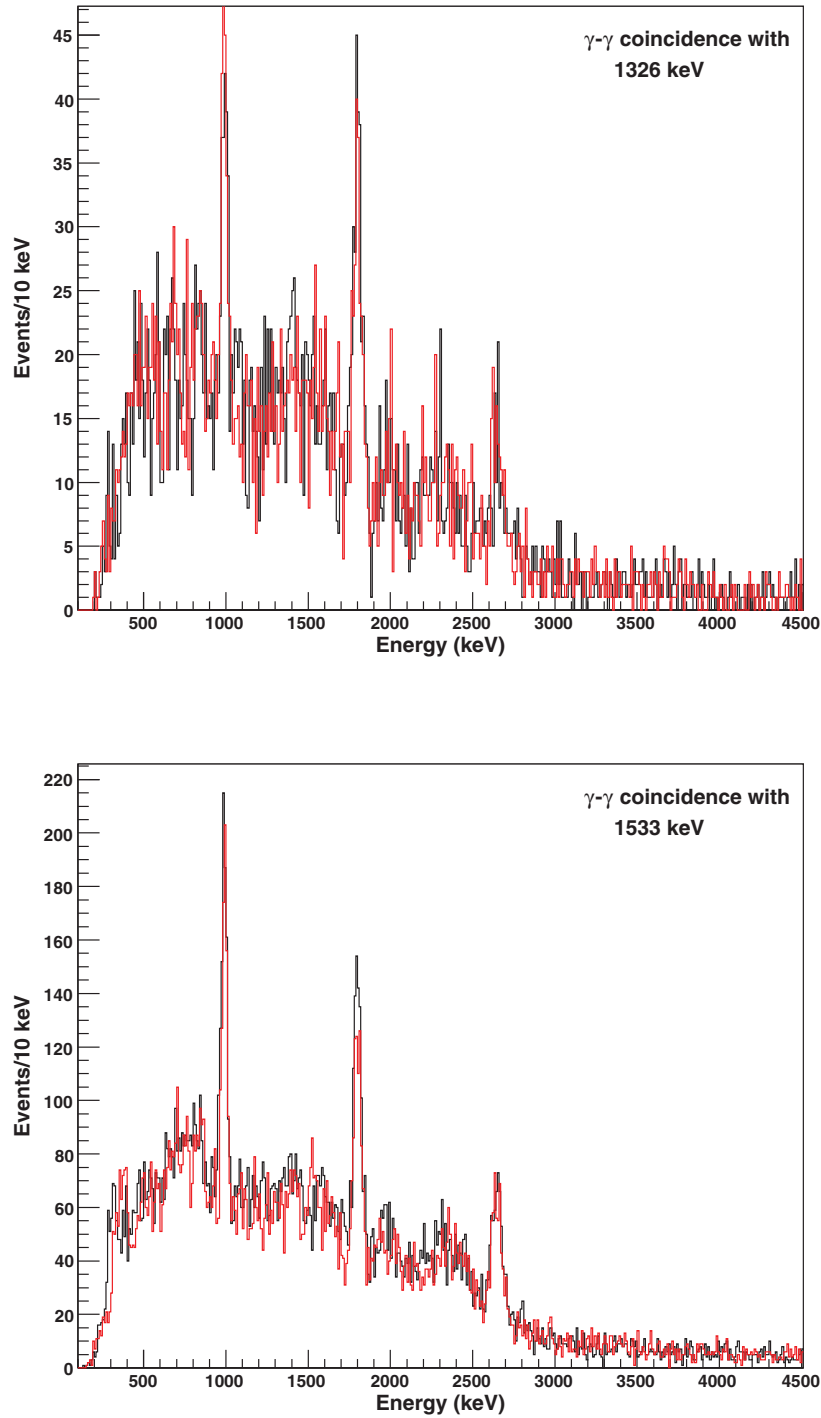


Figure 4.25: Coincidence  $\gamma$ -ray spectra for 1326 keV and 1533 keV  $\gamma$ -rays in black with the background shown in red.

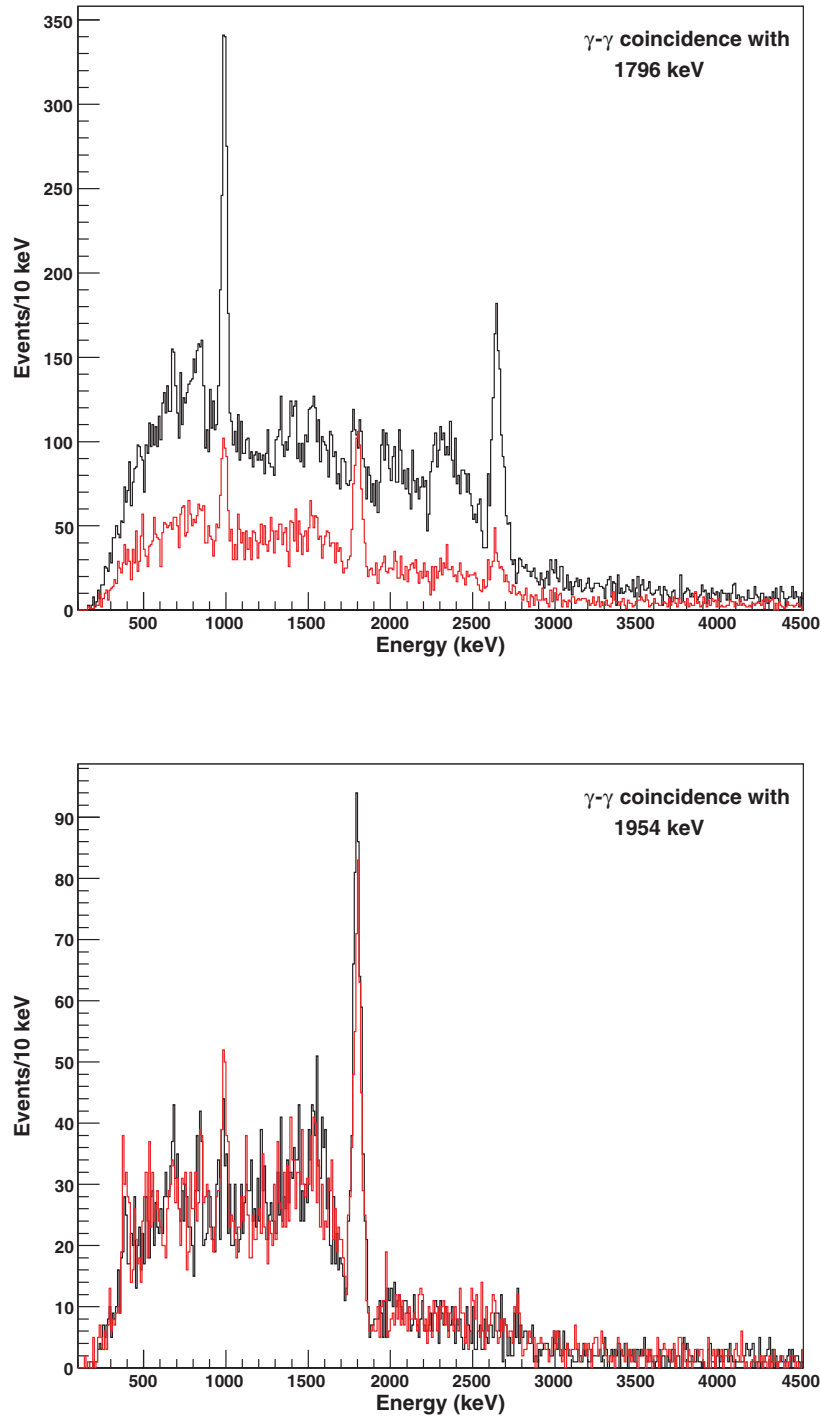


Figure 4.26: Coincidence  $\gamma$ -ray spectra for 1796 keV and 1954 keV  $\gamma$ -rays in black with the background shown in red.

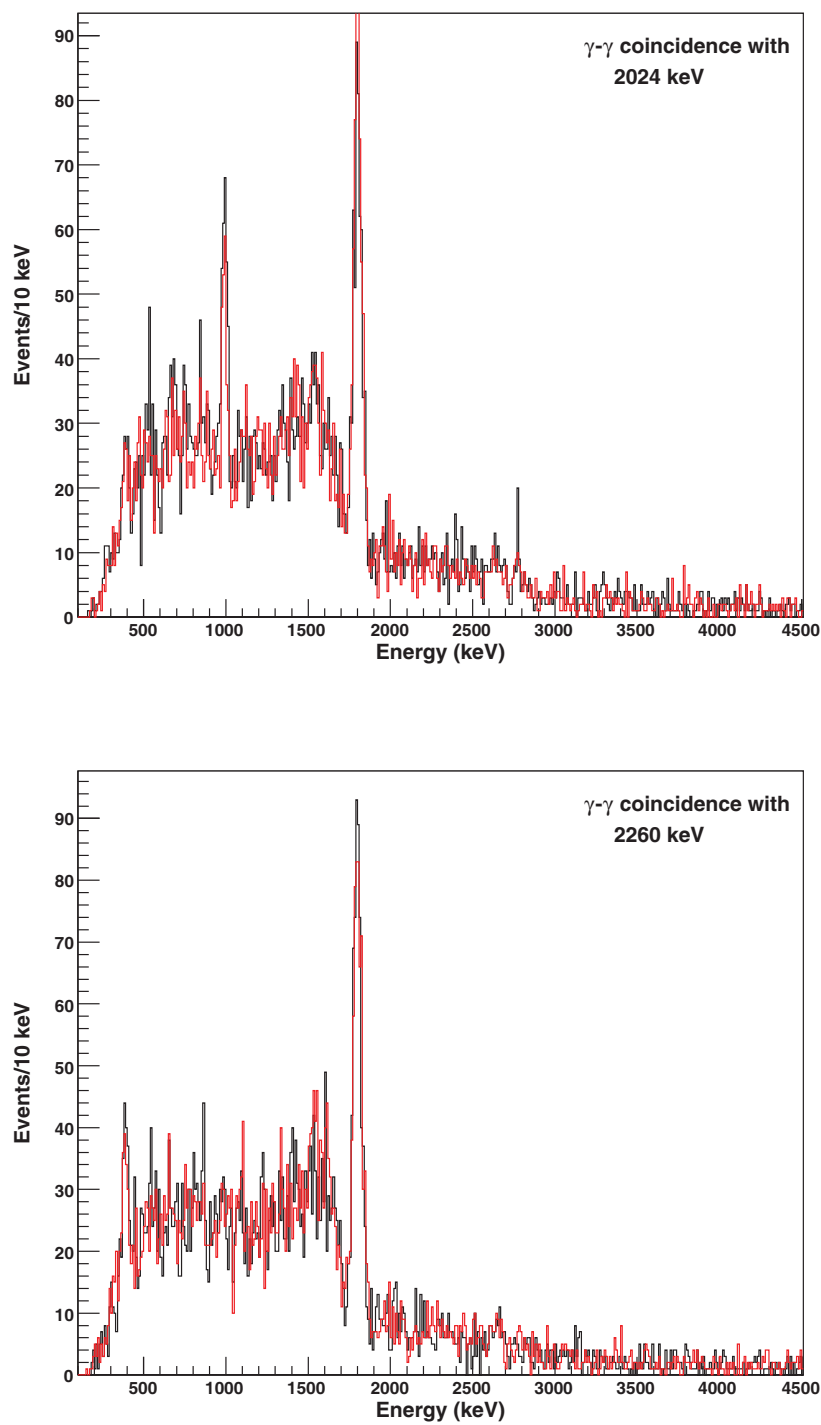


Figure 4.27: Coincidence  $\gamma$ -ray spectra for 2024 keV and 2260 keV  $\gamma$ -rays in black with the background shown in red.

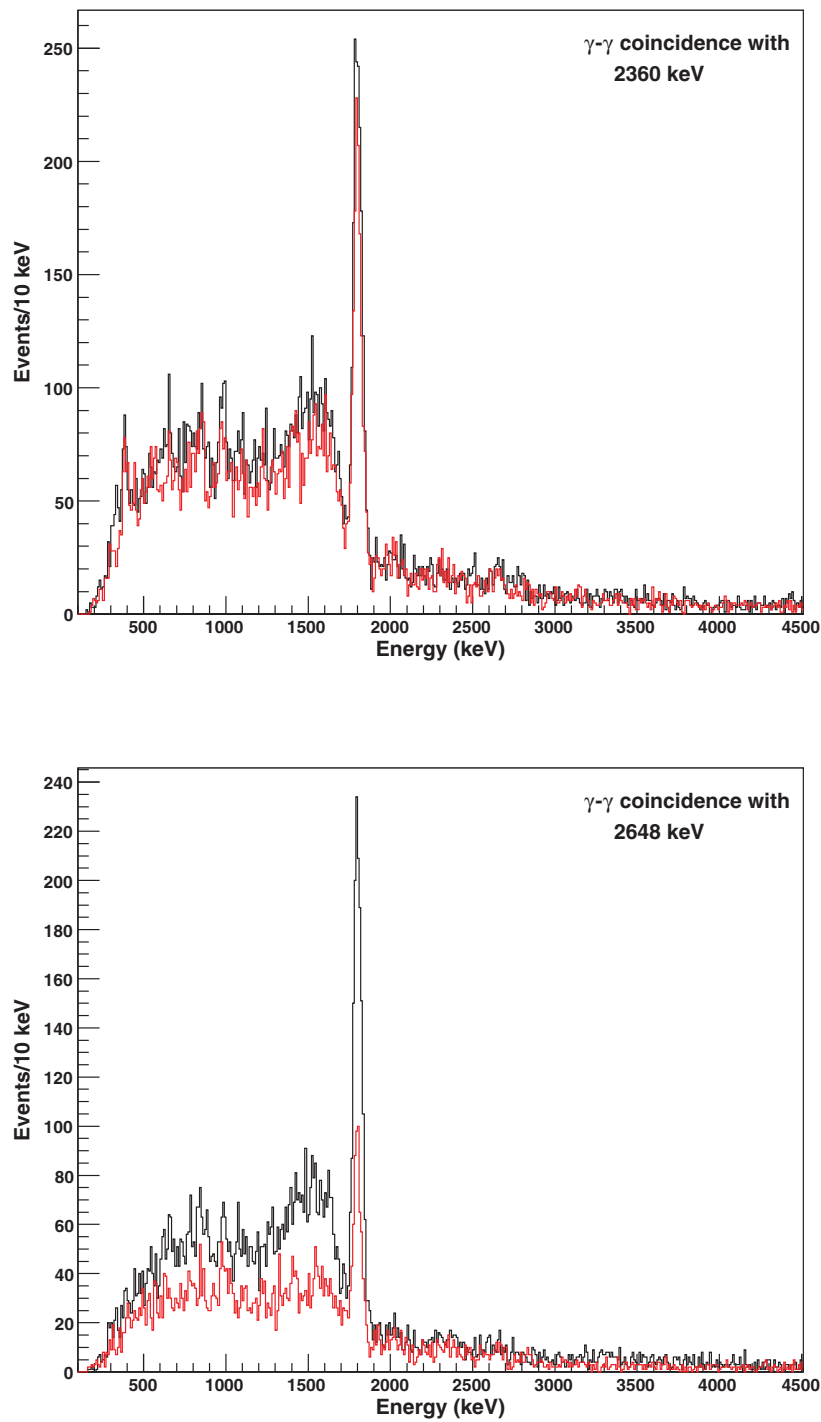


Figure 4.28: Coincidence  $\gamma$ -ray spectra for 2360 keV and 2648 keV  $\gamma$ -rays in black with the background shown in red.

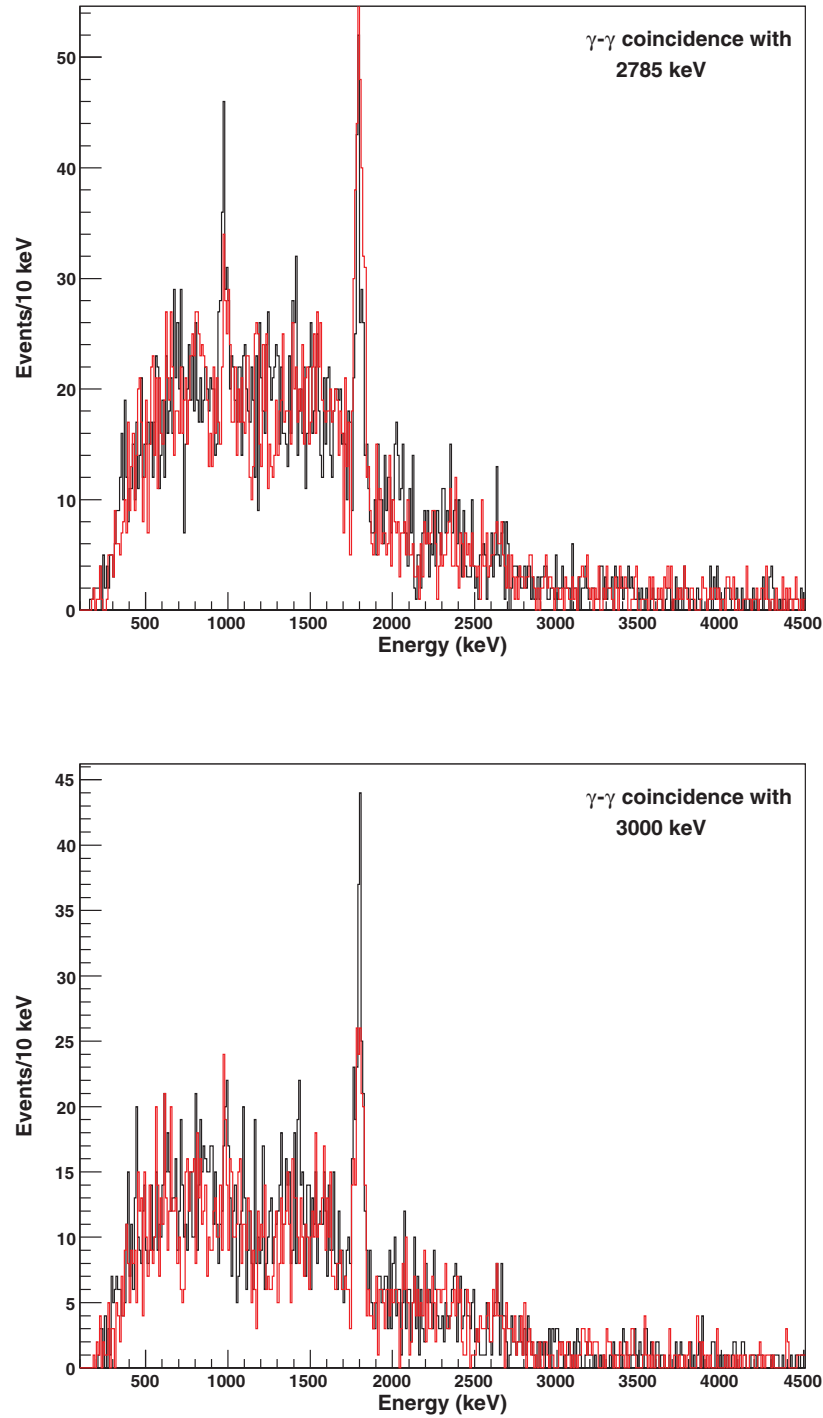


Figure 4.29: Coincidence  $\gamma$ -ray spectra for 2785 keV and 3000 keV  $\gamma$ -rays in black with the background shown in red.

Table 4.5: The energy levels and associated  $\gamma$  transitions extracted from the analysis.

$J^\pi$	$E_x$ (keV)	$\gamma$ cascade (keV)
$2_1^+$	1796.0(1)	1796.0
$2_2^+$	2785.0(4)	989.4 <sup>a</sup> +1796.0 2785.0
$0_2^+$	3329.0(6)	1533.0 <sup>b</sup> +1796.0
$3_1^+$	3750.0(7)	1954.0+1796.0
$3_2^+$	4189.4(5)	1404.0+989.4+1796.0
$2_3^+/4_1^+$	4444.0(4)	2648.0+1796.0
$4_2^+$	4796.0(12)	3000.0+1796.0
$(0_3^+)$	4809.4(6)	2024.0 <sup>c</sup> +989.4+1796.0 2024.0+2785.0
$2_4^+$	5145.4(21)	2360.0+989.4+1796.0
$4_3^+$	5287.6(5)	843.6+2648.0+1796.0
$2_4^+$	5515.4(14)	1326.0+1404.0+989.4+1796.0
$(4_4^+)$	6449.4(14) <sup>d</sup>	2260.0 <sup>e</sup> +1404.0+989.4+1796.0
$(2_5^+/3_3^+)$	5909(4) <sup>f</sup>	4113+1796.0

<sup>a</sup>potential doublet, with the transition from  $E_x=3750$  keV to  $E_x=2785$  keV.

<sup>b</sup>potential doublet, with the transition from  $E_x=5291$  keV to  $E_x=3756$  keV.

<sup>c</sup>potential doublet, with the transition from  $E_x=4831$  keV to  $E_x=2785$  keV.

<sup>d</sup>no match from database [79].

<sup>e</sup>no match from database [79].

<sup>f</sup>could be the known 5912 keV state in the literature or the new state 5886 keV found in the  $^{24}\text{Mg}(^3\text{He}, n\gamma)^{26}\text{Si}$  experiment at the University of Tsukuba [39].

After all cascades are extracted from the  $\gamma$ - $\gamma$  coincidence, they are compared to the equivalent ones from the well known states in  $^{26}\text{Mg}$  [80], the mirror nucleus of  $^{26}\text{Al}$ , to determine their spin-parity assignments. Table 4.5 lists all levels associated with possible transitions extracted from the analysis, based on which the level scheme of  $^{26}\text{Si}$  is constructed, as shown in figure 4.30.

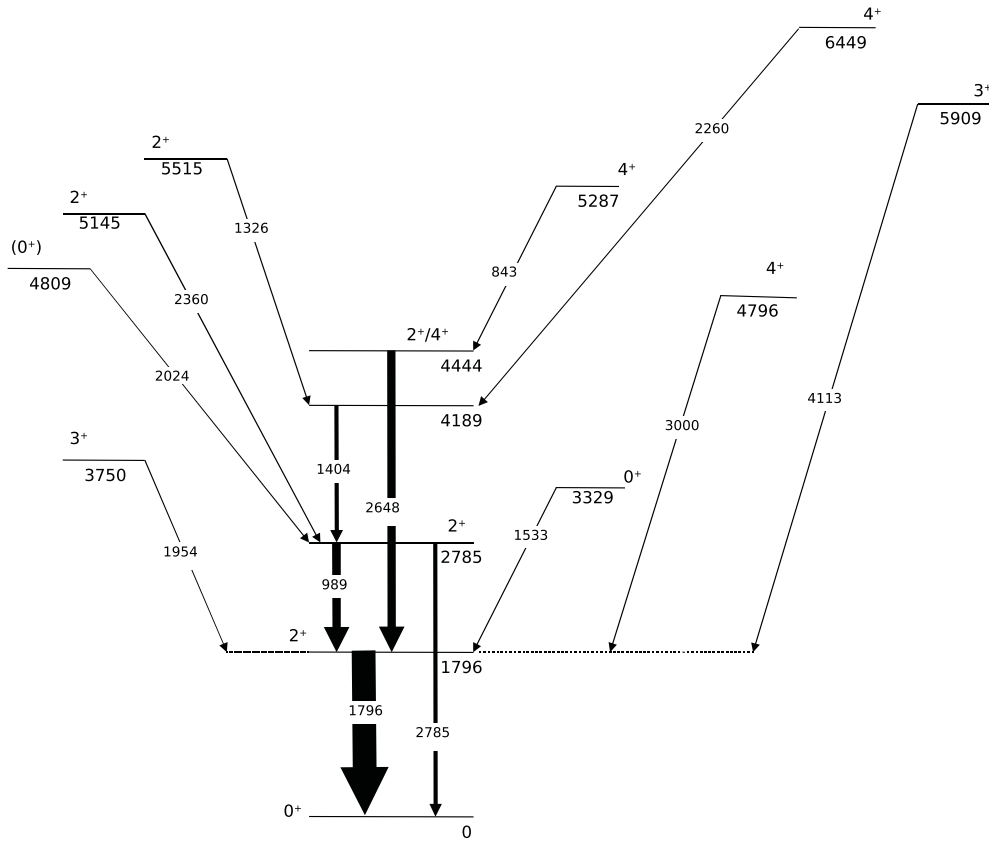


Figure 4.30: Level scheme of  $^{26}\text{Si}$  based on the results from this analysis.

## 4.5.2 The event-by-event technique

The event-by-event analysis is the most straightforward way to make the  $\gamma$ - $\gamma$  coincidence spectrum in that we just need to put constraints on energies to select only the events with  $\gamma$ -ray energies in the constrained peak ranges. This allows us to get more precise coincidence spectra without worrying about the overlap in the

gate area in the total coincidence spectrum caused by the adding-up of the two projected coincidence spectra from the  $\gamma$ - $\gamma$  matrix, as described in the previous section. But the big disadvantage of this method is that it is very slow, hardly interactive and very inconvenient. It is because of that we need to read through all the data every time we make the coincidence spectra and that we need to specify the peak gates and background gates beforehand which we will use to make the coincidence spectra for. As a result, this method was not used in our data analysis.

### 4.5.3 The $\gamma$ - $\gamma$ - $\gamma$ cube technique

By using the  $\gamma$ - $\gamma$  matrix, we can find any two  $\gamma$ -rays that are in coincidence with each other. But in a  $\gamma$  transition cascade, there are usually more than two  $\gamma$ -rays if the transition cascade starts from a high energy level. The ideal situation is that we can find all the  $\gamma$ -rays that are in coincidence in one event, so that the construction of the cascade becomes much easy and straightforward. But this is neither practical nor necessary, as will be explained in the following context. For example, if using the event-by-event method for this purpose, we need to put even more constraints on the  $\gamma$  energies in order to find all coincident  $\gamma$ -rays in a single event at one time, which means more running time and more complexity. Besides, we cannot decide which  $\gamma$ -rays should be in coincidence before the analysis in order to determine the constraints, which is exactly what we want to find out from and after the analysis. We can also consider using a higher dimensional matrix for the purpose of finding all coincident  $\gamma$ -rays at one time, but the problem is that we cannot know how many  $\gamma$ -rays are in one cascade in order to determine the dimension of the matrix, and that the number is not the same for all events. Having said that, although we might not be able to find all the coincident  $\gamma$ -rays from one event, the higher the dimension of the coincidence matrix, the more  $\gamma$ -rays we can find in coincidence. However, another challenge immediately arises in that constructing the matrix is seriously limited by computational power, because additional dimension requires, depending on the size of the data, thousands of times the storage space of what

the lower dimensional matrix has already occupied, and an even faster computer speed. In this sense, a much higher dimensional matrix is not practical. However, the 3-dimensional  $\gamma$ - $\gamma$ - $\gamma$  cube is still practical and could be the upper limit. But the new difficulty now is the challenge of the background subtraction in the projection from the triple  $\gamma$  cube to  $\gamma$ - $\gamma$  matrix when we gate on a  $\gamma$  energy on one dimension of the cube to find the corresponding  $\gamma$ - $\gamma$  coincidence matrix for this energy. This makes the analysis very complicated and a method using this triple  $\gamma$  cube can be found in Ref. [60].

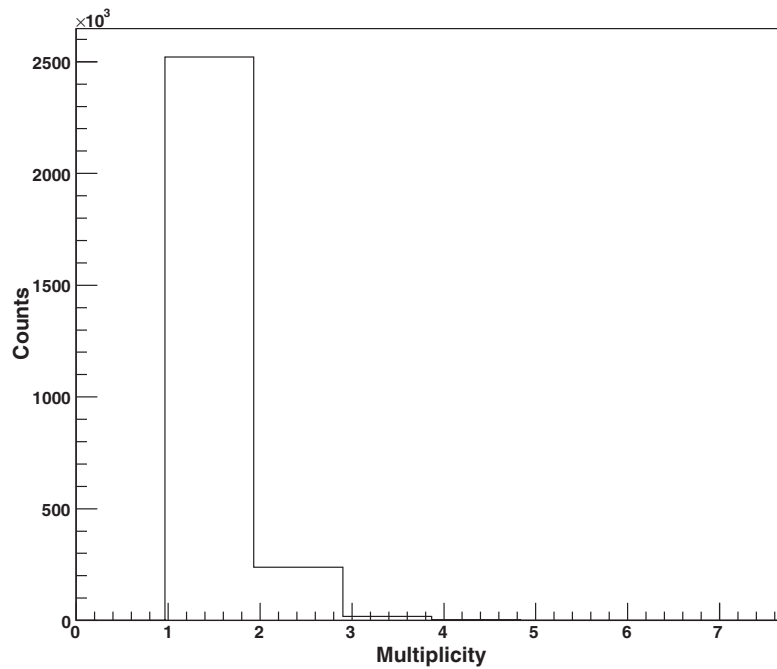


Figure 4.31: Distribution of multiplicities of all the data showing that most of the events have only one or two  $\gamma$ -rays in coincidence. This indicates that the  $\gamma$ - $\gamma$  matrix technique is adequate enough for the data analysis.

Actually, we can check the distribution of multiplicities of all the data to determine whether to use a higher dimensional matrix. Figure 4.31 shows the multiplicities of all our data and we can see that most events have only one or two  $\gamma$ -rays in coincidence probably because other  $\gamma$ -rays in the same events are either

too weak to be detected or miss hitting onto the detectors. Some other reasons such as electronics may also exist. It therefore turns out that for our data, the  $\gamma$ - $\gamma$  coincidence analysis is efficient enough and it is not necessary to use the  $\gamma$ - $\gamma$ - $\gamma$  cube.

## 4.6 Results and discussions

The results extracted from the data analysis of this experiment are listed in table 4.5. The spin-parities are quoted from the literature or assigned by comparison with the possible corresponding levels in the mirror nucleus. Since the experiment aimed to confirm the known levels or to find new levels in  $^{26}\text{Si}$  by measuring only the  $\gamma$ -decays from the excited  $^{26}\text{Si}$  nucleus, no information is obtained at the S800 focal plane for the other reaction product — the deuteron. If such information could be obtained, the reaction kinematics geometry, such as the exit angle, and reaction position on the target could be reconstructed using a transfer matrix calculated in a program called COSY INFINITY [31], developed by researchers at NSCL. Thus, the DWBA (Distorted Wave Born Approximation) [32, 33] analysis of the differential cross-section could be used for making the spin-parity assignments with the analysis code DWUCK [34]. The spin-parity assignments can also be made by the angular correlation measurements (or DCO — directional angular correlation of coincident  $\gamma$ -rays from oriented states of nuclei) of the  $\gamma$  emissions [35, 36, 37, 38], which were not determined in this experiment. The idea is that, by measuring the ratio of the intensity of the  $\gamma$ -ray from the state of unknown spin-parity <sup>1</sup> to the intensity of a coincident  $\gamma$ -ray in the same cascade with known multipolarity, and by comparing the ratio with the theoretical value, we can then find the multipolarity of the former  $\gamma$ -ray and therefore deduce the spin-parity of the state from where this  $\gamma$ -ray comes.

The newly found  $\gamma$ -ray with energy  $E=4113$  keV could be from the decay of the  $3^+$  5914 keV state found in the  $^{28}\text{Si}(p,t)^{26}\text{Si}$  measurement [9, 12] (with

---

<sup>1</sup>That is, the multipolarity of the  $\gamma$ -ray is unknown.

the spin-parities assigned using a DWBA calculation) and the  $^{24}\text{Mg}(^3\text{He},n)^{26}\text{Si}$  measurement [11] (with the spin-parities assigned using the Hauser-Feshbach (HF) calculation of differential cross section [40, 41]), to the first excited state of  $2^+$ , 1796 keV. However, it could also be the 4089 keV  $\gamma$ -ray from the decay to the first excited state from the  $0^+$ , 5886 keV state found in a recent  $^{24}\text{Mg}(^3\text{He},n)^{26}\text{Si}$  re-measurement at Tsukuba University [39], with the spin-parity assigned using the DCO method. According to the 4113 keV centroid determination of the  $\gamma$  peak in our analysis, and the transition probabilities to the  $2^+$  state from the  $3^+$ , 5912 keV state and from the  $0^+$ , 5886 keV state, the former possibility is more likely based on our results.

For the  $\gamma$ -ray with energy around 2260 keV, no match can be found in the literature. But from the coincidence spectra, we can clearly see that this  $\gamma$ -ray is in coincidence with the  $\gamma$ -ray of 1404 keV in the M1/E2 transition from the 4183 keV  $3^+$  level to the 2784 keV  $2^+$  level, as well as with the  $\gamma$ -ray of 843 keV in the E2 transition from the 5291 keV  $4^+$  level to the 4446 keV  $2^+$  level. If this is true, the level from which the 2260 keV can be emitted have  $E_x > 7551$  keV. So far however, such  $\gamma$  transitions have not been experimentally observed [80]. After considering this, we exclude this possibility that such higher energy levels are the candidates for the 2260 keV  $\gamma$  emission. We also found that there is a probable M3 transition with an 851 keV  $\gamma$ -ray from the 4183 keV level to the 3332 keV  $0^+$ , which is however not seen in the total  $\gamma$  spectrum probably because it is too weak compared with the strong 843 keV E2 transition. If the observed  $\gamma$ -ray around the 843 keV, that is coincident with the 2260 keV  $\gamma$ -ray, is really from this transition, then the state responsible for the 2260 keV  $\gamma$  emission could be a level around 6443 keV or above. In this energy region, there is an  $0^+$  level at 6471 keV with a possible weak M3 transition to the 4183 keV, which however, has not been experimentally observed before. In the mirror nucleus  $^{26}\text{Mg}$ , we find that there is an M1/E2 transition with a 2272 keV  $\gamma$ -ray from the 6623 keV,  $4^+$  level to the 4350 keV,  $3^+$  level, where the latter is the mirror level to the 4183 keV,  $3^+$  level

in  $^{26}\text{Si}$ . It is more probable then that the 2260 keV  $\gamma$ -ray seen in our experiment is from the transition between the  $4^+$  mirror level of the 6623 keV,  $4^+$  level in nucleus  $^{26}\text{Mg}$  to the 4183 keV level. Based on these considerations, we therefore tentatively claim a new level in  $^{26}\text{Si}$  at 6446 keV with spin-parity  $4^+$ , taking the level energy of 4183 keV as the average value (4186 keV) of the literature value (4183 keV) [79] and our result (4189 keV).

# Data Analysis for the $p(^{25}\text{Al},p)^{25}\text{Al}$ Experiment at the CRIB Facility

## 5.1 Particle identification (PID)

As mentioned in Chapter 2, the radioactive  $^{25}\text{Al}$  beam is still heavily contaminated by the  $^{24}\text{Mg}$  particles from the primary beam, and these can scatter the protons out of the target as well. Also, the light reaction products include other unwanted particles besides the proton, mostly alpha particles. Therefore, PID for both the beam particles and the reaction products is needed.

### 5.1.1 PID for the $^{25}\text{Al}$ beam

The radioactive  $^{25}\text{Al}$  beam is contaminated with other isotopes from the beam production, among which the primary beam particles  $^{24}\text{Mg}$  is the dominant one. Based on their different properties, such as mass and charge, we can easily separate the  $^{25}\text{Al}$  beams from those contaminants by using the combination of  $B\rho$  settings, time-of-flight (TOF) method and energy-loss measurement at F2 chamber. The RF (Radio Frequency) time <sup>1</sup> was used to separate the  $^{25}\text{Al}$  beam particles from

---

<sup>1</sup>The RF time refers to the time of flight between the RF signals from the AVF cyclotron and the timing signal from the PPAC in the F3 chamber [62]. The AVF cyclotron has two RF

the  $^{24}\text{Mg}$  particles since the  $^{25}\text{Al}$  particles have smaller energies and larger mass than the  $^{24}\text{Mg}$  particles and thus are transported slower. Figure 5.1 shows the RF spectrum in which the  $^{25}\text{Al}$  and  $^{24}\text{Mg}$  can be clearly identified by placing a gate of RF time on each of them. The histogram of X and Y positions of the beam on PPACs can be also used for PID, as shown in figure 5.2. Figure 5.3 shows the positions of  $^{25}\text{Al}$  beam particles on the PPAC after applying the RF cuts for the selection of the  $^{25}\text{Al}$ .

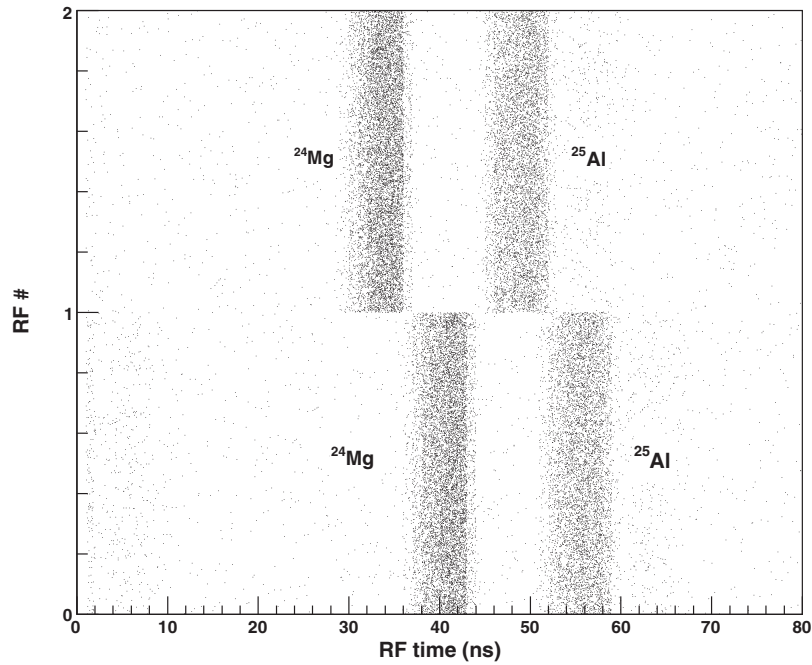


Figure 5.1: Particle identification of  $^{25}\text{Al}$  and  $^{24}\text{Mg}$  using RF time. Left columns correspond to the  $^{24}\text{Mg}$  while right columns correspond to the  $^{25}\text{Al}$ . The Y axis label represents the number of the RF resonators.

### 5.1.2 PID for the proton recoils

The scattered protons that punch through the PSD were identified by using the  $\Delta E$  versus  $E$  spectrum, while the spectrum of PSD energy versus TOF (between resonator systems which provides two kinds of RF signals [63]).

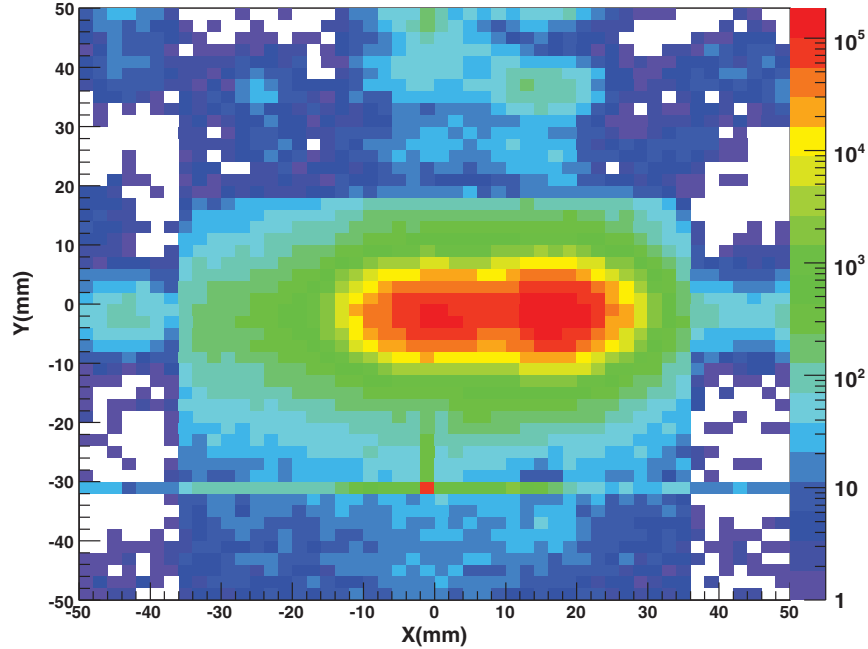


Figure 5.2: Particle identification of  $^{25}\text{Al}$  and  $^{24}\text{Mg}$  using X&Y positions of beam particles on PPACs.  $^{25}\text{Al}$  particles accumulate at the center of the PPAC and the  $^{24}\text{Mg}$  accumulate to the right of the center.

the PSD and the second PPAC) was used to identify protons punching through the PSD and the ones stopping in the PSD. Figure 5.4 and figure 5.5 show the particle identification of protons. When sorting the data, we can apply a gate around the proton region to choose only scattering events in coincidence with protons in the chosen region. The virtual gate is actually a combination of conditions for the associated variables in an event, such as PSD energy and TOF, to confine the event inside the gated region. It has to be pointed out that before this PID all silicon detectors (PSDs and SSDs) must be calibrated first since the different detector channels have different responses to the same energy signals. The calibration of the silicon detectors is explained in the next section.

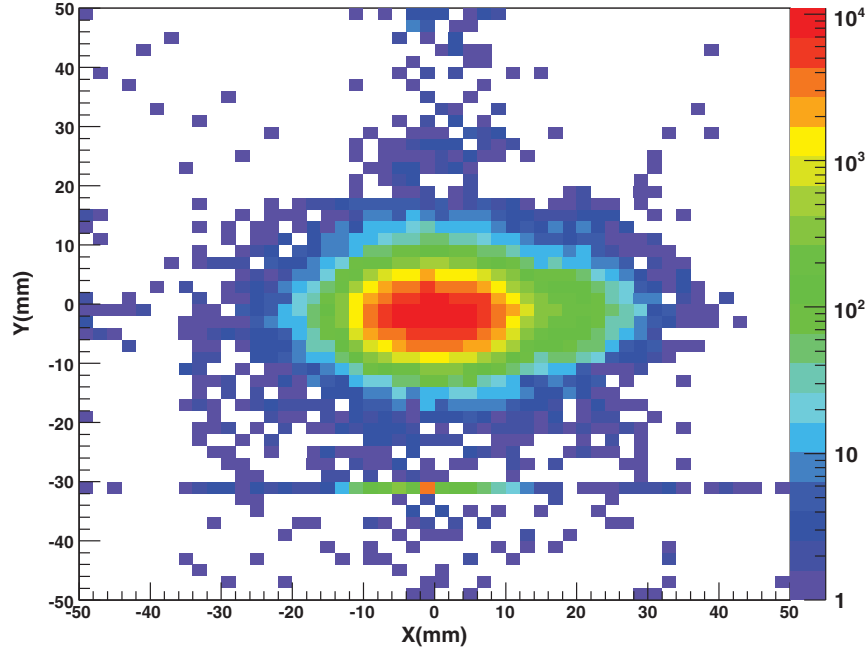


Figure 5.3:  $^{25}\text{Al}$  beam particles on PPACs after applying the RF cuts for  $^{25}\text{Al}$  on the histogram of RF time.

## 5.2 Energy calibration of the silicon detectors

A  $3\text{-}\alpha$  source was used to calibrate the silicon detectors, including the PSD and SSD. Due to the pulse height defect (see page 275 in Ref. [2]), a secondary proton calibration based on the  $\alpha$  calibration was made using proton beams of various energies.

### 5.2.1 Primary calibration using $3\text{-}\alpha$ source

Recall from Chapter-2 that there are in total 96 PSD channels with 32 channels for each PSD and 6 SSD channels for 6 SSDs. Different detector channels have different responses to one energy signal and therefore each channel must be calibrated. For example, figure 5.6 shows the histogram of all PSD channels before calibration for the data runs using a  $3\text{-}\alpha$  source. Table 5.1 is a list of energies of the  $3\text{-}\alpha$  source

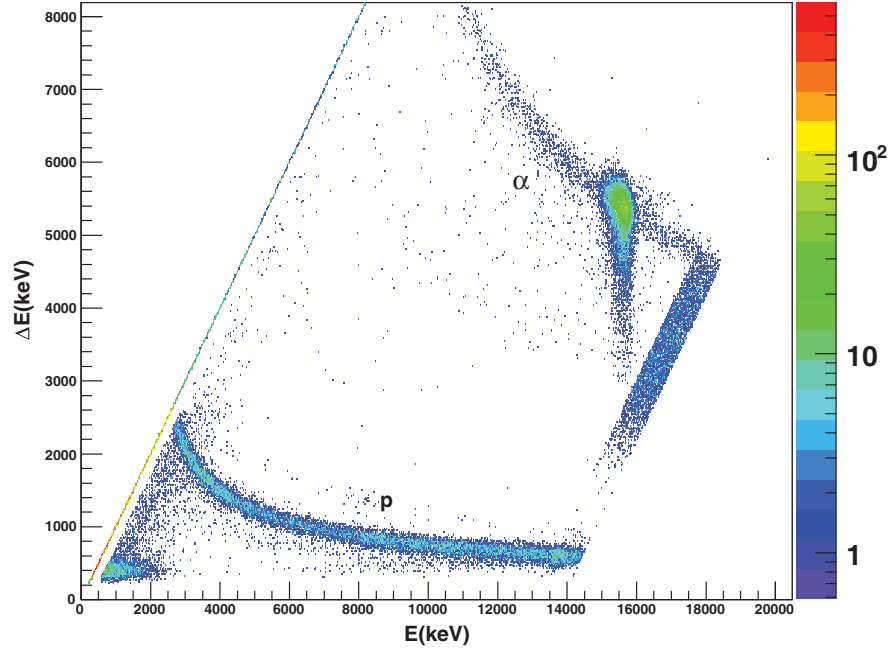


Figure 5.4: Particle identification of protons using a 2-D histogram of  $E$  versus  $\Delta E$  for the silicon telescope at zero degrees only for identifying scattered protons punching through the PSD.

used for the energy calibration. For the  $\alpha$  energy spectrum obtained for each detector, the three peaks are fitted with a Gaussian function and then the peak centroids from the fits are used as the data points for a linear fit (or for a more accurate calibration, a quadratic fit) to find the final calibration parameters, such as the gain and offset for each detector channel. The equation for the calibration is as follows:

$$Energy_{\alpha} = gain_{\alpha} \times (energy\ channel - offset_{\alpha}) \quad (5.1)$$

where  $gain_{\alpha}$  and  $offset_{\alpha}$  are from the  $\alpha$  calibrations.

Figure 5.7 shows an example of the  $\alpha$  spectrum for one PSD, channel and the linear calibration of channel to energy is also shown in the same picture with the

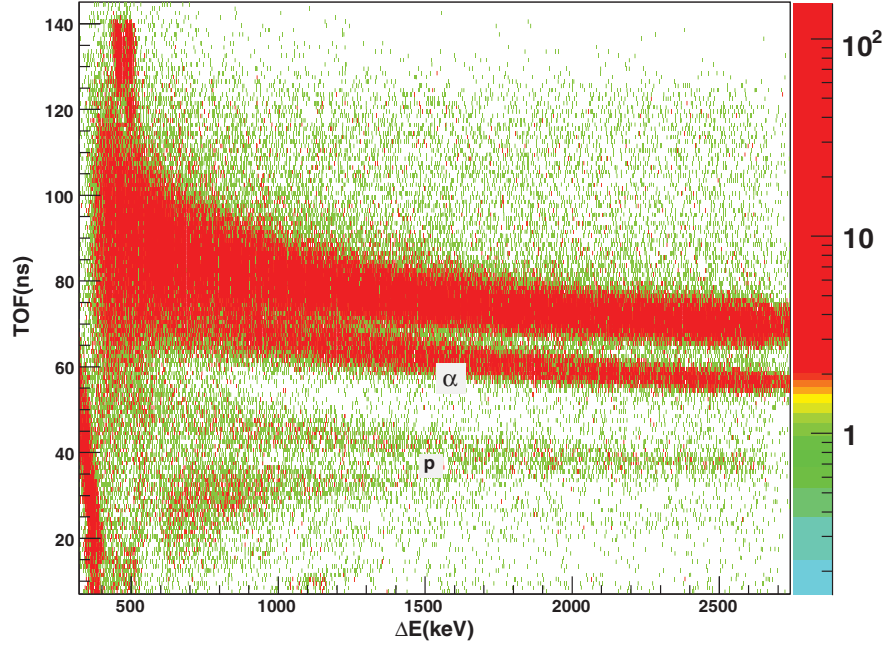


Figure 5.5: Particle identification of protons using a 2-D histogram of  $\Delta E$  versus time-of-flight (TOF) for identifying scattered protons both punching through the PSD and stopping in the PSD.

Table 5.1: List of energies of the 3- $\alpha$  source for the energy calibration of the silicon detectors.

$\alpha$ source	$\alpha$ energy
$^{237}\text{Np}$	4.788 MeV
$^{241}\text{Am}$	5.486 MeV
$^{244}\text{Cm}$	5.805 MeV

axis of energy at right in green.

### 5.2.2 Pulse height defect effect

The silicon detector has different responses to particles with different charges when measuring the energies of the particles. This means that the electron collection

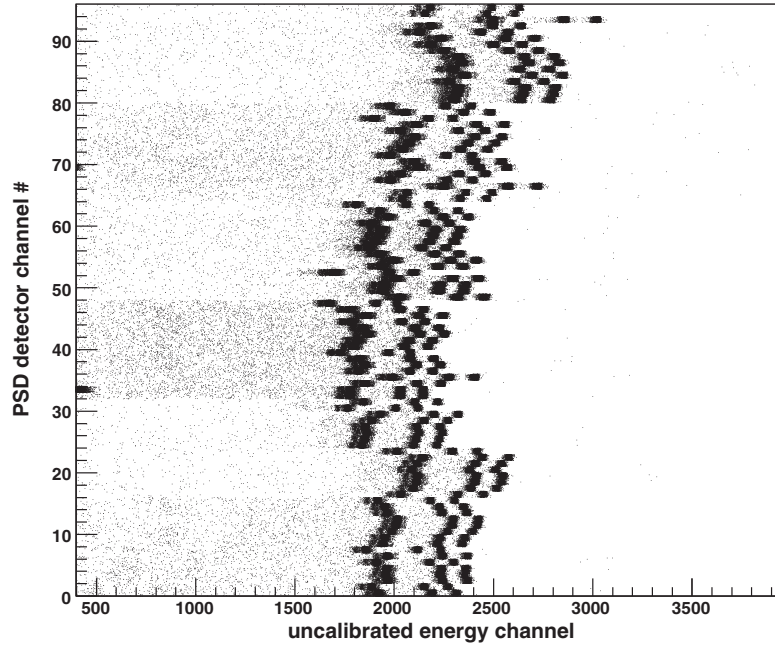


Figure 5.6: Histogram of all PSD channels before calibration for the data runs using a  $3\text{-}\alpha$  source.

efficiency of the detector will be different when particles with different charges deposit energy in the detector, resulting in different measured pulse heights for the same energy that different particles have and makes energy calibration correct just for the measurement of the same particle as used for the calibration. This is so the called “pulse height defect” effect. In our case, we measure the proton energy in the experiment but use the  $\alpha$  source for energy calibration. Therefore, the pulse height effect must be taken into account. This effect is reduced or eliminated by performing a secondary energy calibration using proton beams — the same particles that we measure in the elastic scattering.

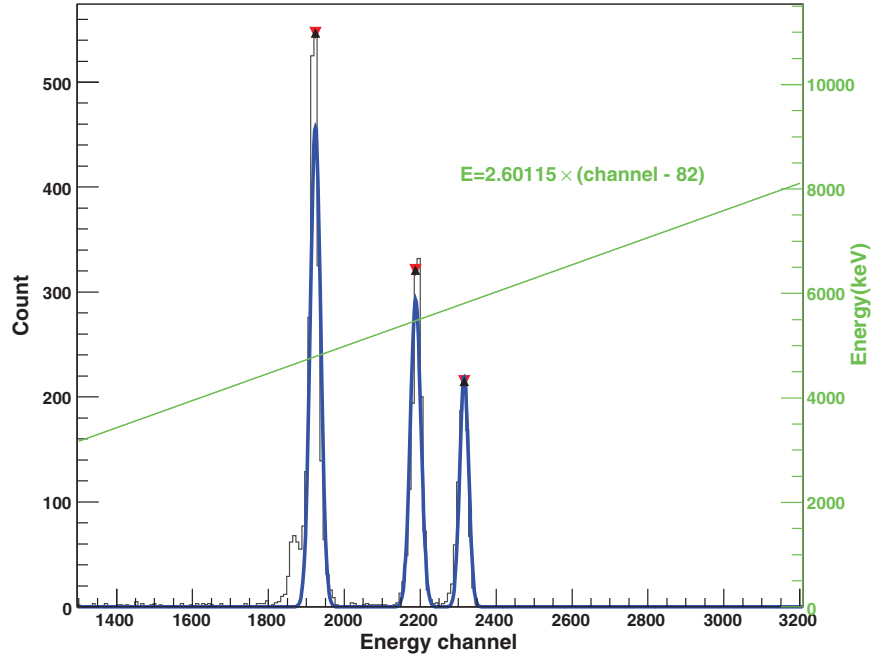


Figure 5.7: An example of  $\alpha$  calibration for a PSD channel. Shown in green is the linear fit of channel vs energy.

### 5.2.3 Secondary calibration using proton beams

Various energies were set for the proton beams used for the calibration: 1.9 MeV, 6.4 MeV, 9 MeV and 14 MeV. While for the  $\alpha$  calibration the PSD and SSD were calibrated separately, for the proton calibration, the PSD and SSD are calibrated together as a  $\Delta E$ -E telescope. According to a SRIM energy-loss calculation [64], the 1.9 MeV proton cannot punch through the PSD to reach the SSD behind the PSD. However, since we calibrate the PSD and SSD as a whole, it can still be used as a calibration energy together with the proton energies of 6.4 MeV, 9 MeV and 14 MeV. Similar to the  $\alpha$  calibration procedure, the peak centroids from the fits to the proton energy peaks in the proton spectrum are used as the data points to

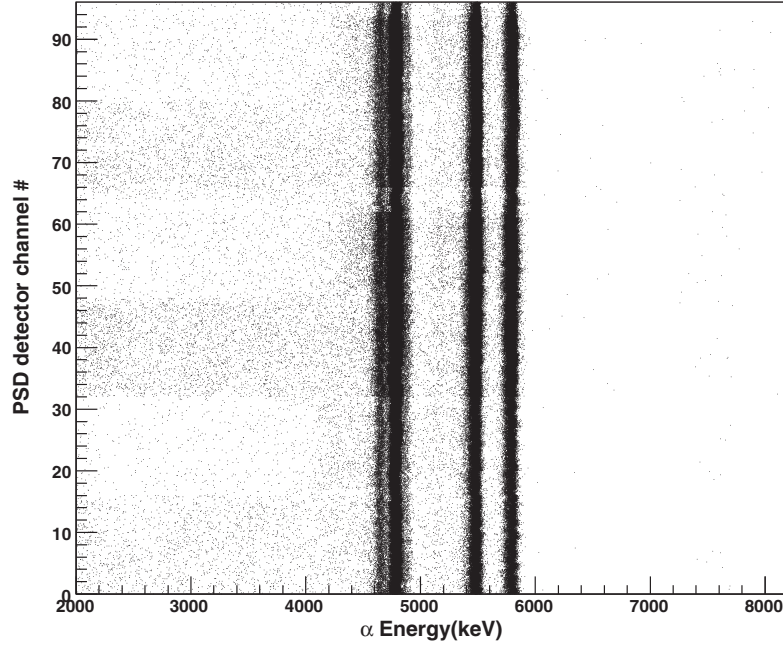


Figure 5.8: Histogram of  $\alpha$  energies for all PSD channels after applying the calibration parameters for each detector channel.

perform a linear calibration fit (or quadratic fit) as follows <sup>2</sup>:

$$Energy = gain_p \times (Energy_\alpha - offset_p) \quad (5.2)$$

where  $gain_p$  and  $offset_p$  are from this proton calibration,  $Energy_\alpha$  is the energy after  $\alpha$  calibration and  $Energy$  is the final energy after both calibrations.

Figure 5.9 shows an example of the proton calibration for one PSD-SSD telescope. It should be pointed out that now the PSD is treated as a whole unit like the SSD instead of being calibrated by channel in the  $\alpha$  calibration because all PSD channels have already been normalized after the  $\alpha$  calibration and they share

<sup>2</sup>Actually, only peaks with good statistics are used for calibration. For example, only the 1.9 MeV, 9 MeV and 14 MeV proton peaks are used because the 6.4 MeV proton peak has very poor statistics compared to the three others, and including it in the calibration results in a large uncertainty in the linear fit.

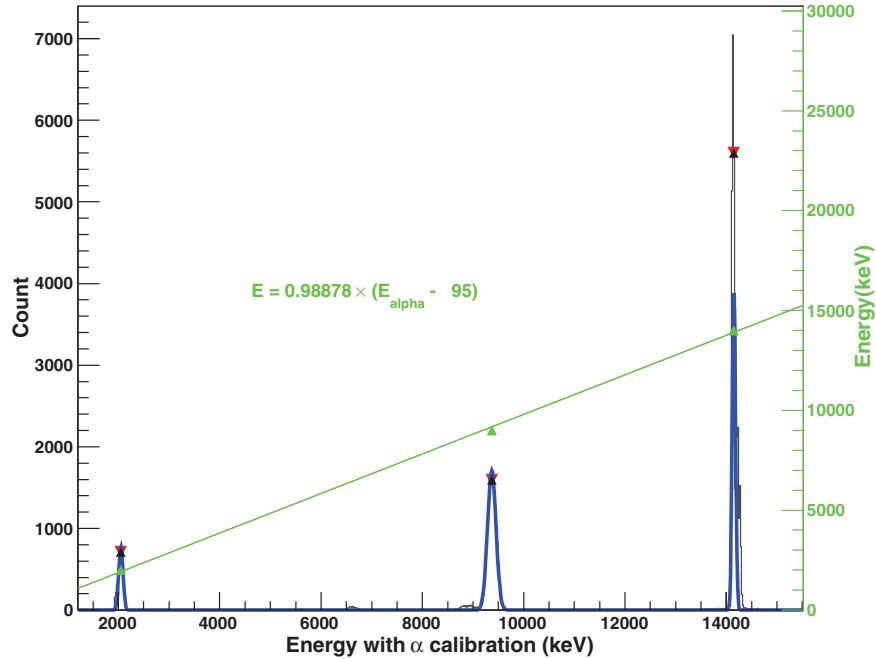


Figure 5.9: An example of the proton calibration for a PSD-SSD telescope.

the same calibration parameters in the proton calibration.

After applying all the calibrations and PID gates for selecting the  $^{25}\text{Al}$  beam ions and proton recoils, the final spectra of the proton energies measured by the three  $\Delta E$ -E (PSD-SSD) telescopes arranged at  $0^\circ$ ,  $17^\circ$  and  $27^\circ$  can be obtained, as shown in figures 5.10 through 5.11.

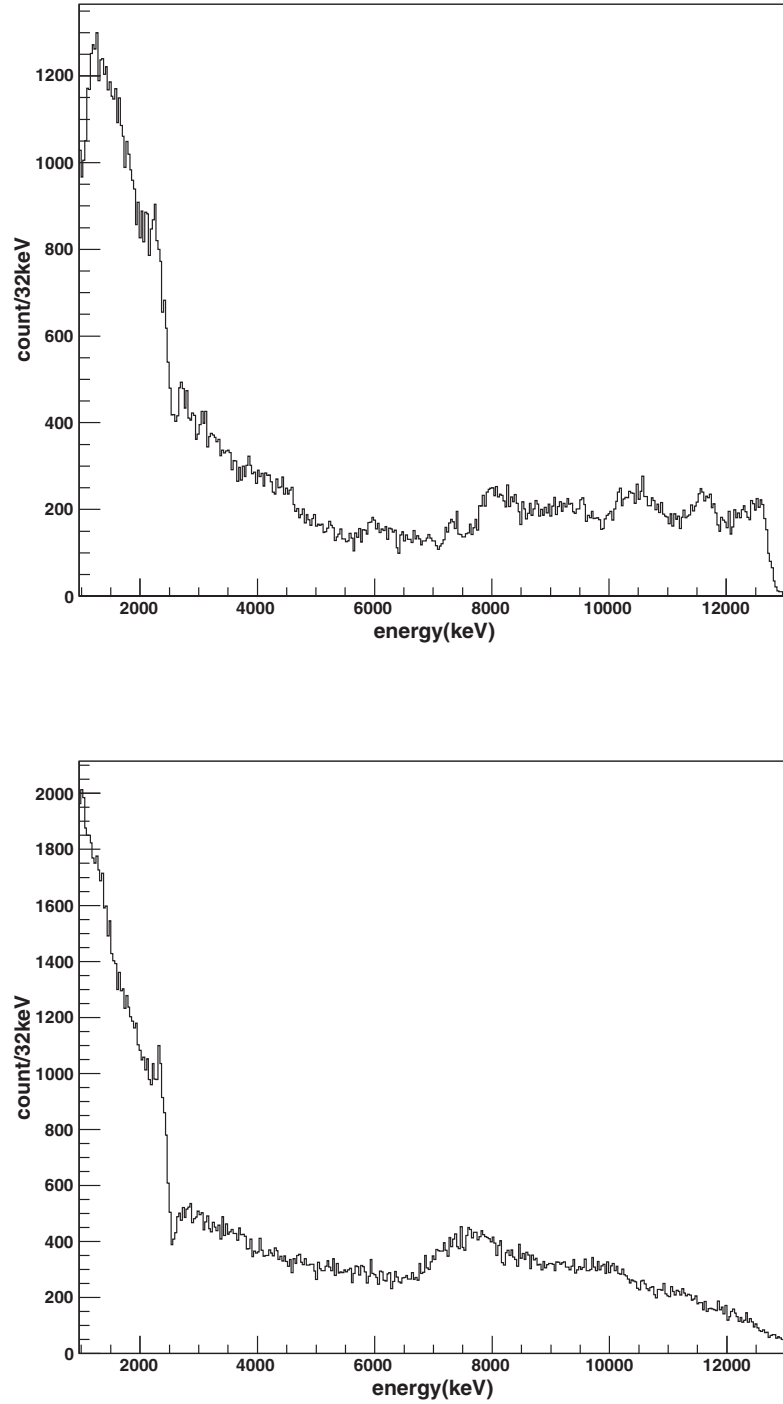


Figure 5.10: Top: the energy spectrum of protons measured by the telescope at  $0^\circ$ . Bottom: the energy spectrum of protons measured by the telescope at  $17^\circ$

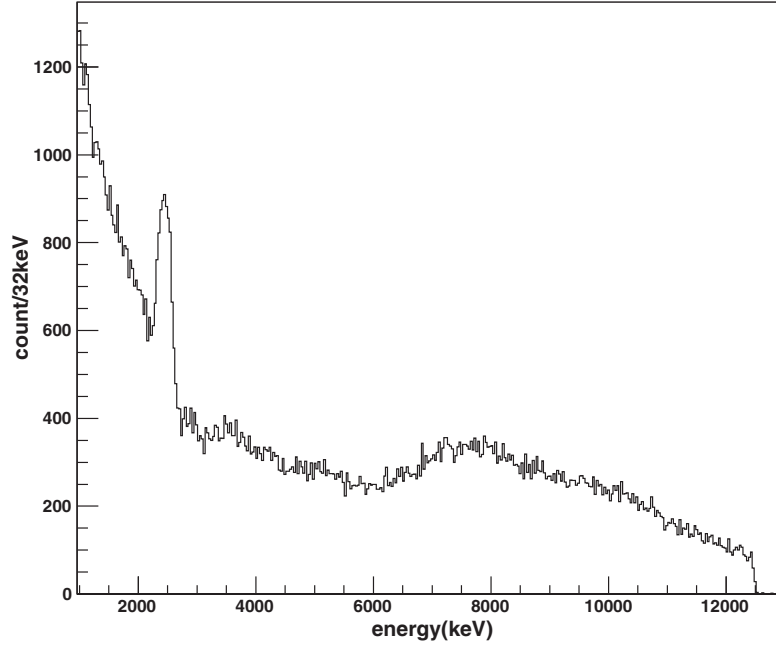


Figure 5.11: The energy spectrum of protons measured by the telescope at  $27^\circ$ .

The uncertainties in proton energy can come from the intrinsic resolution of the silicon detectors (PSD and SSD), the straggling of the beam particles and protons in the thick target, the beam energy spread before entering the target, and the finite solid angle of the detector strips of PSD. The former two sources are the major contributions at the most forward angle, which result in a resolution in center-of-mass energy ( $E_{cm}$ ) of 4070 keV in full width at half maximum (FWHM). At large scattering angles, the contribution due to the finite solid angle of the detector strip becomes important and results in an total energy resolution in  $E_{cm}$  of 70300 keV at  $\theta_{lab} = 25^\circ$  [65].

## 5.3 Energy loss correction for scattered protons

In nuclear experiments involving thin targets, the energy loss of reaction products before leaving the target is small (usually from a few keV to tens of keV), and can be safely neglected compared to the exit energies of these products. But when using the thick target approach, the energy loss of the scattered proton traveling through the remaining part of the target can be considerable<sup>3</sup> and must be taken into account. In the following section, two methods for the energy loss correction are described.

### 5.3.1 The stopping power of charged particles in target materials

Before continuing to the next section, I will briefly explain the frequently mentioned concept of “stopping power” and how I find the stopping powers for the beam particle in the  $CH_2$  and pure carbon targets.

Charged particles moving through matter interact with the electrons of atoms in the material. The interaction excites or ionizes the atoms. This leads to an energy loss of the traveling particle. The Bethe formula which was derived by Hans Bethe in 1930, describes the energy loss per distance traveled, also known as the stopping power of the material traversed. The relativistic stopping power is calculated by the following formula — the Bethe-Bloch formula [20], which describes the energy loss by ionization of fast charged particles (protons, alpha particles, atomic ions, but not electrons) traversing matter.

---

<sup>3</sup>If the beam particles have traveled close to the end of the target, the remaining path for the scattered protons is short and therefore their energy losses can be neglected. But for our experiment, the  $^{25}\text{Al}$  beam particles stop slightly beyond the middle of the target, according to a SRIM energy-loss calculation, and therefore the energy losses still need to be taken into account for all scattered protons. In fact, when the  $^{25}\text{Al}$  beam particles is close to stop, the protons they scatter will not have enough energy to escape from the target.

$$-\frac{dE}{dx} = \frac{4\pi}{m_e c^2} \cdot \frac{nz^2}{\beta^2} \cdot \left(\frac{e^2}{4\pi\epsilon_0}\right)^2 \cdot \left[ \ln\left(\frac{2m_e c^2 \beta^2}{I \cdot (1 - \beta^2)}\right) - \beta^2 \right] \quad (5.3)$$

where,

- $\beta$  =  $v/c$
- $v$  velocity of the particle
- $E$  energy of the particle
- $x$  distance traveled by the particle
- $c$  speed of light
- $z$  particle charge
- $e$  electron charge
- $m_e$  rest mass of the electron
- $n$  electron number density of the target
- $I$  mean excitation potential of the target

The  $n$  is calculated by  $N_A \rho Z/A$ , where the  $N_A$ ,  $\rho$ ,  $A$  are Avogadro's constant, the mass density of the material, and the mass number of the material, respectively. The mean excitation potential  $I$  can be approximated by  $I = (10eV)Z$ . This Bethe-Bloch formula is the one used in the SRIM program [64], which is used here to simulate shooting the beam particle onto the  $CH_2$  and  $C$  targets, to calculate the stopping powers ( $S_1$  and  $S_2$ ) in the two target materials for the different beam energies at different depth inside the target. The calculated stopping powers are tabulated for looking-up, or plotted in a graph and fitted to find the fitting function, which will be used later in this Chapter for the energy loss correction and the normalization of beam yields in these two targets. Figure 5.12 shows the calculated stopping power vs  $^{25}\text{Al}$  beam energy in the  $CH_2$  target (in red) and  $C$  target (in black).

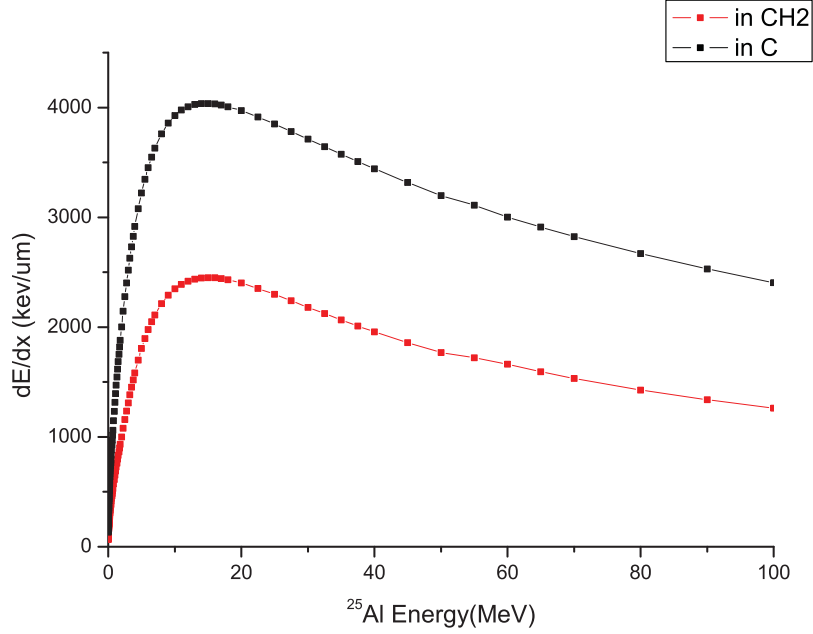


Figure 5.12: Stopping power vs beam energy in  $CH_2$  (red) and pure carbon target (black), calculated with SRIM.

We then made fits to the calculated stopping power to extract the correlations between the stopping power and beam energy. For simplicity, we divided the energy region into two parts ( $E(^{25}\text{Al}) < 15$  MeV and  $E(^{25}\text{Al}) > 15$  MeV) according to the curve shape of the stopping power vs energy plot and fit each part separately with different simple functions instead of the Bethe-Bloch function. Figure 5.13 shows the fits for the two parts for  $^{25}\text{Al}$  passing through the  $CH_2$  target.

The extracted fitting functions are:

1) For the  $CH_2$  target,

$$S_{low} = a \times \{1 + (d - 1)\exp[-k(E - E_c)]\}^{\frac{1}{1-d}} \text{ [keV}/\mu\text{m}] \quad (5.4)$$



with  $a = 2487.8$ ,  $E_c = 1.54$ ;  $d = 0.866$ ;  $k = 0.335$ .

$$S_{high} = A_0 + A_1E + A_2E^2 + A_3E^3 + \dots + A_7E^7 \text{ [keV}/\mu\text{m}] \quad (5.5)$$

with  $A_0 = 2242.7$ ;  $A_1 = 35.11$ ;  $A_2 = -0.971$ ;  $A_3 = -0.0594$ ;  $A_4 = -0.00277$ ;  $A_5 = -4.55 \times 10^{-5}$ ;  $A_6 = 3.38 \times 10^{-7}$ ;  $A_7 = -9.56 \times 10^{-10}$ .

2) For the  $C$  target, the same fit functions are used and the values of fit parameters are,

for  $S_{low}$ ,  $a = 4085.4$ ,  $E_c = 0.653$ ;  $d = 0.684$ ;  $k = 0.341$ .

for  $S_{high}$ ,  $A_0 = 3393.2$ ;  $A_1 = 123.9$ ;  $A_2 = -7.947$ ;  $A_3 = -0.2143$ ;  $A_4 = -0.00325$ ;  $A_5 = -2.84 \times 10^{-5}$ ;  $A_6 = -1.33 \times 10^{-7}$ ;  $A_7 = 2.61 \times 10^{-10}$ .

### 5.3.2 Simple energy correction using the SRIM calculation

In the SRIM calculation, we simulated shooting the  $^{25}\text{Al}$  beam into the target using the actual target thicknesses. SRIM then returns the residual energies of the beam at different spots along the beam axis as well as the scattering and final energies of the associated scattered protons. By plotting the scattering energies of the protons at the scattering spots and the final energies upon leaving the target, we can determine the energy loss or scattering energy from the plot for a proton with any final energy leaving the target. Alternatively, we can make a fit to the plot to find a function for correcting energy loss. Figure 5.14 shows the examples of the plots of the  $E_{cm}$  vs the proton energy after the target from the SRIM calculation for the telescope at  $0^\circ$ , for runs with the  $\text{CH}_2$  target and for runs with the pure carbon target, with the fits to the data also shown.

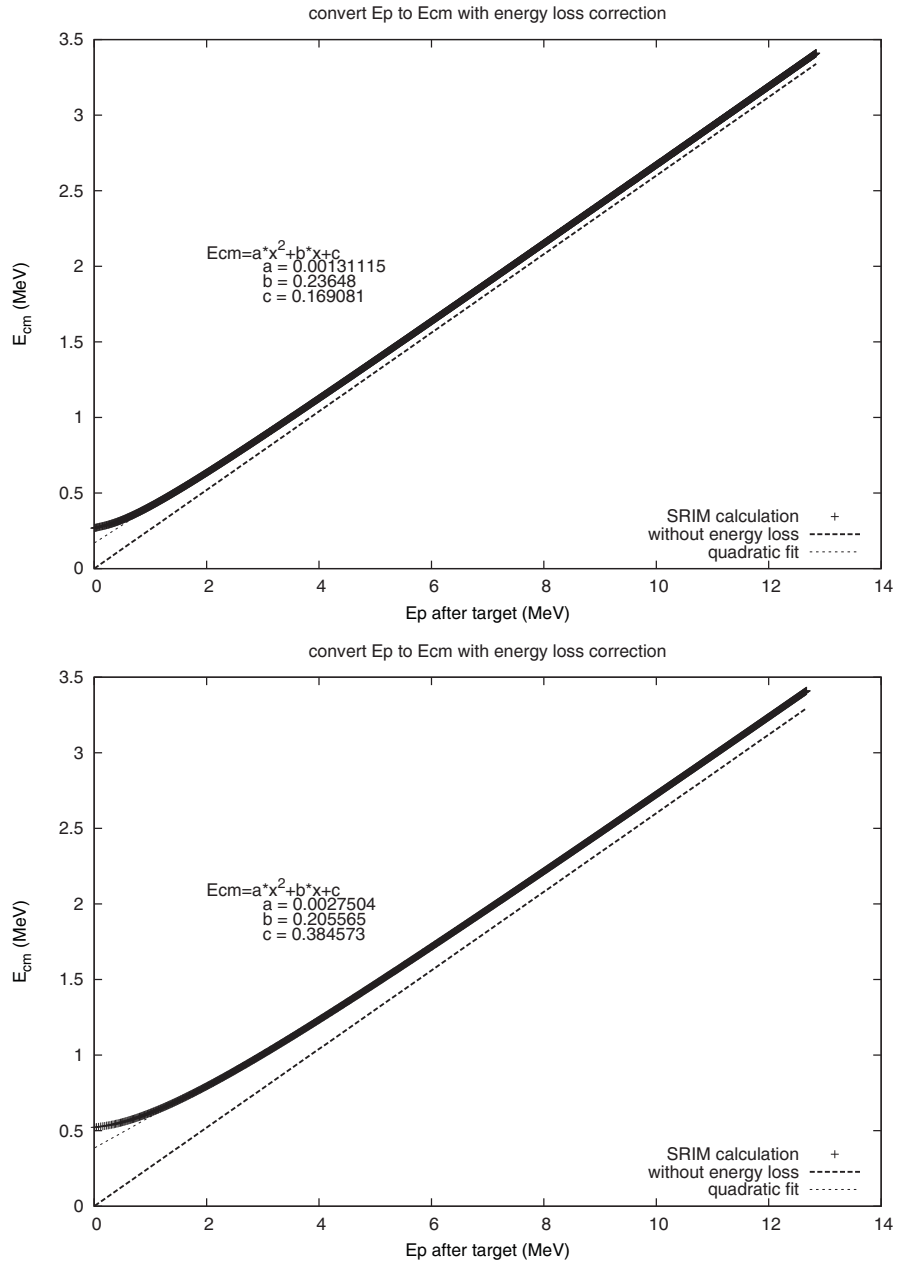


Figure 5.14: Energy loss correction from the SRIM calculation for the CH<sub>2</sub> (top) and the C target (bottom). The fits to the plots are also shown, as well as the plots for the ideal situations with no energy loss.

This correction can be used only for protons with small scattering angle where the change of the proton's path in the target due to the scattering angle from the path along the beam axis can be neglected. For scattering at large angles, the path changes greatly as the angle changes, and consideration has to be made for different SRIM calculations for different paths, so that this method of correction is no longer simple and an other method should be applied.

The fit functions for the two plots are:

1) for CH<sub>2</sub> target,

$$E_{cm} = 0.00131115 \times E_p^2 + 0.23648 \times E_p + 0.169081 [MeV] \quad (5.6)$$

where  $E_{cm}$  is the center-of-mass energy converted from the proton energy after the energy loss correction and  $E_p$  (MeV) represents the proton energy after the target that is not corrected for energy loss.

2) for pure carbon target,

$$E_{cm} = 0.0027504 \times E_p^2 + 0.205565 \times E_p + 0.384573 [MeV] \quad (5.7)$$

### 5.3.3 Event-by-event correction

Ideally, the proton energies measured with the silicon detectors should be corrected for energy loss on an event-by-event basis. The idea is the following. The range of the <sup>25</sup>Al beam in the CH<sub>2</sub> target is determined and then divided into 5000 equal parts. Then from the front end of the target, the residual energy of the <sup>25</sup>Al beam is calculated in each part by Ziegler's energy-loss routines [51], along with the scattered proton energy at the scattering spot. Knowing the length of the path the proton travels through the target, its energy after the target is obtained and compared with the measured proton energy in a single event. The on-spot proton energy of this event, that is, the energy of the proton with energy loss corrected, is then directly deduced from the final match of the comparison.

To determine the range of the <sup>25</sup>Al beam in the target, we need to find first the

angle at which the beam particle goes in the target with respect to the horizontal beam line. This together with the position of the beam on the target, can be calculated using the two positions of the beam particle measured by two PPACs (Parallel Plate Avalanche Counter), located upstream of the target. The calculated target position together with the position of the proton recoil on the PSD will then give us the angle (with respect to the horizontal beam line) at which the proton leaves the target. Let  $\alpha$  and  $\beta$  represent these two angles. They are the angles that the particle tracks make with the horizontal beam line. The scattering angle, say  $\theta$ , is then the angle that is made by the two tracks — the beam particle track and the recoil proton track. Shown in figure 5.15 is the layout of the detector system viewed from the side, along with the particle tracks.

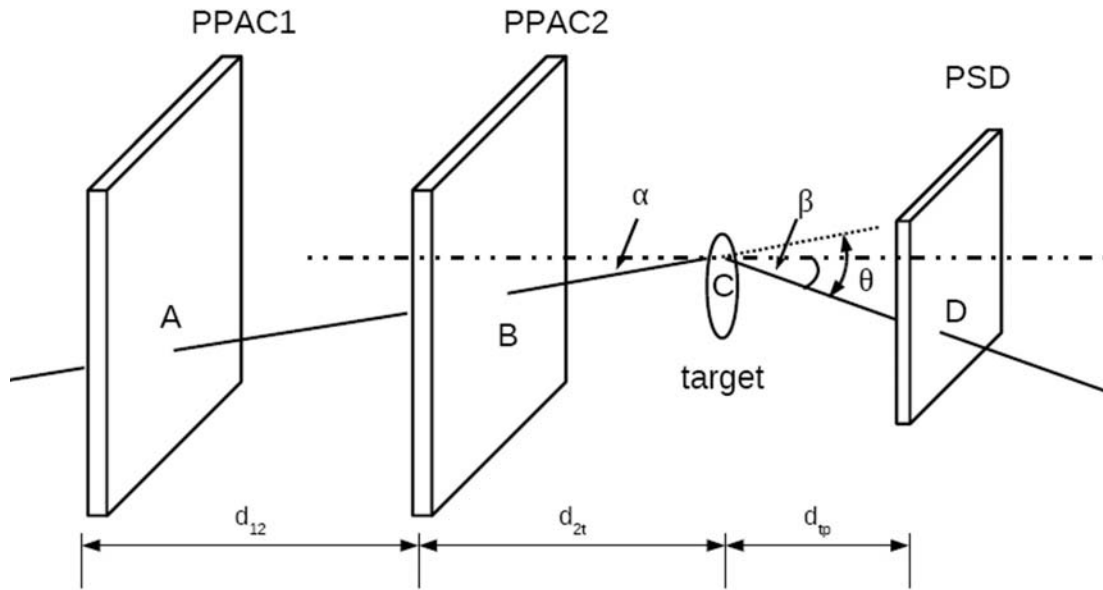


Figure 5.15: Layout of the beam tracking in the detector system obtained using the two PPACs before the target and the PSD after the target.

Let  $A$ ,  $B$ ,  $C$  and  $D$  be the track points of the beam particle in PPAC1, PPAC2,

target and PSD, respectively, with,

$$A = A(x_1, y_1, z_1)$$

$$B = B(x_2, y_2, z_2)$$

$$C = C(x_t, y_t, z_t)$$

$$D = D(x_p, y_p, z_p)$$

in the coordinate system as shown in figure 5.16, with the  $z$ -axis along the horizontal beam line from upstream to downstream and origin on the target plane.

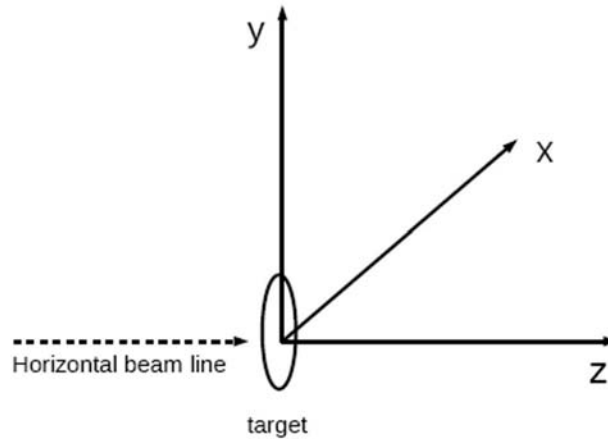


Figure 5.16: Coordinate system for particle tracking in the detector chamber.

The positions  $A$ ,  $B$  and  $D$  are known from the measurements; the position  $C$  is calculated from positions  $A$  and  $B$ . Let  $d_{12}$ ,  $d_{2t}$  and  $d_{tp}$  be the distance between the two PPACs, the distance between the PPAC2 and the target, and the distance between the target and the PSD. Then we find

$$\begin{aligned}
x_t &= x_1 + \frac{x_2 - x_1}{z_2 - z_1}(z_t - z_1) = x_1 + \frac{d_{12} + d_{2t}}{d_{12}}(x_2 - x_1) \\
&= x_1 + \left(1 + \frac{d_{2t}}{d_{12}}\right)(x_2 - x_1) \\
y_t &= y_1 + \frac{y_2 - y_1}{z_2 - z_1}(z_t - z_1) = y_1 + \frac{d_{12} + d_{2t}}{d_{12}}(y_2 - y_1) \\
&= y_1 + \left(1 + \frac{d_{2t}}{d_{12}}\right)(y_2 - y_1) \\
z_t &= 0
\end{aligned} \tag{5.8}$$

and

$$\begin{aligned}
\alpha &= \arccos \frac{d_{12} + d_{2t}}{AC} \\
\beta &= \arccos \frac{d_{tp}}{CD} \\
\theta &= \arccos \frac{AC^2 + CD^2 - AD^2}{2AC \cdot CD}
\end{aligned} \tag{5.9}$$

where

$$d_{12} = z_2 - z_1 \tag{5.10}$$

$$d_{2t} = z_t - z_2 \tag{5.11}$$

$$d_{tp} = z_p - z_t \tag{5.12}$$

$$AC = \sqrt{(x_t - x_1)^2 + (y_t - y_1)^2 + (z_t - z_1)^2} \tag{5.13}$$

$$CD = \sqrt{(x_p - x_t)^2 + (y_p - y_t)^2 + (z_p - z_t)^2} \tag{5.14}$$

$$AD = \sqrt{(x_p - x_1)^2 + (y_p - y_1)^2 + (z_p - z_1)^2} \tag{5.15}$$

Suppose that a beam particle of energy  $E$  enters the target at an angle  $\alpha$  and that  $l_b$  is the range of the beam particle inside the target calculated using the energy-loss routines [51]. The  $l_b$  is then divided into  $N=5000$  equal parts <sup>4</sup> and an iteration procedure is made for each measured proton to find which one of the 5000

<sup>4</sup>The more parts the  $l_b$  is divided into, the more accurate the energy loss correction will be; here  $N=5000$  is enough for an accurate correction.

parts it corresponds to (where in the target the proton was scattered), according to the scattering angle and associated energy loss.

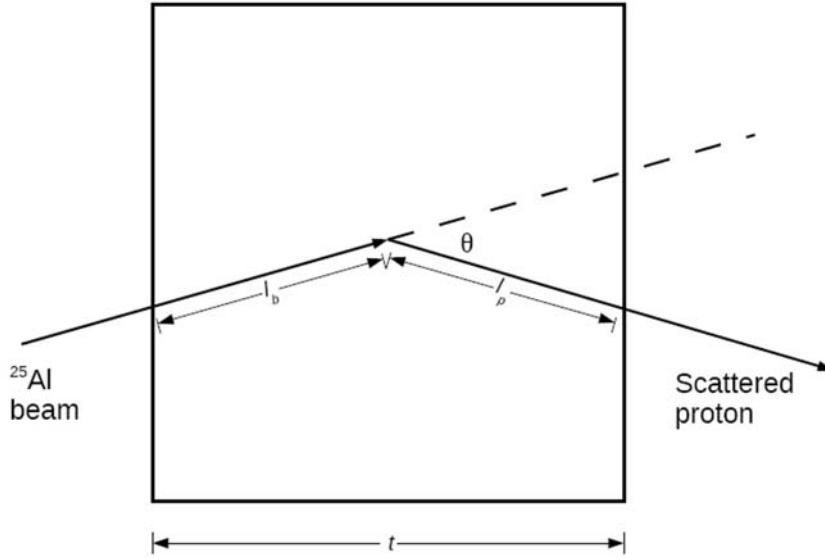


Figure 5.17: Illustration of the paths of a scattering in the target (not to scale).

Let  $t$  be the target thickness and  $l_p$  the path length of the scattered proton inside the target, as shown in figure 5.17. Then according to the geometry, we can find,

$$l_p = \frac{(t - l_b \cdot \cos \alpha)}{\cos \beta} \quad (5.16)$$

By calculating the energy loss of the proton for  $l_p$ , its energy after the target, say  $E_{cal}$ , is obtained and compared with the measured energy  $E_{mea}$ . This process is iterated with an optimization algorithm until the calculated energy matches the measured one. In my calculation, the “match” is achieved whenever  $|E_{cal} - E_{mea}| < 5 \text{ keV}$ , considering the experimental uncertainty of the energy measurement.

The advantage of the event-by-event analysis is that the energy loss correction for each event is separate, so that each event uses its own beam energy for the correction. This allows more accurate correction than the simple one described

in last subsection, where one single beam energy was used for all events. But, in reality, the beam energy fluctuates from event to event and follows a Gaussian distribution instead of just one single energy.

Figure 5.18 shows a proton spectrum after correcting for the energy loss in the target using the event-by-event method. The  $X$  axis represents the center-of-mass energy ( $E_{cm}$ ) transformed from the proton energy according to the kinematics described in Chapter 2. In all the following content of this thesis,  $E_{cm}$  will be used in the proton spectrum instead of the proton energy.

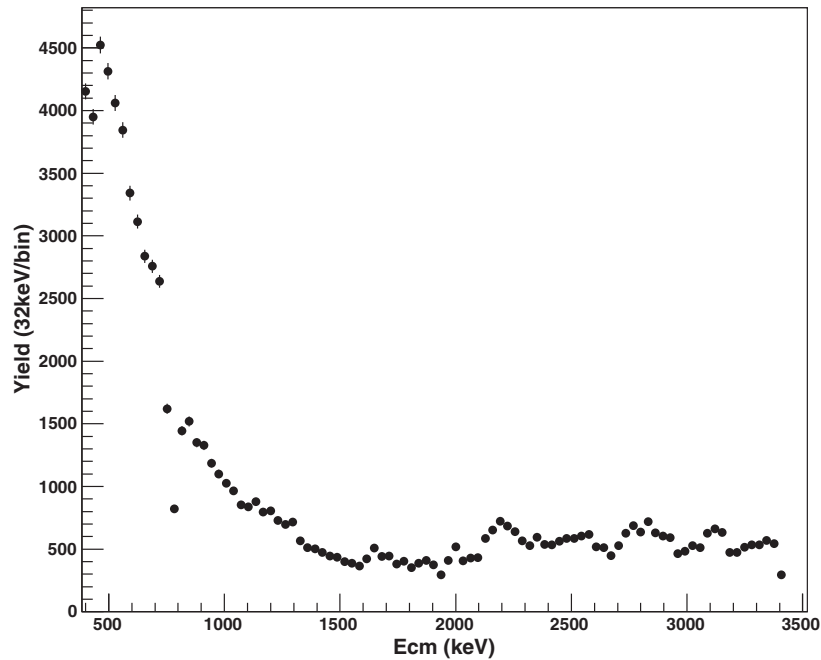


Figure 5.18: An example of the proton spectrum with the energy loss correction, with the  $X$  axis representing the center-of-mass energy ( $E_{cm}$ ) transformed from the proton energy.

There is another method which can be used to directly extract the actual proton energy without adding the energy loss in the target. This involves using an isobaric stable beam and a well-known resonance energy to perform an energy calibration [61].

## 5.4 Deadlayer effect

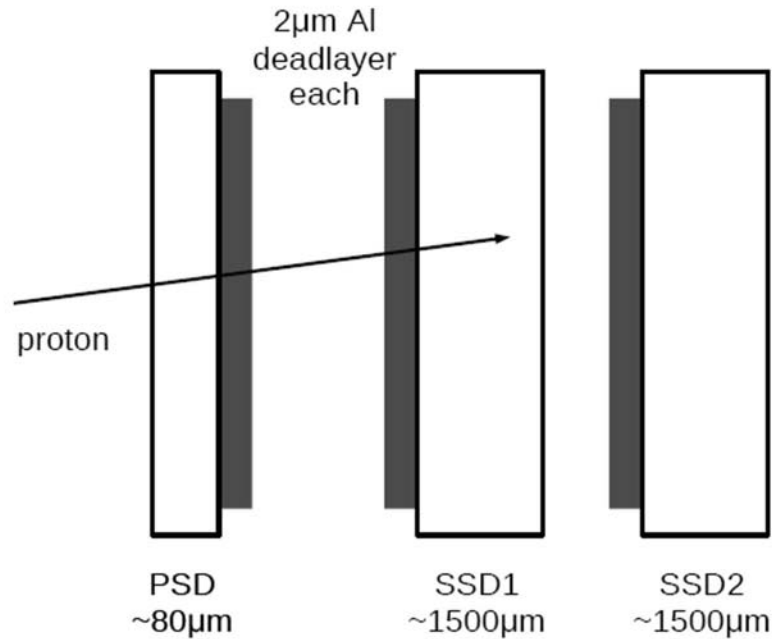


Figure 5.19: The layout of the Silicon detector telescope (PSD-SSDs) with the deadlayers sketched in.

Each of the silicon detectors used in the experiment including the PSD and SSDs has a deadlayer of  $2 \mu\text{m}$  aluminum layer plated on top of the silicon content. Since the deadlayer does not contribute to the charge collection of the detector, there will be an energy loss in the layer which can not be counted as the deposited energy in the detector. This aluminum layer is therefore “dead” to the energy measurement compared to the active layer of silicon content, from which the total deposited energy of particles is recognized by the electronics as the measured energy in the detector. For those protons punching through one detector and its deadlayer and finally stopping in the next detector, their energy loss can be easily corrected in the routine based on their deposited energy in each detector. However, there exist protons that do not punch through to the next detector, and their deposited energy could be interpreted as either due to the relatively lower energy protons

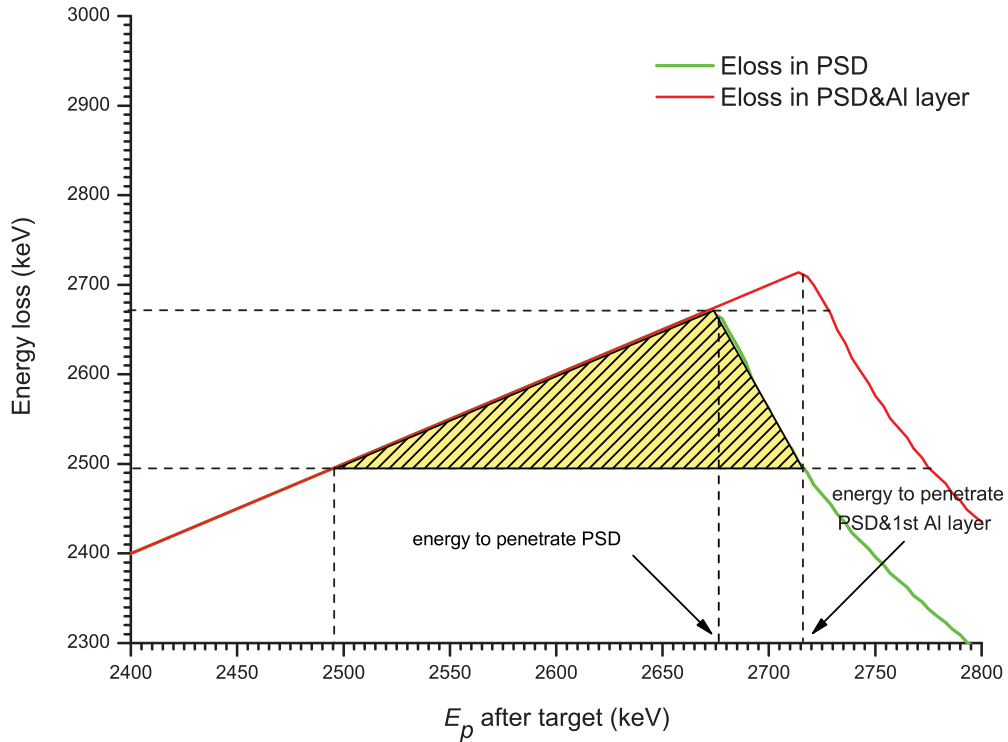


Figure 5.20: Energy loss in the PSD active layer only and energy loss in the PSD and Al deadlayer together as functions of the proton energy when leaving the target (from SRIM simulation). The energies for just punching through the active layer, and through the whole PSD, are indicated.

stopping in the active layer, or due to the higher energy protons punching through the active layer and stopping in the deadlayer. Even if we can distinguish the proton stopping in the deadlayer from that sharing the same energy and stopping in the active layer, we can still not tell where inside the deadlayer it stops, so that it becomes impossible for the energy loss in the deadlayer to be calculated correctly. As a consequence of this deadlayer effect, a gap within which no events are counted will show up in the energy spectrum of the protons for the energy range corresponding to the protons that stop in the deadlayer.

Figure 5.19 shows the layout of the Silicon detector system with the deadlayer

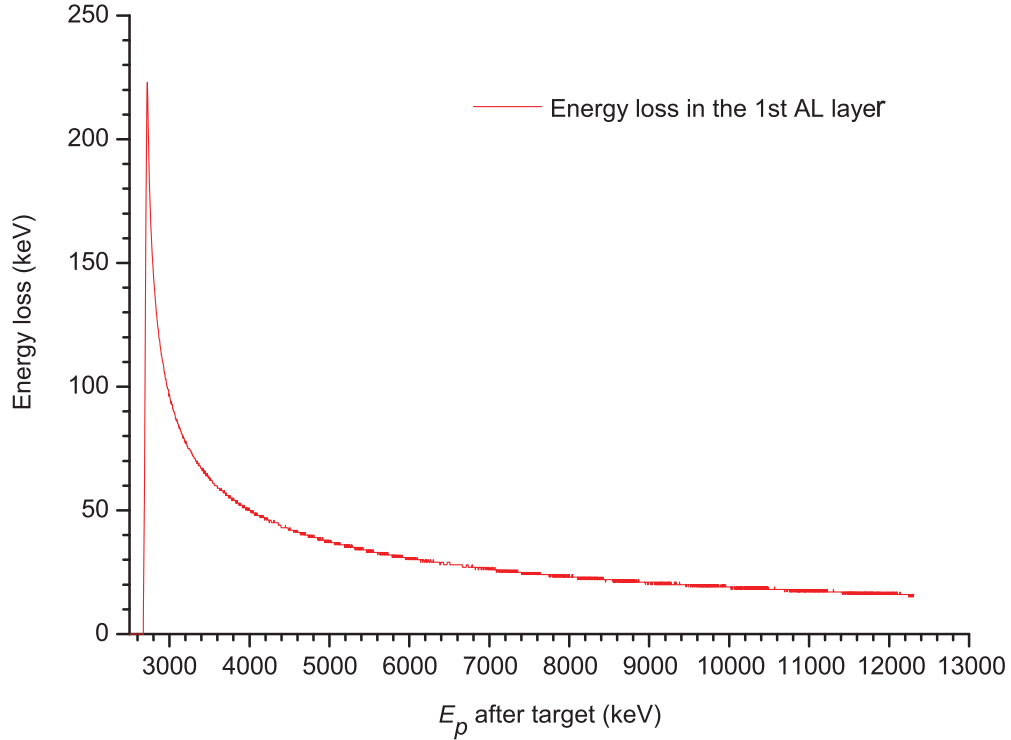


Figure 5.21: Energy loss in just the Al deadlayer only vs the proton energy after leaving the target (from SRIM simulation).

also sketched out. Figure 5.20 shows the calculated energy loss in the active layer of the first PSD and in the whole PSD, including the active layer and the Al deadlayer, vs. the proton energy after leaving the target. The energies for punching through the active layer only and through the whole PSD are indicated.  $E_p$  within the yellow shaded area corresponds to the ambiguous proton detection discussed above. The proton with energy lower than the left end ( $E_p < 2490$  keV) of this area can be clearly identified as a proton stopping in the active layer of the PSD, while the proton with energy beyond the right end ( $E_p > 2715$  keV) will penetrate the deadlayer and reach the second detector, in which case the energy loss in the deadlayer can be corrected. In the ambiguous proton energy range ( $E_p = 2490$  keV–

2715 keV), the region at the left side of the dashed line (2650 keV) corresponds to the protons stopping in the rest of the active layer and the maximum deposited energy is reached where the dashed vertical line is located. In this region, the measured energy by the deposit in the active layer gives the actual proton energy. As  $E_p$  keeps increasing toward the right end of the yellow region in figure 5.20, the proton will punch through the active layer and stop in the deadlayer. The energy deposited in the active layer can be measured, but that in the deadlayer cannot be measured. Since the energy loss in the active layer decreases, which is the measured proton energy but no longer the actual proton energy, this kind of proton will be confused with the protons stopping only in the active layer but with the same energy loss in this layer. So the energy range between the  $E_p$  for penetrating the PSD only and  $E_p$  for penetrating the PSD and Al deadlayer is the deadlayer gap mentioned above. The difference in  $E_{loss}$  between the two plots (red and green) at each  $E_p$  gives the energy loss in the Al deadlayer at this  $E_p$ . Figure 5.21 shows the energy loss in just the Al deadlayer vs. the proton energy after leaving the target. As we can see, at high energies ( $E_p > 5$  MeV) the energy loss in the deadlayer is small and negligible and it can also be easily corrected, but for some energy ( $E_p \sim 2680$  keV, corresponding to  $E_{cm} \sim 720$  keV), the  $E_{loss}$  increases abruptly up to its maximum, leaving us with uncorrectable energy gap.

## 5.5 Background subtraction

Since we use the polyethylene ( $\text{CH}_2$ ) target, most of the background is from reactions with the carbon in the target. Figure 5.22 is an example of the background proton spectrum at  $0^\circ$  with energy loss correction from runs with the pure carbon target, compared with the corrected proton spectrum from runs with the  $\text{CH}_2$  target in figure 5.23, where the same background is also shown in red. To subtract this background from the proton spectrum, we made measurements under the same conditions with the pure carbon target as for the elastic scattering. Then the yield

from the pure carbon target is normalized to the yield from the carbon in the  $\text{CH}_2$  target based on the total accumulated number of beam events, the number density of  $\text{CH}_2$  and C, and the energy-dependent stopping power of the  $^{25}\text{Al}$  beam in  $\text{CH}_2$  and C. The normalization factor of the yield from pure carbon to the yield from carbon in  $\text{CH}_2$  is calculated as follows.

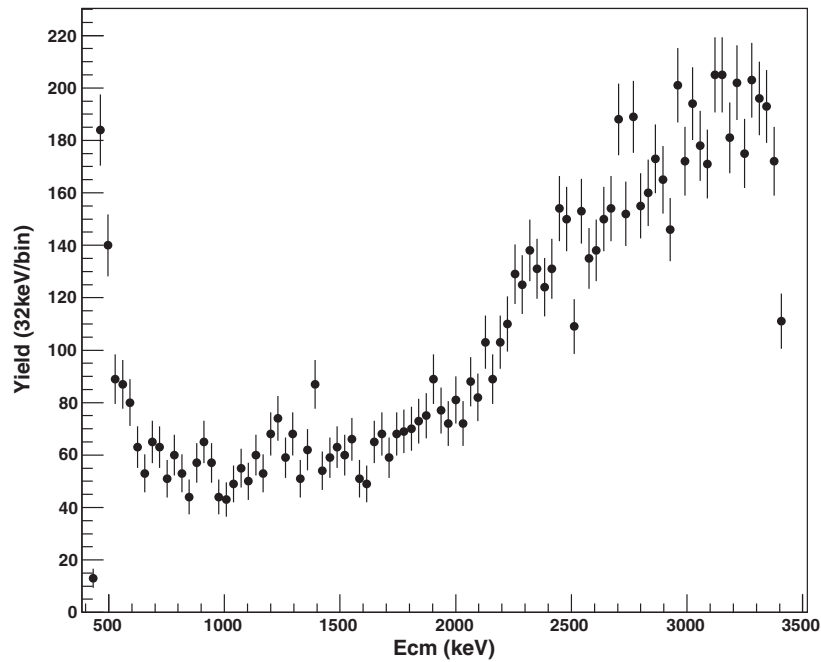


Figure 5.22: Background proton spectrum from runs with the pure carbon target.

### 5.5.1 Normalization of yields from $\text{CH}_2$ and C targets

Suppose that the step size of the beam energy that is equivalent to the bin size ( $\Delta E$ ) of the proton spectrum is  $\Delta E_b$  in the reaction of the beam with the carbon nucleus. The proportionality of  $\Delta E_b$  to  $\Delta E$  is determined by the kinematics of the reaction of the beam particle with the carbon nucleus. Then we can find the corresponding traversed target thickness at any energy bin in the proton spectrum

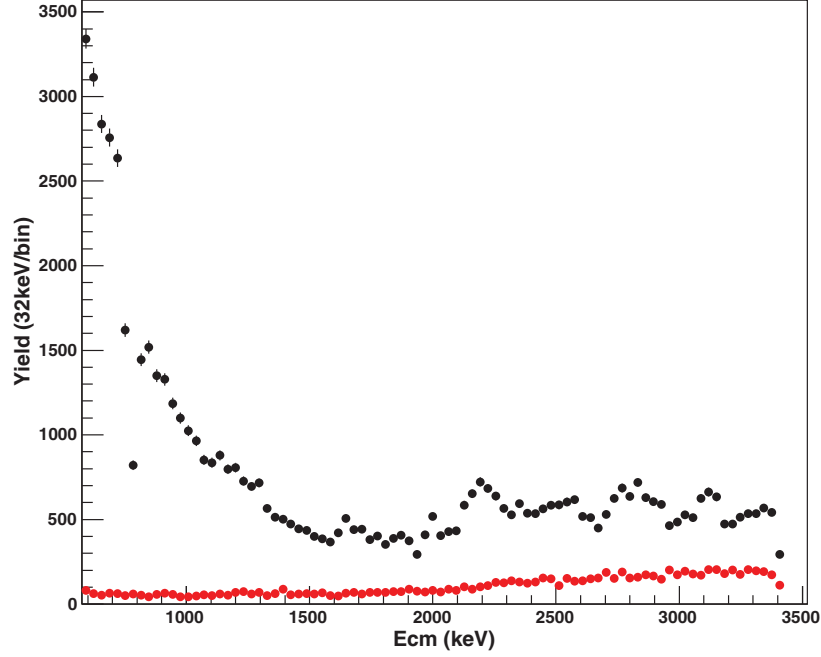


Figure 5.23: Proton spectrum from runs with the  $\text{CH}_2$  target and the background from figure 5.22 (without normalization) is also shown in red.

as

$$\Delta x = \frac{\Delta E_b}{S} \quad (5.17)$$

where  $S = \frac{dE}{dx}$  is the energy dependent stopping power of beam in target material.

This gives us the yield in the thick target method at any energy bin as

$$Y = I\sigma n\Delta x = I\sigma n \frac{\Delta E_b}{S} \quad (5.18)$$

where  $I$  is the total accumulated number of beam events,  $\sigma$  the cross section of the reaction of the beam with carbon, and  $n$  the number density of carbon.

Finally, the normalization factor  $N$  can be obtained by

$$N = \frac{Y_1}{Y_2} = \frac{I_1}{I_2} \cdot \frac{n_1}{n_2} \frac{S_1}{S_2} \quad (5.19)$$

where  $I_1$ ,  $I_2$  are the total accumulated number of beam particles bombarding the  $\text{CH}_2$  and C targets respectively, and considered to be constant over the whole path that the beam particles have traveled;  $n_1$  is the equivalent number density of carbon in the  $\text{CH}_2$ ,  $n_2$  the number density of pure carbon; and  $S_1$  and  $S_2$  are the stopping powers of  $^{25}\text{Al}$  beam in  $\text{CH}_2$  and C, respectively.

We apply the normalization factor for the yield of each bin in the proton spectrum from the runs with the pure carbon target, and then subtract it from the proton spectrum from the runs with the  $\text{CH}_2$  target. Figure 5.24 is the proton spectrum after background subtraction with the conversion of the proton energy in lab to the energy of center-of-mass ( $E_{cm}$ ). One issue that one should be careful about is that, subtraction of one spectrum from another can be made only when the two spectra have the same bin size, that is, energy per bin.

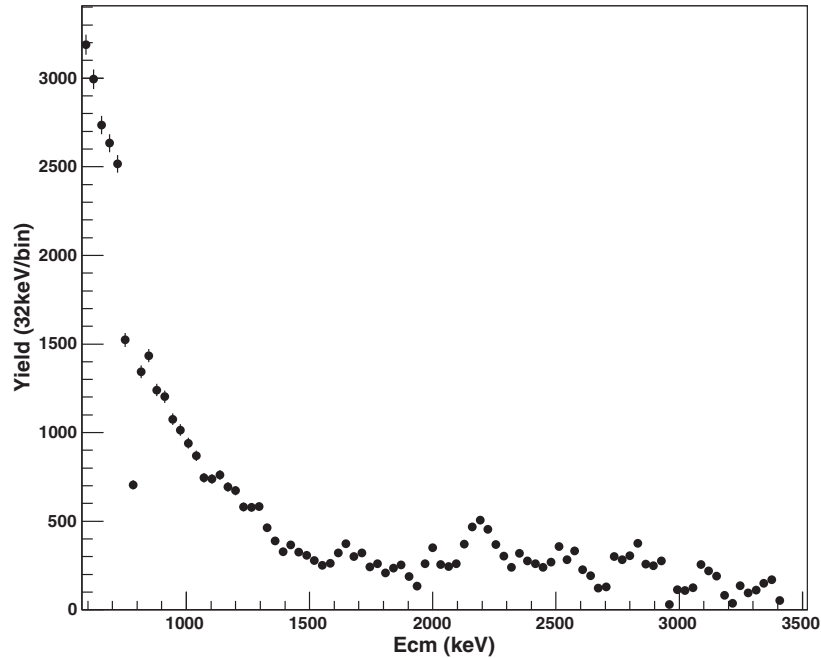


Figure 5.24: Proton spectrum after background subtraction.

## 5.6 Cross section from the yield spectrum of protons

In the proton spectrum (see figure 5.18), each data point represents a total yield of protons at the corresponding center-of-mass energy ( $E_{cm}$ ). The “total” means that the yield is the sum of all the protons with the same  $E_{cm}$  within the solid angle covered by the detector in use. Recall the experimental yield function in the thick target method, described in section 5.5.1

$$Y = I\sigma n\Delta x = I\sigma n \frac{\Delta E_b}{S} \quad (5.20)$$

where  $I$  is the total accumulated number of beam events,  $\sigma$  the scattering cross section into the solid angle covered by the detector in use,  $n$  the number density of the protons in the  $CH_2$  target, and  $S$  is the energy-dependent stopping power of the  $^{25}Al$  beam in the  $CH_2$  target.

Recall that from inverse kinematics the correlation between the beam energy  $E_b$  and the center-of-mass energy  $E_{cm}$ , that is,

$$E_{cm} = \frac{m}{M+m} E_{beam} \quad (5.21)$$

where  $M$  and  $m$  are the masses of the beam particle and proton respectively.

Using this equation, we can find the beam’s energy range  $\Delta E_b$  corresponding to the bin size  $\Delta E$  in the proton spectrum as

$$\Delta E_b = \left(1 + \frac{M}{m}\right) \Delta E \quad (5.22)$$

With this, the cross section can be obtained from the yield function as,

$$\sigma = \frac{Y \cdot S}{In\Delta E_b} = \frac{Y \cdot S}{In\Delta E} \cdot \frac{m}{M+m} \quad (5.23)$$

With the solid angle in the laboratory  $\Delta\Omega_{lab}$  calculated according to the ge-

ometry of the target-detector system, the experimental differential cross section in the laboratory will simply be [19],

$$\frac{d\sigma}{d\Omega_{lab}} = \frac{\sigma}{\Delta\Omega_{lab}} = \frac{Y \cdot S}{In\Delta E\Delta\Omega} \cdot \frac{m}{M+m} \quad (5.24)$$

Based on the fact that the integrals of the differential cross sections over the same solid angle in the laboratory frame and the center-of-mass frame are equal, that is,

$$\frac{d\sigma}{d\Omega_{lab}} \cdot d\Omega_{lab} = \frac{d\sigma}{d\Omega_{cm}} \cdot d\Omega_{cm} \quad (5.25)$$

and,

$$d\Omega_{lab} = \sin\theta_{lab}d\theta_{lab}d\phi \quad (5.26)$$

$$d\Omega_{cm} = \sin\theta_{cm}d\theta_{cm}d\phi \quad (5.27)$$

$$2\theta_{lab} + \theta_{cm} = 180^\circ \quad (5.28)$$

where  $\theta_{lab}$  and  $\theta_{cm}$  are the scattering angles in the laboratory frame and the center-of-mass frame, we find the differential cross sections in the center-of-mass frame as given by,

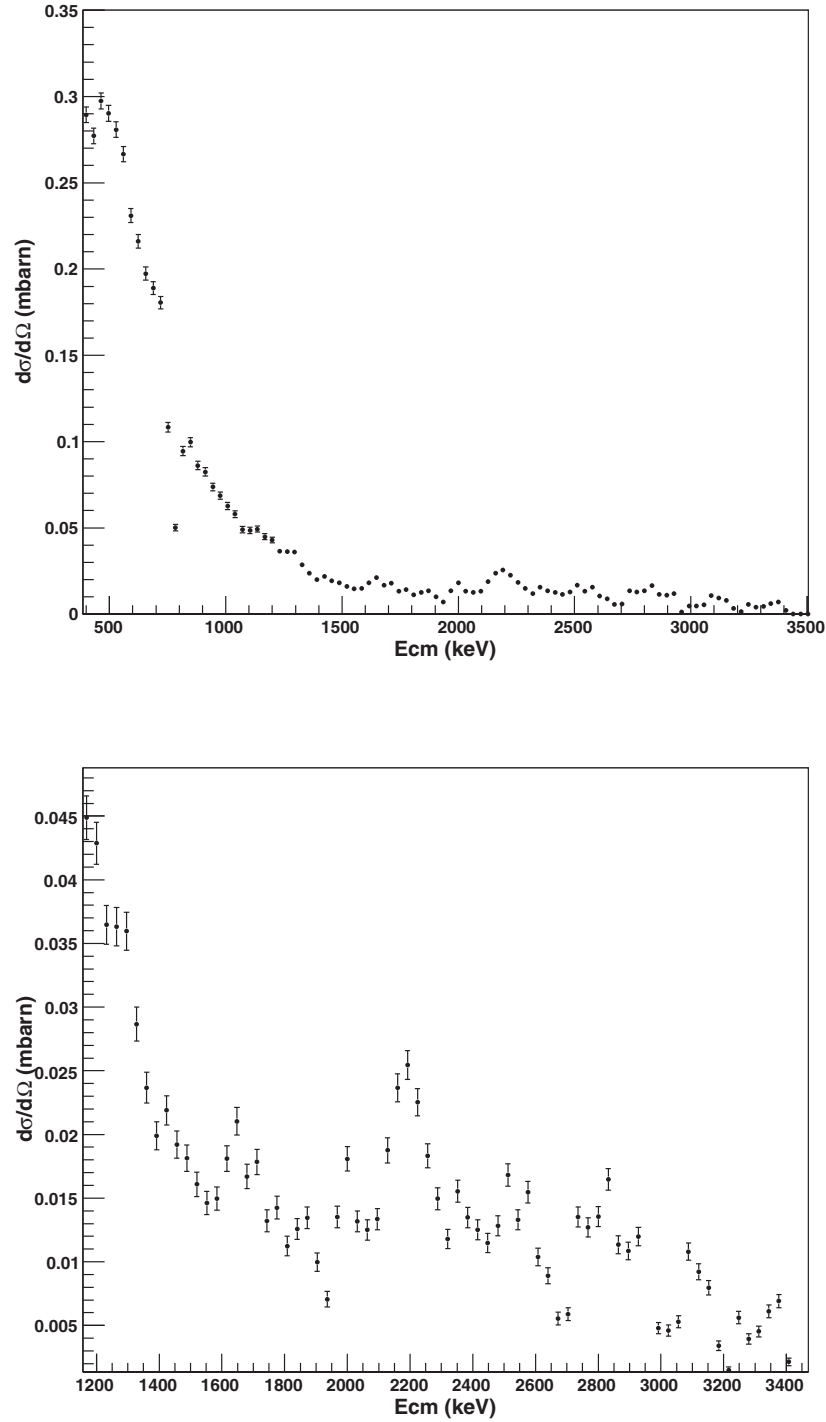


Figure 5.25: Excitation function at  $0^\circ$  in the center of mass frame after energy loss correction and background subtraction. The bottom one is the enlargement of this spectrum in the range of 1200 keV to 3400 keV.

$$\frac{d\sigma}{d\Omega_{cm}} = \frac{d\Omega_{lab}}{d\Omega_{cm}} \frac{d\sigma}{d\Omega_{lab}} = \frac{1}{4 \cos \theta_{lab}} \frac{d\sigma}{d\Omega_{lab}} = \frac{1}{4 \cos \theta_{lab}} \frac{Y \cdot S}{In\Delta E \Delta\Omega} \cdot \frac{m}{M + m} \quad (5.29)$$

It should be pointed out that, since the beam intensity was attenuated in the experiment, the actual total intensity  $I$  should be the total intensity extracted from the PPAC1-XY histogram times an attenuation factor, which in our case is 3000. Figures 5.25 to 5.27 are the final excitation functions at the three angles in the center of mass frame.

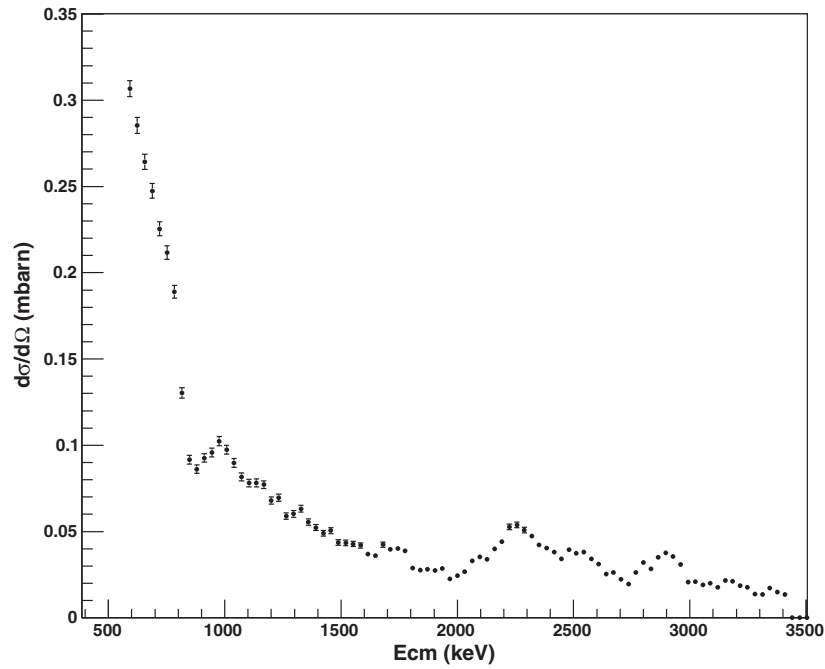


Figure 5.26: Excitation function at  $17^\circ$  in the center of mass frame after energy loss correction and background subtraction.

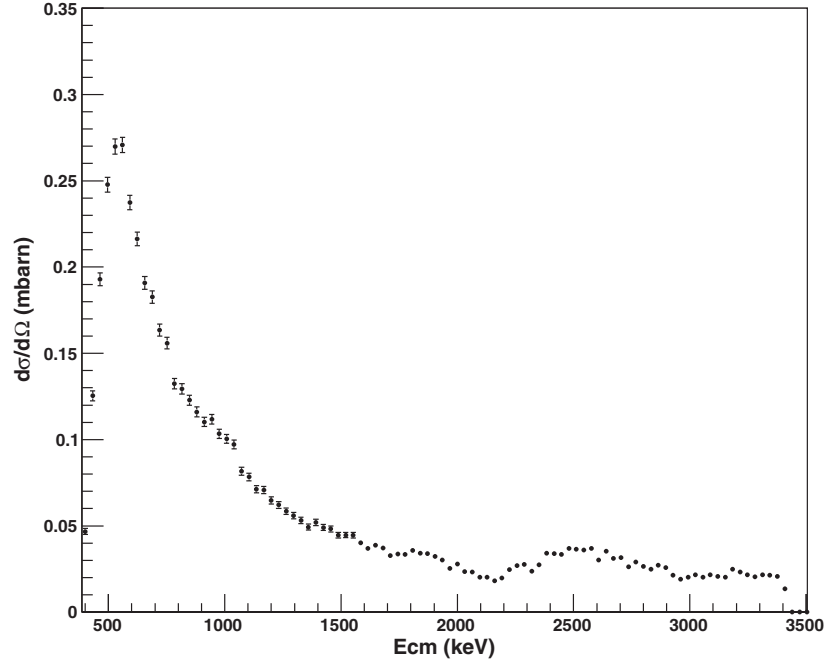


Figure 5.27: Excitation function at  $27^\circ$  in the center of mass frame after energy loss correction and background subtraction.

## 5.7 Breit-Wigner analysis

In this analysis, the Breit-Wigner formula will be used to fit for the proton resonances in the elastic scattering, using the  $\chi$ -estimation fitting procedure. We start with this simpler approach with the aim to extracting only the resonance energy  $E_R$  as preliminary results, which can then be used as input and confirmed in the R-Matrix analysis, no spin-parity assignments will be made, as these can also be done in the R-Matrix analysis. For the following fits, a s-wave ( $l = 0$ ) scattering is assumed, since it is the dominant contribution<sup>5</sup> to the cross section at the low center-of-mass energy in our experiment.

<sup>5</sup>The angular momentum satisfies:  $l = pR/\hbar = \sqrt{2\mu ER}/\hbar$ , where  $R$  is the range of interaction. Let  $b$  the impact parameter, then  $R < b$  and we find  $l < \sqrt{2\mu Eb}/\hbar$ . The lower the energy, the lower the  $l$  of the partial waves that can contribute to the cross-section.

### 5.7.1 Breit-Wigner formula for resonant elastic scattering

In the Breit-Wigner mechanism, the differential cross section for the elastic scattering in the center-of-mass frame is approximated by [66]

$$\frac{d\sigma}{d\Omega_{cm}} = |f_c|^2 + \omega |f_r|^2 + 2\omega \Re(f_c^* f_r) \quad (5.30)$$

where  $f_c$  and  $f_r$  refer to the Coulomb scattering and the single-channel nuclear resonant scattering of an s-wave (quantum number of the orbital angular momentum  $l=0$ ), respectively; the third term refers to the interference between the Coulomb scattering and the resonant scattering;  $\omega$  is the statistical factor  $= (2J+1)/[(2J_1+1)(2J_2+1)]$  with  $J$ ,  $J_1$  and  $J_2$  as the spins of the resonance, the beam nucleus and the target nucleus, respectively. The three terms are given by

$$\begin{aligned} |f_c|^2 &= \frac{1}{4k^2} \eta^2 \csc^4\left(\frac{\theta_{cm}}{2}\right) \\ |f_r|^2 &= \frac{1}{4k^2} \frac{\Gamma(E)^2}{(E - E_R)^2 + [\frac{1}{2}\Gamma(E)]^2} \\ 2\omega \Re(f_c^* f_r) &= \frac{1}{4k^2} \cdot 2\eta \csc^2\left(\frac{\theta_{cm}}{2}\right) \frac{\Gamma(E)}{(E - E_R)^2 + [\frac{1}{2}\Gamma(E)]^2} \\ &\quad \times \left[ (E - E_R) \cos \beta + \frac{1}{2}\Gamma(E) \sin \beta \right] \end{aligned} \quad (5.31)$$

where  $k$  is the wave number,  $\eta$  the Sommerfeld parameter,  $\theta_{cm}$  the scattering angle in the center-of-mass frame,  $\Gamma(E)$  the energy-dependent Breit-Wigner total width at the center-of-mass energy  $E_{cm} = E$ ,  $E_R$  the resonance energy and  $\beta$  the Coulomb phase. The parameters  $k$ ,  $\eta$ , and  $\beta$  are given by

$$\begin{aligned} k &= \frac{\sqrt{2\mu E}}{\hbar} \\ \eta &= \frac{Z_M Z_m e^2}{\hbar v} = C Z_M Z_m \sqrt{\frac{\mu}{E}} \\ \beta &= \eta \ln \sin^2\left(\frac{\theta_{cm}}{2}\right) \end{aligned} \quad (5.32)$$

where  $\mu$  is the reduced mass  $= mM/(m + M)$ ,  $v$  the relative velocity,  $Z_M$  and  $Z_m$  the charges of the two interacting particles, and  $2\pi C = 31.29$  when  $E$  is in keV and  $\mu$  is in amu .

The total width  $\Gamma_R$  of a resonance is related to the energy-dependent total width  $\Gamma(E)$  by

$$\Gamma(E) = \Gamma_R \exp(-2\pi\Delta\eta) \quad (5.33)$$

where  $\exp(-2\pi\Delta\eta)$  is referred to as the energy-dependent penetration factor,  $\Delta\eta = \eta - \eta_R$  where  $\eta_R$  is the value of  $\eta$  evaluated at the resonant energy  $E = E_R$ .

Figure 5.28 shows an example of the proton spectrum calculated using the Breit-Wigner formula with realistic values for the parameters.

### 5.7.2 Breit-Wigner fit for the experimental cross section

To fit the experimental cross section in the figure 5.25 (in the center-of-mass frame), firstly we need to rewrite the Breit-Wigner formula as follows [66],

$$\begin{aligned} \frac{d\sigma}{d\Omega_{cm}} = \frac{1}{4k^2} & \left[ A_1 \eta^2 \right. \\ & + A_2 \frac{\exp(-4\pi\Delta\eta)}{(E - A_4)^2 + A_5^2 \exp(-4\pi\Delta\eta)} \\ & \left. + A_3 \eta \exp(-2\pi\Delta\eta) \frac{(E - A_4) \cos \beta + A_5 \exp(-2\pi\Delta\eta) \sin \beta}{(E - A_4)^2 + A_5^2 \exp(-4\pi\Delta\eta)} \right] \end{aligned} \quad (5.34)$$

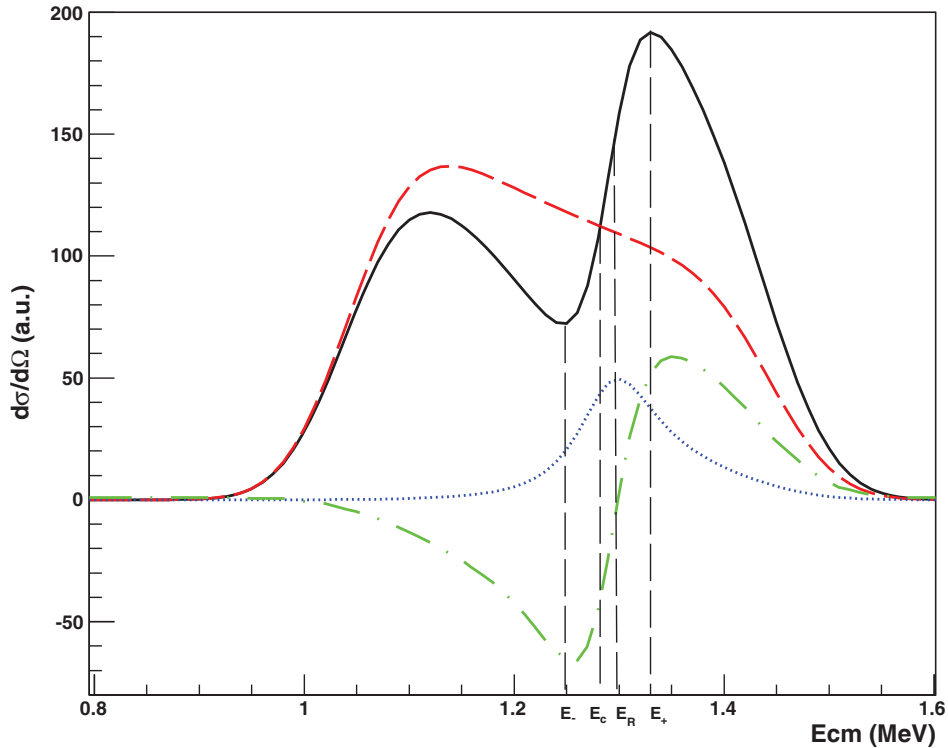


Figure 5.28: Calculated proton spectrum using the Breit-Wigner formula with realistic values of the parameters in the formula. The solid line is the total spectrum and it is divided into three components: a pure Coulomb scattering (dashed line), a pure resonant scattering (dotted line), and an interference between the former two scattering processes (dot-dashed line). This figure is adapted from reference [66]. Unless mentioned, all the subsequent proton spectra titled with the Breit-Wigner formula will have the same format. The  $E_+$  and  $E_-$  mark the two characteristic energies where the two extrema are located;  $E_c$  is the critical energy where there is only the Coulomb contribution, with the resonant and the interference parts canceling out;  $E_R$  marks where the pure resonance component peaks.

where the five parameters  $A_1$  to  $A_5$  have the following expressions (the correlation  $2\theta_{cm} + \theta_{lab} = \pi$  is used;  $N$  is a normalization factor):

$$\begin{aligned}
 A_1 &= \frac{N}{\cos^4 \theta_{lab}} \\
 A_2 &= N\omega\Gamma_R^2 \\
 A_3 &= \frac{2N\omega\Gamma_R}{\cos^2 \theta_{lab}} \\
 A_4 &= E_R \\
 A_5 &= \frac{\Gamma_R}{2}
 \end{aligned} \tag{5.35}$$

The five parameters are left free in the fitting procedure and the values of  $A_4$  and  $A_5$  deduced from the fitting will directly determine the resonant energy  $E_R$  and width  $\Gamma_R$ . Each single resonance in the spectrum of the differential cross section is fitted separately. In the fitting procedure, we have considered uncertainties due to the beam spread and the straggling inside the target which have been convoluted into the fit function when the fitting is in progress. Figures 5.29 and figure 5.30 show the fits for three different resonances with each component of the Breit-Wigner cross section shown as well. The fitting results are listed in table 5.2.

Not all peaks in the excitation function can be successfully fitted by the Breit-Wigner function due to the quality of the data, such as the statistics and the energy uncertainty. The fits shown here are for the two most prominent resonances in the spectrum at  $E_R=1634$  keV and  $E_R=2170$  keV as well as for a possible resonance around 3100 keV. We expect that more resonances will be able to extracted from the R-Matrix fit to the data, to be discussed in Section 5.8.

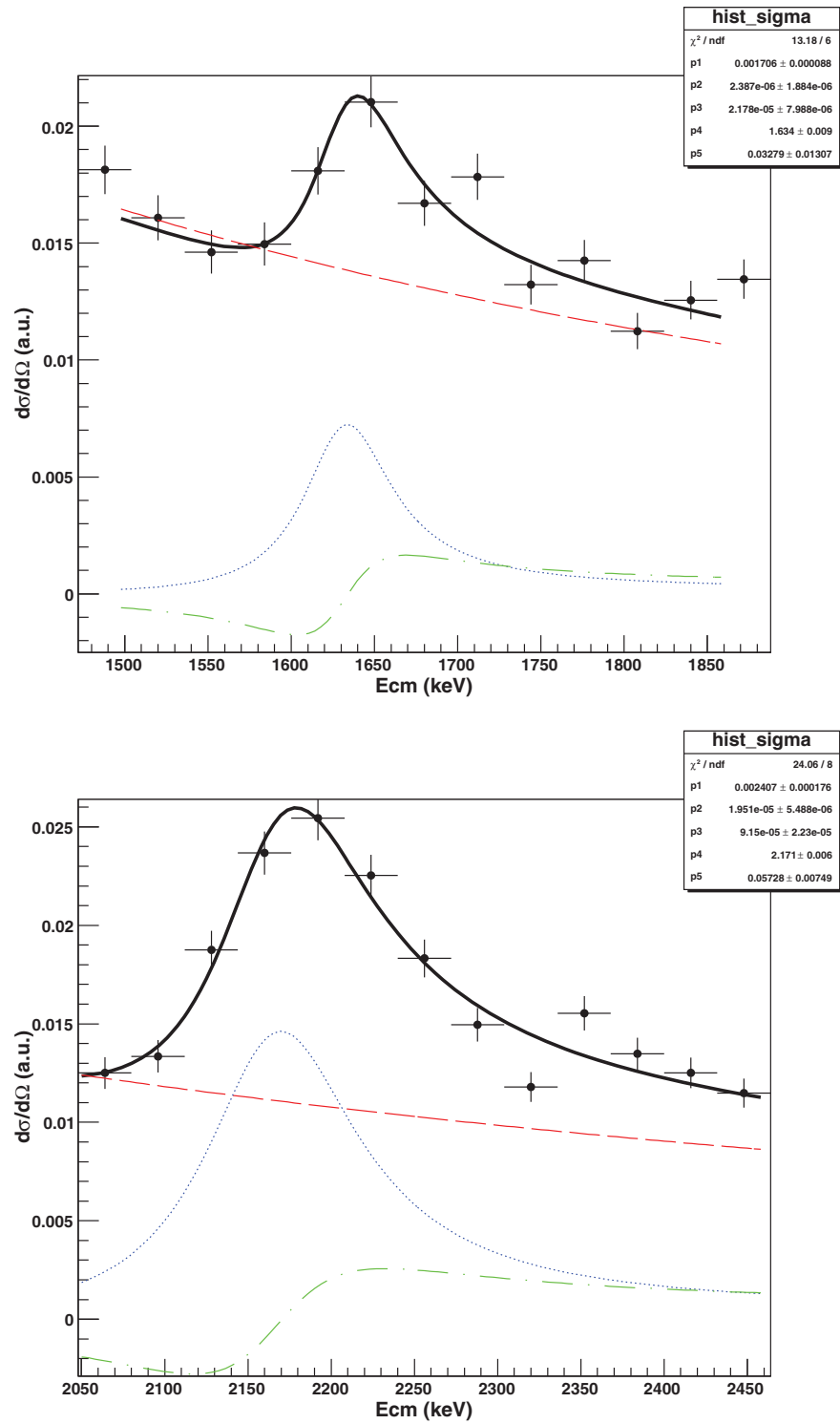


Figure 5.29: Breit-Wigner fits for the resonances at  $E_R=1.634$  MeV (top) and at  $E_R=2.170$  MeV (bottom).

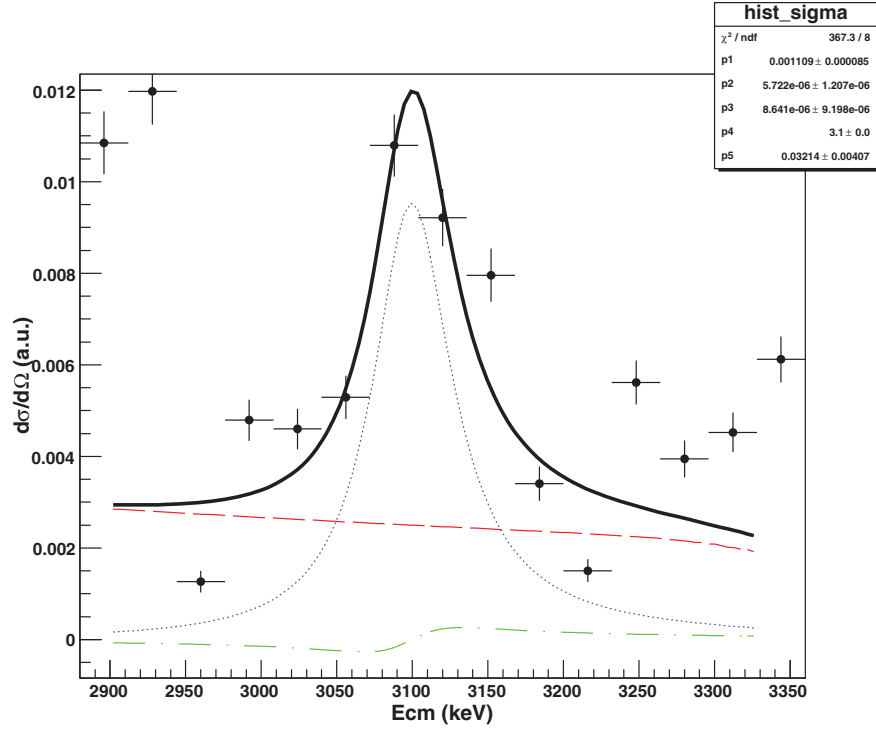


Figure 5.30: A Breit-Wigner fit for the resonance at  $E_R=3.100$  MeV.

Table 5.2: List of Breit-Wigner parameters of three resonances for the Breit-Wigner fits of the experimental differential cross sections.  $E_R$  and  $\Gamma_R$  are in units of keV. The  $\chi^2/d.o.f$  represents the chi-square per degree of freedom ( $d.o.f$ ) for each fit. The quoted uncertainties are directly from the fits.

$E_R(A_4)$	$\Gamma_R(2A_5)$	$\chi^2/d.o.f$
$1634 \pm 9$	$65 \pm 26$	2.19
$2171 \pm 6$	$115 \pm 15$	3.01
3100	$64 \pm 8$	45.9

## 5.8 R-Matrix analysis

In this section, an advanced data fitting using the R-matrix formalism will be described and used to extract physical parameters such as energy levels and proton widths. R-matrix theory [52] is now the standard and the best framework for describing resonant processes leading to compound nuclei in low-energy nuclear physics, because the nuclear parameters it yields, such as level energies and widths, are strongly tied to the physics of nuclear spectroscopy. It is the foundation of the Breit-Wigner formula described previously, which is an approximation of the resonant cross section only valid for a single-level and narrow resonance.

### 5.8.1 R-matrix formula for the cross section of compound nuclear scatterings and reactions

The general multi-channel multi-level formula for the differential cross section of any resonant process from an entrance channel  $\alpha$  to an exit channel  $\alpha'$  is given as follows [52]

$$\frac{d\sigma_{\alpha\alpha'}}{d\Omega_{\alpha'}} = [(2I_1 + 1)(2I_2 + 1)]^{-1} \sum_{ss'} (2s + 1) \frac{d\sigma_{\alpha s, \alpha' s'}}{d\Omega_{\alpha'}} \quad (5.36)$$

where  $I_1$  and  $I_2$  are the spins of the nuclei in the entrance channel — beam particle and target particle;  $\alpha$  and  $\alpha'$  symbolize the entrance and exit channels;  $s$  and  $s'$  are the channel spins of the entrance and the exit channels; the summation is over all of the partial differential cross sections of different combinations of channel spins  $s$  and  $s'$ ; and the partial differential cross section can be written as

$$\frac{d\sigma_{\alpha s, \alpha' s'}}{d\Omega_{\alpha'}} = \frac{\pi}{(2s + 1)k_{\alpha}^2} (CT + RT + IT) \quad (5.37)$$

where  $CT$ ,  $RT$ , and  $IT$  represent the three components of the resonant differential cross section — the Coulomb term, resonant term and interference term,

respectively. They are given by

$$\begin{aligned}
 CT &= (2s + 1) \left| \frac{1}{\sqrt{4\pi}} \eta_\alpha \sin^{-2} \left( \frac{\theta}{2} \right) \exp \left[ -2i\eta_\alpha \ln \sin \left( \frac{\theta}{2} \right) \right] \right|^2 \delta_{\alpha s, \alpha' s'} \\
 RT &= \frac{1}{\pi} \sum_L B_L P_L(\cos \theta) \\
 IT &= \frac{1}{\sqrt{4\pi}} \sum_{Jl} (2J + 1) 2\Re [i (T_{\alpha sl, \alpha' s' l'}^J)^* C_\alpha P_l(\cos \theta)] \delta_{\alpha s, \alpha' s'}
 \end{aligned} \tag{5.38}$$

where  $\theta$  is the scattering angle;  $\eta_\alpha$  is the Sommerfeld parameter; the summation integer  $L$  is over  $|l_i - l'_i|$ , where  $l$  is the quantum number of the orbital angular momentum of the scattering system.

The  $B_L$  coefficients are given by

$$B_L = \frac{1}{4} (-1)^{s-s'} \sum_{Jl} \bar{Z}(l'_1 J_1 l'_2 J_2, s' L) \bar{Z}(l_1 J_1 l_2 J_2, s L) T_{\alpha' s' l'_1, \alpha s l_1}^J (T_{\alpha' s' l'_2, \alpha s l_2}^J)^* \tag{5.39}$$

The  $\bar{Z}$  coefficients are related to the Racah coefficients,  $W$ , by

$$\begin{aligned}
 \bar{Z}(l_1 J_1 l_2 J_2, s L) &= (2l_1 + 1)^{\frac{1}{2}} (2l_2 + 1)^{\frac{1}{2}} (2J_1 + 1)^{\frac{1}{2}} (2J_2 + 1)^{\frac{1}{2}} \\
 &\times (l_1 l_2 00 | L 0) W(l_1 J_1 l_2 J_2, s L)
 \end{aligned} \tag{5.40}$$

where  $(l_1 l_2 00 | L 0)$  are the Clebsch-Gordan coefficients. These terms are also related to the  $Z$  coefficients of Blatt and Biedenharn [52] by

$$\bar{Z}(l_1 J_1 l_2 J_2, s L) = i^{l_1 - l_2 - L} Z(l_1 J_1 l_2 J_2, s L) \tag{5.41}$$

The transition matrix element  $T_{\alpha' s' l'_1, \alpha s l_1}^J$  is given by

$$T_{\alpha' s' l'_1, \alpha s l_1}^J = \delta_{\alpha' s' l'_1, \alpha s l_1} \exp(2i\omega_{\alpha' l'}) - U_{\alpha' s' l'_1, \alpha s l_1}^J \tag{5.42}$$

where  $U_{\alpha' s' l'_1, \alpha s l_1}^J$  is the collision matrix element given by

$$U_{\alpha' s' l'_1, \alpha s l_1}^J = \exp 2i(\omega_{\alpha l} + \delta_{\alpha s l}^J) \quad (5.43)$$

The  $\delta_{\alpha s l}^J$  here is the phase shift and it should be distinguished from the Kronecker delta symbol  $\delta_{\alpha s, \alpha' s'}$  used elsewhere.

The CT and IT terms, as we can see, will vanish if the entrance channel  $\alpha$  is different from the exit channel  $\alpha'$ ; that is for nuclear reactions or inelastic scattering. They are non-zero only when the entrance channel and exit channel are identical; elastic scattering is the only such case. For our experiment, it is safe to assume only one open channel (elastic scattering). Since s-wave is dominant in our case of low-energy scattering,  $l = 0$  is assumed also. Then the multi-channel multi-level R-matrix formula is reduced to the single-channel R-matrix formula and the three terms can be simplified as follows [67],

$$\begin{aligned} CT &= (2s + 1) \frac{1}{4\pi} \eta_\alpha^2 \sin^{-4} \left( \frac{\theta}{2} \right) \\ RT &= \frac{1}{4\pi} \sum_{Jl} (2J + 1) \{ [\cos 2\omega_l - \cos 2(\omega_l + \delta_l^J)]^2 \\ &\quad + [\sin 2\omega_l - \sin 2(\omega_l + \delta_l^J)]^2 \} P_l(\cos \theta) \\ IT &= \frac{1}{2\pi} \sum_{Jl} (2J + 1) \eta_\alpha \sin^{-2} \left( \frac{\theta}{2} \right) \\ &\quad \times \left\{ \sin \left( \eta_{2\alpha} \ln \sin \left( \frac{\theta}{2} \right) \right) [\cos 2\omega_l - \cos 2(\omega_l + \delta_l^J)] \right. \\ &\quad \left. + \cos \left( \eta_{2\alpha} \ln \sin \left( \frac{\theta}{2} \right) \right) [\sin 2\omega_l - \sin 2(\omega_l + \delta_l^J)] \right\} P_l(\cos \theta) \end{aligned} \quad (5.44)$$

where the Coulomb phase shift  $\omega_l$  and the total phase shift  $\delta_l^J$  are given by

$$\begin{aligned}\omega_l &= \sum_{n=1}^l \tan^{-1} \left( \frac{\eta_\alpha}{n} \right) \\ \delta_l^J &= \tan^{-1} \left( \frac{R_l P_l}{1 + R_l (B_l - S_l)} \right) - \phi_l\end{aligned}\tag{5.45}$$

where  $P_l$  is the penetrating function,  $S_l$  the shift function, and  $\phi_l$  the hard-sphere phase shift. They are given by

$$\begin{aligned}P_l &= \frac{kr_c}{F_l^2 + G_l^2} \\ S_l &= \frac{F_l F_l' + G_l G_l'}{F_l^2 + G_l^2} \\ \phi_l &= \tan^{-1} \frac{F_l}{G_l}\end{aligned}\tag{5.46}$$

where  $r_c$  is the channel radius; and  $F_l$  and  $G_l$  are the regular and irregular solutions of the radial wave equation and evaluated at  $r_c$ .

The  $B_l$  in the phase shift is the boundary condition number and  $R_l$  is the energy dependent R-matrix element, which is given for our simplified case by

$$R = \sum_{\lambda} \frac{\gamma^2}{E_{\lambda} - E}\tag{5.47}$$

where  $\gamma$  and  $E_{\lambda}$  are the reduced width and pole energy for a resonance, respectively. These are the two resonance parameters to be extracted from the fitting.

More details about the R-matrix theory and its derivations can be found in the R-Matrix theory section in Appendix B.

## 5.8.2 Boundary transformation from R-matrix parameters to physical parameters

The boundary condition parameter  $B_l$  [54, 55, 57, 56] is a constant specified to determine the boundary conditions satisfied by the eigenfunctions of resonant states

in R-matrix theory. This parameter can be arbitrarily chosen when making a fit to experimental data since the R-matrix differential cross section is independent of it. However, the R-matrix parameters of fitting results, such as level energies and level widths, do depend on the boundary condition parameters, which causes different sets of level energies and widths to be deduced for the same resonance from R-matrix fits with different choices of the boundary parameter  $B_l$ . Fortunately, these “formal” resonance parameters directly deduced from R-matrix fits and varying with the boundary parameter  $B_l$  are not the actual resonance energy and resonant width. They are called the pole energy and pole width of a resonance, defined and used only in the R-matrix differential cross section and also referred to as the formal resonance energy and width. When some specific boundary condition is satisfied for a specific value of  $B_l$ , the deduced formal parameters will match the actual resonance parameters. The latter are also referred to as the observed parameters (resonance energy and width) or the physical parameters. A number of methods have been developed to convert the formal R-matrix parameters to the actual physical parameters of a resonance by the so-called boundary transformation, based on the fact that different formal parameters of the same resonance are related by their boundary conditions.

Consider a transformation  $B_c \rightarrow B'_c$ ,  $E_\lambda \rightarrow E'_\lambda$  and  $\gamma_{\lambda c} \rightarrow \gamma'_{\lambda c}$ . Here we use the notation of  $B_c$  for the boundary condition parameter of channel  $c$ ;  $E_\lambda$  for the pole resonance energy of level  $\lambda$ ;  $\gamma_{\lambda c}$  for the reduced pole resonant width of channel  $c$  and level  $\lambda$ . The transformation is made by constructing the following real and symmetric matrix first

$$C_{\lambda\mu} = E_\lambda \delta_{\lambda\mu} - \sum_c (B'_c - B_c) \gamma_{\lambda c} \gamma_{\mu c} \quad (5.48)$$

Since  $\mathbf{C}$  is real and symmetric, it can be diagonalized by an orthogonal matrix  $\mathbf{K}$  such that

$$\mathbf{KCK}^T = \mathbf{D} \quad (5.49)$$

where  $\mathbf{D}$  is a diagonal matrix. Its diagonal elements are the eigenvalues of the matrix  $\mathbf{C}$ , i.e.,

$$D_{\lambda\mu} = D_{\lambda}\delta_{\lambda\mu} \quad (5.50)$$

Then we can get

$$\begin{aligned} E'_{\lambda} &= D_{\lambda} \\ \gamma'_c &= \mathbf{K}\gamma_c \end{aligned} \quad (5.51)$$

where  $\gamma_c$  is a vector of reduced widths of all levels at channel  $c$ .

For the special case of a single channel and single level, the transformation is reduced to,

$$\begin{aligned} E'_{\lambda} &= E_{\lambda} - \gamma_{\lambda}^2(B' - B) \\ \gamma' &= \gamma_{\lambda} \end{aligned} \quad (5.52)$$

where the notion of channel is ignored.

In the actual transformation process, the boundary condition parameter is always set equal to the energy dependent shift function  $S_c(E_{\lambda})$ , evaluated at the initial input of the pole energy  $E_{\lambda}$  for each resonance, and then applied to the fit function to deduce the new  $E_{\lambda}$  from the best fit. This fit is compared with the old one to check if they match within the uncertainty range. We can also do it in a simple way as described above by using the boundary transformation matrix to calculate the new  $E_{\lambda}$  from the original  $E_{\lambda}$  without repeating the fit. If they do not match, the process is repeated (either by iterating the R-Matrix fit or by iterating the calculation with the boundary transformation matrix) with the newly obtained  $E_{\lambda}$  as the input for the pole energy and the boundary condition parameter evaluated at this input energy. This iteration of the boundary transformation ends when the pole energy converges, and the final pole energy and reduced width have been transformed to correspond to the physical parameters of the resonance

in use. The physical resonance width can then be calculated from the observed or physical reduced width  $\gamma_{\lambda c}$  with the relation

$$\Gamma_{\lambda c}^o = \frac{\Gamma_{\lambda c}(E_\lambda)}{1 + \sum_c \gamma_{\lambda c}^2 \left(\frac{dS_c}{dE}\right)_{E_\lambda}} = \frac{2P_c(E_\lambda)\gamma_{\lambda c}^2}{1 + \sum_c \gamma_{\lambda c}^2 \left(\frac{dS_c}{dE}\right)_{E_\lambda}} \quad (5.53)$$

where  $\Gamma_{\lambda c}(E_\lambda) = 2P_c(E_\lambda)\gamma_{\lambda c}^2$  is called the formal resonance width.

### 5.8.3 R-matrix fit for the experimental cross section

The R-matrix fit was performed using a code based on R. E. Azuma's R-matrix subroutine [68, 69]. Besides the data file, an input parameter file is required when performing the fit, which includes reaction information such as the reaction channel radius ( $r_c = 1.2(A_1 + A_2)^{1/3}$ ), the possible combinations of quantum numbers, spin-parities assigned to the resonances to be fitted, and so on. An example of this input file can be found in the Appendix C. The final spin-parities for the resonances are determined when the best fit with these combinations of spin-parities in the input file has the smallest  $\chi^2$  of all the best fits with different nuclear inputs; while the resonance energies and widths are directly extracted from the fitting and the boundary transformation procedure.

Table 5.3: List of all possible combinations of channel spin  $S$ , relative orbital angular momentum  $l$ , and spin-parity  $J^\pi$  of the compound nucleus.

$l$	$S$	$J^\pi$
0	2	$2^+$
	3	$3^+$
1	2	$1^-$
		$2^-$
		$3^-$
	3	$2^-$
		$3^-$
		$4^-$
2	2	$0^+$
		$1^+$
		$2^+$
		$3^+$
		$4^+$
	3	$1^+$
		$2^+$
		$3^+$
		$4^+$
		$5^+$

The possible combinations of the nuclear quantum numbers are determined according to the conservation of total angular momentum before and after the scattering. The ground state of the  $^{25}\text{Al}$  nucleus has a spin-parity of  $\frac{5}{2}^+$  and the proton has  $\frac{1}{2}^+$ , which couple together to give the channel spin  $S = \frac{5}{2} \oplus \frac{1}{2} = 2$  or 3. The spin-parity  $J^\pi$  of the compound nucleus is determined by  $J = l \oplus S$  and  $\pi_f = \pi_i \pi_p (-1)^l$ , where  $l$  is the relative orbital quantum number of the proton with respect to the heavy reacting nucleus, and  $\pi_i$ ,  $\pi_f$  and  $\pi_p$  represent the parities of the initial heavy reacting nucleus, the final compound nucleus and the proton, respectively. Table 5.3 lists all the possible combinations of  $S$ ,  $l$  and  $J^\pi$  with  $l$  up to 2 (d-wave).

According to scattering theory, the s-wave ( $l=0$ ) scattering is dominant and the higher partial waves make less or negligible contributions to the scattering. Since at low energies ( $E_R < 1.2$  MeV) the Coulomb scattering is dominant, no apparent resonance signature was observed in the excitation function. At the high energy region ( $E_R > 2.5$  MeV) in the excitation function, there are several resonance-alike signatures and they are very difficult to be identified and fitted due to the poor statistics. Therefore, we only fit the three prominent resonances in the range from the 1424 keV to 2484 keV by s-wave scattering, as shown in figure 5.31. This corresponds to the level range of 6.942 MeV to 8.002 MeV, which is within the Gamow window at the temperatures of astrophysical interest (supernovae temperatures  $T_9$ , see figure 1.6 in Chapter. 1). The uncertainty ( $\sim 15\%$ , systematic and statistical) for the data is adopted from reference [77] considering the similar experimental set-up. In all previous histograms, the uncertainties are the statistical ones calculated by default in the ROOT program using the standard deviation of a Poisson distribution <sup>6</sup>,  $\sigma_N = \sqrt{N}$ , where  $N$  is the total yield at each energy (or energy bin in the histogram).

Table 5.4 lists the resonance parameters for the three resonances extracted from

---

<sup>6</sup>The counts  $N$  at any energy fluctuates around its mean value  $\lambda$ , following a Poisson probability distribution with its mean  $\langle N \rangle = \lambda$  and its standard deviation  $\sigma_N = \sqrt{\lambda}$ . In the experimental histogram, the measured value for  $N$  at any energy is taken as its expected value at that energy, that is  $\lambda = N$  and  $\sigma_N = \sqrt{N}$ .

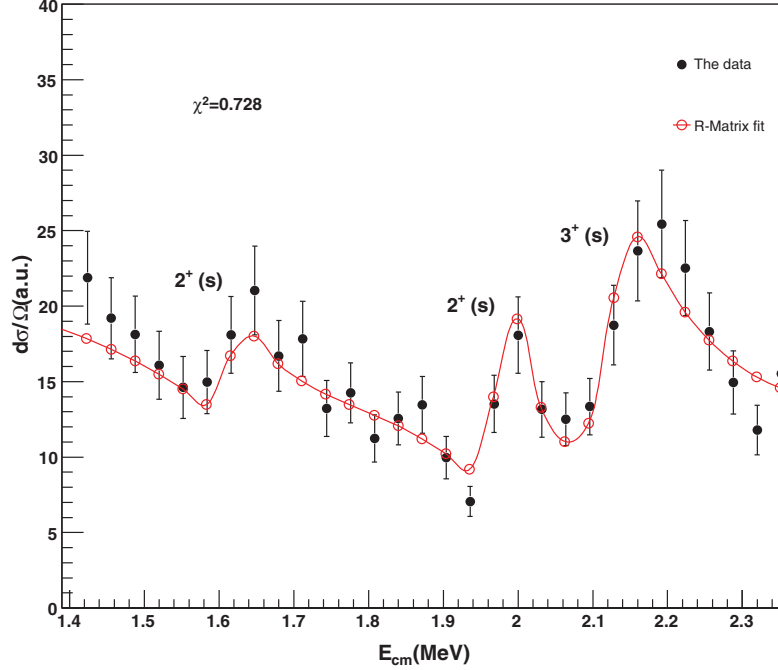


Figure 5.31: An R-Matrix fit for the three resonances at  $E_R \sim 1.62$  MeV, 1.97 MeV and 2.13 MeV, with s-wave ( $l=0$ ) scattering for all and  $J^\pi=2^+$ ,  $2^+$  and  $3^+$ , respectively.

the R-Matrix fit to the data.

We also tried fitting the data using other spin-parity assignments for the three resonances and found that with  $J^\pi=2^+$  for both of the first two resonances, the data is fitted the best, with the smallest  $\chi^2$  compared with fits with other spin-parity assignments. Therefore,  $J^\pi=2^+$  is assigned to the first two resonances. These two resonances correspond to the energy levels of  $E_x=7.156$  MeV and 7.498 MeV in  $^{26}Si$  in previous study with ( $^3He,n$ ) [11] and (p,t) [9, 12] reactions and our spin-parity assignments agree with their studies using a DWBA analysis. But there is a controversy between our assignment for the third resonance ( $E_x=7.647$  MeV) and their assignments for the excited state at  $E_x=7.687$  MeV, if they correspond to the same energy level in  $^{26}Si$ . Our best fit to the data as shown in figure 5.31 indicates that the third resonance can be best described by s-wave scattering with  $J^\pi=3^+$ ,

Table 5.4: List of parameters of resonances from a R-Matrix fit to the three resonances in the experimental differential cross section in the energy range 1424 keV — 2484 keV. The pole energy  $E_\lambda$ , the resonance energy  $E_R$  and the level energy  $E_x$  are in units of MeV and the resonance width  $\Gamma_R$  is in units of keV. The proton separation energy (or proton threshold energy) is  $S_p=5.518$  MeV. The uncertainties quoted are directly from the fits.

$J^\pi$	$E_\lambda$	$E_R$	$E_x$	$\Gamma_R$
$2^+$	1.882(45)	1.617(76)	7.135(76)	43(10)
$2^+$	2.018(11)	1.977(15)	7.495(15)	10(3)
$3^+$	2.251(19)	2.129(28)	7.647(28)	89(15)

while from their DWBA analysis this state has  $J^\pi=3^-$ , which would correspond to a p-wave scattering in our experiment. By assigning  $J^\pi=3^-$  to the third resonance, we got a best R-Matrix fit as shown in figure 5.32, not as good as the one with the  $J^\pi=3^+$  assignment.

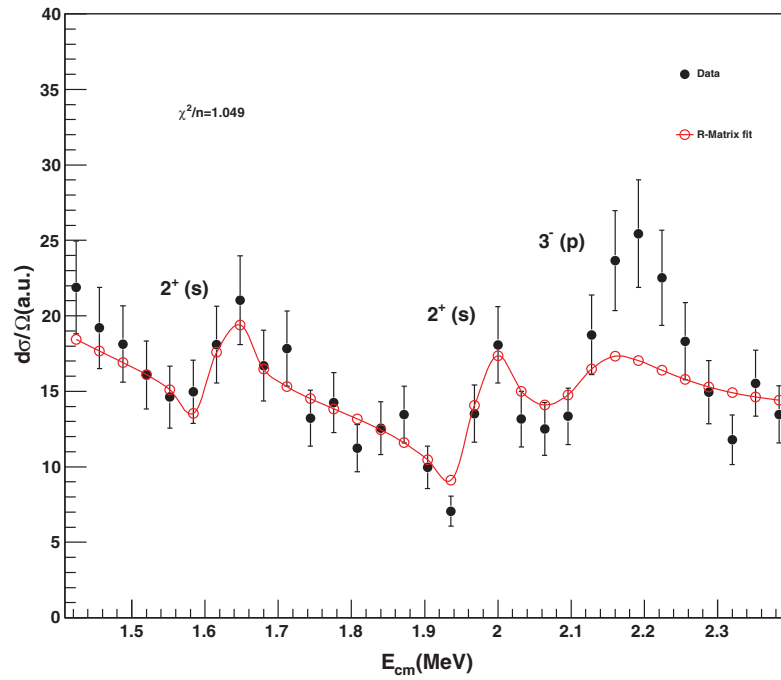


Figure 5.32: A R-Matrix fit for the three resonances at  $E_R \sim 1.62$  MeV, 1.97 MeV and 2.13 MeV, with s-wave ( $l=0$ ) scattering for the first two and p-wave scattering ( $l=1$ ) for the third resonance ( $J^\pi=2^+$ ,  $2^+$  and  $3^-$ , respectively).

# Chapter 6

## Thermonuclear Reaction Rate of $^{25}\text{Al}(p, \gamma)^{26}\text{Si}$ in Explosive Stellar Environments

In this chapter, I will first give the general derivation and theoretical background of the thermonuclear reaction rate. Following that, our new reaction rate of  $^{25}\text{Al}(p, \gamma)^{26}\text{Si}$  will be presented, calculated based on our new results on the structure of  $^{26}\text{Si}$ , already described in Chapter 4 and Chapter 5.

### 6.1 General derivation of the thermonuclear reaction rate

Based on the qualitative description of thermonuclear reactions in Chapter 1, we can derive the rate of the thermonuclear reaction<sup>1</sup>. Consider thermonuclear reactions in a stellar gas between particles of type  $A$  with number density  $n_A$  and mass  $m_A$ , and particles of type  $B$  with number density  $n_B$  and mass  $m_B$  (both number densities in units of particles per cubic centimeter). Assume that the cross section

---

<sup>1</sup>Here we only discuss the general 2-body charged-particle-induced nuclear reactions. For neutron-induced reactions and more details about the derivation, refer to references [1, 2]

of this reaction is  $\sigma(v)$ , which depends only on the relative velocity between two reacting particles because according to the theory of nuclear reactions [71], the energy dependence of the cross section for a nuclear reaction only involves the total kinetic energy ( $E_{cm}$ ) of the two interacting particles in the center-of-mass system with

$$E_{cm} = \frac{1}{2}\mu v^2 \quad (6.1)$$

where  $\mu = m_A m_B / (m_A + m_B)$  is the reduced mass of the two reacting particles and  $v$  is their relative velocity.

Since in the center-of-mass frame it does not matter which reacting particle should be treated as the projectile or ejectile, we let particle  $A$  be the projectile and  $v$  its velocity relative to particle  $B$ . The nuclear cross section is defined as the probability<sup>2</sup> that a reaction occurs when a reacting particle bombards a target containing only one target particle per unit area in the plane perpendicular to the incident direction of the projectile. In a volume  $V_{gas}$  of gas mentioned above, the total number of particles  $A$  is  $n_A V_{gas}$  and they will encounter, in a time interval  $\Delta t$ , a number  $n_B v \delta t$  of particles  $B$  per unit area along the trajectory of particle  $A$ . Then we can simply write the reaction rate (number of reactions per second per unit volume) as

$$r = \frac{n_A V_{gas} \times n_B v \Delta t \times \sigma(v)}{V_{gas} \Delta t} = n_A n_B v \sigma(v) \quad (6.2)$$

In the stellar gas, the relative velocity  $v$  varies over a wide range and its probability follows the Maxwell-Boltzmann (MB) distribution, given by

$$\phi(v) = 4\pi v^2 \left( \frac{\mu}{2\pi kT} \right)^{3/2} \exp\left( -\frac{\mu v^2}{2kT} \right) \quad (6.3)$$

---

<sup>2</sup>This can be regarded as the total number of reactions even though it is a fraction for this definition; as a matter of fact, in a nuclear reaction, there are a large number of projectiles and a large number of target particles per unit area in the target surface, which will result in an integer number of reactions.

with

$$\int_0^{\infty} \phi(v) dv = 1 \quad (6.4)$$

So the actual reaction rate  $r$  should be an average weighted by the MB probability function above<sup>3</sup>

$$r = n_A n_B \langle \sigma v \rangle \quad (6.5)$$

where  $\langle \sigma v \rangle$  is the weighted average and represents the reaction rate per particle pair, given by

$$\begin{aligned} \langle \sigma v \rangle &= \int_0^{\infty} \phi(v) \sigma(v) dv \\ &= 4\pi \left( \frac{\mu}{2\pi kT} \right)^{3/2} \int_0^{\infty} v^3 \sigma(v) \exp\left(-\frac{\mu v^2}{2kT}\right) dv \\ &= \left( \frac{8}{\pi\mu} \right)^{1/2} \frac{1}{(kT)^{3/2}} \int_0^{\infty} E \sigma(E) \exp\left(-\frac{E}{kT}\right) dE \end{aligned} \quad (6.6)$$

where  $E = E_{cm} = \frac{1}{2}\mu v^2$  is the total kinetic energy in the center-of-mass frame and the transformation from  $v$  to  $E$  has been used;  $k=8.6173 \times 10^{-5}$  eV/K is the Boltzmann constant;  $T$  is the temperature. One thing that should be pointed out is that, besides the relative velocity, the center-of-mass velocity  $V$  of the two reacting particles also follows a BW distribution and its integral should also be included in the calculation of  $\langle \sigma v \rangle$ ; however, since the motion of the center-of-mass is independent of the relative motion and the nuclear cross section depends only on the relative velocity, the integral over  $V$  is integrated out to be unity.

Until now we have not elaborated on the physics of the nuclear reaction, specifically, the energy dependence of the cross section  $\sigma(E)$ . First, let us introduce in the cross section the astrophysical S-factor  $S(E)$ , which contains all the nuclear

<sup>3</sup>This is for nonidentical reacting particles ; for identical particles, a factor of  $\frac{1}{2}$  should be introduced. So the general form is  $r = \frac{n_A n_B \langle \sigma v \rangle}{1 + \delta_{AB}}$ , where  $\delta_{AB}$  is the Kronecker symbol evaluated as 1 when  $A = B$ , and 0 when otherwise.

physics effects, and varies relatively flatly with energy, leaving most of the energy dependence of  $r$  outside the  $S$ -factor, i.e.,

$$\sigma(E) = \frac{1}{E} \exp(-2\pi\eta) S(E) \quad (6.7)$$

where  $P = \exp(-2\pi\eta)$  is so called Gamow factor which represents the energy dependent penetrability of the charged particle through the Coulomb barrier. The Gamow factor is an approximation for low energies far below the height of Coulomb barrier which is precisely the region where the energies in stellar thermonuclear reactions mostly occur. The  $S$ -factor is very useful in that due to its smooth variation with energies, it can be used for extrapolating the cross section data of stellar nuclear reactions to very low stellar energies that we can not reach in laboratories.

The quantity  $\eta$  is the Sommerfeld parameter, defined as

$$2\pi\eta = 2\pi \frac{Z_A Z_B e^2}{\hbar v} = 2\pi \frac{Z_A Z_B e^2}{\hbar} \sqrt{\frac{\mu}{2E}} = 31.29 Z_A Z_B \sqrt{\frac{\mu}{E}} \quad (6.8)$$

where  $Z_A, Z_B$  are the charges of the two reacting particles, respectively; the numerical form is obtained when  $E$  is in units of keV and  $\mu$  in amu (atomic mass unit).

Inserting the above expressions into the form of  $\langle\sigma v\rangle$ , we find

$$\begin{aligned} \langle\sigma v\rangle &= \left(\frac{8}{\pi\mu}\right)^{1/2} \frac{1}{(kT)^{3/2}} \int_0^\infty S(E) \exp\left(-\frac{E}{kT}\right) \exp\left(-\frac{2\pi Z_A Z_B e^2}{\hbar} \sqrt{\frac{\mu}{E}}\right) dE \\ &= \left(\frac{8}{\pi\mu}\right)^{1/2} \frac{1}{(kT)^{3/2}} \int_0^\infty S(E) \exp\left(-\frac{E}{kT} - \sqrt{\frac{E_G}{E}}\right) dE \end{aligned} \quad (6.9)$$

where

$$E_G = \left(-\frac{2\pi Z_A Z_B e^2}{\hbar}\right)^2 \frac{\mu}{2} \quad (6.10)$$

is called the Gamow energy.

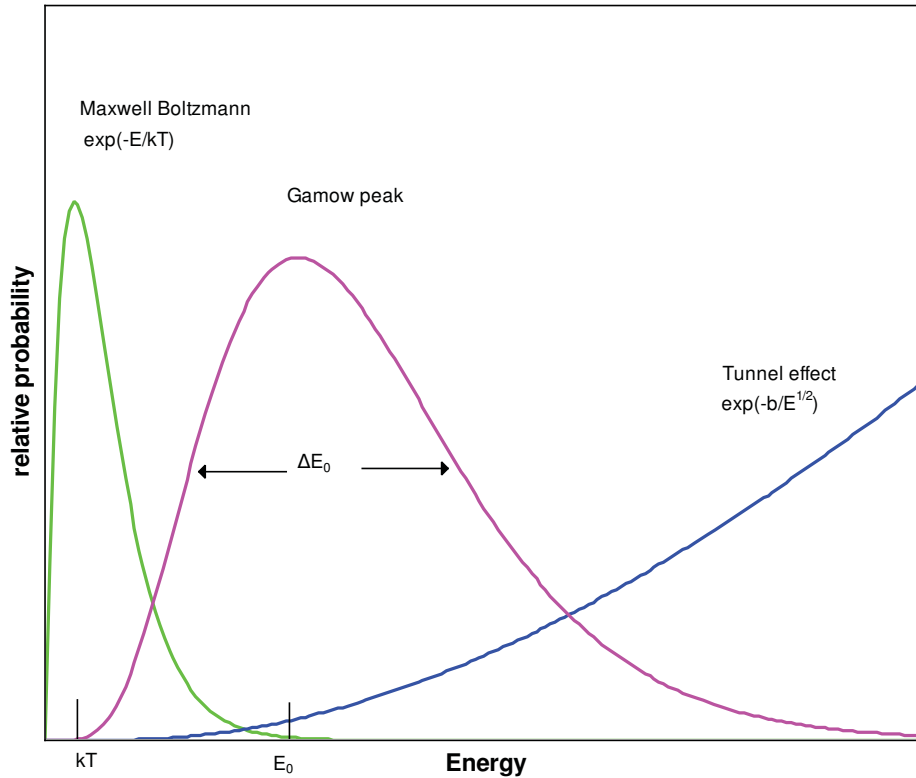


Figure 6.1: The probability distribution of a thermonuclear reaction with respect to the stellar energy  $E$  in the stellar environment at a given temperature  $T$ . It results from the combined effect of the Maxwell-Boltzmann distribution for the stellar gas and the energy dependent penetrability function arising from the Coulomb barrier in the cross section of the thermonuclear reaction. Instead of peaking at the maximum of the MB distribution, the combined distribution has its so-called Gamow peak at an energy  $E_0$ , representing the most probable energy for which the thermonuclear reaction will happen.

By plotting the MB probability function giving the term  $\exp(-E/kT)$ , the penetrability factor giving the term  $\exp(-\sqrt{E_G/E})$  and their product on the same graph (figure 6.1), we find that, even though the MB distribution indicates that at a temperature  $T$  the most probable energy a particle in a stellar gas can have is  $E = kT$ , the energy at which a reaction will most probably take place at  $T$  is shifted up to a new peak energy  $E_0$ , due to the rapid increase of the Coulomb

penetrability with energy. The new energy  $E_0$  is called the Gamow peak energy and is derived by setting the first derivative of the product of the exponential terms in Eq. 6.9 with respect to  $E$  to zero. We obtain

$$E_0 = \left( \frac{kT\sqrt{E_G}}{2} \right)^{2/3} = 1.22(Z_A^2 Z_B^2 \frac{m_A m_B}{m_A + m_B} T_6^2)^{1/3} \quad (6.11)$$

where the numerical form has the unit of keV, and  $T_6$  is in units of  $10^6$  Kelvin. From here we can also rewrite  $E_G$  as  $E_G = \left( \frac{2E_0}{kT} \right)^2 E_0$ .

In figure 6.1, the width of the Gamow peak is the energy window where a thermonuclear reaction predominantly takes place at a given temperature  $T$ . We call this energy window the Gamow window for this reaction at the temperature  $T$ . To find the Gamow window analytically, we approximate the product of the exponential terms in the integrand of  $\langle \sigma v \rangle$  by a Gaussian function with the same peak energy and peak height as the Gamow peak, and the same curvature at  $E = E_0$  (that is the second derivative at  $E_0$ ). The width of the Gamow peak  $\Delta$  is approximated as the width of the Gaussian peak at its  $1/e$  peak height. Then we can write the product of the exponential terms in Eq. 6.9 as,

$$\exp\left(-\frac{E}{kT} - \sqrt{\frac{E_G}{E}}\right) \approx \exp\left(-\frac{3E_0}{kT}\right) \exp\left[-\left(\frac{E - E_0}{\Delta/2}\right)^2\right] \quad (6.12)$$

By matching the second derivatives at both sides of Eq. 6.12 at  $E_0$ , we find the effective width  $\Delta$  of the Gamow peak in units of keV as

$$\Delta = \frac{4}{\sqrt{3}} \sqrt{E_0 kT} = 0.749 \left( Z_A^2 Z_B^2 \frac{m_A m_B}{m_A + M_B} \right)^{1/6} \quad (6.13)$$

So the corresponding Gamow window should be the energy window from  $E_0 - \Delta/2$  to  $E_0 + \Delta/2$ .

After discussing the concepts above, now we can continue with the derivation of the thermonuclear reaction rate. The form of  $\langle \sigma v \rangle$  we have derived so far is for the general case of charged-particle-induced reactions. Actually all these reactions

can be categorized into two cases: non-resonant direct nuclear reactions and resonant nuclear reactions. All nuclear reactions not forming a resonant compound nucleus can be regarded as non-resonant direct nuclear reactions, such as direct capture reactions, stripping reactions, pickup reactions and Coulomb excitation. In the calculation of the stellar nuclear reaction rate, the non-resonant reactions is specified as the direct capture reaction, i.e., proton capture reactions and neutron capture reactions. The previous statement that the  $S$ -factor varies smoothly with energy applies to the non-resonant nuclear reactions but not to the resonant reactions. A resonant nuclear reaction arises from the formation of the compound nucleus of the two reacting nuclei and the rearrangement in the compound nucleus of the contributing nucleons. When the reaction energy  $E$  (the sum of the total energy in the CM frame and the reaction Q-value) matches a level energy in the compound nucleus, this level will be strongly populated and a peak at this energy in the plot of the  $S$ -factor or cross section versus energy will show up instead of the smooth variation for non-resonant reactions. The total reaction rate includes the contributions from both the non-resonant and resonant reactions, and their rates can be derived separately and simplified differently according to their different natures.

### 6.1.1 Non-resonant reaction rate formalism

As discussed in the previous subsection, the  $S$ -factor for non-resonant reactions varies smoothly with energy and thus it can be regarded to first order as a constant, i.e.,  $S(E) = S(E_0) = \text{constant}$ . Then we can take the  $S(E)$  out of the integrand in Eq. 6.9 and replace the Gamow peak function with the Gaussian function of the

previous subsection. We find

$$\begin{aligned}
\langle \sigma v \rangle_{dc} &= \left( \frac{8}{\pi \mu} \right)^{1/2} \frac{1}{(kT)^{3/2}} S(E_0) \int_0^\infty \exp \left( -\frac{E}{kT} - \sqrt{\frac{E_G}{E}} \right) dE \\
&\approx \left( \frac{8}{\pi \mu} \right)^{1/2} \frac{1}{(kT)^{3/2}} S(E_0) \int_0^\infty \exp \left( -\frac{3E_0}{kT} \right) \exp \left[ -\left( \frac{E - E_0}{\Delta/2} \right)^2 \right] dE \\
&= \left( \frac{8}{\pi \mu} \right)^{1/2} \frac{1}{(kT)^{3/2}} S(E_0) \exp \left( -\frac{3E_0}{kT} \right) \frac{\sqrt{\pi} \Delta}{2} \\
&= \left( \frac{2}{\mu} \right)^{1/2} \frac{\Delta}{(kT)^{3/2}} S(E_0) \exp \left( -\frac{3E_0}{kT} \right)
\end{aligned} \tag{6.14}$$

In this approximation, we use a symmetric Gaussian function to replace the asymmetric Gamow peak function. Therefore, to find a more accurate reaction rate, we need to make corrections to the rate derived above for the replacement of the peak function and the assumption of constant S-factor, since for many non-resonant reactions the S-factor is not constant but varies with energy  $E$ . Due to its slow variation with energy, the energy-dependent non-resonant S-factor can be expanded in a Taylor series, with respect to  $E = 0$  for ease of computation,

$$S(E) = S(0) + S'(0)E + \frac{1}{2}S''(0)E^2 + \dots \tag{6.15}$$

where the prime represents the derivative with respect to  $E$ . We insert this expression for  $S(E)$  into the general formula (Eq. 6.9) for the non-resonant reaction rate and we get a sum of integrals, with each corresponding to one term in the expansion of  $S(E)$ . With this, we have made some corrections to the energy dependence of the S-factor. We then find that we can replace the Gamow peak function by a Gaussian function in each integral, as described previously, since the quantity related to the S-factor is a constant and can be taken out of each integrand. Finally we arrive at the formula for the non-resonant nuclear reaction rate, with an

effective constant  $S$ -factor  $S_{eff}(E_0)$  [1] in place of the  $S(E_0)$  in Eq.(6.14),

$$S_{eff}(E_0) = S(0) \left[ 1 + \frac{5}{12\tau} + \frac{S'(0)}{S(0)} \left( E_0 + \frac{35}{36}kT \right) + \frac{1}{2} \frac{S''(0)}{S_0} \left( E_0^2 + \frac{89}{36}E_0kT \right) \right] \quad (6.16)$$

where  $\tau \equiv 3E_0/kT$ ; the first two terms in the square bracket arise from the correction for the asymmetry of the Gamow peak, while the remaining terms account for the variation of the  $S$ -factor with energy; the coefficients of  $S(0)$ ,  $S'(0)$ ,  $S''(0)$  are in units of MeV·b, b, and b/MeV, respectively, and their values can be either obtained from fits to the experimental cross-section data; or deduced from its definition in Eq. 6.7 using the cross section from shell model calculations, with the  $S(0)$  regarded as the averaged value of the calculated  $S(E)$  over the energy range of interest [72, 74, 75].

The formula of the reaction rate (per reacting particle pair) can be numerically written as [1]

$$\begin{aligned} \langle \sigma v \rangle_{dc} = & 1.30 \times 10^{-14} \left( Z_A Z_B \frac{m_A + m_B}{m_A m_B} \right)^{1/3} T_9^{-2/3} S_{eff} \\ & \times \exp \left[ -4.2487 \left( \frac{Z_A^2 Z_B^2}{T_9} \frac{m_A + m_B}{m_A m_B} \right)^{1/3} \right] \quad [cm^3 s^{-1}] \end{aligned} \quad (6.17)$$

Sample calculations can be found in Ref. [76, 77]. At low stellar temperatures, non-resonant thermonuclear reactions are the dominant contributors to the reaction rate but as the temperature increases, the resonant reactions compete with the non-resonant ones and finally become the dominant contributors.

### 6.1.2 Resonant reaction rate formalism

In non-resonant nuclear reactions (direct capture), the light energetic projectile, e.g., the proton, interacts only with the surface of the heavy target nucleus and goes directly to form the final nucleus with the simultaneously emission of  $\gamma$ -rays. The

configuration of the nucleons inside the target nucleus remains unchanged. This is a single-step and direct process in which no intermediate state is formed, and it can occur at all center-of-mass energies. In contrast to this single-step and direct process, the resonant reaction is a two-step process in which the projectile travels into the target nucleus and shares its kinetic energy among all the nucleons in the target nucleus, rearranging their configuration according to the level structure of the final nucleus. As a result, an intermediate state of the compound nucleus of two reacting particles is formed when the total kinetic energy  $E_{cm}$  of the two reacting particles plus the Q-value or threshold energy, which the compound nucleus can absorb completely to rearrange and excite the internal nucleons, matches the level energy  $E_x$  of an excited state in the compound nucleus. The excited compound nucleus will then subsequently de-excite to low-lying states by  $\gamma$ -decays or break up into other nuclei by particle decays. The  $E_{cm}$  for which this happens is therefore called the resonant energy  $E_R$ . The relation between the energy of the excited state  $E_x$  in the compound nucleus and the resonant energy  $E_R$  is given by

$$E_x = E_R + Q \quad (6.18)$$

Since  $E_R > 0$ , we can see that  $E_x > Q$  and the resonant reaction can thus only populate excited states in the compound nucleus with energies above the particle threshold.

The energies ( $E_{cm}$ ) of astrophysical interest are in the low energy range: for example, the Gamow peak energy of the  $^{25}\text{Al} + p$  capture reaction is  $E_0 \approx 1$  MeV at temperatures characteristic of supernova explosions of about  $T_9 = 1$  ( $T_9$  is the astrophysical notation of temperatures, equivalent to GK.). The level density in this low energy range is relatively small which means that the resonant states do not overlap significantly and can be regarded as isolated and narrow resonant states (by “narrow” we mean the total width of the resonant state  $\Gamma \ll E_R$ ). With this assumption, the cross-section for populating a resonant state can be described

by the single-level Breit-Wigner cross section, which is given by

$$\sigma_{BW} = \frac{\lambda^2}{4\pi} \frac{2J+1}{(2J_A+1)(2J_B+1)} (1 + \delta_{AB}) \frac{\Gamma_1 \Gamma_2}{(E - E_R)^2 + \Gamma^2/4} \quad (6.19)$$

where  $\lambda$  is the de Broglie wavelength, given by  $\lambda = 2\pi/k = 2\pi\hbar/\sqrt{2\mu E}$  with  $k = p/\hbar = \sqrt{2\mu E}/\hbar$  as the wave number;  $J_A$ ,  $J_B$ , and  $J$  are the spins of the two particles in the entrance channel<sup>4</sup> and the compound nucleus, respectively. They are related through angular momentum conservation by  $S \oplus l = J$  with the channel spin  $S = J_A \oplus J_B$  and with  $l$  representing the relative orbital angular momentum of the two reacting particles; the factor  $(1 + \delta_{AB})$  accounts for the fact that the two reacting particles are identical.  $E$  is the total energy in the center-of-mass frame, and  $\Gamma_1$ ,  $\Gamma_2$  are the partial widths of a resonant state for the entrance channel and exit channel and  $\Gamma = \Gamma_1 + \Gamma_2$  is the total resonance width. The ratio of the partial resonance width to the total width is the probability of the formation of the compound nucleus by the corresponding channel. The total width of a state is a quantity related to its mean life time  $\tau$  by the uncertainty principle  $\Gamma t \approx \hbar$ , through which the total width can be also obtained using a half-life measurement.

After replacing the cross section reaction rate formula (Eq. 6.6) with the  $\sigma_{BW}$  and realizing that the Maxwell-Boltzmann distribution function,  $E \exp(-E/kT)$  is almost constant over the total width of a narrow and isolated resonance, as shown in figure 6.2 and therefore can be evaluated at  $E = E_R$  and taken out of the integral, we can arrive at a simplified formula for the reaction rate for a narrow

---

<sup>4</sup>“Channel” refers to the way the compound nucleus is formed or decays, with the entrance channel for formation and the exit channel for decay.

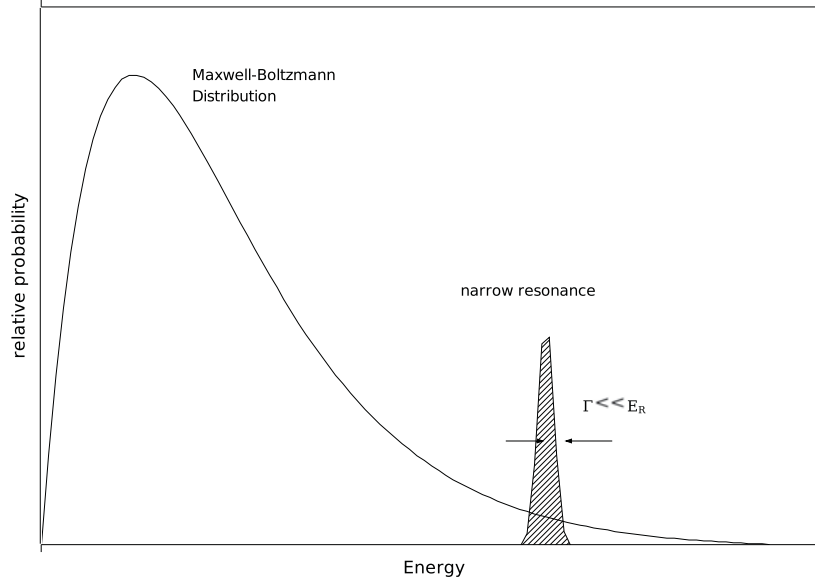


Figure 6.2: The Maxwell-Boltzmann distribution and a narrow resonance.

resonance

$$\begin{aligned}
 \langle \sigma v \rangle &= \left( \frac{8}{\pi \mu} \right)^{1/2} \frac{1}{(kT)^{3/2}} \int_0^\infty E \sigma_{BW}(E) \exp\left(-\frac{E}{kT}\right) dE \\
 &= \frac{\sqrt{2\pi} \hbar^2^{3/2}}{(\mu kT)} \omega \int_0^\infty \frac{\Gamma_1 \Gamma_2}{(E - E_R)^2 + \Gamma^2/4} \exp\left(-\frac{E}{kT}\right) dE \\
 &= \frac{\sqrt{2\pi} \hbar^2^{3/2}}{(\mu kT)} \exp\left(-\frac{E_R}{kT}\right) \omega \Gamma_1 \Gamma_2 \\
 &\quad \times \int_0^\infty \frac{1}{(E - E_R)^2 + \Gamma^2/4} \exp\left(-\frac{E}{kT}\right) dE \\
 &= \left( \frac{2\pi}{(\mu kT)} \right)^{3/2} \hbar^2 \exp\left(-\frac{E_R}{kT}\right) \omega \frac{\Gamma_1 \Gamma_2}{\Gamma} \\
 &= \left( \frac{2\pi}{(\mu kT)} \right)^{3/2} \hbar^2 \exp\left(-\frac{E_R}{kT}\right) \omega \gamma
 \end{aligned} \tag{6.20}$$

where  $\omega$  is the statistical factor, given by

$$\omega = \frac{2J + 1}{(2J_A + 1)(2J_B + 1)} (1 + \delta_{AB}) \tag{6.21}$$

and the  $\gamma = \Gamma_1\Gamma_2/\Gamma$ . The product of  $\omega$  and  $\gamma$  is called the strength of a resonance,

$$\omega\gamma = \frac{2J+1}{(2J_A+1)(2J_B+1)}(1+\delta_{AB})\frac{\Gamma_1\Gamma_2}{\Gamma_1+\Gamma_2} \quad (6.22)$$

For the capture reactions  $((p, \gamma)$  or  $(\alpha, \gamma)$ ) in the stellar environment, the entrance channel is the proton capture by the heavy nucleus and the exit channel is the  $\gamma$ -decay of the intermediate compound nucleus. The entrance and exit widths will be denoted by  $\Gamma_p$  and  $\Gamma_\gamma$ . If the compound state is in a higher resonant state, it is more probable for a proton inside the compound nucleus to penetrate the Coulomb barrier (proton decay) than for the nucleus to decay by  $\gamma$ -transitions ( $\gamma$ -decay). For this case,  $\Gamma_p \gg \Gamma_\gamma$  and  $\Gamma \approx \Gamma_p$  and the resonance strength is thus reduced to  $\omega\gamma \approx \omega\Gamma_\gamma$ , depending only on the  $\gamma$  width. For low-lying resonant states just above proton threshold, the compound nucleus is relatively stable for proton decay compared with  $\gamma$ -decay. This implies that  $\Gamma_p \ll \Gamma_\gamma$  and  $\Gamma \approx \Gamma_\gamma$  and the resonance strength is thus reduced to  $\omega\gamma \approx \omega\Gamma_p$ , depending only on the proton width. It is recalled from the non-resonant reaction rate formalism that only reactions with the total energy  $E$  in the center-of-mass frame within the Gamow window contributes greatly to the reaction rate. This also applies to the resonant reaction rate in that only the resonant states within the Gamow window at a stellar temperature contributes greatly to the reaction rate. Contributions from resonances beyond the Gamow window can be neglected.

If there are many resonances within the Gamow window, the total reaction rate is just the sum of the rate for each individual resonance, and it is written as

$$\begin{aligned} \langle \sigma v \rangle_{res} &= \left( \frac{2\pi}{\mu kT} \right)^{3/2} \hbar^2 \sum_i (\omega\gamma)_i \exp\left(-\frac{E_{R_i}}{kT}\right) \\ &= 2.557 \times 10^{-19} \left( \frac{m_A m_B}{m_A + m_B} T_9 \right)^{-3/2} \sum_i (\omega\gamma)_i \exp\left(-\frac{11.605 E_{R_i}}{T_9}\right) [cm^3 s^{-1}] \end{aligned} \quad (6.23)$$

where the masses are in units of amu, the resonance strength  $\omega\gamma$  in eV and the resonant energy  $E_R$  in MeV.

## 6.2 Stellar reaction rate of the $^{25}\text{Al}(p,\gamma)^{26}\text{Si}$ reaction

We calculated the new reaction rate of the  $^{25}\text{Al}(p,\gamma)^{26}\text{Si}$  reaction using our results of energy levels or resonances in  $^{26}\text{Si}$  from the two experiments. The contribution from the direct capture reaction will not be recalculated in this thesis and is taken directly from Ref. [75]. The resonant contribution from each resonance is calculated using Eq. 6.23 given in the last section. Since only energy levels above the proton threshold energy can be populated in this reaction, only these levels contribute to the reaction rate. From the NSCL experiment, two levels at  $E_x=5.909$  MeV ( $3^+$ ) and  $6.446$  keV ( $3^+$ ) are adopted for the rate calculation, while from the elastic scattering experiment at CRIB, three resonances at  $E_x=7.135$  MeV ( $2^+$ ),  $7.495$  MeV ( $2^+$ ) and  $7.647$  MeV ( $3^+$ ) are used as inputs for the calculation. We will also include the levels from previous work [10, 11, 12] in our calculations.

For the level at  $E_x=5.909$  MeV ( $E_R=E_x-5.518=391$  keV,  $3^+$ ), the value of the  $\gamma$  width ( $\Gamma_\gamma=0.033$  eV) is taken from Ref. [75] while the proton width  $\Gamma_p$  is taken as the average of the value ( $\Gamma_p=2.3$  keV) in Ref. [12] and that ( $\Gamma_p=2.68$  keV) in Ref. [11]. Therefore, the resonance strength is calculated to be  $\omega\gamma=1.9\times 10^{-2}$  eV. In the rate calculation, the  $E_R$  will be taken as the average value (394 keV) of that (396 keV) from Ref. [12] and our result (391 keV), as well as for the level energy (averaged  $E_x=5.912$  MeV).

For the level at  $E_x=6.446$  MeV ( $E_R=928$  keV,  $4^+$ ), there are no experimental information on  $\Gamma_\gamma$  and  $\Gamma_p$ . Instead,  $\Gamma_\gamma$  for this state can be calculated or estimated using the experimental transition information of the mirror state in  $^{26}\text{Mg}$  at  $E_x=6.622$  MeV. The  $\gamma$  width of a state associated with a  $M1$  or  $E2$  transition is calculated by

$$\Gamma_\gamma(M1) = \frac{B(M1)}{B^W(M1)} \Gamma_\gamma^W(M1) [eV] \quad (6.24)$$

$$\Gamma_\gamma(E2) = \frac{B(E2)}{B^W(E2)} \Gamma_\gamma^W(E2) [eV] \quad (6.25)$$

where  $B(M1)$  and  $B(E2)$  are transition probabilities from measurements or calculations in Weisskopf-units;  $B^W(M1)$  and  $B^W(E2)$  are the corresponding Weisskopf units;  $\Gamma_\gamma^W(M1)$  and  $\Gamma_\gamma^W(E2)$  are the Weisskopf-unit  $\gamma$  widths for  $M1$  and  $E2$  transitions (in eV), respectively. They are given by [78],

$$\Gamma_\gamma^W(M1) = 2.1 \times 10^{-2} E_\gamma^3 [eV] \quad (6.26)$$

$$\Gamma_\gamma^W(E2) = 4.9 \times 10^{-8} A^{4/3} E_\gamma^5 [eV] \quad (6.27)$$

where  $E_\gamma$  is in units of MeV. Using the  $B(M1)$  and  $B(E2)$  of transitions from the  $E_x=6.622$  MeV state in  $^{26}\text{Mg}$  [80], we calculated  $\Gamma_\gamma=1.7 \times 10^{-2}$  eV. The proton width  $\Gamma_p$  can be either taken from its mirror state in  $^{26}\text{Mg}$  or calculated based on the fact that it is proportional to the penetrability through the Coulomb barrier [1]. Therefore we can find  $\Gamma_p$  by scaling the proton width of a known resonance by the ratio of the penetrability (if the reduced widths are the same), that is

$$\Gamma_p(E_{R1}) = \frac{P(E_{R1})}{P(E_{R2})} \Gamma_p(E_{R2}). \quad (6.28)$$

The penetrability is given by

$$P(E) = \exp(-2\pi\eta) = \exp\left(-31.29 \times Z_A Z_B \sqrt{\frac{1}{E} \frac{m_A m_B}{m_A + m_B}}\right) \quad (6.29)$$

where  $m$  is the mass of the reacting nucleus and  $Z$  is the proton number;  $A$  and  $B$  refer to the  $^{25}\text{Al}$  and proton respectively.

From Ref. [79], the  $E_x=6.622$  MeV state in  $^{26}\text{Mg}$  has a half life of  $T_{1/2}=19$  fs. According to uncertainty principle, the total width of this level can be calculated to be  $\Gamma=0.693h/T_{1/2}=0.15$  eV. Assuming the total width  $\Gamma = \Gamma_p + \Gamma_\gamma$ , the proton

width is then calculated to be  $\Gamma_p=0.13$  eV and the resonance strength

$$\begin{aligned}\omega\gamma &= \frac{2J+1}{(2J_A+1)(2J_B+1)} \times \frac{\Gamma_\gamma\Gamma_p}{(\Gamma_\gamma+\Gamma_p)} \\ &= \frac{(2 \times 4 + 1)}{(2 \times \frac{5}{2} + 1)(2 \times \frac{1}{2} + 1)} \times \frac{0.017 \times 0.13}{(0.017 + 0.13)} \\ &= 1.13 \times 10^{-2} \text{ eV}.\end{aligned}$$

We take this as the resonance strength for the  $E_x=6.446$  MeV level in the reaction rate calculation.

For the three levels at  $E_x=7.135$  MeV ( $E_R=1617$  keV,  $2^+$ ), at  $E_x=7.495$  MeV ( $E_R=1977$  keV,  $2^+$ ) and at  $E_x=7.647$  MeV ( $E_R=2129$  keV,  $3^+$ ), no transition information is available from their mirror states in  $^{26}\text{Mg}$ . But we can still obtain an upper limit of the  $\gamma$  width  $\Gamma_\gamma$  for each level by calculating the Weisskopf-unit  $\gamma$  widths of single-particle transitions. They are calculated as  $E2$ ,  $E2$  and  $M3$  transitions<sup>5</sup>, respectively and we get,

$$\Gamma_\gamma(E2; E_\gamma = 7.135 \text{ MeV}) = 4.9 \times 10^{-8} A^{4/3} \times 7.135^5 = 6.98 \times 10^{-2} \text{ [eV]}$$

$$\Gamma_\gamma(E2; E_\gamma = 7.495 \text{ MeV}) = 4.9 \times 10^{-8} A^{4/3} \times 7.495^5 = 8.93 \times 10^{-2} \text{ [eV]}$$

$$\Gamma_\gamma(M3; E_\gamma = 7.647 \text{ MeV}) = 6.8 \times 10^{-15} A^{4/3} \times 7.647^7 = 8.01 \times 10^{-7} \text{ [eV]}$$

Combining these  $\gamma$  widths with their proton widths extracted from the R-Matrix fit for the three resonances,  $\Gamma_p=42$  keV, 10 keV and 89 keV, respectively, we find that  $\Gamma_\gamma \ll \Gamma_p$  at these high energy levels. Therefore, we can simplify the resonance strength as  $\omega\gamma = \omega \times \Gamma_\gamma\Gamma_p/(\Gamma_\gamma + \Gamma_p) \simeq \omega\Gamma_\gamma$ , as discussed earlier. The resonance strength of these levels are calculated to be  $\omega\gamma = 2.91 \times 10^{-2}$  eV,  $3.72 \times 10^{-2}$  eV and  $4.67 \times 10^{-7}$  eV.

Table 6.1 lists all the input parameter values to be used in the calculation of the  $^{25}\text{Al}(p, \gamma)^{26}\text{Si}$  reaction rate.

The calculated reaction rates within the temperature range of astrophysical

---

<sup>5</sup>For an  $M3$  transition, the Weisskopf-unit  $\gamma$  width is calculated by  $\Gamma_\gamma^W(M3) = 6.8 \times 10^{-15} A^{4/3} E_\gamma^7 \text{ [eV]}$

Table 6.1: List of parameters to be used in the calculations of the  $^{25}\text{Al}(p, \gamma)^{26}\text{Si}$  stellar reaction rate. The parameters of the last two resonances are adopted from Ref [12].

$J^\pi$	$E_x(\text{MeV})$	$E_R(\text{keV})$	$\Gamma_p$ (eV)	$\Gamma_\gamma(\text{eV})$	$\omega\gamma(\text{eV})$
3 <sup>+</sup>	5.912	394	2.49	$3.30 \times 10^{-2}$	$1.90 \times 10^{-2}$
4 <sup>+</sup>	6.446	928	0.13	$1.70 \times 10^{-2}$	$1.13 \times 10^{-2}$
2 <sup>+</sup>	7.135	1617	$4.3 \times 10^4$	$6.98 \times 10^{-2}$	$2.91 \times 10^{-2}$
2 <sup>+</sup>	7.495	1977	$1.0 \times 10^4$	$8.93 \times 10^{-2}$	$3.72 \times 10^{-2}$
3 <sup>+</sup>	7.647	2129	$8.9 \times 10^4$	$8.01 \times 10^{-7}$	$4.67 \times 10^{-7}$
1 <sup>+</sup>	5.673	155	$1.3 \times 10^{-9}$	$1.10 \times 10^{-1}$	$3.25 \times 10^{-10}$
0 <sup>+</sup>	5.946	428	$1.9 \times 10^{-2}$	$8.80 \times 10^{-3}$	$5.01 \times 10^{-4}$

interest (see Chapter 1), are listed in Table 6.3, where  $E_{R1}$ ,  $E_{R2}$ ,  $E_{R3}$ ,  $E_{R4}$ , and  $E_{R5}$  refer to the first five resonances in Table 6.1 in that order, and  $E_{R6}$  and  $E_{R7}$  are the resonances found in other studies [10, 11]. The rates from the resonances  $E_{R6}=155$  keV ( $J^\pi = 1^+$ ) and  $E_{R7}=428$  keV ( $J^\pi = 0^+$ ) are directly adopted from Ref [12]. The plots of these rates are shown in figure 6.3 and 6.4. From the plots, we can see that the high energy resonances ( $E_{R3}$ ,  $E_{R4}$ ,  $E_{R5}$ ) only make significant contributions to the rate at high temperature ( $T_9 > 1$ ) and their contributions at low temperatures are negligible compared with non-resonant contribution (DC), due to their much weak resonance strengths and high resonance energies (far away from Gamow windows at low temperatures). The  $E_{R1}$  starts to make significant contribution at  $T_9 > 0.1$  and then becomes dominant. The rate from  $E_{R2}$  can be neglected at  $T_9 < 0.7$  but is comparable with the DC rate at higher temperatures. The DC contribution is dominant over the resonances at low temperatures ( $T_9 < 0.1$ ). As the temperature increases, its percentage in the total reaction rate keeps dropping until a minimum is reached at  $T_9 \sim 0.5$ , although its absolute contribution keeps increasing. After that, its percentage in the total rate increases slowly as the temperature increases but it will no longer dominate.

A comparison of the total rates from our calculations to the rates in Ref. [12] and in Ref. [11] is shown in figure 6.5. Agreement can be seen between our calculations and rates from Bardayan *et al.* [12] except that there is a slight difference within the temperature range 0.15 — 0.3 GK, arising mainly from the difference of the energies of the resonance at  $E_R=394$  keV used in the calculations. The discrepancy between our calculations and the rate from Parpottas *et al.* [11] at lower temperatures ( $T < 0.2$  GK) is thought to be possibly due to their calculation mistake of the resonance strength for the resonance at  $E_R=428$  keV, which is calculated to be  $\omega\gamma=5.01\times 10^{-4}$  eV in this study.

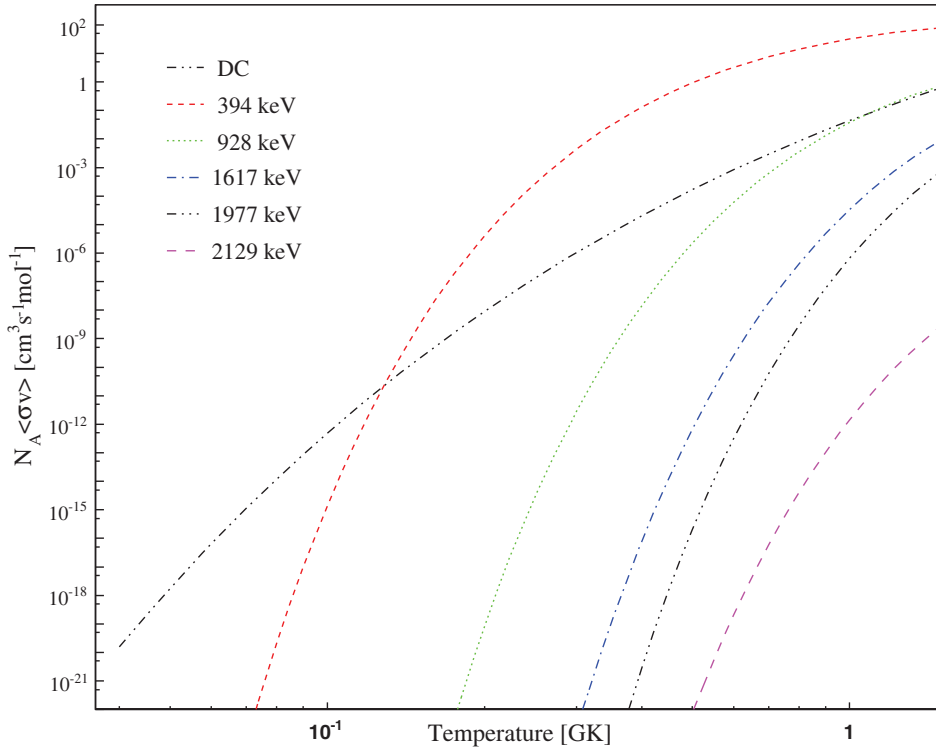


Figure 6.3: The  $^{25}\text{Al}(p,\gamma)^{26}\text{Si}$  reaction rates from direct capture reaction and individual resonances from our study.

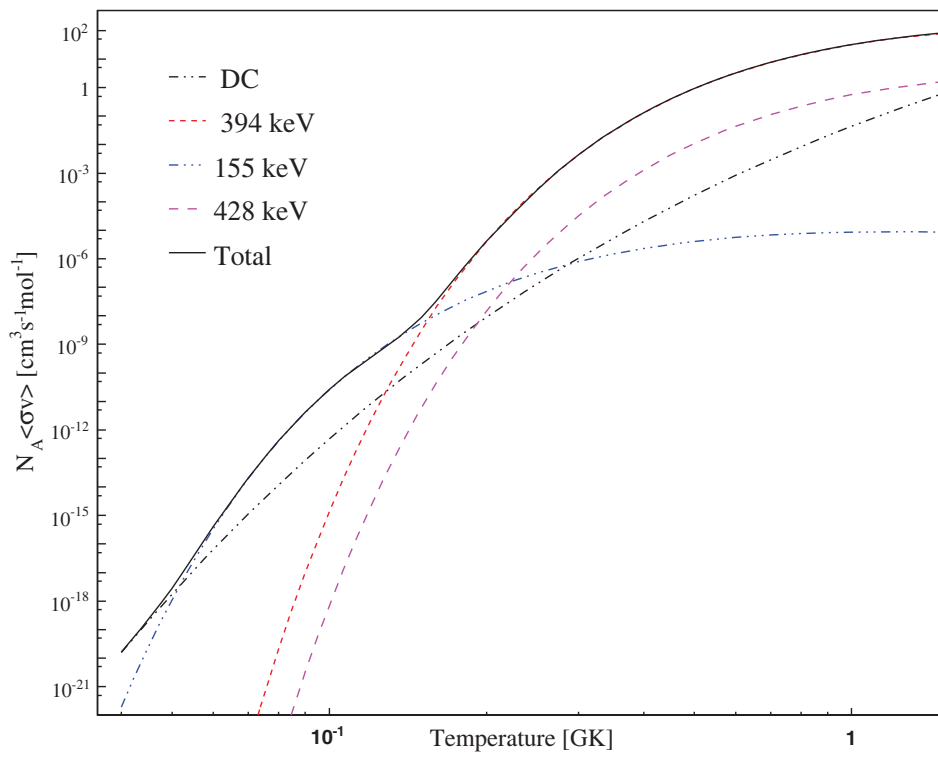


Figure 6.4: The  $^{25}\text{Al}(p,\gamma)^{26}\text{Si}$  reaction rates from direct capture reaction and from the major contributing resonances. The sum of all contributions is also shown as the solid line.

Table 6.2: List of calculated rates  $N_A(\sigma v)$  of the  $^{25}\text{Al}(p, \gamma)^{26}\text{Si}$  stellar reaction from individual resonances at different stellar temperatures, in units of  $\text{cm}^3\text{s}^{-1}\text{mol}^{-1}$ .

$T(GK)$	DC	$E_{R1}$	$E_{R2}$	$E_{R3}$	$E_{R4}$	$E_{R5}$
0.04	$1.590 \times 10^{-20}$	$8.713 \times 10^{-45}$	$2.695 \times 10^{-112}$	$1.066 \times 10^{-198}$	$5.949 \times 10^{-244}$	$5.263 \times 10^{-268}$
0.05	$1.770 \times 10^{-18}$	$5.291 \times 10^{-35}$	$4.686 \times 10^{-89}$	$4.272 \times 10^{-158}$	$2.814 \times 10^{-194}$	$1.685 \times 10^{-214}$
0.06	$6.410 \times 10^{-17}$	$1.675 \times 10^{-28}$	$1.388 \times 10^{-73}$	$4.757 \times 10^{-131}$	$3.500 \times 10^{-161}$	$7.497 \times 10^{-179}$
0.07	$1.120 \times 10^{-15}$	$7.105 \times 10^{-24}$	$1.506 \times 10^{-62}$	$9.570 \times 10^{-112}$	$1.471 \times 10^{-137}$	$2.101 \times 10^{-153}$
0.08	$1.190 \times 10^{-14}$	$2.044 \times 10^{-20}$	$2.773 \times 10^{-54}$	$2.798 \times 10^{-97}$	$7.474 \times 10^{-120}$	$2.491 \times 10^{-134}$
0.09	$8.720 \times 10^{-14}$	$9.813 \times 10^{-18}$	$7.281 \times 10^{-48}$	$4.888 \times 10^{-86}$	$4.323 \times 10^{-106}$	$1.670 \times 10^{-119}$
0.10	$4.840 \times 10^{-13}$	$1.348 \times 10^{-15}$	$9.780 \times 10^{-43}$	$4.739 \times 10^{-77}$	$4.349 \times 10^{-95}$	$1.192 \times 10^{-107}$
0.15	$2.040 \times 10^{-10}$	$3.052 \times 10^{-09}$	$2.073 \times 10^{-27}$	$3.776 \times 10^{-50}$	$3.870 \times 10^{-62}$	$3.796 \times 10^{-72}$
0.20	$9.110 \times 10^{-09}$	$4.044 \times 10^{-06}$	$8.401 \times 10^{-20}$	$9.384 \times 10^{-37}$	$1.016 \times 10^{-45}$	$1.886 \times 10^{-54}$
0.30	$1.040 \times 10^{-06}$	$4.490 \times 10^{-03}$	$2.854 \times 10^{-12}$	$1.955 \times 10^{-23}$	$2.237 \times 10^{-29}$	$7.850 \times 10^{-37}$
0.40	$2.040 \times 10^{-05}$	$1.317 \times 10^{-01}$	$1.464 \times 10^{-08}$	$7.853 \times 10^{-17}$	$2.922 \times 10^{-21}$	$4.459 \times 10^{-28}$
0.50	$1.680 \times 10^{-04}$	$9.271 \times 10^{-01}$	$2.284 \times 10^{-06}$	$6.675 \times 10^{-13}$	$2.006 \times 10^{-16}$	$7.395 \times 10^{-23}$
0.60	$8.350 \times 10^{-04}$	$3.238 \times 10^{+00}$	$6.295 \times 10^{-05}$	$2.644 \times 10^{-10}$	$3.198 \times 10^{-13}$	$2.123 \times 10^{-19}$
0.70	$2.980 \times 10^{-03}$	$7.633 \times 10^{+00}$	$6.489 \times 10^{-04}$	$1.829 \times 10^{-08}$	$5.983 \times 10^{-11}$	$6.043 \times 10^{-17}$
0.80	$8.520 \times 10^{-03}$	$1.413 \times 10^{+01}$	$3.634 \times 10^{-03}$	$4.271 \times 10^{-07}$	$2.946 \times 10^{-09}$	$4.077 \times 10^{-15}$
0.90	$2.060 \times 10^{-02}$	$2.235 \times 10^{+01}$	$1.359 \times 10^{-02}$	$4.850 \times 10^{-06}$	$5.975 \times 10^{-08}$	$1.057 \times 10^{-13}$
1.00	$4.400 \times 10^{-02}$	$3.172 \times 10^{+01}$	$3.840 \times 10^{-02}$	$3.331 \times 10^{-05}$	$6.529 \times 10^{-07}$	$1.405 \times 10^{-12}$
1.50	$6.310 \times 10^{-01}$	$7.928 \times 10^{+01}$	$7.572 \times 10^{-01}$	$9.441 \times 10^{-03}$	$7.448 \times 10^{-04}$	$2.885 \times 10^{-09}$

Table 6.3: Cont'd: List of calculated rates  $N_A\langle\sigma v\rangle$  of the  $^{25}\text{Al}(p, \gamma)^{26}\text{Si}$  stellar reaction from individual resonances at different stellar temperatures, in units of  $\text{cm}^3\text{s}^{-1}\text{mol}^{-1}$ .

$T(GK)$	DC	$E_{R6}$	$E_{R7}$	Total
0.04	$1.590 \times 10^{-20}$	$1.937 \times 10^{-22}$	$1.195 \times 10^{-50}$	$1.609 \times 10^{-20}$
0.05	$1.770 \times 10^{-18}$	$1.116 \times 10^{-18}$	$5.217 \times 10^{-40}$	$2.886 \times 10^{-18}$
0.06	$6.410 \times 10^{-17}$	$3.412 \times 10^{-16}$	$6.153 \times 10^{-33}$	$4.053 \times 10^{-16}$
0.07	$1.120 \times 10^{-15}$	$1.962 \times 10^{-14}$	$6.678 \times 10^{-28}$	$2.074 \times 10^{-14}$
0.08	$1.190 \times 10^{-14}$	$3.987 \times 10^{-13}$	$3.887 \times 10^{-24}$	$4.106 \times 10^{-13}$
0.09	$8.720 \times 10^{-14}$	$4.063 \times 10^{-12}$	$3.228 \times 10^{-21}$	$4.151 \times 10^{-12}$
0.10	$4.840 \times 10^{-13}$	$2.560 \times 10^{-11}$	$6.871 \times 10^{-19}$	$2.609 \times 10^{-11}$
0.15	$2.040 \times 10^{-10}$	$5.599 \times 10^{-09}$	$5.798 \times 10^{-12}$	$8.861 \times 10^{-09}$
0.20	$9.110 \times 10^{-09}$	$7.290 \times 10^{-08}$	$1.483 \times 10^{-08}$	$4.141 \times 10^{-06}$
0.30	$1.040 \times 10^{-06}$	$7.954 \times 10^{-07}$	$3.178 \times 10^{-05}$	$4.524 \times 10^{-03}$
0.40	$2.040 \times 10^{-05}$	$2.313 \times 10^{-06}$	$1.295 \times 10^{-03}$	$1.330 \times 10^{-01}$
0.50	$1.680 \times 10^{-04}$	$4.068 \times 10^{-06}$	$1.110 \times 10^{-02}$	$9.384 \times 10^{-01}$
0.60	$8.350 \times 10^{-04}$	$5.637 \times 10^{-06}$	$4.424 \times 10^{-02}$	$3.283 \times 10^{+00}$
0.70	$2.980 \times 10^{-03}$	$6.864 \times 10^{-06}$	$1.145 \times 10^{-01}$	$7.751 \times 10^{+00}$
0.80	$8.520 \times 10^{-03}$	$7.747 \times 10^{-06}$	$2.276 \times 10^{-01}$	$1.437 \times 10^{+01}$
0.90	$2.060 \times 10^{-02}$	$8.334 \times 10^{-06}$	$3.802 \times 10^{-01}$	$2.277 \times 10^{+01}$
1.00	$4.400 \times 10^{-02}$	$8.690 \times 10^{-06}$	$5.637 \times 10^{-01}$	$3.237 \times 10^{+01}$
1.50	$6.310 \times 10^{-01}$	$8.616 \times 10^{-06}$	$1.607 \times 10^{+00}$	$8.228 \times 10^{+01}$

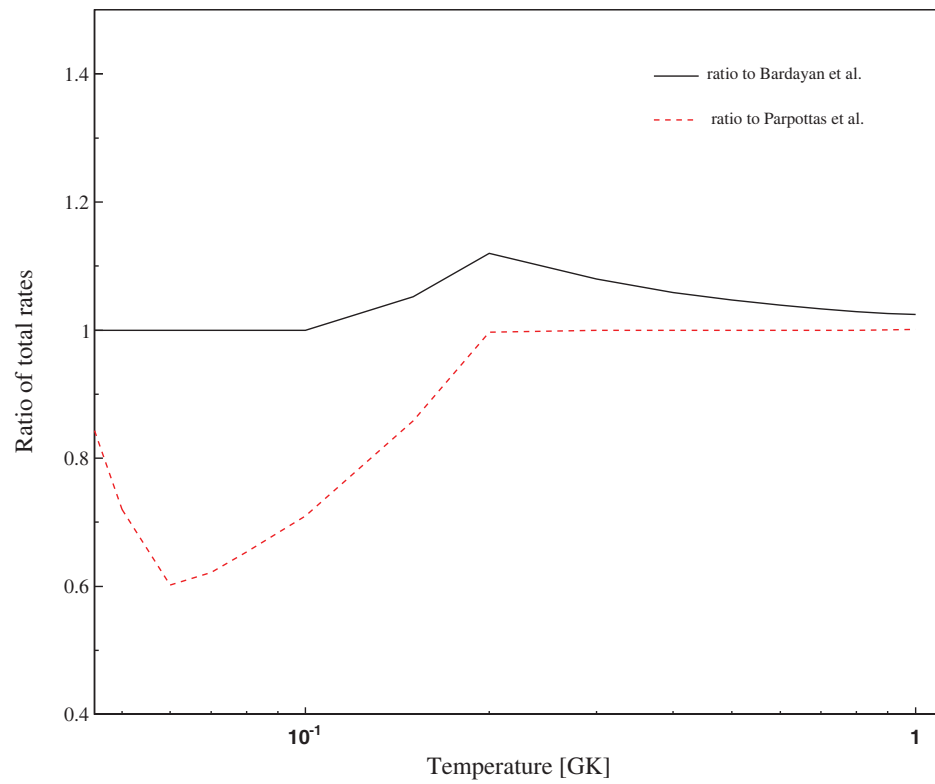


Figure 6.5: The ratios of the total reaction rates from our calculations to the rates from Bardayan *et al.* [12] and Parpottas *et al.* [11]

## Summary and outlook

As an important probe of the inter-stellar medium (ISM), the amount of galactic  $^{26}\text{Al}$  needs to be calculated more accurately in order to understand stellar evolution better by its constraints on the stellar models. The  $^{25}\text{Al}(p,\gamma)^{26}\text{Si}$  reaction plays an important role in producing the  $^{26}\text{Al}$  at the explosive burning temperatures (nova and supernova explosions), and determining the accuracy of the final total  $^{26}\text{Al}$  yield predictions. Large uncertainties however (in resonance energies and spin-parity assignments) exist for the states of astrophysical interest (right above the proton threshold energy  $S_p=5.518$  MeV) in  $^{26}\text{Si}$  in the Gamow window at these temperatures. More input data are clearly needed in the calculation of the  $^{25}\text{Al}(p,\gamma)^{26}\text{Si}$  reaction rate at the temperatures of astrophysical interest.

A few recent experiments have been done to study the astrophysically important states in  $^{26}\text{Si}$ . Caggiano et al found two new states above the proton threshold at  $E_x=5.678(8)$  MeV ( $E_R=160$  keV)<sup>1</sup> and  $E_x=5.945(8)$  MeV ( $E_R=527$  keV) using the  $^{29}\text{Si}(^3\text{He},^6\text{He})^{26}\text{Si}$  reaction, and assigned  $J^\pi=1^+$  and  $3^+$  to these two states [10]. In the experiment, they detected the  $^6\text{He}$  to find the excited states in  $^{26}\text{Si}$ . Bardayan et al. performed a  $^{28}\text{Si}(p,t)^{26}\text{Si}$  experiment in which tritons were measured at different angles to deduce the excited states in  $^{26}\text{Si}$  and the angular distributions of the differential cross-section. They found a new state at

---

<sup>1</sup>The number in the square following the energy value represents the associated uncertainty for the last digit. For example, in “5.678(8) MeV”, the uncertainty is 0.008 MeV.

$E_x=5.914(2)$  MeV ( $E_R=396$  keV) which was assigned  $J^\pi=0^+$  in their first DWBA calculations [9] and later assigned  $J^\pi=3^+$  in their re-evaluation with the FRESKO code [12]. They however did not observe the two states found by Caggiano et al. Parpottas et al. used the ( $^3\text{He},n$ ) reaction to study the  $^{26}\text{Si}$  structure by measuring the neutron at different angles. They confirmed the three states found in the two experiments above with  $E_x=5.670(4)$  MeV ( $E_R=152$  keV),  $5.912(4)$  MeV ( $E_R=394$  keV) and  $5.946(4)$  MeV ( $E_R=428$  keV) and  $J^\pi=1^+$ ,  $3^+$  and  $0^+$ , respectively, made by the Hauser-Feshbach (HF) calculations of differential cross-section [11].

A more recent experiment (by Komatsubara et al. with McMaster participation) has been performed using the ( $^3\text{He},n\gamma$ ) reaction in which instead of detecting the neutrons they measured the  $\gamma$ -rays from the decays of the excited  $^{26}\text{Si}$  states [39]. By constructing cascades of  $\gamma$  emissions with the  $\gamma$ - $\gamma$  coincidence technique, they confirmed the state at  $E_x=5.674$  MeV ( $E_R=156$  keV) and also found a new state at  $E_x=5.886$  MeV ( $E_R=368$  keV) which decays to the first excited state of 1.796 MeV with a 4.089 MeV  $\gamma$ -ray emission. In their preliminary analysis for the spin-parity assignments by the directional angular correlation (DCO) technique for coincident  $\gamma$ -rays, they tentatively assigned  $J^\pi=0^+$  to this newly found level.

We successfully performed two different experiments via the  $p(^{27}\text{Si},^{26}\text{Si}^*)d$  reaction (referred to as (p,d) in the following) and the  $p(^{25}\text{Al},^{25}\text{Al})p$  (referred to as (p,p) in the following) elastic scattering with radioactive beams to study the structure of  $^{26}\text{Si}$  for the first time with these reactions.

In the (p,d) experiment, we also measured the  $\gamma$ -emissions from the excited  $^{26}\text{Si}$  and constructed the  $\gamma$ -cascades with the  $\gamma$ - $\gamma$  coincidence technique to determine the level energies. We found one state within the range of 5.6 MeV to 6 MeV with  $E_x=5.909$  MeV ( $E_R=391$  keV) which decays to the 1.796 MeV state with a 4.113 MeV  $\gamma$ -ray emission. According to our analysis, this state is the same state as that  $3^+$  state around 5.912 MeV found by Bardayan et al. and Parpottas et al. and we adopted the spin-parity assignment of  $J^\pi=3^+$  from them. We also believe that the

4.113 MeV  $\gamma$ -ray corresponds to the 4.089 MeV  $\gamma$ -ray observed in the experiment by Komatsubara et al. and therefore we cannot confirm that the state found by them ( $E_x=5.886$  MeV) is a new state. Above  $E_x=6$  MeV in  $^{26}\text{Si}$ , we found a new state at  $E_x=6.443$  MeV ( $E_R=925$  keV) which decays to the  $E_x=4.183$  MeV state with a 2.260 MeV  $\gamma$ -ray emission. We suggest a spin-parity of  $J^\pi=4^+$  for this state by matching this cascade with those from the corresponding level ranges in its mirror nucleus  $^{26}\text{Mg}$ . We did not find the  $E_x=5.674$  MeV and 5.946 MeV levels from our analysis.

In the (p,p) experiment, we measured the scattered protons to deduce the experimental differential cross-section. An energy range of 0–3 MeV ( $E_{cm}$ ; corresponding to  $E_x=5.518$  MeV – 8.518 MeV) above the proton threshold in  $^{26}\text{Si}$  was scanned using a thick target. Actually, we did not see peak signatures in the excitation function in the region of  $E_{cm} \lesssim 1.2$  MeV because the Coulomb scattering cross-section is dominant in this low energy region. In the region above that, we can see many peak-like signatures but we can definitively identify three peaks as true resonances. Furthermore, only for these three peaks could good fits be made with the R-Matrix calculations of the differential cross-section. From the fit, we extracted the three resonances at  $E_R=1.882$  MeV ( $E_x=7.135$  MeV) with  $J^\pi=2^+$ ,  $E_R=2.018$  MeV ( $E_x=7.495$  MeV) with  $J^\pi=2^+$  and  $E_R=2.251$  MeV ( $E_x=7.647$  MeV) with  $J^\pi=3^+$ . The first two resonances likely correspond to the levels at  $E_x=7.150$  MeV and 7.493 MeV found by both Bardayan et al. and Parpottas et al. The third resonance matches the level at  $E_x=7.694$  MeV found by both Bardayan et al. and Parpottas et al. within a reasonable error range. As for the spin-parity assignments for the three states, our R-Matrix fit results agree with those from Bardayan et al. and Parpottas et al. but there is a discrepancy for the third one for which our R-Matrix fit indicates  $J^\pi=3^+$ , whereas both Bardayan et al. and Parpottas et al. assigned  $J^\pi=3^-$ .

Based on our results from both experiments, a new reaction rate for  $^{25}\text{Al}(p,\gamma)^{26}\text{Si}$  was calculated. The contributions from the three high-energy resonances with

$E_x > 7$  MeV are negligible at low temperatures (nova temperatures  $\sim T_8$ , Gamow window range  $E_x = 5.621$ - $6.461$  MeV) but will come to play a role at high temperatures (supernova temperatures  $\sim T_9$ , Gamow window range  $E_x = 5.907$ - $10.493$  MeV). The newly found  $6.443$  MeV ( $E_R = 925$  keV) state contributes to the reaction rates at high temperatures ( $T_9 > 1$ ), comparable with the non-resonant contribution. Therefore, the most significant contributions at nova temperatures are from resonances with  $E_R < 1$  MeV.

Although much progress has been made from all of these experiments performed for the study of the astrophysical important states in  $^{26}\text{Si}$  at nova and supernova temperatures, we note that further study to resolve uncertain states and find more new states will require the measurement of the angular distribution of the transfer reactions and the  $\gamma$ -emission cascades with higher-precision and more efficient detectors, and with beams of higher intensity. As the development of the radioactive beam (RIB) technique proceeds further, direct measurements of the  $^{25}\text{Al}(p,\gamma)^{26}\text{Si}$  reaction with low-energy and high-intensity RIBs will be the best choice for further study in the future.

## Production of RIBs in laboratory

The methods for producing the short-lived radioactive beams (RIBs) in the laboratory can be categorized into two types: the ISOL method and the In-flight method, which can produce RIBs in different energy regimes and thus are complementary. Figure A.1 shows a schematic diagram of the beam production by these two methods in comparison.

### A.1 ISOL – Isotope Separator On-Line

In the ISOL method, radioactive ions are first produced by a primary accelerator or by the neutrons from a nuclear reactor and then stopped by a production target after which the radioactivity is transported into an ion-source. The radioactive nuclei from the ion source are extracted in the form of ions with the desired charge-states and then go through the selection of mass separators to remove the unwanted particles from the beam. After this mass separation, the beam will get re-accelerated by a second accelerator to the desired energy for the nuclear experiments.

With the ISOL technique, beams of high quality can be produced, which is comparable to that of stable beams because the process is similar to that for the stable beam production. Strong ISOL beams can be produced but the intensity

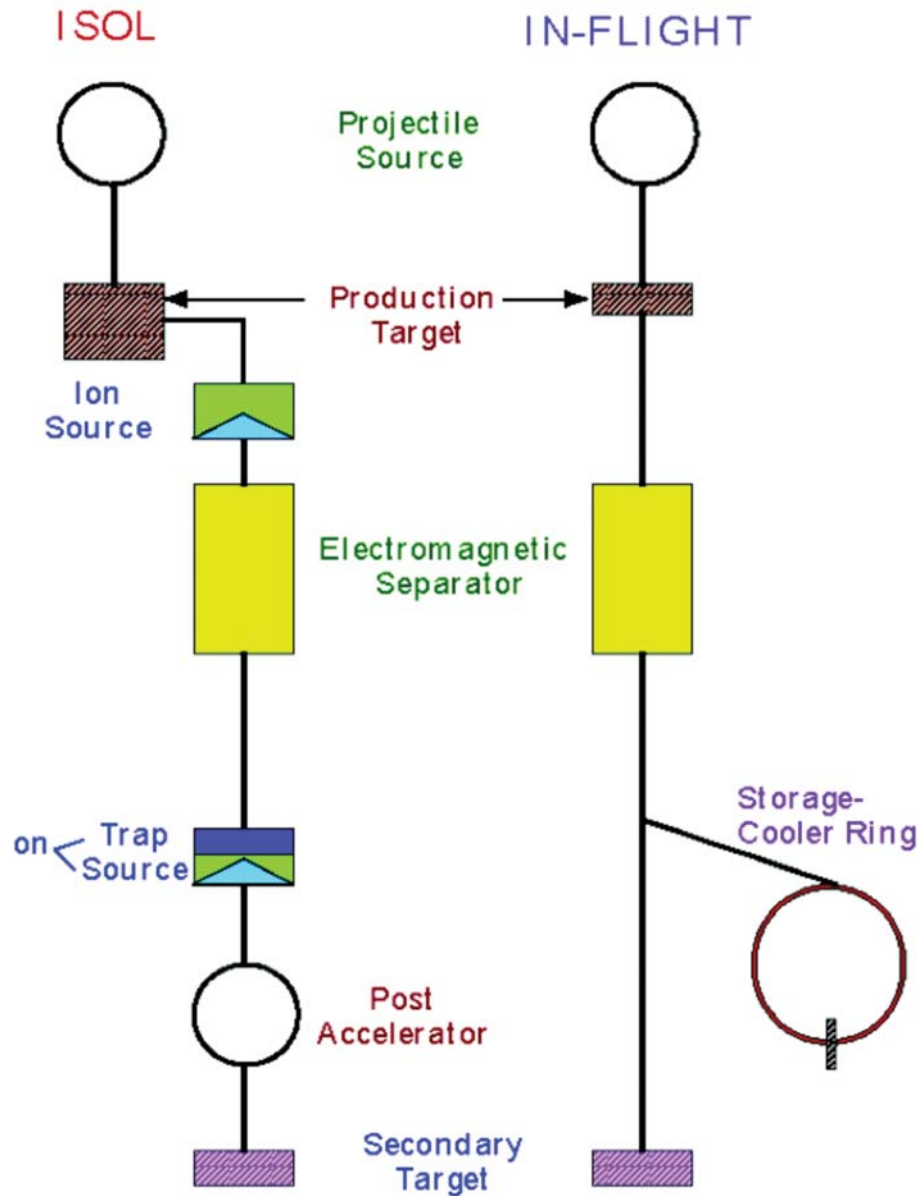


Figure A.1: The schematic diagram of the RIB productions by the ISOL method and the in-flight method.

varies with the chemical species used for the ion-source and their radioactivities. This technique also depends on the diffusion and effusion of the radioactive atoms in the production target. To facilitate the production process, the production target is always maintained at high temperatures (about 2500°C). Since the time

of the diffusion processes vary, this method is not suitable for short-lived nuclear species with half-lives of milliseconds or less because the radioactive nuclei could decay before they get re-accelerated to the secondary target.

## A.2 In-flight method

In the in-flight method, the radioactive beam is produced by the fragmentation of heavy primary beam on a light target. Interactions with the light target nuclei can result in fragmentation and the produced nuclei can leave the target with velocities close to those of the beam projectiles. Due to the nature of fragmentation, many different species will be produced. Since the produced beam particles already have high velocities, they do not need further acceleration as in the ISOL method to transport them to the secondary target and therefore it is suitable for production of short-lived radioactive beams. Before the beam particles reach the secondary target beam, a beam separation is necessary, by which the beam particles can be identified and separated by mass, charge and momentum in a spectrometer (fragment separator). But even after this separation, the beam can be still contaminated by other particles with characteristics close to the desired beam particle. Further identification for the beam particles are needed on an event-by-event basis.

Using in-flight, we can produce all chemical species with half-lives greater than about 150 ns which is the time of transit through the fragment separator. The main disadvantage of this method due to the nature of fragmentation is that it is difficult to produce RIBs with high intensities and high purities and the produced beams have poorer quality in terms of energy and focusing.

Both of our experiments at the NSCL facility and the CRIB facility use the in-flight method to produce the RIBs.

The best method for the RIB production in the future is the one that combines the ISOL and in-flight methods by stopping fragmentation products in a gas cell.

# Appendix **B**

## R-Matrix theory

The R-Matrix theory is a theory of the cross-section of compound nuclear reaction. A compound nucleus is formed via the strong short-range nuclear force which exists only inside the nucleus. Outside the nucleus the Coulomb force plays the dominant role. Therefore the wave functions inside and outside the nucleus in the formation of compound nuclei behave differently, and a nuclear surface is then defined as existing at a radius  $a_c$  representing the boundary between the internal and external region. Outside the surface, due to the weak electromagnetic interaction, the wave function is simply described as a linear combination of the incoming and outgoing waves. But in the internal region, the wave function is confined in the nuclear volume enclosed by the nuclear surface and thus can be expressed as a standing wave, the eigenvalue of which gives the resonant energy of a resonant state in the compound nucleus. But since the compound nucleus cannot last forever, and it can break out or decay in many exit reaction channels, the wave function is actually not an exact standing wave but a complete orthonormal set of such standing wave functions associated with all resonant states.

In the following, the derivation of the R-Matrix formalism for a simple particle scattering from a central potential is described. In the internal region, the total

radial wave function  $\Psi$  satisfies the radial Schrödinger equation,

$$-\frac{\hbar^2}{2m} \frac{d^2\Psi}{dr^2} + V(r)\Psi = E\Psi \quad (\text{B.1})$$

where the mass  $m$  is actually the reduced mass the scattering system.

As mentioned above, the internal wave function is described by a complete set of wave functions of resonant states, as follows

$$\Psi = \sum_{\lambda} C_{\lambda} X_{\lambda} \quad (\text{B.2})$$

where  $X_{\lambda}$  represent the standing wave functions of the resonances labeled  $\lambda$ . All these resonances satisfy the Schrödinger equation,

$$HX_{\lambda} = E_{\lambda}X_{\lambda} \quad (\text{B.3})$$

where  $E_{\lambda}$  are the energy eigenvalues of the resonant states. The energy-dependent coefficients  $C_{\lambda}$  are given by

$$C_{\lambda} = \int_0^{a_c} X_{\lambda}^* \Psi dV \quad (\text{B.4})$$

where the  $V$  represents the nuclear volume enclosed by the surface at  $r = a_c$ .

Since the  $X_{\lambda}$  are stationary, they must satisfy the boundary condition on the nuclear surface  $r = a_c$ , given by

$$\left[ r \frac{dX_{\lambda}}{dr} - bX_{\lambda} \right]_{r=a_c} = 0 \quad (\text{B.5})$$

where  $b$  is the boundary condition number and can be arbitrarily chosen.

By multiplying Eq. B.1 by  $X_{\lambda}^*$  and the conjugate of Eq. B.3 by  $\Psi$ , subtracting, and integrating over the nuclear volume  $V$ , we obtain

$$-\frac{\hbar^2}{2m} \left( \Psi \frac{dX_{\lambda}^*}{dr} - X_{\lambda}^* \frac{d\Psi}{dr} \right)_{r=a_c} = (E - E_{\lambda}) \int_0^{a_c} X_{\lambda}^* \Psi dr \quad (\text{B.6})$$

Using Eq. B.4 and Eq. B.5, we obtain

$$C_\lambda = \frac{\hbar^2}{2ma_c} \frac{X_\lambda(a_c)}{E - E_\lambda} \left( r \frac{d\Psi}{dr} - b\Psi \right)_{r=a_c} \quad (\text{B.7})$$

Substituting this expression of  $C_\lambda$  to Eq. B.2, we get

$$\Psi(r) = G(r, a_c) \left( r \frac{d\Psi}{dr} - b\Psi \right)_{r=a_c} \quad (\text{B.8})$$

where the Green's function  $G(r, a_c)$  is given by

$$G(r, a_c) = \frac{\hbar^2}{2ma_c} \sum_\lambda \frac{X_\lambda(r)X_\lambda(a_c)}{E_\lambda - E} \quad (\text{B.9})$$

which relates the value of the wave function in the internal region to its derivative on the surface and defines the R function as its value at  $r = a_c$

$$R \equiv G(a_c, a_c) = \sum_\lambda \frac{\gamma_\lambda^2}{E_\lambda - E} \quad (\text{B.10})$$

where

$$\gamma_\lambda = \left( \frac{\hbar^2}{2ma_c} \right)^{1/2} X_\lambda(a_c) \quad (\text{B.11})$$

is referred to as the reduced the reduced width of the resonant state.

The R-function then relates the internal stationary parameters such as the wave functions and eigenenergies to the total wave function  $\Psi$  at the nuclear surface  $r = a_c$ .

From Eq. B.8, we get

$$\Psi(a_c) = G(a_c, a_c)(a_c\Psi'(a_c) - b\Psi(a_c)) \quad (\text{B.12})$$

then we can find that

$$\frac{\Psi'(a_c)}{\Psi(a_c)} = \frac{1 + bR}{a_c R} \quad (\text{B.13})$$

This implies that if we know the logarithmic derivative of the wave function at

$r = a_c$  for all energies, we will know the cross-section for all energies as well.

In the external region, the total wave function can be written as a linear combination of the linearly independent incident and outgoing radial waves,  $I_l$  and  $O_l$ , in the form

$$\Phi_l = I_l - U_l O_l \quad (\text{B.14})$$

where the coefficient  $U_l$  is so-called collision function which is the amplitude of the unit-flux outgoing wave  $O_l$  associated with a unit-flux incoming wave  $I_l$ . The index  $l$  here denotes the incident relative orbital angular momentum of the scattering system.

The radial incoming and outgoing wave functions at large distance can be written as

$$\begin{aligned} I_l &= -\exp[i(kr - \pi l/2 - \eta \ln(kr))] \\ O_l &= \exp[i(kr - \pi l/2 - \eta \ln(kr))] \end{aligned} \quad (\text{B.15})$$

where  $k$  is the wave number and  $\eta$  is the Coulomb parameter– the Sommerfeld parameter, depending on the charge  $Z_1$  and  $Z_2$  of the scattering pair and their relative velocity  $v$ , and they are given by

$$\begin{aligned} k &= \frac{\sqrt{2mE}}{\hbar} \\ \eta &= \frac{Z_1 Z_2 e^2}{\hbar v} \end{aligned} \quad (\text{B.16})$$

If we let  $\rho = kr$ ,  $I_l$  and  $O_l$  will be functions of  $\rho$ .

Alternatively, the incoming and outgoing radial wave functions can be written in terms of the regular and irregular Coulomb functions  $F_l$  and  $G_l$  as

$$\begin{aligned} I_l &= (G_l(kr) - iF_l(kr))\exp(i\omega_l) \\ O_l &= (G_l(kr) + iF_l(kr))\exp(-i\omega_l) \end{aligned} \quad (\text{B.17})$$

where  $\omega_l$  is the Coulomb phase shift, and is given by

$$\omega_l = \sum_{n=1}^l \tan^{-1}(\eta_l/n). \quad (\text{B.18})$$

If there is no Coulomb field in the external region (neutron scattering) or at large distances ( $r \gg a_c$ ), we will have  $\eta \sim 0$ , that is, zero Coulomb phase shift  $\omega = 0$ .

The regular and irregular Coulomb function  $F_l$  and  $G_l$  are given by (Pg. 269 in [52])

$$\begin{aligned} F_l(kr) &= \sqrt{\frac{\pi kr}{2}} J_{l+\frac{1}{2}}(kr) = kr j_l(kr) \\ G_l(kr) &= (-1)^l \sqrt{\frac{\pi kr}{2}} J_{-(l+\frac{1}{2})}(kr) = -kr n_l(kr) \end{aligned} \quad (\text{B.19})$$

where  $J_{l+\frac{1}{2}}(kr)$  and  $J_{-(l+\frac{1}{2})}(kr)$  is half-integer Bessel functions,  $j_l kr$  is the spherical Bessel functions and  $n_l kr$  is the spherical Neumann function.

By evaluating the logarithmic derivative of the external wave function at the nuclear surface  $r = a_c$  and matching it with that of the external wavefunction in Eq. B.13, we obtain

$$\frac{1 + bR}{Ra_c} = \left( \frac{I'_l - U_l O'_l}{I_l - U_l O_l} \right)_{r=a_c}, \quad (\text{B.20})$$

where the prime means  $\frac{d}{dr}$  and it follows that

$$\begin{aligned} U_l &= \frac{I_l + bRI_l - RI'_l}{O_l + bRO_l - RO'_l} \Big|_{r=a_c} \\ &= \frac{1 - L_l^* R}{1 - L_l R} \frac{I_l}{O_l} \Big|_{a_c} \end{aligned} \quad (\text{B.21})$$

where we use the fact that  $I_l = O_l^*$  and  $L_l$  is the logarithmic derivative quantity at  $r = a_c$ , given by

$$L_l \equiv a_c \left( \frac{O'_l}{O_l} \right)_{r=a_c} - b \equiv S_l + iP_l \quad (\text{B.22})$$

Here  $S_l$  is defined as the shift function leading to level shifts and  $P_l$  is the penetrability leading to level widths. Both of them are evaluated at  $r = a_c$ . Then using

Eq. B.17 in above equation, we can find the expressions of the shift function and penetrability function in terms of the Coulomb functions as follows

$$\begin{aligned} S_l &= a_c \frac{F_l(kr)F_l'(kr) + G_l(kr)G_l'(kr)}{F_l^2(kr) + G_l^2(kr)} \Big|_{r=a_c} \\ P_l &= \frac{ka_c}{F_l^2(kr) + G_l^2(kr)} \Big|_{r=a_c} \end{aligned} \quad (\text{B.23})$$

Then we can rewrite the collision function  $U_l$  in Eq. B.21 in terms of  $S_l$ ,  $P_l$  and the  $R$  function using Eq. B.17, Eq. B.21 and Eq. B.22, as

$$U_l = \frac{(1 - S_l R) + iP_l R \frac{G_l(kr) - iF(kr)}{G_l(kr) + iF_l(kr)}}{(1 - (S_l R) - iP_l R \frac{G_l(kr) + iF_l(kr)}{G_l(kr) - iF(kr)})} \exp(2i\omega_l) \quad (\text{B.24})$$

It follows that

$$U_l = \exp(2i\delta_l^R) \exp(-2i\phi_l) \exp(2i\omega_l) = \exp[2i(\delta_l^R - \phi_l + \omega_l)] = \exp(2i\delta_l), \quad \text{at } r = a_c \quad (\text{B.25})$$

As we can see the collision function can finally expressed as a simple form as  $U_l = \exp(2i\delta_l)$  with the  $\delta_l$  is called the total phase shift,

$$\delta_l = \delta_l^R - \phi_l + \omega_l \quad (\text{B.26})$$

with

$$\begin{aligned} \delta_l^R &= \tan^{-1} \frac{P_l R}{1 - S_l R} \\ \phi_l &= \tan^{-1} \frac{F_l(ka_c)}{G_l(ka_c)} \end{aligned} \quad (\text{B.27})$$

and  $\omega_l$  from Eq. B.18, the Coulomb scattering phase shift.  $\delta_l^R$  is the resonance contribution to the phase shift and  $\phi_l$  is the hard sphere scattering phase shift.

Now in order to find the relation between the collision function  $U_l$  and the differential cross-section, we start with the total wave functions. The total incoming

and outgoing wave functions,  $\mathcal{I}_l$  and  $\mathcal{O}_l$ , are given by (Pg. 270 in [52])

$$\begin{aligned}\mathcal{I}_l &= i^l Y_{l0} \frac{I_l}{v^{1/2} r} \psi \\ \mathcal{O}_l &= i^l Y_{l0} \frac{O_l}{v^{1/2} r} \psi\end{aligned}\tag{B.28}$$

where  $\psi$  is the wave function associated with other quantum numbers and the spherical harmonics function  $Y_{l0}$  is just

$$Y_{l0}(\theta) = \sqrt{\frac{2l+1}{4\pi}} P_l(\cos\theta)\tag{B.29}$$

Therefore the total wave function  $\Psi_T$  can be written as the linear combinations of the total incoming and outgoing wave functions, as follows

$$\Psi_T = \sum_l A_l (\mathcal{I}_l - U_l \mathcal{O}_l)\tag{B.30}$$

It follows that

$$\begin{aligned}\Psi_T &= \sum_l A_l \left( i^l Y_{l0} \frac{I_l}{v^{1/2} r} \psi - U_l i^l Y_{l0} \frac{O_l}{v^{1/2} r} \psi \right) \\ &= \sum_l \frac{A_l i^l Y_{l0} \psi}{v^{1/2} r} (I - U O) \\ &= \sum_l \frac{A_l i^l Y_{l0} \psi}{v^{1/2} r} (I - O) + \sum_l \frac{A_l i^l Y_{l0} \psi}{v^{1/2} r} (1 - U) O\end{aligned}\tag{B.31}$$

Substituting the expression of  $Y_{l0}$  and Eq. B.17 (the Coulomb shift is taken as zero at large distances) into the above equation and using Eq. B.19, we obtain

$$\begin{aligned}\Psi_T &= \sum_l \frac{A_l i^l Y_{l0} \psi}{v^{1/2} r} (-2iF_l) + \sum_l \frac{A_l i^l Y_{l0} \psi}{v^{1/2} r} (1 - U)(G_l + iF_l) \\ &= \sum_l \sqrt{\frac{2l+1}{\pi}} \frac{A_l k \psi}{v^{1/2}} (-i^{l+1}) P_l(\cos\theta) j_l(kr) \\ &\quad + \sum_l \sqrt{\frac{2l+1}{4\pi}} \frac{A_l k \psi}{v^{1/2}} i^l (1 - U_l) P_l(\cos\theta) (j_l(kr) + in_l(kr))\end{aligned}\tag{B.32}$$

Recall that a plane wave  $exp(ikz)$  can be expanded as follows

$$exp(ikz) = exp(ikrcos\theta) = \sum_l i^l (2l+1) j_l(kr) P_l(cos\theta) \quad (B.33)$$

and  $h_l(kr) = j_l(kr) + in_l(kr)$  is the spherical Hankel function of the first kind and is approximated as  $h_l(kr) \sim -iexp(ikr)/(kr)$  at large distances. Then the above expression of  $\Psi_T$  can be written as

$$\begin{aligned} \Psi_T = & \sum_l A_l \frac{(-ik)}{\sqrt{v^{1/2}\pi(2l+1)}} \times i^l (2l+1) j_l(kr) P_l(cos\theta) \\ & + \sum_l \sqrt{\frac{2l+1}{4\pi}} \frac{A_l}{v^{1/2}} (-i^{l+1}) (1-U_l) P_l(cos\theta) \frac{exp(ikr)}{r} \end{aligned} \quad (B.34)$$

Now we define a value of  $A_l$  so that the first term in the expression  $\Psi_T$  is just a plane wave  $exp(ikz)$ , that is,

$$A_l = \frac{i\sqrt{\pi(2l+1)}v^{1/2}}{k} \quad (B.35)$$

Using this value of  $A_l$  in the expression of  $\Psi_T$ , we obtain

$$\Psi_T = exp(ikz) + f(\theta) \frac{exp(ikr)}{r} \quad (B.36)$$

with

$$f(\theta) = \frac{1}{2k} \sum_l i^l (2l+1) (1-U) P_l(cos\theta) \quad (B.37)$$

Thus we find that the total wave function is just a superposition of an incoming plane wave and an outgoing scattering radial wave. The  $f(\theta)$  is thus the nuclear scattering amplitude and the differential cross-section is then given by

$$\frac{d\sigma(\theta)}{d\Omega} = |f(\theta)|^2 = \frac{1}{4k^2} \left| \sum_l (2l+1) (1-U_l) P_l(cos\theta) \right|^2 \quad (B.38)$$

Finally we find that the differential cross-section depends on the collision func-

tion  $U_l$  which in turn depends on the phase shifts associated with Coulomb scattering ( $\omega_l$ ), hard-sphere scattering ( $\phi_l$ ), and resonant scattering ( $\delta_l^R$ ), with the third one determined by the  $R$  function. It is the  $R$  function within which all the information about the stationary states, such as resonance energies and widths is contained. Therefore, if we know the resonance energies and widths of resonances, we can calculate the  $R$  function and then the collision function from which the differential cross-section can be calculated. Likewise, if we have data of resonant scatterings or reactions from experiments and use the formula of differential cross-section with  $R$  function to fit the data, we can extract the resonance energies and widths for unknown resonances, the spin-parity  $J^\pi$  as well.

The above derivations are for the simple case of the single channel resonant scatterings or reactions. If there are more scattering or reaction channels involved to populate different resonance states, the multi-channel representation is needed. For this case, the  $R$ -function will become an  $R$ -matrix with each element representing the correlation between two channels. In turn, the collision function in Eq. B.21 is then a collision matrix and it should be re-written as [page 732 in Ref. [53]]

$$U = (kr)^{1/2}O^{-1}(1 - LR)^{-1}(1 - L^*R)I(kr)^{-1} \quad (\text{B.39})$$

where  $(kr)^{1/2}$  and  $(kr)^{-1/2}$  are the diagonal matrices with diagonal elements  $(kr)^{1/2}$  and  $(kr)^{-1/2}$ , respectively;  $O$ ,  $I$  and  $L$  are also diagonal matrices with component  $O_c$ ,  $I_c$  and  $L_c$  ( $c$  the channel label); the simple inverse calculation of a real value in Eq. B.21 now becomes the complicated inverse calculation of the matrix, that is  $(1 - LR)^{-1}$ .

Actually, the resonance energies and widths extracted from the fit are not the physical ones and they are called formal resonance energies and widths. Different energies and widths can be obtained if different boundary constants are used. They depend on the choice of the boundary condition and they are related to the real physical resonance energies and width by this boundary condition. There is always a boundary constant at which the formal resonance energy matches the physical

one for each resonance. The process of finding the physical resonance parameters from the formal ones is called boundary transformation, which is explained in Chapter 5. The differential cross-section does not depend on the boundary constant, which means all combinations of boundary constants and the resonance parameters calculated at the corresponding boundary constant will give the same value of the differential cross-section for the same resonant scattering or reaction.

## More analysis details

### C.1 File formats of the experimental data at CRIB and NSCL

The raw experimental data collected during the experiment were binary data. It usually include two parts: the first part is the header including the run information about the data file, such as file name, run time, file size, and so on; the second part is the binary data. The data formats used in different laboratories might be different in the details of the header and data body due to the different data acquisition systems (DAQs) and different encoding method used to making the raw binary data. Here the two data formats used in this thesis project are described: the data format of the rdf data file at CRIB with extension `.rdf` and that of the evt data file at NSCL with extension `.evt`. Figure C.1 shows the format of each event stored in the `.evt` file at NSCL. Figure C.2 shows the format of `.rdf` file at CRIB.

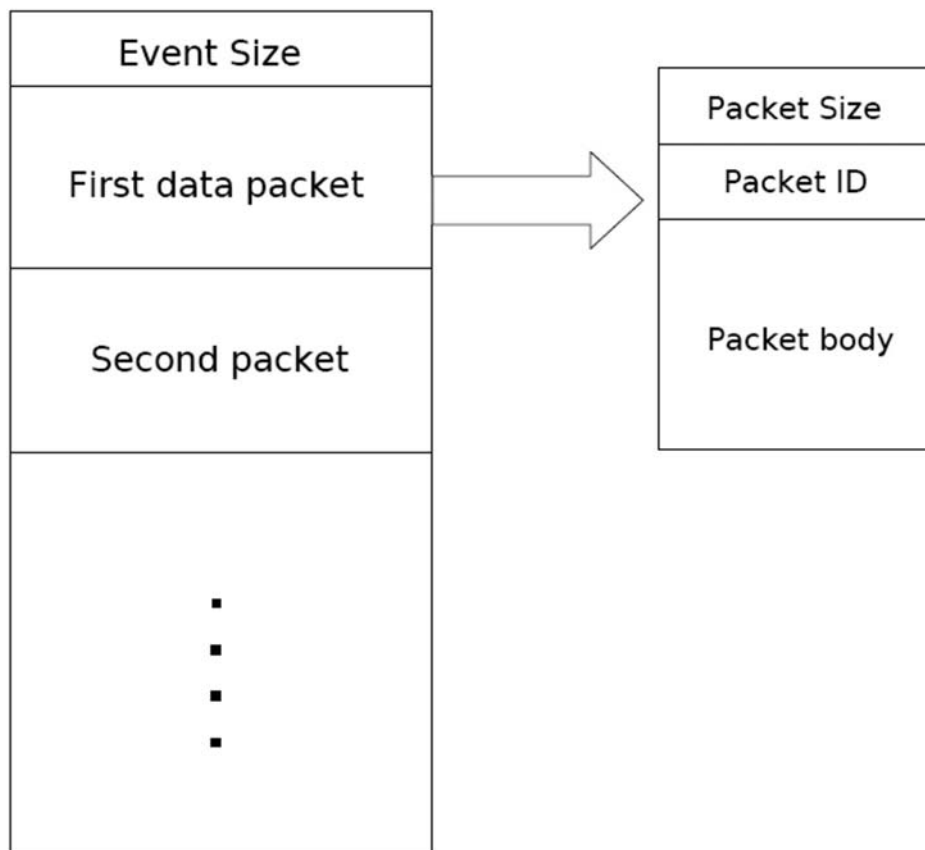


Figure C.1: Event format of data file at NSCL.

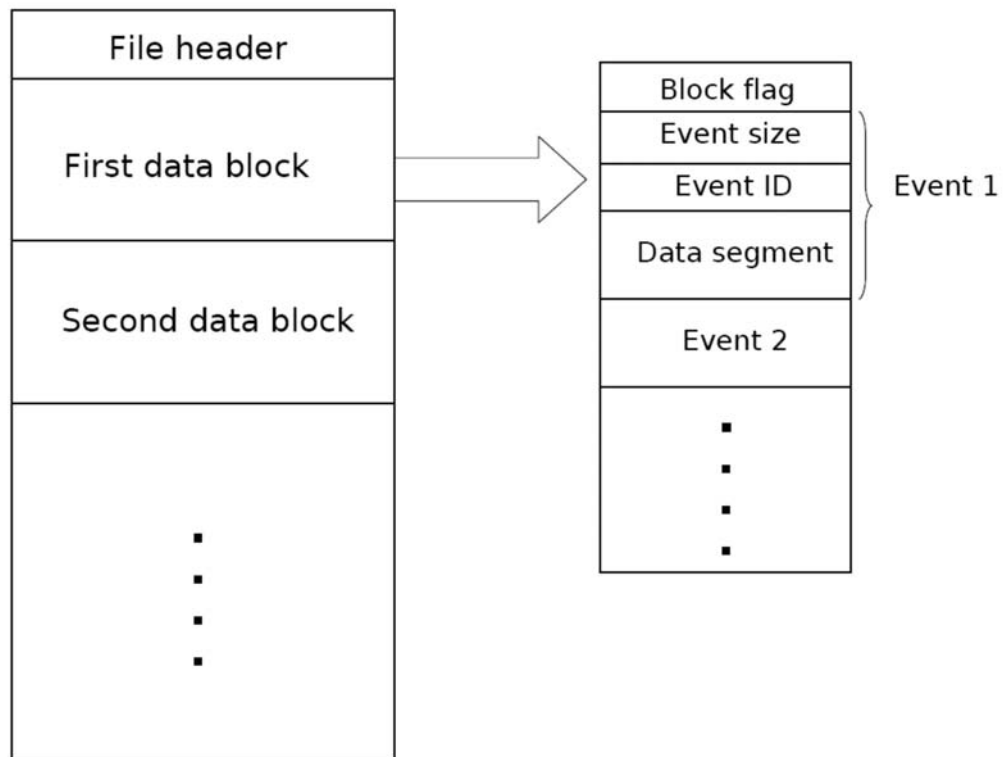


Figure C.2: Data format of the .rdf file at CRIB.

## C.2 Input file for the R-Matrix fitting program

Displayed below is the content of the input file “param.par” used for the R-Matrix fit to our resonance data. For example,  $1'e(3,1)$  represents the reduced width of the first resonance, with the first number in the square equal to  $J_\pi + 1$  and the second number indicating the number of the resonance; the two values after  $1'e(3,1)$  are the values of this reduced width and its uncertainties, respectively.  $5'g(31321)$  represents the formal energy of the first resonance indicated by the last number in the square; the first number in the square again is equal to  $J_\pi + 1$  with  $J_\pi$  the spin of the resonance; the second one means the number of reaction channel, 1 for elastic scattering and 2 for inelastic scattering; the third number in the square is equal to  $S + 1$  with  $S$  the channel spin of this reaction channel; the fourth number is equal to  $l + 1$  with  $l$  the quantum number of the orbital angular momentum.

SET TITLE

Elastic scattering      R-matrix fit      to CRIB data

PARAMETERS

$1'e(3,1)$	'	0.17100E+01	0.61545E-02
$2'e(3,2)$	'	0.20540E+01	0.75266E+01
$3'e(4,3)$	'	0.22340E+01	0.75266E+01
$4'e(3,4)$	'	0.10840E+02	0.75266E+01
$5'g(31321)$	'	0.42415E+00	0.12376E-01
$6'g(31312)$	'	0.24185E+00	0.23795E+00
$7'g(41413)$	'	0.42415E+00	0.12376E-01
$8'g(31314)$	'	0.29485E+01	0.23795E+00
$23'signorm$	'	0.21941E+00	0.27899E-02

minimize 1000

save

return

### C.3 Creating .spe file used in gf3 program

gf3 is a useful program for gamma spectrum analysis in the RadWare package [81]. This program takes an input spectrum file of its own format with the extension .spe, plot it, and analyzes it. The .spe file is a binary file only for 1 dimensional spectra and it contains two parts of information for a spectrum. The first part is the information about the name and size of the spectrum, while the second part is the spectrum data. Each data point in the file is just the count of the spectrum at the channel corresponding to the index of its placement in the file. For example, if the 14th data point in the file is 100, that means that at channel 14 on the spectrum, there are 100 counts.

To use the gf3 program, we need to create a .spe file from our data if one does not already exist. We can simply create it from a .txt file, which consists of only two columns of data with the first column the channel number and the second the count at that channel number for each row in the file. Then we can write a short code reading the channel and count from the .txt file, creating a .spe file and writing into the .spe file the count by order of its channel number using a subroutine named "wspec" in the gf3 code package. The following is for those who are reading this section and are not familiar with linking to a library. When compiling and building this short code, we need to link it to the library which contains the subroutine we used for creating .spe file. For example, if the short code is "CreateSpe.c" and the library is a archive "util.a" in the directory of "/usr/local/gf3/src/libs/util", we just do,

```
gcc -o CreateSpe -c CreateSpe.c /usr/local/gf3/src/libs/util/util.a -lm
```

Regarding how to use gf3, refer to the manual on its website [81].

## C.4 Geometry of the detector system in the F3 chamber at CRIB

Figure C.3 shows the geometry of the detector system in the F3 chamber from the top view. All of the measured distances are listed in Table C.1.  $d_0$ ,  $d_1$  and  $d_2$  are the distances from the target center to the centers of PSD0 ( $0^\circ$ ), PSD1 ( $17^\circ$ ) and PSD2 ( $27^\circ$ ), respectively. In the calculation of the scattering angles, we use  $d_0 = d_1 = d_2 = 204$  mm. The horizontal center of the PSD0 is not on the beam axis; instead it is off axis to the right by 16 mm as viewed from upstream to downstream. The active area of each PSD is  $50\text{mm} \times 50\text{mm}$  in X & Y dimensions. Each dimension has 16 divisions with each having a size of 3.1 mm.

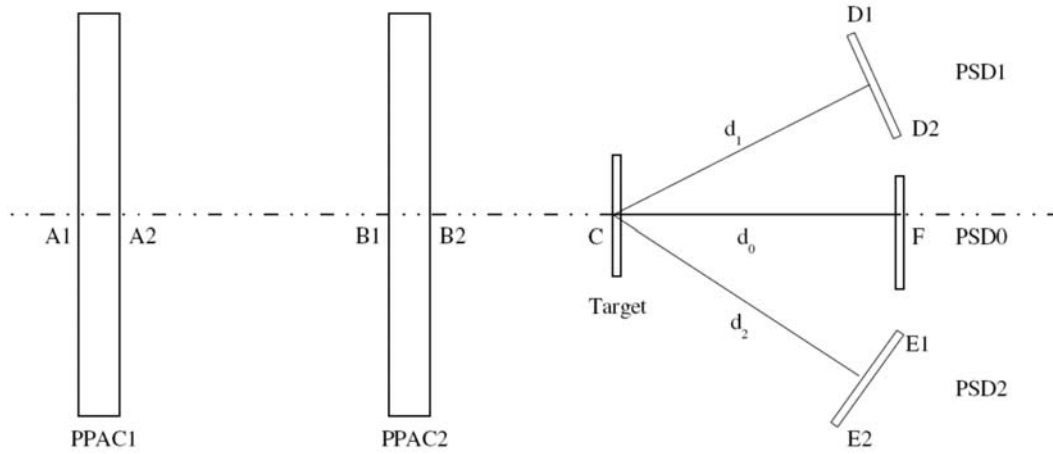


Figure C.3: Geometry of detectors in the F3 chamber at CRIB, from top view.

Table C.1: List of measured distances (mm) in the detector system in F3 chamber at CRIB for our experimental set-up (refer to figure C.3).

A1A2	52	B1B2	51	A2B2	56.8	B1C	248
B2C	197	B1F	453	B1D1	435	B1D2	441
B1E1	445	B1E2	429	CD1	193	CD2	189
CF	208	CE1	205	CE2	207		

# Bibliography

- [1] Glaus E. Rolfs and William S. Rodney, *Cauldrons in the Cosmos — Nuclear Astrophysics*, The University of Chicago Press, 1988
- [2] Christian Iliadis, *Nuclear physics of Stars*, WILEY-VCH, 2007
- [3] Roland Diehl *et al.*, *Radioactive  $^{26}\text{Al}$  from massive stars in the Galaxy*, *Nature* **439** (2006) 45-47.
- [4] Jordi José, Margarita Hernanz and Alain Coc, *New results on  $^{26}\text{Al}$  production in classical novae*, *APJ* **479** (1997) L55-L58.
- [5] Jordi José, Alain Coc and Margarita Hernanz, *Nuclear uncertainties in the NeNa-MgAl cycles and production of  $^{22}\text{Na}$  and  $^{26}\text{Al}$  during nova outbursts*, *APJ* **520** (1999) 347-360.
- [6] Shinya Wanajo, Masa-aki Hashimoto and Ken'ichi Nomoto, *Nucleosynthesis in ONeMg novae: models versus observations to constrain the masses of ONeMg white dwarfs and their envelopes*, *APJ* **523** (1999) 409-431.
- [7] Sumner Starrfield *et al.*, *Nuclear reaction rates and the nova outbursts*, *NPA* **688** (2001) 110c-117c.
- [8] Marco Limongi and Alessandro Chieffi, *The nucleosynthesis of  $^{26}\text{Al}$  and  $^{60}\text{Fe}$  in solar metallicity stars extending in mass from 11 to 120 solar mass: the hydrostatic and explosive contributions*, *APJ* **647** (2006) 483-500.
- [9] D. W. Bardayan *et al.*, *Astrophysically important  $^{26}\text{Si}$  states studied with the  $^{28}\text{Si}(p,t)^{26}\text{Si}$  reaction*, *PRC* **65** (2002) 032801.
- [10] J. A. Caggiano *et al.*, *Identification of new states in  $^{26}\text{Si}$  using the  $^{29}\text{Si}(^3\text{He}, ^6\text{He})^{26}\text{Si}$  reaction and consequences for the  $^{25}\text{Al}(p,\gamma)^{26}\text{Si}$  reaction rate in explosive hydrogen burning environments*, *PRC* **65** (2002) 055801.

- [11] Y. Parpottas *et al.*, *Astrophysically important  $^{26}\text{Si}$  states studied with the  $(^3\text{He}, n)$  reaction and the  $^{25}\text{Al}(p, \gamma)^{26}\text{Si}$  reaction rates in explosive hydrogen burning environments*, PRC **70** (2004) 065805.
- [12] D. W. Bardayan *et al.*, *Astrophysically important  $^{26}\text{Si}$  states studied with the  $^{28}\text{Si}(p, t)^{26}\text{Si}$  reaction. II. Spin of the 5.914-MeV  $^{26}\text{Si}$  level and galactic  $^{26}\text{Al}$  production*, PRC **74** (2006) 045804.
- [13] D. Seweryniak *et al.*, *Level structure of  $^{26}\text{Si}$  and its implications for the astrophysical reaction  $^{25}\text{Al}(p, \gamma)^{26}\text{Si}$* , PRC **75** (2007) 062801(R).
- [14] R. C. Runkle, A. E. Champagne, and J. Engel, *Thermal Equilibration of  $^{26}\text{Al}$* , APJ **556** (2001) 970-978
- [15] D. Bazin *et al.*, *The S800 spectrograph*, NIM B **204** (2003) 629-633.
- [16] J. Yurkon *et al.*, *Focal plane detector for the S800 high-resolution spectrometer*, NIM A **422** (1999) 291-295.
- [17] W. F. Mueller *et al.*, *Thirty-two-fold segmented germanium detectors to identify  $\gamma$ -rays from intermediate-energy exotic beams*, NIM A **466** (2001) 492-498.
- [18] A. H. Hernández *et al.*, *Proton resonance reactions using thick targets in inverse kinematics*, NIM B **143** (1998) 569-574.
- [19] S. Kubono, *Experimental determination of astrophysical reaction rates with radioactive nuclear beams*, NPA **693** (2001) 221-248.
- [20] Glenn F. Knoll, *Radiation Detection and Measurement*, 3rd edition, John Wiley & Sons, 2000
- [21] S. Kubono *et al.*, *New low-energy RIB separator CRIB for nuclear astrophysics*, EPJ A **13** (2002) 217-220
- [22] H. Kumagai *et al.*, *Delay-line PPAC for high-energy light ions*, NIM A **470** (2001) 562-570
- [23] J. Chen *et al.*, *Study of Astrophysically Important States in  $^{26}\text{Si}$  through Elastic Scattering with CRIB*, CNS Annual Report **2006** (2007) 5
- [24] Seiya Hayakawa, MSc thesis, 2007
- [25] , *The BAQ/Data Acquisition/DAQ System in nuclear experiments at RIKEN*, <http://ribf.riken.jp/baba/acquisition/system/index.html>
- [26] O. B. Tarasov *et al.*, *LISE++: a simulation of fragment separators*, <http://groups.nsl.mscl.msu.edu/lise/lise.html>

- [27] T. Baumann *et al.*, *Discovery of  $^{40}\text{Mg}$  and  $^{42}\text{Al}$  suggests neutron drip-line slant towards heavier isotopes*, *Nature* **449** (2007) 1022-1024
- [28] S. Takeuchi, ANAPAW data analysis tool for nuclear experiments at CRIB, [http://rarfexp.riken.go.jp/gibelin/riken\\_guide/node10.html](http://rarfexp.riken.go.jp/gibelin/riken_guide/node10.html)
- [29] R. Fox, SpecTCL — a powerful nuclear event data analysis tool, <http://docs.nscl.msu.edu/daq/spectcl/>
- [30] Rene Brun *et al.*, ROOT - An Object Oriented Framework For Large Scale Data Analysis, <http://root.cern.ch/drupal/>
- [31] M. Berz *et al.*, *Cosy infinity users guide and reference manual, version 7*. Technical report, Michigan State University National Superconducting Cyclotron Laboratory, 1995, MSUCL-997.
- [32] G. R. Satchler, *Direct Nuclear Reactions*, OUP, Oxford, 1983.
- [33] N. Austern, *Direct Nuclear Reaction Theories*, John Wiley, New York, 1970.
- [34] D. Kunz, DWUCK — A Distorted Wave Born Approximation Program for calculating the angular distribution of the differential cross-section, <http://spot.colorado.edu/kunz/Readme.html>
- [35] K. S. Krane, R. M. Steffen, and R. M. Wheeler, *Directional correlations of gamma radiations emitted from nuclear states oriented by nuclear reactions or cryogenic methods*, *Atomic Data and Nuclear Data Tables* **11** (1973) 351-406.
- [36] P. Tarasa and B. Haas, *Spin assignments following heavy-ion induced reactions*, *NIM* **123** (1975) 73.
- [37] Chr. Bargholtz and P. -E. Tegnér, *Gamma-gamma directional correlations: Simplifications at high spin*, *NIM* **A256** (1987) 513.
- [38] A. Krämer-Flecken *et al.*, *Use of DCO ratios for spin determination in coincidence measurements*, *NIM* **A275** (1989) 333.
- [39] T. Komatsubara *et al.*, in preparation.
- [40] A. C. Douglas and N. McDonald, *Compound nucleus processes in medium mass nuclei*, *Nuclear Physics* **13** (1959) 382.
- [41] S. M. Grimes *et al.*, *Level density and spin cutoff parameters from continuum (p,n) and (n) spectra*, *PRC* **10** (1974) 2373.
- [42] S. Flibotte *et al.*, *Multidimensional analysis of high resolution  $\gamma$ -ray data*, *NIM* **A 320** (1992) 325.

- [43] D. C. Radford, *ESCL8R and LEVIT8R: Software for interactive graphical analysis of HPGe coincidence data sets*, NIM A **361** (1995) 297.
- [44] G. Palametaa and J.C. Waddington, *Background subtraction of (HI, xn $\gamma$ ) coincidence spectra*, NIM A **234** (1985) 476
- [45] G. Hackman and J. C. Waddington, *Background subtraction of multiple-fold gamma-ray coincidence data: an operator approach*, NIM A **357** (1995) 559.
- [46] B. Crowell *et al.*, *Background subtraction for high-fold gamma-ray coincidence data*, NIM A **355** (1995) 575.
- [47] D. C. Radford, *Background subtraction from in-beam HPGe coincidence data sets*, NIM A **361** (1995) 306.
- [48] J. N. Wilson *et al.*, *Determination of optimum gating fold, shape and width for analysis of high-fold gamma-ray coincidence data*, NIM A **399** (1997) 147.
- [49] K. Starosta *et al.*, *Background subtraction for Doppler-shift attenuation and angular correlation measurements with multi-detector Ge arrays*, NIM A **515** (2003) 771.
- [50] J. C. Thomas *et al.*, *Beta-decay properties of  $^{25}\text{Si}$  and  $^{26}\text{P}$* , EPJ A **21** (2004) 419-435.
- [51] J. F. Ziegler, *The Stopping and Ranges of Ions in Matter*, vols. 3. and 5, Pergamon Press, Oxford, 1980.
- [52] A. M. Lane, and R. G. Thomas, *R-Matrix Theory of Nuclear Reactions*, Rev. Mod. Phys. **30** (1958) 257
- [53] Erich Vogt, *Theory of Low Energy Nuclear Reactions*, Rev. Mod. Phys. **34** (1962) 723
- [54] F. C. Barker, *Calculation of the  $^{12}\text{C}+\alpha$  capture cross section at stellar energies*, Aust. J. Phys **24** (1971) 777
- [55] F. C. Barker, *The Boundary Condition Parameter in R-matrix Theory*, Aust. J. Phys **25** (1972) 341
- [56] C. R. Brune, *Alternative parametrization of R-matrix theory*, PRC **66** (2002) 044611
- [57] C. Angulo and P. Descouvemont, *R-matrix analysis of interference effects in  $^{12}\text{C}(\alpha, \alpha)^{12}\text{C}$  and  $^{12}\text{C}(\alpha, \gamma)^{16}\text{O}$* , PRC **61** (2000) 064611

- [58] D. V. Booker, *The divergence from Gaussian of peak shapes in gamma-ray spectra with germanium detectors*, Journal of Radioanalytical Chemistry **48** (1979) 83-90
- [59] J. D. Valentine, and A. E. Rana, *Centroid and Full-Width at Half Maximum Uncertainties of Histogrammed Data with an underlying Gaussian Distribution - The Moments Method*, IEEE Transactions on Nuclear Science **43** (1996) 5
- [60] D. Radford *et. al*, *GF3: Interactive graphical analysis of gamma-ray coincidence method for segmented germanium detectors*, physics Division at Oak Ridge National Laboratory. <http://radware.phy.ornl.gov/main.html>.
- [61] R. Coszach *et. al*, *Resonant scattering of isobaric  $^{19}\text{Ne}$  and  $^{19}\text{F}$  beams on an H target*, PRC **50** (1994) 1695
- [62] Y. Yanagisawa *et. al*, *Low-energy radioisotope beam separator CRIB*, NIM **A539** (2005) 74-83
- [63] S. Kohara *et. al*, *Flat-top acceleration system in the RIKEN AVF cyclotron*, NIM **A526** (2004) 230-238
- [64] J. F. Ziegler, *SRIM - The Stopping and Range of Ions in Matter*, <http://www.srim.org/>
- [65] H. Yamaguchi *et. al*, *Low-lying non-normal parity states in  $^8\text{B}$  measured by proton elastic scattering on  $^7\text{Be}$* , Physics Letters **B672** (2009) 230-234
- [66] Th. Delbar *et al.*, *One-step energy scanning of wide low-lying  $1^-$  resonances in  $^{13}\text{C}+p$  and  $^{13}\text{N}+p$  scattering*, NPA **542** (1992) 263-277
- [67] Chris Ruiz, *Aspects of Nuclear Phenomena Under Explosive Astrophysical Conditions*, Ph.D thesis, 1993
- [68] Chris. Ruiz, private communication
- [69] E. C. Simpson, *R-matrix analysis of CNO cycle reactions*, Ph.D thesis, 2006
- [70] N. M. Larson, *A code system for multilevel R-matrix fits to neutron data using Bayes' equations*, ORNL/TM-9179/R5 (2000, unpublished)
- [71] George R. Satchler, *Introduction to Nuclear Reactions*, WILEY, 1980
- [72] G. M. Bailey, G. M. Griffith and T. W. Donnelly, *The photodisintegration of  $^3\text{He}$  from a direct capture model of the  $d(p, \gamma)^3\text{He}$  reaction*, NPA **94** (1967) 502
- [73] C. Rolfs, *Spectroscopic factors from radiative capture reactions*, NPA **217** (1973) 29

- [74] H. Herndl, J. Görres and M. Wiescher, *Proton capture reaction rates in the  $rp$  process*, PRC **52** (1995) 1078
- [75] C. Iliadis *et al.*, *New stellar reaction rates for  $^{25}\text{Mg}(p, \gamma)^{26}\text{Al}$  and  $^{25}\text{Al}(p, \gamma)^{26}\text{Si}$* , PRC **53** (1996) 475
- [76] J. A. Caggiano *et al.*, *Spectroscopy of  $^{23}\text{Al}$  and  $^{27}\text{P}$  using the  $(^7\text{Li}, ^8\text{He})$  reaction and the implications for  $^{22}\text{Na}$  and  $^{26}\text{Al}$  nucleosynthesis in explosive hydrogen burning*, PRC **64** (2001) 025802
- [77] J. J. He *et al.*, *Investigation of structure in  $^{23}\text{Al}$  via resonant proton scattering of  $^{22}\text{Mg} + p$  and the  $^{22}\text{Mg}(p, \gamma)^{23}\text{Al}$  astrophysical reaction rate*, PRC **76** (2007) 055807
- [78] D. H. Wilkinson, in *Nucleare Spectroscopy*, edited by F. Ajzenberg-Selove, Academic Press, New York, 1988
- [79] P. M. Endt, *Supplement to Energy Levels of  $A=21-44$  Nuclei (vii)*, NPA **633** (1998) 1
- [80] *Evaluated Nuclear Structure Data File*, <http://www.nndc.bnl.gov/ensdf/>.
- [81] *RadWare - a software package for interactive graphical analysis of gamma-ray coincidence data*, <http://radware.phy.ornl.gov/gf3/gf3.html>.